Ultrasonic Testing of ML80 and Grade 483 Q&T Steel

by

Kartik Vasudev

A thesis submitted in partial fulfillment of the requirements for the degree of

Master of Science

in

Materials Engineering

Department of Chemical and Materials Engineering
University of Alberta

Abstract

ML80 and Grade 483 are heat treatable steels, produced by a quench and temper process, that are used in the oil and gas industry. The development of the microstructure during heat treatment is important to ensure that the correct properties are achieved for these steels. However, a real-time monitoring method to ensure that the proper microstructure has been formed is not available at this time. Ultrasonic testing has the possibility of being used to measure the microstructure of steels after heat treatment. The purpose of this research is to investigate the connection between ultrasonic parameters and the martensite microstructure fraction in heat treated steel. Ultrasonic measurements are conducted in pulse-echo mode, using longitudinal and shear wave modes. Using ultrasonic velocity and attenuation measurements, this research analyzes the relationship between the ultrasonic parameters, steel hardness measurements, and microstructure fraction measurements. These measurements are taken at varying distances along the axial direction of Jominy end quench specimens of ML80 and Grade 483 Q&T steel.

Lower ultrasonic longitudinal velocity is measured for steel materials with higher hardness, and lower velocity is correlated with higher martensite fractions for both steel types examined. Ultrasonic attenuation is found to be highest in martensite for both steel types. Ultrasonic wave energy loss (ultrasonic energy attenuation) is measured using a Fourier transform method and is observed to obey the same trend seen in attenuation, with martensitic microstructures showing increased energy loss. Calculation of Poisson's ratio from ultrasonic measurements is examined as an alternative to ultrasonic velocity calculations.

- L’essential est invisible pour les yeux, répéta le petit prince, afin de se souvenir.
- C’est le temps que tu as perdu pour ta rose qui fait ta rose si importante.

- *Le Petit Prince,* Antoine de Saint-Exupéry

Table of Contents

List of Tables

List of Figures

Glossary of Terms

Acoustic Impedance (AI) - The physical value of a material's resistance to the entry of acoustic perturbations, measured in $Pa*s/m^3$.

Attenuation - The measurement of the decay of a signal as it propagates in time or space, measured in dB/mm or dB/s. *See Decibel*.

Bainite - A microstructure found in steel, composed of clusters of fine networks of ferrite, often with cementite or retained austenite between ferrite sheaves. Bainite is typically characterized by high hardness and moderate ductility.

Casing - A component of oil and gas wells, used to line the borehole, providing structure and allowing a channel for oil and gas to be extracted.

CCT - **C**ontinuous **c**ooling **t**ransition, a type of graph showing the microstructure formed for a range of cooling rates.

Cementite - A microstructural component with chemical composition Fe_3C, often resulting from diffusion of carbon out of solid solution during the transformation from austenite to ferrite.

Decarburization - The diffusion of carbon into the external environment during high-temperature heating of steel.

Decibel (dB) - The logarithmic scale used to measure the spatial or temporal decay of a signal as it propagates. Decibel scales are not used to communicate a signal strength, but rather the comparative strengths at two points in space or time.

Digital - Represented by only 0's and 1's. When referring to a signal, digital refers to having discreet (not continuous) values in both the x and y (and additional) dimensions. *See Signal.*

Discreet - Having values specified at only certain point-values rather than being defined along a continuous spectrum. *See Signal.*

Ductility - The ability of a material to undergo stretching without failure.

Effective Velocity - The apparent, or average, velocity at which an ultrasonic wave travels through a material, as determined by the initial and final time measurements, without accounting for momentary fluctuations in velocity caused by material inhomogeneity.

Electron Backscatter Diffraction (EBSD) - A technique for measuring the crystallographic structure of a material on a microscopic level. The process uses a beam of electrons that interacts with a thin-depth of the material surface.

	The electrons are deflected in characteristic patterns, used to identify the crystal structure.
Ferrite	- Body-centered cubic atomic structured iron, most commonly found in room-temperature steel.
Filtering	- In signal processing, filtering is a method of selecting frequencies or a range of frequencies to be kept or rejected from the signal. Filtering is often applied prior to taking a Fourier Transform to reduce the amount of high-frequency components resulting from sharp edges.
Fitting	- A component of an oil and gas transport system, used to route and control the flow of fluids. - A statistical method of determining a line or curve that best fits a set of data.
Fourier Transform (FT)	- A mathematical method of decomposing a discreet signal into the frequency components, showing the strength of each component and the phase shift present on each. Used to convert a function from the time-domain to the frequency-domain (and vice versa).
Frequency-domain	- Signals when seen after transformation by a Fourier Transform.
Hardness	- A measurement of how much force is required to produce an indentation in the surface of a material. Many different methods for making these measurements exist, depending on the type of materials and the size scale being used.
Jominy End Quench Test	- A uniaxial heat treatment method where a cylindrical rod is heated, then quenched on only one end, producing a spectrum of hardness values and microstructures along the length. Used to investigate the states resulting from varying cooling rates. *See Quenching.*
Kernel Average Misorientation (KAM)	- The difference between individual EBSD crystallographic orientation measurement locations and the measurements obtained for the neighboring test locations. *See Electron Backscatter Diffraction.*
Longitudinal	- In wave propagation, waves where the particle motion is in the direction of the wave travel.
Martensite	- A meta-stable phase in iron forming from an incomplete transformation from austenite to ferrite, occurring more easily in materials with certain chemical compositions, including higher carbon fractions. Martensite is characterized by high hardness and low ductility.

Microalloyed Steel - Low carbon steel very small additions of certain elements, including niobium, vanadium and titanium, to improve strength.

Microstructure - The structure of a material when seen on a microscopic level.

Noise - Random, usually high-frequency, fluctuation in a signal.

Non-destructive Testing (NDT) - A class of methods used to examine material properties without the need to break cut or otherwise change the material before examination.

Parseval's Theorem - A theory by Marc-Antoine Parseval stating that the sum of square of a function is equal to the sum of the square of the function's transform. Usually used to state the equivalence of energy calculated from time-domain signals and their transformed frequency-domain signals.

Pearlite - A microstructure of steel composed of alternating lamella (plates) of ferrite and cementite.

Pitch-Catch - Ultrasonic measurement mode in which the transducer producing the ultrasonic disturbance is different than the transducer used to collect the ultrasonic signal.

Probe - Another name for *Transducer*, but specifically referring to the entire device used to deliver an ultrasonic perturbation resulting from an electrical signal.

Pulse-Echo - Ultrasonic measurement mode in which the same transducer is used to produce and receive the ultrasonic disturbance.

Quenching - Cooling method where a heated piece of steel is cooled in water or oil to achieve a high-cooling rate.

Sampling - Conversion from an analog (continuous) signal to a digital or discreet signal by making period measurements.

Shear - In wave propagation, where the particle motion is perpendicular to the travel direction of the wave.

Signal - A mathematical function, usually characterized by the change in function value with time.

Smoothing - Low-pass filtering method in which high frequency components are eliminated, resulting in a signal with less rapid changes. Usually used to reduce the amount of noise in the signal.

Spectrum - Continuously defined, 1-dimensional set of values.

Tempering - Heating treatment using moderate temperatures to allow diffusional changes in a material to reduce internal stresses and allow continued crystallographic transformations.

Thermomechanical Controlled Processing (TMCP)	- Method of producing steel using temperature control and deformation to produce steel with a desired set of mechanical properties.
Time-domain	- A representation of a signal where the x-axis represents changes in time.
Transducer	- Device used to convert an electrical signal into a physical disturbance, or vice versa.
Ultrasonic	- Acoustic waves with frequency greater than 20kHz, the upper limit of the range of human hearing.
Ultrasonic Testing	- A non-destructive testing method where acoustic disturbances are made in a material, with the reflections of the waves or the properties of the wave at collection being used to make inferences about the material.
Wavelength	- The distance between two peaks or troughs in a wave. Mathematically represented as the spatial distance covering a 2π complex-valued rotation.
Yield Strength	- The force-per-unit area required to cause a material to undergo plastic, non-reversible changes in shape.

Chapter 1 - Introduction

Ultrasonic testing (UT) is a common method of detecting cracks and defects in materials. UT has the potential to be used to evaluate the microstructure of a material based on the velocity or attenuation of ultrasonic waves. Studies conducted on medium-carbon steel show lower ultrasonic velocities for martensitic microstructures when compared to ferritic, pearlitic, bainitic or mixed microstructures [1][2] [3]. This relationship is found for both longitudinal and shear wave modes. Measurements on L80 steel, a casing steel with a minimum yield strength of 552 MPa (80 ksi), were performed by Kennedy [4]. Shear wave mode velocity was found to be lower in martensite, when compared to bainite and ferrite-pearlite microstructure. Ultrasonic longitudinal attenuation is found to be highest in martensitic microstructures [1] [4].

During manufacturing, steel may be quenched to produce a microstructure consisting entirely of martensite. Tempering is subsequently applied to the steel to improve the ductility. The predominance of a martensitic microstructure after quenching is necessary to achieve the strength requirements of casing and fitting steel. Evaluation of the steel properties and microstructure is typically undertaken only after the tempering process. A method of evaluating the quenching process, ensuring that a martensitic microstructure has been achieved through the thickness of the steel, does not exist. The potential exists to use ultrasonic measurements of velocity and attenuation to make real-time measurements on the success of quenching during steel manufacturing.

This research presents ultrasonic velocity and attenuation measurements made on ML80 casing steel and Grade 483 quenched and tempered (Q&T) fitting steel to assess the possibility of ultrasonic measurement of quenching success. ML80 is a casing steel with high molybdenum content and with a minimum yield strength of 552 MPa (80 ksi). Grade 483 Q&T steel is used in pipeline fittings and has a minimum yield strength of 483 MPa (70 ksi) Jominy end quench specimens are produced and tested for both ML80 and Grade 483 Q&T steel types. Jominy end quench tests allow the production of a wide spectrum of microstructures within a single specimen, allowing for easy comparison between ultrasonic parameters and microstructures.

Samples for UT are cut from Jominy specimens to produce samples with microstructures ranging from predominantly martenisitic- to a predominant mix of pearlite and ferrite. The microstructure of the samples is compared to the ultrasonic velocity and attenuation through the samples. Spectral analysis is also performed on ultrasonic signals from steel samples to measure the rate of signal energy attenuation. The goal of this research is to investigate the relationship between ultrasonic parameters with martensite microstructure fraction. A method is also proposed for using ultrasonic velocity and attenuation values to estimate martensite fraction in specimens with simple geometries, such as in the walls of steel casings or fittings.

Chapter 2 - Literature Review

This chapter presents information on steel, Jominy end quench tests and UT of steel. A background on steel materials is provided, including a description of phase diagrams and information on microstructures that are important for this work. The section discussing general information of steel also presents data on hardness testing of steel and on continuous cooling transformation (CCT) diagrams. The section about Jominy end quench tests presents general information on end quench tests and provides literature results of cooling rates observed through measurements and modelling. Fundamentals of UT are then presented, followed by literature results discussing the measurement of ultrasonic parameters on carbon steels. Ultrasonic parameter sections are divided into information on ultrasonic velocity and ultrasonic attenuation. Ultrasonic velocity is discussed in relation to hardness, microstructure, dislocation density and ultrasonic frequency. Literature on ultrasonic attenuation covers the relationship between attenuation, hardness and microstructure. Literature results of ultrasonic attenuation measurement by echo energy are also presented.

2.1 Background on Steel

This section presents background information on steel, including the iron-carbon phase diagram, descriptions of microstructures, hardness testing methods and CCT diagrams. The phase diagram, provided in Figure 2.1, shows the phase of an iron-carbon system that form on equilibrium cooling [5, p. 333]. At high temperatures, a high temperature iron phase called austenite forms. Austenite has a face-centered cubic crystal structure and high solubility of carbon. Ferrite, or α-ferrite, is formed by iron atoms in a body-centered cubic crystal structure, and is an important component of most carbon steel [5, p. 333]. Solubility of carbon in ferrite is low, and as the temperature decreases precipitation can occur, forming Fe_3C, or cementite. The arrangement of cementite formations within the steel provides important contributions to mechanical properties. Thermomechanical controlled processing (TMCP) can be used to control the formation and arrangement of phases in steel, producing microstructures with desirable mechanical properties, i.e. a mix of high strength and ductility.

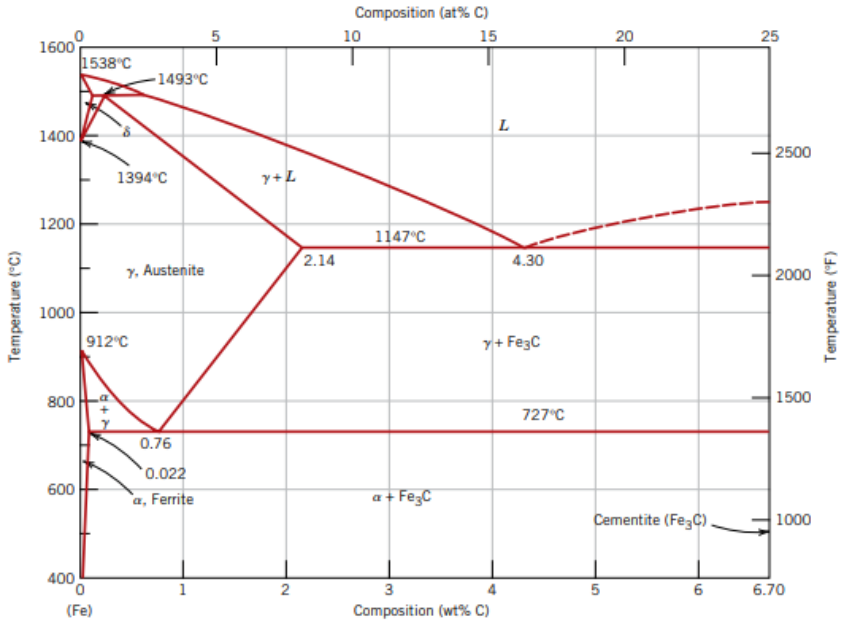

Figure 2.1 – The iron-carbon phase diagram (up to a 6.7 weight percent carbon), showing the phase range of carbon steel for equilibrium cooling [5, p. 333].

Microalloyed (MA) steels are a type of low carbon steel used for high strength applications, such as in oil and gas wells and pipelines [6] [7]. MA steels are designed to provide good weldability, which means a good combination of high strength and ductility is produced after the welding process. They may also be designed for wet or sour (where H_2S is found) environments [8]. A variety of alloying elements are used to provide the properties required of MA steels, including manganese, niobium, molybdenum, titanium and vanadium [9]. The addition of these alloying elements helps to improve strength by refining grain structure and inducing precipitation [9] without the need for a costly and energy intensive quenching and tempering process [10]. In the case of molybdenum, alloying can also reduce embrittlement in sour environments [8].

A quench and temper (Q&T) process occurs in two steps. The first step, quenching, is the rapid cooling of the steel from an austenitic temperature using water. Quenching is used to produce a martensitic microstructure with high hardness and low ductility. The second stage in a Q&T process is tempering, where the steel is reheated to a temperature below austenitization to improve the toughness and ductility of the steel [11].

Several common formations of phases, called microstructure, are important for this work. Ferrite microstructures form when the iron-carbon solution solidifies in blocks of α-ferrite, called grains. The formation of this microstructure is common when carbon content is low enough to produce limited amounts of cementite and when cooling rates are low enough to allow the formation of large crystals of α-ferrite [5, p. 334].

The mixture of α-ferrite and cementite is common in many microstructures found in steel. When alternating lamellar structures of α-ferrite and cementite form, the microstructure is known as pearlite. Pearlite is named for its similarity in appearance to mother-of-pearl when viewed under an optical microscope [5, p. 337]. Pearlite has intermediate hardness and ductility values [5, p. 337].

Bainite is a microstructure formed of scattered, elongated ferrite grains. Bainite can consist of a mixture of ferrite and cementite or can be entirely ferrite [12]. Cementite can be found along grain boundaries or in non-lamellar distributions within the ferrite grains [12]. The mechanical properties of bainite usually include a high strength and moderate ductility, making it a desirable microstructure for a variety of applications [12].

Martensite is a metastable phase of iron, forming on rapid cooling [5, p. 338]. Martensite forms in elongated slats, called laths, between carbon concentrations of 0 and 0.6 weight percent (wt. %). Above 1 wt. % carbon, lenticular martensite forms, which takes on a lens-shaped appearance. At carbon concentrations in-between, a mix of martensite types occurs [13]. Martensite is characterized by very high hardness and strength, but very low ductility. The low ductility makes it an undesirable microstructure for many applications, including oil and gas pipelines. According to measurements by Ohmura et al., in 0.2 wt. % carbon steel, the microhardness of martensite is approximately 480 HV [14]. Many applications use a tempering process after the formation of martensite, by heat treating below austenitic temperatures for several hours [15]. The tempering process allows the transformation of the metastable martensite phase into ferrite, substantially increasing ductility at the cost of strength.

After cooling from an austenitic temperature, a certain amount of austenite can remain within the steel microstructure. Austenite that has remained stable during cooling is called retained austenite. In low carbon steel, volume fractions of retained austenite remain small (below 10%), unless alloying additions are used to increase retained austenite fractions [16]. Certain steel grades are specifically designed to incorporate retained austenite, such as quenched and partitioned (Q&P) steels, which include high-silicon content to stabilize austenite [17]-[19]. These steels often have similar chemistry to pipeline steels, but with additional silicon content of around 1.5 wt. % [19]. Retained austenite content in these steels is often around 10% [18]. In low carbon API X70 steel, [20], specimens were homogenized and quenched in an examination of microstructure. Quenching of the steel resulted in a primarily martensite microstructure with the presence of some retained austenite, although volume fractions of the retained austenite phase were not given [20]. Retained austenite was also found in the microstructure of low carbon X80 steel [21] after hot-rolling.

During cooling of steel, microstructural features known as martensite-austenite (M-A) can form [22]. M-As are small (typically with grain sizes around 1 μm), block-shaped particles formed of

martensite and retained austenite [23].The formation of M-A constituents has been observed in low carbon steel [22]-[25] and are typically formed during rapid cooling, such as in the heat affected zone of weldments in pipeline steel [24]. M-A constituents have been reported in low carbon steel at cooling rates as low as 5 K/s [23], with volume fractions of 0.1 %. In the intercritically reheated coarse grained heat affected zone (ICRCGHAZ) of X70 pipeline steels, M-A fractions as high as 7.5 % are reported [24]. M-A constituents are known to form along the prior-austenite grain (PAG) boundaries [22], and have been studied for their adverse impact on strength and toughness in microalloyed steels [24] [26].

2.1.1 Hardness of Steel

Two primary types of hardness measurements are examined in this work, namely Rockwell C Hardness (HRC) and Vickers hardness (HV), discussed in detail in ASTM Standards E-18 [27] and E-384 [28], respectively. For HRC measurements, a diamond spheroconical indenter is pressed against the test specimen with a 10 kilogram-force (kgf), shown in Stage 1 of Figure 2.2a. In Stage 2, the force is increased to 150 kgf creating a deeper, wider indentation. The difference in the depth of the indentation between the two stages is measured and the value of hardness is calculated using Equation 2.1:

$$HRC = 100 - \frac{h}{0.002}, \qquad \text{(Equation 2.1)}$$

where *HRC* is a unitless measure of hardness and *h* is the difference in indentation height, measured in mm.

For Vickers hardness (Figure 2.2b), a diamond indenter is placed on the test specimen with a force F_{HV} (in gf) for a dwell period between 10 to 15 seconds [28]. The Vickers hardness value is calculated by dividing the applied force by the surface area of the indentation, as shown in Equation 2.2:

$$HV = 1854.4\frac{F_{HV}}{d^2}, \qquad \text{(Equation 2.2)}$$

where HV is a unitless value, F_{HV} is the applied force (in gf) and *d* is the mean diagonal length of the indentation (in µm). The mean diagonal length, *d*, is calculated from the two diagonal lengths, labeled 'height' and 'width' in Figure 2.2b, by optical measurement and allows calculation of the surface area of the indentation. Typical diagonal lengths for steels range from 50 to 100 µm [28].

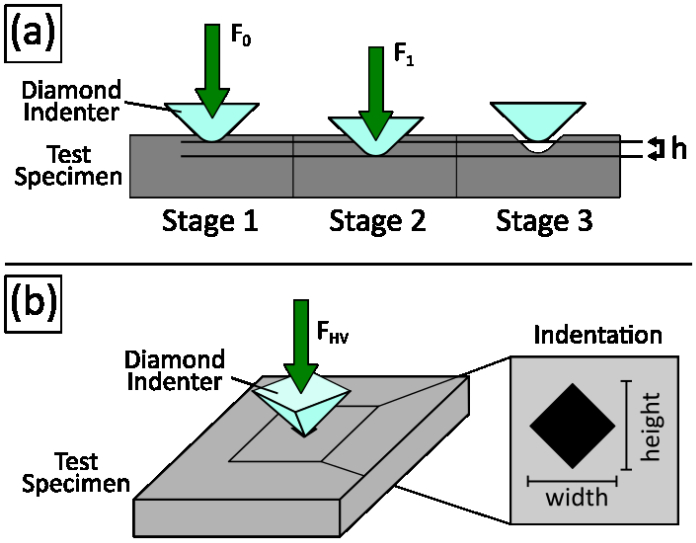

Figure 2.2 – Hardness measurement procedures by (a) Rockwell and (b) Vickers hardness methods.

Literature sources cite a difference between microhardness and macrohardness (often simply called hardness) as being dependent on the load force that is used for Vickers hardness testing. Microhardness is defined as hardness measurements made with a force between 1 gram and 1 kilogram [29][30]. Measurement of Vickers microhardness and macrohardness show that consistent results are found across load ranges of 10 g to 10 kg for a wide range of hardness values in steel specimens, with differences primarily occurring at the lower end of optical resolution for a given hardness tester [30]. The relationship between varying load ranges allows for direct comparison of Vickers microhardness values with loads of 500 g to 1 kg. Typical Vickers hardness values range from 200 to 600 HV in steel, depending on material, the force and the dwell time used [30].

2.1.2 CCT Diagrams for Steel

A continuous cooling transformation (CCT) diagram shows the development of different microstructures for a unique steel chemistry. CCT curves show the microstructures that can be formed with constant cooling rates, the temperature at which they begin, and sometimes the hardness achieved. The CCT curve is unique for each chemical composition and is useful for estimating microstructures formed on cooling, and an example is shown in Figure 2.3.

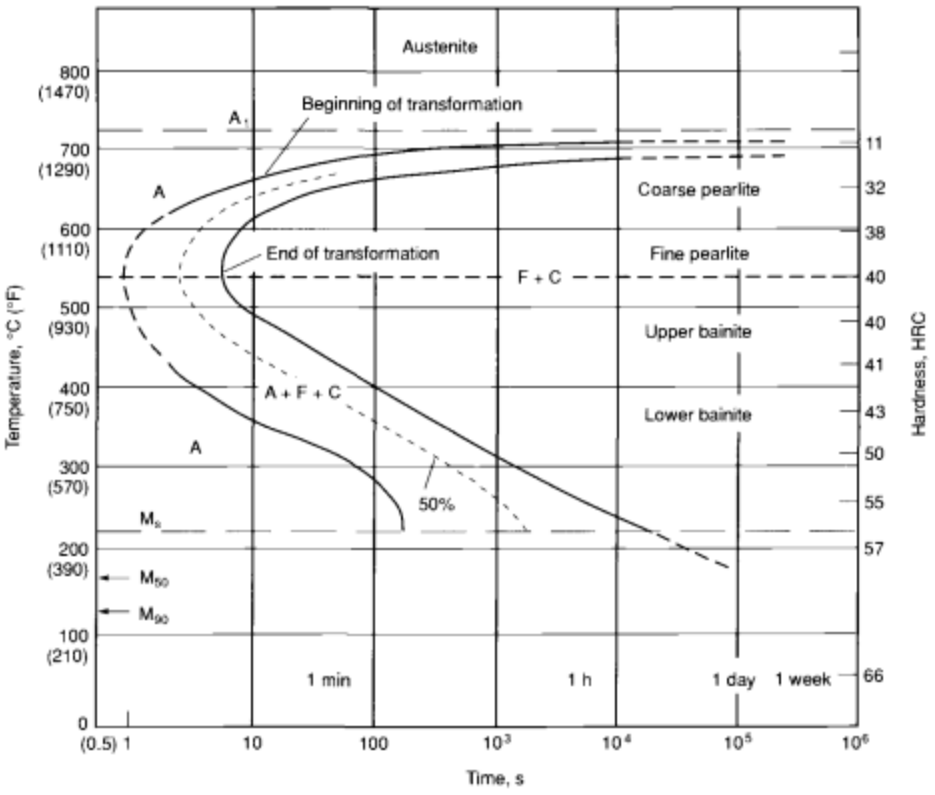

Figure 2.3 – A CCT diagram for AISI 1080 steel, showing microstructure formation during isothermal cooling [31, pp. Vol. 1, pp. 128]

2.2 Jominy End Quench Specimens

The Jominy end quench test uses a cylindrical steel rod with a 2.54 cm (1 inch) diameter, which is heated to an austenitic temperature (800-925 °C). A stream of water is then directly vertically onto the bottom surface of the specimen [32]. A high cooling rate is achieved at the bottom surface where the specimen is in contact with the water stream. The cooling rate decreases at further distances from the quenched end, producing a spectrum of cooling rates between the quenched end and the top end of the specimen. The spectrum of cooling rates results in a range of hardness and microstructures being produced along the length of the specimen, with the highest hardness values found at the quenched end [33]. The benefit of the Jominy end quench test is that a full range of hardness and microstructures can be formed on a single specimen.

Cooling rates for Jominy end quench specimens have been estimated through computer simulation [34]-[36] and thermocouple placement within test specimens during quenching [35]-[39]. Minor differences in properties along the radial direction of Jominy end quench specimens were observed [33], but those differences were reduced by increased heating times [40], which is accounted for in the Jominy end quench standard, ASTM A255-10 [32]. Table 2.1 shows cooling rates at various distances from the quenched end of the specimen. High cooling rates were

observed near the quenched end, dropping off rapidly as the distance from the quenched end is increased.

Table 2.1 – Jominy end quench cooling rates measured by embedded thermocouple placement [37][38].

Distance from Quenched End (mm)	Cooling Rate (°C/s)	Reference
1.6	158-238	[37]
3.2	56-73	[37]
4.8	24-28	[37]
6.4	20-23	[37]
9.6	12-13	[37]
12.7	9-10	[37]
25	3.5-5	[38]

2.3 Effect of Materials Properties on Ultrasonic Velocity and Attenuation

This section provides background information of ultrasonic testing (UT) and literature sources on measurements made in steel for ultrasonic velocity and ultrasonic attenuation. Background information on the applications of UT, common testing methods and theory of wave propagation is discussed. Ultrasonic velocity is discussed in relation to steel hardness, microstructure and dislocation density. The relationship between ultrasonic velocity and wave frequency is also discussed. Ultrasonic attenuation is discussed in relation to hardness, grain size and specimen thickness. Higher ultrasonic velocity, for both longitudinal and shear wave modes, is generally correlated with lower hardness. No clear relationship was found between attenuation and hardness. Frequency dependant velocity was not observed in steel, but higher frequency waves were generally found to have higher attenuation.

2.3.1 Background on Ultrasonic Testing

UT is a type of non-destructive testing (NDT) commonly used to detect cracks and defects in metal, and to determine component thickness [41, p. 528]. In NDT, materials can see continued use after examination. In UT, an ultrasonic probe (also called a transducer), capable of producing ultrasonic waves (acoustic waves with a frequency >20kHz) is placed against a test piece. Ultrasonic waves pass from the probe to the test piece, travel through the test piece, and pass to a collection probe where data is acquired for analysis. The collected ultrasonic waves produce an electric signal that can be analyzed to determine important information about the state of the test piece. As an acoustic wave travels through a material, wave energy is lost due to transmission

loss, thermal loss and wave scattering [41, p. 108] [42]. The loss of wave energy is observed as attenuation.

Two methods for collecting ultrasonic waves are common [43, p. 7.33]. One method is called pulse-echo mode, in which the same transducer used to produce the ultrasonic wave is used to collect it after the wave is reflected off surfaces within the test piece. The other method, known as pitch-catch mode, uses a second transducer to collect the ultrasonic wave which is usually placed opposite the first transducer on the test piece.

When traveling through a material, ultrasonic waves propagate around small obstacles without changing the path of the wave. Half the wavelength of the propagating wave is usually used as the cut-off for obstacle size [43, p. 7.11]. Obstacles larger than this threshold act as barriers, blocking and reflecting the ultrasonic wave. Small obstacles, when taken in aggregate, can cause changes in the attenuation of the wave and cause scattering, affecting the overall propagation speed of the wave. The measurement of the wave velocity in a material gives the effective velocity, which provides insight into the overall state of the material. Fine-grained changes to the wave occurring within the material cannot be investigated using UT.

When acoustic waves strike a boundary between two materials some of the wave energy is reflected backwards, and some energy is transmitted forwards into the new material [41, p. 18]. The ratio of reflected to transmitted wave energy increases with greater difference in acoustic impedance between the materials [41, p. 53]. Acoustic impedance is a measure of the resistance of a material to the entry of acoustic disturbances and has units of $Pa \times s/m^3$. The acoustic impedance in a vacuum is 0 $Pa \times s/m^3$ and is in the range of 2×10^7 to 10^8 $Pa \times s/m^3$ for metals. For carbon steel the acoustic impedance is approximately 4.5×10^7 $Pa \times s/m^3$ [44].

Two types of acoustic waves are typically used for UT. One type is known as the longitudinal wave mode (Figure 2.4a), and the other is known as shear (or transverse) wave mode (Figure 2.4b) [43, p. 7.8]. For longitudinal waves, the motion of particles is along the axis of wave travel. For shear waves the motion of particles is perpendicular to the direction of wave travel.

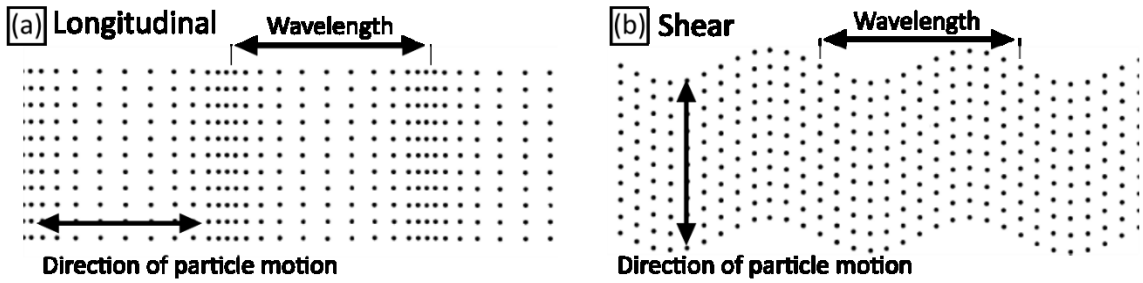

Figure 2.4 – A 2-dimensional representation of (a) longitudinal waves and (b) shear waves. Images used from reference [41, pp. 5,6].

Theoretical calculation of wave velocity is discussed in depth in several literature sources [45] [46, pp. 179-186] [47, pp. 274-309]. The velocity of longitudinal waves in a long thin rod is given by the bar velocity, V_b (in m/s), shown in Equation 2.3:

$$V_b = \sqrt{\frac{E}{\rho}}, \qquad \text{(Equation 2.3)}$$

where E is the Young's modulus (in Pa) and ρ is the density (in kg/m^3) [45, p. 30]. This equation can be extended for the longitudinal velocity of a general plane wave in a homogeneous, isotropic, linearly elastic medium, shown in Equation 2.4 [45, p. 124] [48] [49]:

$$V_L = \sqrt{\frac{E}{\rho}\frac{(1-\nu)}{(1+\nu)(1-2\nu)}}, \qquad \text{(Equation 2.4)}$$

where V_L is the longitudinal velocity, in m/s, and ν is Poisson's ratio, a unitless measure of the ratio of the transverse strain to the axial strain [50]. Similarly, the shear wave of a plane wave can be expressed using Equation 2.5 [45, p. 124]

$$V_T = \sqrt{\frac{E}{2\rho}\frac{1}{(1+\nu)}}, \qquad \text{(Equation 2.5)}$$

where V_T is the transverse, or shear, velocity (in m/s). Kim et al calculated Young's modulus and Poisson's ratio in martensitic and ferritic-pearlitic specimens of SAE 1050 steel [50], using measurements of ultrasonic longitudinal and shear velocity. The calculated values are shown in Table 2.2, along with values of density found in the literature [31, pp. Vol. 15, pp. 795] [51].

Table 2.2 – Elastic constants and densities for martensite and ferrite-pearlite microstructures in SAE 1050 steel [31][50].

	Martensite	Ferrite-Pearlite
E (kg/ms^2)	203.5	210.3
ν	0.2921	0.2877
ρ (kg/m^3)	7630 [51]-7690 [31, pp. Vol. 15, pp. 795]	7870 [31, pp. Vol. 15, pp. 795]

From Table 2.2 and Equations 2.4 and 2.5, an estimate of ultrasonic longitudinal and shear velocities can be obtained for martensite and ferrite-pearlite. Calculations are shown in Appendix A.2.1 for both microstructures, resulting in ultrasonic longitudinal velocity values of 5905-5928 m/s for martensite and 5900 m/s for ferrite. Shear velocities of 3200-3212 m/s for martensite and 3221 m/s for ferrite-pearlite result from calculations using Equation 2.5.

2.3.2 Ultrasonic Velocity in Steel

This section presents literature results for ultrasonic velocity measurements on steel specimens. The relationship between hardness of steel and ultrasonic velocity is shown, as well as the relationship between steel microstructure and velocity. An analysis of the effect on dislocation density is presented next. The possibility of measuring differences in ultrasonic velocity based on frequency is discussed afterwards. Literature sources discuss ultrasonic velocity measurements in a variety of steel types, including low carbon steel [1] [49], medium-carbon steel [1]-[3] [49], cast-iron [1] [52], interstitial free steel [53], stainless steels [48][54]-[60], and tool steels [61]. Different specimen dimensions and shapes are often examined and specimen thicknesses in the literature span a wide range, from 2 mm [53][58], to 32 mm [62]. Studies performed by Bouda et al. examined ultrasonic velocity along the length of Jominy end quench specimens on low- and medium-carbon steels [63][64], and demonstrate the importance of specimen dimensions in making accurate velocity measurements.

2.3.2.1 Hardness and Ultrasonic Velocity

Hamidnia and Honarvar measured ultrasonic shear and longitudinal velocity on 6 mm thick samples of an AISI 52100 steel, which has high carbon (1 wt. %) and high chromium (1.5 wt. %) content [15]. Samples were quenched and then tempered between 200 and 400 °C for one hour. The velocity values were then used to estimate hardness, Young's modulus, shear modulus, bulk modulus and Poisson's ration. The authors attribute an increase in ultrasonic velocity to an increase in ferrite, citing previous studies on the relationship between increasing ultrasonic velocity and decreasing hardness due to microstructural change, although no physical mechanism was described.

Bouda et al. measured ultrasonic velocity and attenuation on Jominy end quench specimens of low- and medium-carbon steels [63] [64]. In low carbon steel, a U-shaped relationship between hardness and ultrasonic longitudinal velocity was observed, with the highest longitudinal and shear velocities measured at the quenched end of the specimen [64]. For the medium-carbon steel, velocity dropped with decreasing hardness (as distance from the quenched end increased) [63]. The measurements performed by Bouda et al. are the only results from the literature sources examined that show an increase in ultrasonic velocity with increasing hardness for steel. No physical explanation for the observed relationship was provided, but the authors described the difficulty in achieving parallel front- and backwall surfaces as a possible source of error in ultrasonic measurements.

In a study on wear-resistant medium-carbon steel, Lukomski and Stepinski measured hardness and ultrasonic velocity of samples in the as-received state (martensite) and after tempering for 30 minutes between temperatures of 200°C to 600°C (tempered martensite) [65]. Ultrasonic longitudinal and shear velocity increased with decreasing hardness for all samples, resulting from

tempering. Longitudinal velocity in martensite samples, with Brinell Hardness (HB) of 550, was 5845-5900 m/s and increased to as high as 5940 m/s in tempered martensite (HB 300). Shear velocity in martensite samples was 3180-3225 m/s, with tempering increasing the velocity to as high as 3260 m/s. The authors used multiple linear regression using heat treatment and chemical composition to correlate hardness and ultrasonic shear velocity. These comparisons yielded the strongest dependence on the alloying elements nickel (Ni), chromium (Cr), silicon (Si), molybdenum (Mo) and manganese (Mn), but no physical mechanism was discussed that would explain the effect of these alloying elements on ultrasonic velocity.

In a study on SAE 1040 steel (with 0.4 wt. % carbon), Gur and Tuncer measured hardness and velocity for microstructures of martensite and tempered martensite, tempered for 2 hours between 200 and 600 °C [2]. Higher hardness was correlated with decreasing ultrasonic velocity. Samples with a martensite microstructure, with Vicker's hardness (HV) of 700, had longitudinal velocities of 5895 m/s, while tempering increased velocities to as high as 5930 m/s for tempered martensite (300 HV). Shear velocity was 3195 m/s for martensite microstructures and increased to as high as 3240 m/s with tempering. Changes in velocity are attributed to the difference in dislocation density, with increases in dislocation density purportedly decreasing ultrasonic velocity.

In general, literature sources reveal that longitudinal and shear wave velocity increases in steels as hardness decreases, whether those hardness changes are due to grain size or microstructure changes. In studies where the results showed the opposite relationship, measurement techniques cast doubt on the accuracy of the measured ultrasonic velocities [64]. Figure 2.5 shows the relationship between hardness and velocity for chosen literature sources. Decreases in ultrasonic longitudinal velocity are seen with an increase in hardness values. Further reading on the relationship between ultrasonic velocity and hardness can be found in the literature [3][60][66][67][68][69][70].

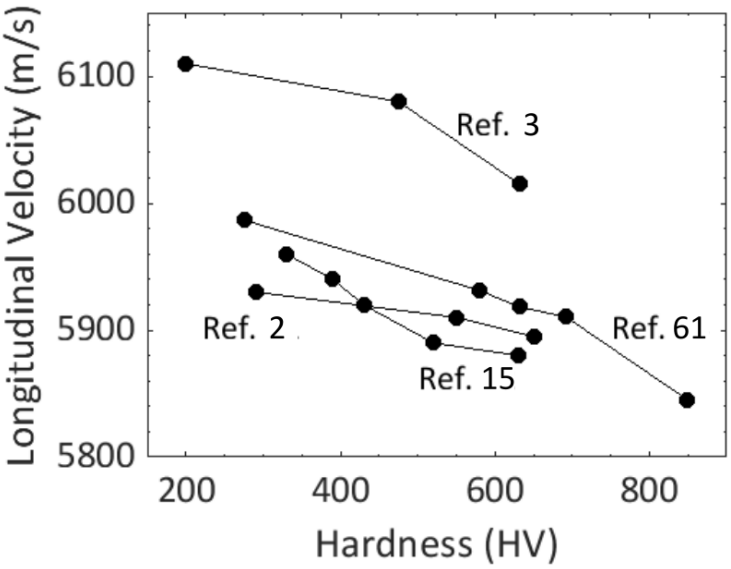

Figure 2.5 – Literature sources showing an inverse relationship between steel hardness and ultrasonic velocity [2] [3] [15] [61].

2.3.2.2 Microstructure and Ultrasonic Velocity

Freitas et al. studied ultrasonic velocity in plain carbon steels with martensite, ferrite and ferrite-pearlite microstructures [1], along with AISI 1045 steel that was heat treated to produce martensite and mixed ferrite-pearlite microstructures. Ultrasonic velocities were lowest for samples with martensitic microstructures, at 5985 m/s for longitudinal wave modes and 3185 m/s for shear wave modes. Ferrite and ferrite-pearlite microstructures produced longitudinal velocities near 5925 m/s and shear velocities near 3235 m/s. The authors of this study attribute changes in velocity to the resistance of the materials to acoustic waves, but do not provide a physical basis for this claim.

In a study on medium-carbon steel (0.45 wt. % C) Behjati et al. measured ultrasonic velocity of water-quenched (lath martensite), oil-quenched (ferrite and fine-pearlite) and air-cooled (ferrite and coarse-pearlite) samples [3]. The lath martensite sample produced the lowest longitudinal velocity at 6010 m/s. Longitudinal velocities of 6080 m/s and 6110 m/s were found for samples with ferrite and fine- and coarse-pearlite microstructures, respectively.

Kennedy examined L80 steel with 0.244 wt.% C using longitudinal and shear wave UT. Ultrasonic longitudinal velocity values for martensite microstructures were between 5895 and 5900 m/s, velocities in ferrite and pearlite microstructures were between 5895 and 5905 m/s [4, p. 102], and velocity in bainite was 5910 m/s [4, p. 102]. Shear velocity measurements showed greater differences, ranging between 3195 and 3210 m/s for martensite microstructures, and 3245-3260 m/s for ferrite and pearlite microstructures [4, p. 101]. Lower ultrasonic velocity for

microstructures with martensite were found across a variety of steel types, which are discussed in the additional literature on ultrasonic velocity measurements [55] [59] [66] [70]-[75].

2.3.2.3 Dislocation Density and Ultrasonic Velocity

The role played by dislocations on the ultrasonic surface velocity was investigated by Barannikova et al. [58] in a study on high chromium (12.5 wt. %) steel. No change in velocity was observed during linear deformation in the elastic regime, but in the presence of plastic deformation under tension velocity changes of up to 0.5% were observed. These observations were made for microstructures of pearlite and tempered martensite. No change in velocity was observed in martensitic samples, owing to the absence of plastic deformation under tension. Velocities were not compared between pearlite, tempered martensite and martensite samples. The authors attribute the change in velocity to an increase in dislocation density imparted during specimen strain, causing a reduced ultrasonic velocity.

Palanichamy et al. measured ultrasonic longitudinal and shear wave velocities in AISI 304 stainless steel with grain sizes between 65 and 170 μm [55]. Increasing grain size was tied to decreasing longitudinal and shear wave velocity. Khan et al. examined ultrasonic longitudinal velocity in AISI 316L stainless steel [54], observing an increasing velocity with increasing grain size. In both cases, no physical explanation is discussed for how grain size can affect ultrasonic velocity. A similar result was found by Mutlu et al. in measurements of longitudinal and shear velocity on Cr-Mo-V steel [61]. The authors suggest that changes in velocity may be a result of dislocation density changes between the microstructures, most notably the higher dislocation density of martensite, when compared to ferrite.

Research by Zhang et al. on interstitial-free steel, named because of the vanishingly small carbon concentration (0.008 wt. %), used variations in heating temperatures and holding times to produce samples with mean grain sizes ranging from 16 μm to 38 μm [53]. Ultrasonic longitudinal velocity measurements showed no difference between specimens with varying grain size. Similarly, Ahn et al examined grain sizes between 5 μm and 30 μm on low carbon steels and found no discernable relationship between ultrasonic velocity and grain size [76].

For pearlitic rail steel Kendarian et al. measured ultrasonic longitudinal velocity during fatigue testing [77]. Ultrasonic longitudinal velocity increased through the fatigue lifecycle by nearly 0.1 %. Absolute velocity values were not given. The authors attribute decreasing ultrasonic velocity with increasing dislocation density. Kim et al. characterized creep-fatigue in ferritic stainless steel by ultrasonic longitudinal velocity and x-ray diffraction [48]. The authors observed an increase in velocity by 15 m/s during the recovery phase, while at the same time dislocation density was observed to decrease. The author report that an increase in dislocation density was tied to an increase in lattice distortion. The authors use the increased lattice distortion as the reason for

the increasing ultrasonic velocity, which they use to tie the ultrasonic velocity changes to changes observed in the microstructure of the steel.

For steels ranging from low to medium carbon, content Buitrago et al. found that increasing carbon content was correlated with increasing ultrasonic longitudinal velocity over a wide range of frequencies, as shown in Figure 2.6 [78]. Differences in microstructure, such as grain size, was not accounted for. A mechanism by which carbon content would affect ultrasonic velocity was not discussed. In the work by Freitas et al., differences in ultrasonic velocity between steels with different carbon content were not observed [1].

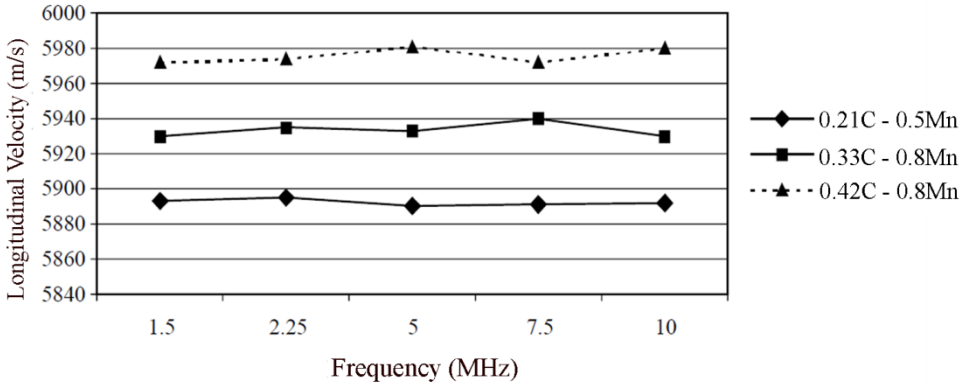

Figure 2.6 - Longitudinal velocity values from three distinct steels, showing increasing velocity with increasing carbon content [78].

2.3.2.4 Frequency Dependence of Ultrasonic Velocity

Freitas et al. measured ultrasonic velocities in carbon steels using 4, 5 and 10 MHz wave frequencies [1]. Differences were observed between the velocity values measured by each, with 5 MHz producing the highest velocity in most cases. Differences between the velocities were as much as 10 m/s for any one specimen. Hsu et al. used 1 MHz and 5 MHz frequencies to measure ultrasonic velocities in martensitic stainless steels [62]. The wave velocity measured using 1 MHz frequencies produced higher velocities, with differences as high as 30 m/s. Neither the work by Freitas et al. nor the work by Hsu et al. explains the difference in ultrasonic velocity with varied wave frequencies.

Phonon dispersion curves, such as those provided in Figure 2.7, show the relationship between wave frequency and wave number [79, p. 432]. Wave number is the reciprocal of wavelength and is calculated using Equation 2.6:

$$k = \frac{2\pi}{\lambda}, \qquad \text{(Equation 2.6)}$$

where *k* is the wavenumber, with units of m^{-1}, and λ is the wavelength, with units of m. In Figure 2.7, the domain spanned by the wavenumber corresponds to a decrease in wavelength, from infinity, at $K/K_{max}=0$, to the length of the unit cell in the [111] direction, at $K/K_{max}=1$.

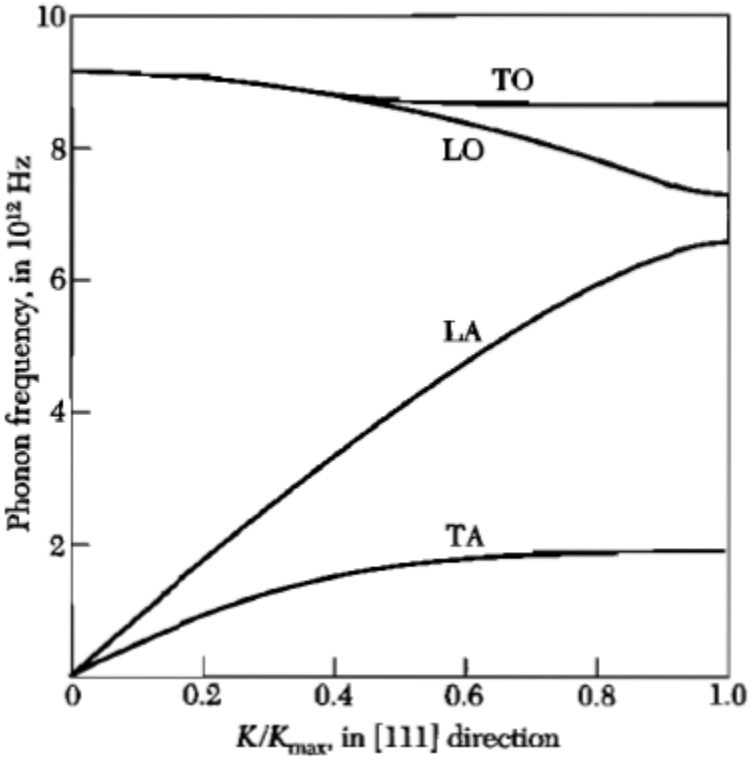

Figure 2.7 – The dispersion relation in a face-centered diamond cubic structure, showing longitudinal (L) and transverse (T) branches for acoustic (A) and optical (O) phonon modes [80, p. 96].

The y-axis (ordinate) of the dispersion curve is expressed in frequency or angular frequency, ω, both with units of Hz, and related by Equation 2.7:

$$\omega = 2\pi f, \qquad \text{(Equation 2.7)}$$

where *f* is the frequency. From the slope of the dispersion curve, wave velocity can be obtained using Equation 2.8:

$$v = \frac{\omega}{k} = f\lambda, \qquad \text{(Equation 2.8)}$$

where *v* is the wave velocity (in m/s), *ω* is the angular frequency (in s^{-1}), *k* is the wave number (in m^{-1}), *f* is the frequency (in s^{-1}) and *λ* is the wavelength (in m). It can be shown that the lower branches of the dispersion curve, which describe ultrasonic wave motion, are always linear in the small wavenumber limit, i.e., for very large wavelengths [79, p. 442] [80, p. 94]. The linear slope,

i.e., linear velocity, for large wavelengths means that no frequency dependent wave velocity is observed in periodic solid crystals.

Wave velocities in steel are approximately 5900 m/s [15] [1] for frequencies around 10 MHz. Equation 2.8 can be used to determine that ultrasonic wavelengths in steel are approximately 0.59 mm, which is several orders of magnitude larger than the length of the unit cell of the material [5], placing ultrasonic waves within the frequency-independent, small wavenumber, region of the dispersion curve. Minkiewicz et al. [81] measured the phonon dispersion in single crystal ferrite using neutron scattering. A dispersion curve of similar shape to that observed in Figure 2.7 was obtained. Further discussion on wave dispersion can be found in Appendix A.2.4.

2.3.3 Ultrasonic Attenuation in Steel

This section presents results from the literature examining ultrasonic attenuation in steel specimens. The effect of hardness and microstructure on ultrasonic attenuation is presented first. Ultrasonic attenuation values from 0.05 dB/mm [60] to 0.9 dB/mm [61] were measured, and have not been clearly correlated to hardness or microstructures changes. Frequency dependence of ultrasonic attenuation is presented next, showing that higher frequencies are attenuated more strongly than lower frequencies.

2.3.3.1 Material Properties and Ultrasonic Attenuation

Freitas et al. [1] measured ultrasonic attenuation for longitudinal waves (at 4 and 5 MHz) in plain carbon steel with martensite, ferrite, and ferrite-pearlite microstructures, as well as for AISI 1045 steel with martensite and ferrite-pearlite microstructures. Ultrasonic attenuation was 0.5 dB/mm for martensite microstructures. Ferrite and ferrite-pearlite microstructures gave longitudinal attenuation values near 0.3 dB/mm. The authors attribute the higher attenuation to the dense structure of martensite, increasing absorption of ultrasonic waves at lath boundaries.

In measurements on AISI 52100 bearing steel, Hamidnia and Honarvar [15] correlated decreasing hardness to an increase in ultrasonic attenuation for both longitudinal and shear wave modes. Attenuation values ranged between 0.054 and 0.206 dB/mm for 5 MHz waves. The decreases in attenuation are attributed to increased scattering resulting from carbides within the steel. Similarly, for low carbon steel (0.16 wt. % C), Kwun et al. measured longitudinal attenuation through ferrite-pearlite microstructures, with ultrasonic attenuation ranging between 0.17 and 0.61 dB/mm. Larger ferrite-pearlite grain sizes were found to yield higher ultrasonic attenuation [49]. The authors attribute the increased attenuation to greater scattering from larger grains, as a result of the larger grains approaching the Rayleigh scattering regime [49], where the size of grains is of similar size to ultrasonic wavelengths.

Ahn and Lee measured ultrasonic attenuation in low carbon steels with carbon content between 0.05 and 0.2 wt. % [82]. Ferrite grain sizes between 30 and 150 µm were observed, with

increasing carbon content reducing grain size. Larger grains were correlated with greater ultrasonic attenuation. Large grain sizes are associated with wave scattering in the Rayleigh regime. The authors attribute changes in attenuation to the presence of scattering, rather than to atomistic effects resulting from the presence of carbon or effects from the presence of carbides within the microstructure.

In a study of an 11.5 wt. % Cr martensitic-ferritic stainless steel (used in power plants), specimens 30 mm in thickness were aged at 700° C for durations between 300 and 1350 hours [83]. Aging caused the spheroidizaton and dissolution of carbides. Specimens aged for longer periods show lower ultrasonic attenuation values. The lower attenuation values for aged samples were attributed to a reduction in carbides, leading to a decrease in wave scattering occurring at the interface between the carbides and the surrounding matrix.

Mutlu et al. measured ultrasonic attenuation in Cr-Mo-V tool steel with varying microstructures [61]. Attenuation decreased with decreasing hardness, with martensitic and ferritic microstructures showing attenuation values of 0.8 and 0.6 dB/mm, respectively. The authors of that study state that the higher attenuation in harder microstructures is due to the small grain sizes and the resulting increase in dislocation density. Higher dislocation densities are suggested to restrict deformation of the material during wave transit, increasing attenuation.

Ogi et al. measured ultrasonic attenuation in AISI 1045 steel during bending fatigue [84]. Attenuation increased in the later stages of fatigue, which the authors attribute to an increase in dislocation density, as well as the formation of microcracks within the structure. Specific attenuation values were not given.

In L80 steel, ultrasonic attenuation was measured for microstructures of martensite, bainite and ferrite-pearlite. Ultrasonic attenuation for both longitudinal and shear wave modes differed little in terms of microstructure. Longitudinal wave mode attenuation values were near 0.25 dB/mm, and shear wave mode attenuation ranged between 0.20 and 0.35 dB/mm [4, p. 103].

Figure 2.8 shows attenuation values as a function of hardness measurements from several literature sources. [15] [60]-[62]. In the work of Hamidnia and Honarvar, increasing hardness was correlated with decreasing attenuation [15]. In work by Mutlu et al. increasing hardness was correlated with increasing attenuation [61]. Other literature sources show no distinct relationship between ultrasonic attenuation and hardness [62][85], suggesting that a more complicated relationship exists between ultrasonic attenuation and the hardness of steel specimens. Additional reading on ultrasonic attenuation can be found in the literature [54] [60] [62][86]-[91]. Much of the literature on ultrasonic attenuation focuses on stainless steels and steels used in the power generation industry.

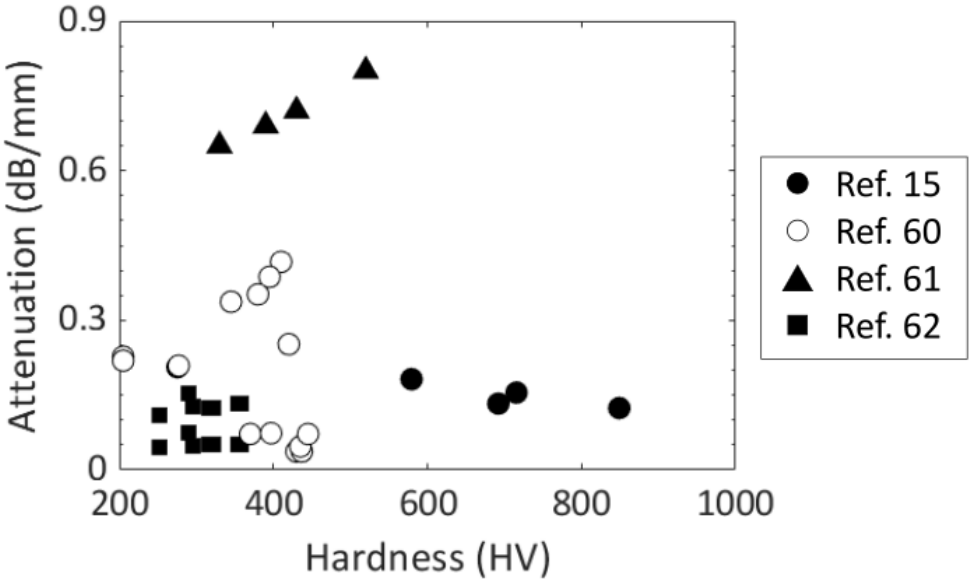

Figure 2.8 – Attenuation plotted against hardness from a variety of literature sources. Hardness does not appear to be directly correlated to ultrasonic attenuation [15] [60] [61] [62].

Figure 2.9 shows the relationship between ultrasonic attenuation and the thickness of steel test specimens; no clear relationship exists. Some sources cite attenuation changes due to differences in specimen preparation [64] and to the quality of transducer contact [1].

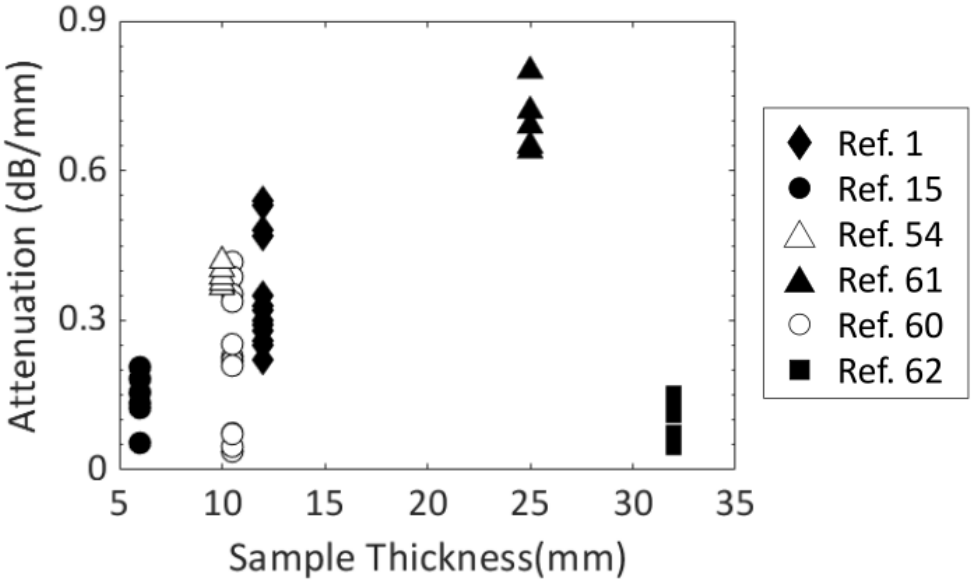

Figure 2.9 – Attenuation plotted against test sample thickness for a variety of literature sources. Sample thickness is not an accurate predictor for attenuation based on literature sources [1] [15] [54] [60] [61] [62].

In most literature sources, attenuation is measured by determining the decrease in amplitude of subsequent backwall echoes from each ultrasonic echo pulse. A few literature sources use the energy of the ultrasonic pulse as a means of determining the ultrasonic attenuation [92] [93] [94] [95] [53]. Calculation of backwall echo energy requires more sophisticated equipment or computer software to perform, and so was not an available means of measuring ultrasonic attenuation through the early development and adoption of ultrasonic testing methods [93]. Attenuation of the total signal energy within ultrasonic echoes was measured for hot-rolled steel plate with an unspecified chemistry [92]. Attenuation of echo energy and was on average 16% higher than standard attenuation values calculated using the peak amplitude of ultrasonic echoes. On measurements in stainless steel, ultrasonic energy attenuation values between 0.2 and 0.9 dB/mm were measured [93].

2.3.3.2 Frequency Dependence of Ultrasonic Attenuation

Using plain-carbon steel Smith studied the effect of changing carbon concentration on ultrasonic attenuation [96]. Attenuation dropped from 1.0 dB/mm to 0.2 dB/mm as carbon concentration was increased from 0.06-0.51 wt. % (at 15 MHz frequencies). Smith found that at pulse frequencies of 30 MHz, attenuation increased to >3.0 dB/mm and 1.2 dB/mm for 0.06 and 0.51 wt.% C steels, respectively. The author explains changes in ultrasonic attenuation though scattering and absorption. Increased numbers of dislocations and carbides are sources of increased wave scattering and energy absorption, thereby increasing attenuation. At higher frequencies (smaller wavelengths), an increasing number of grains and carbides act as scattering sources, increasing the overall attenuation for higher frequency waves.

Kumar et al. studied frequency dependent attenuation in ferritic stainless steel specimens with a 10 mm thickness [60]. Microstructures of martensite, mixed ferrite-martensite and ferrite were obtained by soaking at temperatures between 800 and 1350 °C, followed by oil-quenching. Ultrasonic testing was performed with ultrasonic echoes forming a bimodal frequency distribution. The ratio of the peak amplitudes from the bimodal frequency distribution was correlated to prior austenite grain size, with a close proportionality between the two. The authors explained this result in terms of the relationship between prior austenite grain size and the grain size of the resulting microstructure, stating that a larger prior austenite grain size causes the formation of larger grains. They also state that smaller grains will attenuate higher frequencies more strongly, acting as a larger number of scattering sites.

In a study using AISI 304 austenitic stainless steel, the frequency spectrum of ultrasonic backwall echoes was divided into five frequency bands [93]. Specimens were heat treated to achieve a range of average grain sizes from 23 µm to 175 µm. The attenuation in the energy of each of the five frequency bands was correlated with grain size. The authors showed that, in general, higher frequencies are attenuated more strongly. It was also shown that larger grain sizes caused

greater attenuation in all frequency bands, but that the effect was greatest at high frequencies, where the largest wavelengths were of a similar order of magnitude to the largest of the average grain sizes examined.

In measurements made on AISI 316 austenitic stainless steel, Sharma et al. [97] studied the frequency spectrum of the first, second and third backwall ultrasonic echoes. With a 16 MHz ultrasonic pulse, the effect of grain size on the movement of the peak frequency was investigated. The peak frequency is the largest frequency component present in an ultrasonic echo, as shown in Figure 2.10, at the highest point on each of the three curves. The authors found that peak frequency of each of the backwall echoes, resulting from increasing attenuation at higher frequencies. Peak frequency decreased more quickly with increasing grain size, with specimens with larger grain sizes losing high frequency wave components more rapidly than specimens with smaller grain size. The phenomenon was explained using the scattering theory of grains, with larger grains having a greater effect on the scattering of high frequency wave components. Large grains, being of a similar size to the wavelength, behave as obstacles, scattering waves, while small grains form a continuum through which waves propagate more freely. Frequency dependant attenuation was studied in several other sources as well [53][57] [97]- [103] and was found to show higher attenuation at high frequencies.

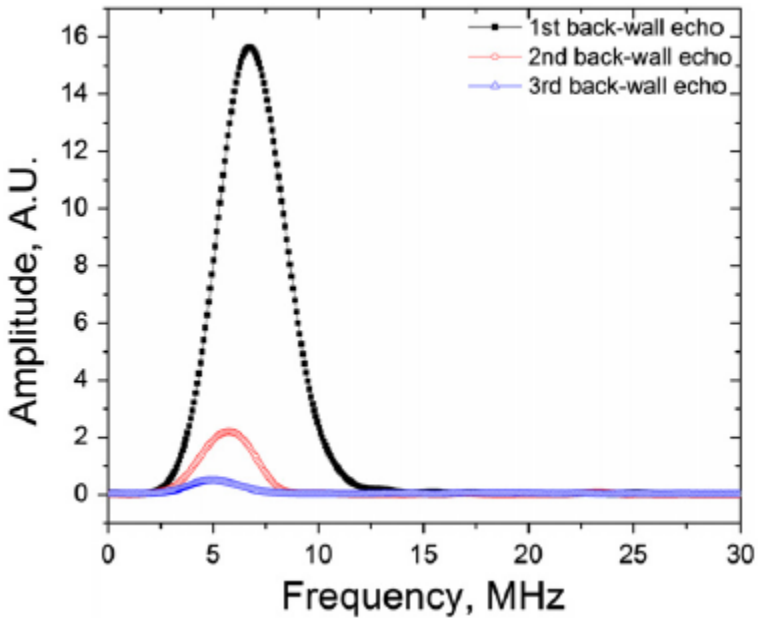

Figure 2.10 – The Fourier transforms of subsequent ultrasonic backwall echoes, showing higher attenuation of high frequency wave components, causing peak frequencies to shift towards lower frequencies [97].

2.3 Summary of Literature Review

A survey of the relevant literature provided a background on steel, cooling rates of Jominy end quench specimens and information on the relationship to ultrasonic parameters to steel hardness and microstructure. Cooling rates for Jominy end quench specimens are high (>150 °C/s) near the quenched end, dropping off rapidly as the distance from the quenched end increases [37]. Ultrasonic velocity decreased with increasing hardness for both longitudinal and shear wave modes [65] in medium-carbon steel. Wave theory predictions of ultrasonic velocity produce higher velocities for martensitic microstructures (5905-5928 m/s) than for ferritic microstructure (5900 m/s), but measurements in carbon steel shows the opposite relationship, with martensite producing longitudinal velocities between 5885 and 5895 m/s and shear velocities between 3185 and 3195 m/s [2]. Higher velocities were observed for other microstructures, with most measured longitudinal velocities between 5900 and 6000 m/s [1] [61]. A dependence of ultrasonic velocity on the acoustic frequency is not expected, based on phonon dispersion theory [79, p. 432], and was not observed in any literature results. Ultrasonic attenuation values were measured between 0.2 and 0.6 dB/mm [1] [15], and were higher for martensitic microstructures than for ferritic and pearlitic microstructures. Ultrasonic attenuation was dependent on frequency for many materials, including plain-carbon steel [96] and stainless steels [60], with higher frequency components being attenuation more strongly in all the relevant literature.

Chapter 3 - Experimental Methods

This chapter presents a description of the two types of steel examined in this work, followed by Jominy end quench specimen testing. ML80 steel and Grade 483 quenched and tempered (Q&T) steel were used to make end quench specimens, which are described for both steels. A description is given of hardness testing performed on the end quench specimens followed by methods used to section end quench specimens into samples for characterization. Information on microstructure characterization by optical microscopy and Electron Backscatter Diffraction (EBSD) analysis methods are presented next. The method for ultrasonic signal collection is then presented, which describes the ultrasonic probes used in this work and lists the Jominy end quench specimens that were examined. Lastly, the methods for calculating ultrasonic velocity and ultrasonic attenuation are shown.

3.1 Types of Steel Examined

Two types of steel were examined in this work, an ML80 casing steel, and a Grade 483 Q&T fitting steel. The ML80 steel studied comes from a section of casing, while the Grade 483 Q&T steel comes from a portion of a tee-fitting from an oil and gas pipeline. This research evaluates the relationship between ultrasonic parameters and martensite fraction in low carbon steel. This section presents information about the origin and chemical composition of the steel used for this research.

3.1.1 ML80 Casing Steel

ML80 is a heat-treatable low to medium carbon steel used as a casing material in the oil and gas industry. ML80 steel has high molybdenum concentration to improve corrosion resistance in sour environments [8]. The ML80 casing steel used in this work was made by continuous casting and rolling to a final skelp thickness of 11 mm. The skelp was manufactured into pipe by the electric resistance welding (ERW) process to produce the final ML80 casing product. Following the ERW pipe forming process, the ML80 pipe was austenitized, quenched and tempered to the required mechanical properties, which is a minimum yield strength of 550 MPa (80 ksi).

The portions of ML80 steel that are studied were taken at a 45° angle from the weld, as shown in Figure 3.1. A portion from the 45° angle is used because all other portions of this casing were scheduled for other research experiments. The chemical composition of the ML80 steel is shown in Table 3.1, with carbon equivalent content, C_{Eq}, calculated according to Equation 3.1 [104, p. 322]:

$$C_{Eq} = \%C + \left(\frac{\%Mn + \%Si}{6}\right) + \left(\frac{\%Cr + \%Mo + \%V}{5}\right) + \left(\frac{\%Cu + \%Ni}{15}\right), \quad \text{(Equation 3.1)}$$

where all chemical constituents are given in weight percentage (wt. %). Higher carbon equivalent content facilitates the formation of martensitic microstructures. The ML80 steel was chosen for its high carbon equivalent content. ML80 steel has high molybdenum (Mo) content, which serves to increase strength through hardening and to improve hydrogen cracking resistance [7].

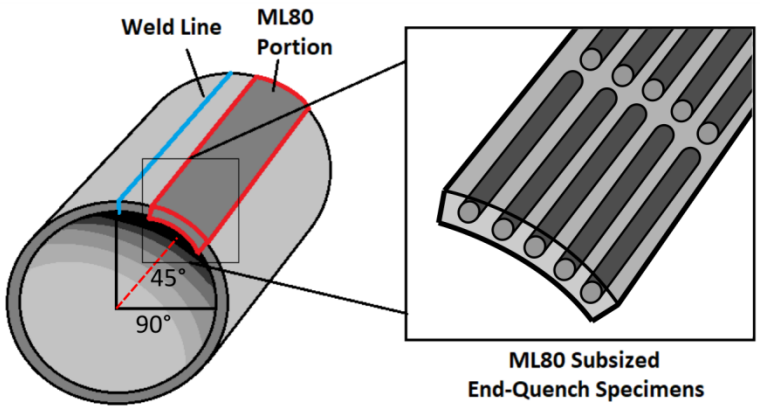

Figure 3.1 – ML80 steel was sourced from a portion of ERW casing steel.

Table 3.1 – The chemical composition of the ML80 casing steel. Nitrogen content is not known.

Steel Type	C	Mn	Cr	Si	Mo	Al	N (ppm)	Carbon Equivalent
ML80	0.25	0.66	0.22	0.15	0.49	0.019	--	0.528

In Figure 3.2 a CCT curve is shown for a casing steel with a similar chemistry to that of the ML80 steel examined in this work. The chemical composition of the steel in Figure 3.2 is shown in Table 3.2. The steel shown in the CCT curve has higher Mn content and lower Mo content, causing an increase in hardenability when compared to the ML80 steel, producing hard microstructures more readily. Mn and Mo are not expected to have a very large effect on the hardness of steel microstructures, so it is difficult to estimate which steel would produce higher hardness values [105]. Using cooling rates of Jominy end quench specimens (Table 2.1, Section 2.2), microstructures from ML80 end quench specimens can be estimated from the CCT curve.

The quenched end of the specimen, with cooling rates above 150 °C/s [37], is expected to produce an entirely martensitic microstructure. The reduced manganese content of ML80 steel compared to the steel in Figure 3.2 would decrease hardenability, and some fraction of bainite may be present in the quenched end microstructure. At 3.2 mm from the quenched end, cooling rates are 56-73 °C/s [37]. At these cooling rates, Figure 3.2 predicts a microstructure with primarily martensite and bainite, with the presence of some ferrite. At 10 mm from the quenched end of the specimen, cooling rates drop to approximately 10 °C/s [37], at which point a ferrite

and bainite dominant microstructure is expected, with little or no martensite present. At cooling rates lower than 5 °C/s, achieved at distances of 25 mm from the quenched end [35], pearlite is expected to be found in the microstructure, along with a complete absence of martensite.

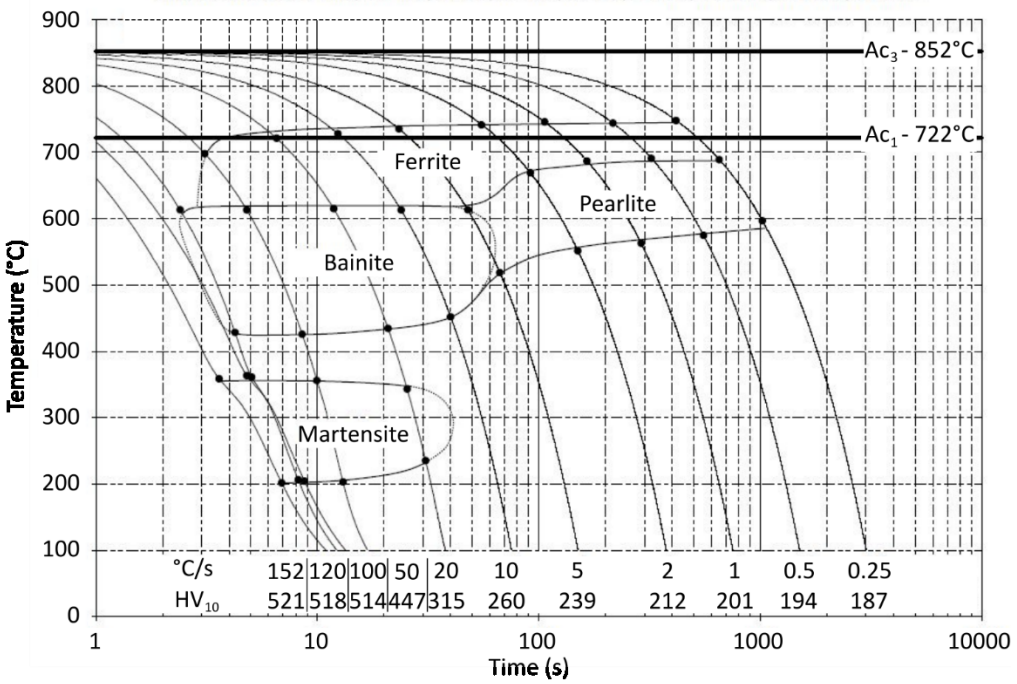

Figure 3.2 – A CCT curve for an L80 casing steel, with chemistry shown in Table 3.2. This curve is similar to the curve for the ML80 steel used in this work [106].

Table 3.2 – The chemical composition of the steel shown in Figure 3.2.

Element	C	Mn	Si	Cu	Ni	Cr	Mo	Nb
wt. %	0.26	1.53	0.25	0.05	0.02	0.25	0.008	0.003

3.1.2 Grade 483 Quenched and Tempered Fitting Steel

Grade 483 Q&T fitting steel is a heat-treatable low carbon steel used as pipeline fittings for the oil and gas industry. Grade 483 Q&T steel was obtained from tee-fittings, which are 3-way junctions used to control fluid flow in pipelines. Fittings are austenitized, quenched and then tempered to achieve the required mechanical properties, i.e. a minimum yield strength of 483 MPa (70 ksi). The fittings are made to a final wall thickness of 51 mm.

Chemical composition of the Grade 483 Q&T fitting steel can be seen in Table 3.3, with carbon equivalent content calculated according to Equation 3.1. Grade 483 Q&T steel is a low carbon steel with high manganese (Mn) content.

Table 3.3 – Chemical composition of Grade 483 Q&T fitting steel.

Steel Type	C	Mn	Cr	Si	Mo	Al	N (ppm)	Carbon Equivalent
Grade 483 Q&T	0.17	1.14	0.2	0.31	0.07	0.022	20	0.458

The Grade 483 Q&T Tee fitting is shown in Figure 3.3. The portion of steel in Figure 3.3, taken from the full fitting, is used to produce end quench specimens that are studied in this work.

Figure 3.3 – Grade 483 Q&T Tee fittings at a testing facility, where sections were removed for this research project.

Figure 3.4 shows a portion of the Grade 483 Q&T fitting, with the source location of Jominy end quench specimen holders outlined. Specimens were extracted from the center of the fitting wall. A portion of the pipe that was welded to the fitting is shown in Figure 3.4, to the right of the weld line.

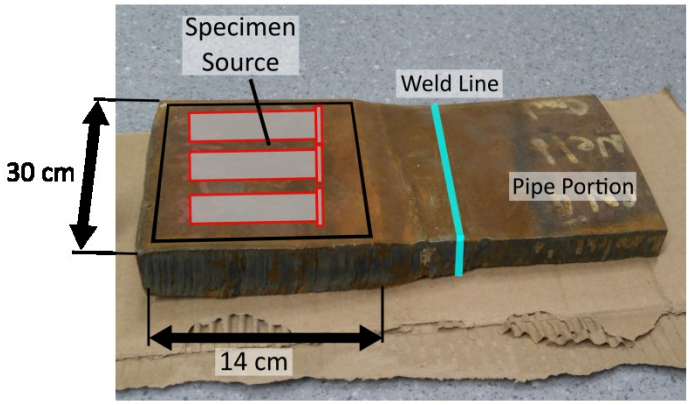

Figure 3.4 – Portions of Grade 483 Q&T steel like this one are used to make full sized end quench specimens and subsized specimen holders.

In Figure 3.5 a CCT curve is shown for a steel with similar nominal composition to the Grade 483 Q&T steel examined in this work. The nominal chemical composition is shown in Table 3.4. It may be noted that the CCT curve is for a steel with 0.2 wt. % higher manganese content than the Grade 483 Q&T steel studied in this work. Manganese is reported to have an important effect on hardenability in steel [105]. Manganese is additionally reported to have a small effect on the hardness of individual phases or microstructures, with the additional Mn content causing an increase in hardness for the steel in Figure 3.5 [105].

Using estimated cooling rates on end quench specimens from the literature (Table 2.1, Section 2.2), estimates can be made of the microstructures expected to form in Grade 483 Q&T end quench specimens. The quenched end experiences cooling rates above 150 °C/s [37], and is expected to form a martensitic microstructure. Hardness values should be above 400 HV at this point. At 3.2 mm from the quenched end of the specimen, cooling rates below 100 °C/s are found, and a mixed bainitic and martensitic microstructure is expected. As cooling rates drop below 50 °C/s, as is expected at depths of 5 mm, ferrite is expected within the otherwise bainitic and martensitic microstructure. Beyond 10 mm from the quenched end of the specimen pearlite may begin to appear in the microstructure, as cooling rates dip below 10 °C/s.

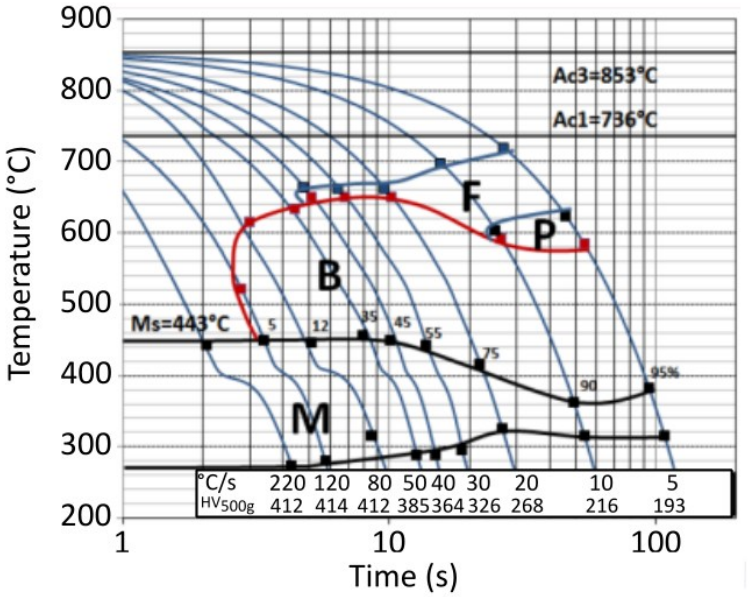

Figure 3.5 – A CCT diagram for the steel chemistry in Table 3.4.This CCT diagram would be very similar to that of a Grade 483 Q&T steel specimens [107].

Table 3.4 – The nominal composition for the steel producing the CCT diagram seen in Figure 3.5 [107].

Element	C	Mn	Cr	Si	Mo	Al	V
Content (wt. %)	0.17	1.36	0.03	0.32	0.01	0.029	0.05

3.2 Jominy End Quench Testing

This section describes two types of Jominy end quench specimens used in this study. A total of 10 subsized end quench specimens were produced from ML80 casing steel. A total of 9 full sized end quench specimens were produced from Grade 483 Q&T steel. Heat treatment parameters of Jominy specimens are presented, followed by the process for cutting the end quench specimens into discs samples. Disc samples are used to compare microstructure fraction (Section 3.4) with ultrasonic velocity and attenuation (Section 3.6) from different locations along the length of the specimen.

3.2.1 Subsized Jominy End Quench Specimens

Subsized Jominy end quench specimens were extracted at the centerline of the ML80 steel portion. The casing wall was insufficiently thick to produce standard sized specimens, so subsized specimens were made instead. Specimen holders for subsized specimens were made from Grade 483 Q&T fitting steel. Figure 3.6 shows the dimensions of subsized Jominy end quench specimens and specimen holders, along with a schematic of how they fit together.

Five grams of Wood's metal was placed inside each Grade 483 Q&T specimen holder to improve thermal conduction between the sample holder and the ML80 subsized sample. Wood's metal is an alloy of bismuth, lead, cadmium and tin, with a low melting point (near 70°C), allowing it to easily conform to the interface between the ML80 specimen and the specimen holder. After placing the Wood's metal, the subsized specimen was put in the specimen holder, which was then sealed to prevent interaction between the subsized specimen and the atmosphere.

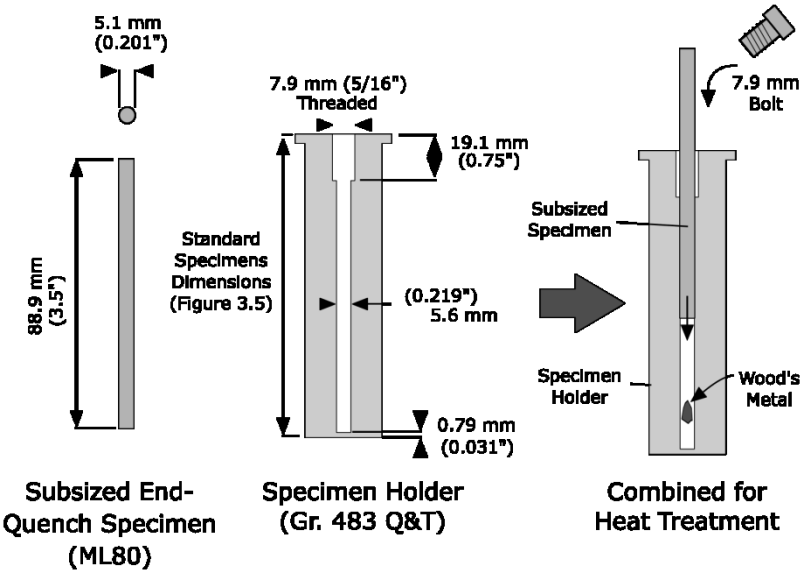

Figure 3.6 – The ML80 subsized end quench specimen (left) and specimen holder (center) dimensions. The subsized specimen was placed inside the specimen holder (right) for heat treatment.

Ten subsized end quench specimens were produced, eight of which were quench tested and two of which remain in the as-received condition.

Table 3.5 gives the heat treatment, physical processing and the analysis conducted on each ML80 subsized specimen. The physical processes named 'Sectioned in discs' (Section 3.2.4) and 'Edge ground' (Section 3.3.1) are described later in this chapter.

Table 3.5 – ML80 end quench specimen along with the processing and testing methods applied to them.

Sample Identifier	Heat Treatment	Physical Processing	Hardness Testing	Other Sample Analyses
ML80-S1	End quenched	Edge ground	HRC	
ML80-S2	End quenched	Sectioned in discs		UT
ML80-S3	End quenched	Edge ground	HRC	
ML80-S4	Quench failed	--	--	--
ML80-S5	End quenched	Sectioned in discs		Metallography

ML80-S6	End quenched	Edge ground	HRC	
ML80-S7	End quenched	Cut along length	HV (center)	EBSD
ML80-S8	End quenched	Sectioned in discs	HV (outer Edge)	
ML80-S9	As-received	Sectioned	HV	Metallography, UT
ML80-S10	As-received			

3.2.2 Full Sized Jominy End Quench Specimens

Full sized Jominy end quench specimens were cut from Grade 483 Q&T fitting steel. End quench specimens were extracted at the centerline of the fitting wall (Section 3.1.2). Figure 3.7 shows the dimensions of full sized end quench specimens.

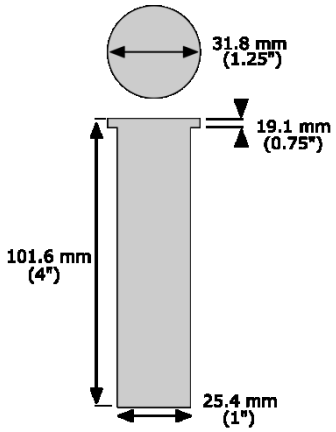

Figure 3.7 – Specimen dimensions of the Grade 483 Q&T full sized Jominy end quench specimens.

Nine full sized Jominy end quench specimens were produced, 8 of which were end quenched, while 1 remains in the as-received condition.

Table 3.6 gives a list the heat treatment, physical processing and the analysis conducted on each Grade 483 Q&T full sized end quench specimen.

Table 3.6 – Grade 483 Q&T full sized end quench specimen along with the processing and testing methods applied to them.

Sample Identifier	Heat Treatment	Physical Processing	Hardness Testing	Other Sample Analyses
TCPL-S1	End quenched	Sectioned in discs		UT, EBSD
TCPL-S2	End quenched	Edge ground	HRC	
TCPL-S3	End quenched	Sectioned in discs	HV (center)	Metallography, UT
TCPL-S4	End quenched	Edge ground	HRC	
TCPL-S5	End quenched	Edge ground	HRC	

TCPL-S6	End quenched	Edge ground	HRC	
TCPL-S7	End quenched			
TCPL-S8	End quenched	Edge ground	HV (outer edge)	UT (radial)
TCPL-S9	As-received	Sectioned	HV	Metallography, UT

3.2.3 Heat Treatment

Jominy end quench specimens were normalized at 925°C for one hour and then air cooled to allow for proper hardening characteristics during end quenching [32]. Specimens were then heated for 30 minutes at 925°C, followed by end quenching for 25 minutes. Figure 3.8 provides a schematic of the normalizing and end quenching process that was applied to both Jominy specimen steel types. During heating, decarburization was controlled by the placement of cast-iron chips inside the furnace along with specimens. Some decarburization was observed after removing specimens from the furnace, appearing as black flakes on the exterior of the end quench specimen. Eight specimens of each steel type were heat treated.

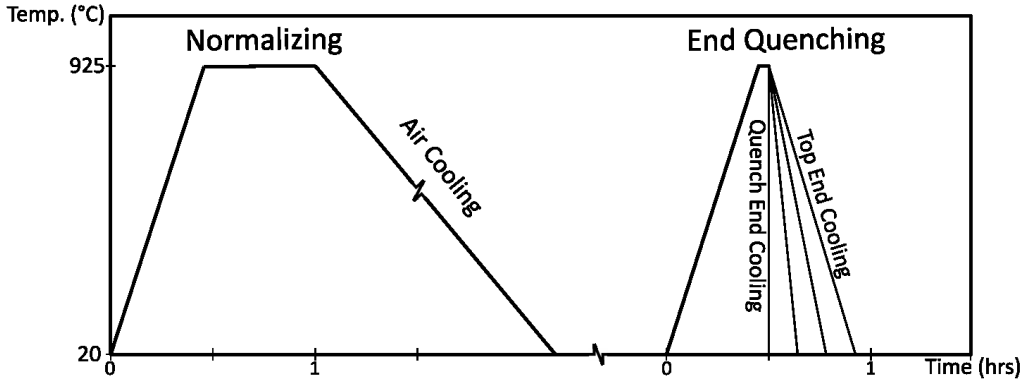

Figure 3.8 – The heat treatment applied to each of the ML80 and Grade 483 Q&T end quench specimens.

After removal from the furnace, end quench specimens were placed within the Jominy test fixture and the water stream was started. Figure 3.9 shows a quench in progress after 1 minute of quenching, where a distribution of temperatures can be seen by the colour of the specimen. ASTM Standard A255 provides the full method that was used for heat treatment of end quench specimens, including furnace arrangement, movement of specimens between the furnace and the quench location, and water flow parameters [32].

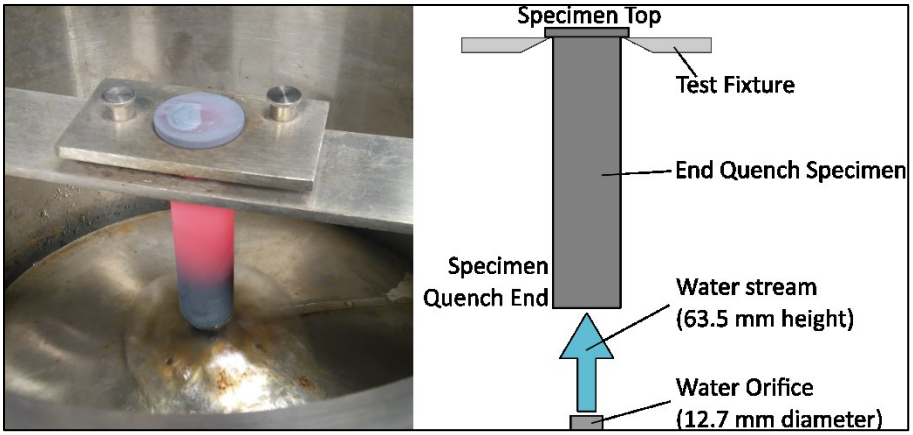

Figure 3.9 – A Grade 483 Q&T full sized Jominy end quench specimen during quenching.

3.2.4 End Quench Sample Sectioning

Disc samples were produced from 3 ML80 subsized end quench specimens and 2 Grade 483 Q&T full sized end quench specimens. These specimens were designated as ML80-S2, ML80-S5, ML80-S8 (Table 3.5), TCPL-S1 and TCPL-S3 (Table 3.6). Disc samples were produced using an IsoMet 4000 Precision Cut-off saw with a 7" abrasive blade, with each cut made in the radial direction of end quench specimens. Figure 3.10 shows a schematic of disc samples produced from end quench specimens. Disc samples were used to test hardness, to acquire metallographic data and to measure ultrasonic parameters.

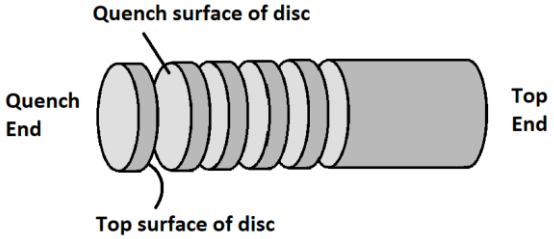

Figure 3.10 – ML80 and Grade 483 Q&T end quench specimens were cut into discs for microstructure analysis and UT.

Disc samples of Grade 483 full sized specimens TCPL-S1 and TCPL-S3 were surface ground to control sample thickness uniformity. Following sectioning, disc faces for specimen ML80-S2 were smoothed by hand with 480 grit grinding paper. Smoothing of disc faces helps to improves coupling between ultrasonic probes and the steel surface, increasing the amplitude of ultrasonic signals. Surface grinding provided a sufficiently smooth surface to acquire strong signals using UT.

As-received specimen ML80-S9 and TCPL-S9 were sectioned into a variety of sample types for examination by ultrasonic testing, metallography and hardness testing. ML80 subsized specimen

ML80-S9 was sectioned into 7 pieces, as shown in Figure 3.11Figure 3.11. Ultrasonic testing was carried out on Pieces A and E, metallography on Piece B, and hardness testing on Pieces C and D. Piece B from ML80-S9 was additionally examined by SEM using a Vega3 Tescan SEM was used, with a voltage of 20 kV. Hardness testing was carried out in two perpendicular radial directions (Piece C) and in the axial direction (Piece D). The pieces examined by ultrasonic measurement were surface ground to a thickness of 15 mm prior to testing. The pieces at the two extremities were not examined in this work. The same sectioning method was used for Grade 483 Q&T specimen TCPL-S9, shown in Figure 3.12.

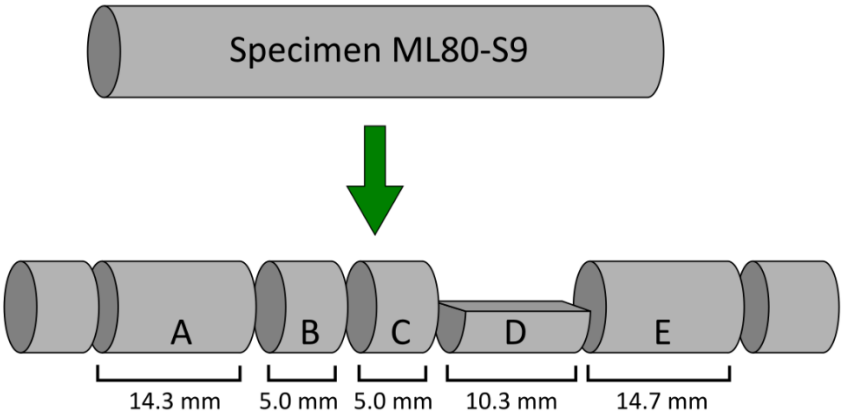

Figure 3.11 – Sectioning of as-received ML80 subsized specimens by ultrasonic testing (A & E), metallography (B) and hardness testing (C & D).

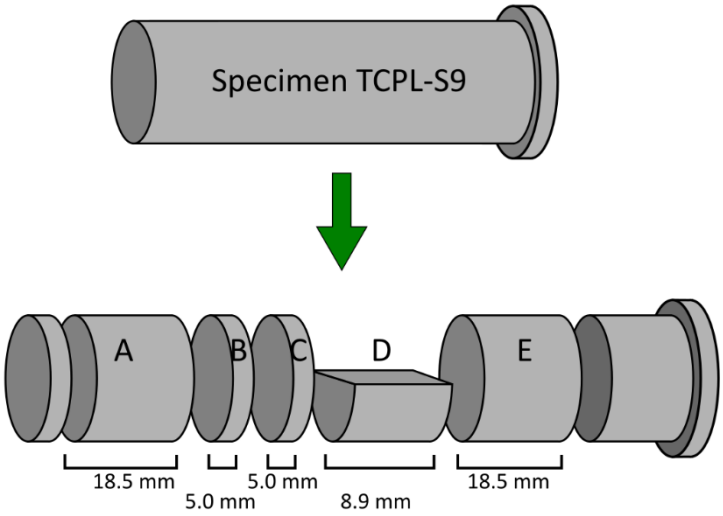

Figure 3.12 – Sectioning of as-received Grade 483 Q&T specimen TCPL-S9 by ultrasonic testing (A & E), metallography (B) and hardness testing (C & D).

3.2.5 Thickness Measurement of Disc Samples

Thickness measurements were carried out on all disc samples using a Mitutoyu MDC-Lite digital micrometer with 1µm resolution. Calculations of average thickness and standard deviation were made for disc samples of both ML80 steel specimens and Grade 483 Q&T specimens. Table 3.7 shows general information for disc samples produced from both ML80 and Grade 483 Q&T steel. Discs from specimen ML80-S2 were sectioned after the other specimens, when UT practices had been refined and increasing disc sample thickness was found to improve ultrasonic measurements. The higher thickness of disc samples from specimen ML80-S2 helps to reduce the error in ultrasonic velocity calculation. The minimum sample thickness measurements for specimens TCPL-S1 and TCPL-S3 both came from the disc nearest to the quenched end of the specimen. Data on individual disc samples can be found in Appendix A.1.

Table 3.7 – General information of disc samples cut from end quench specimens.

End Quench Specimen	Thickness (mm)		
	Average	Minimum	Maximum
ML80-S2	3.68	2.35	5.12
ML80-S5	1.25	0.88	1.33
ML80-S8	1.11	1.03	1.15
TCPL-S1	1.04	0.74	1.24
TCPL-S3	1.15	0.93	1.23

3.3 Hardness Testing

This section presents the Rockwell C hardness (HRC) testing method followed by the Vicker's hardness (HV) testing method used in this work. HRC and HV measurements were taken on both ML80 subsized end quench specimens and Grade 483 Q&T full sized end quench specimens. HRC measurements are used to check the uniformity of the end quenching process, while HV measurements are used to correlate ultrasonic parameters with martensite fraction.

3.3.1 Rockwell C Hardness Testing

HRC measurements were collected from three ML80 subsized specimens (ML80-S1, ML80-S3 and ML80-S6 in (Table 3.5), and from four Grade 483 Q&T full sized specimens (TCPL-S2, TCPL-S4, TCPL-S5 and TCPL-S6 in (Table 3.6). Results from HRC measurements were used to evaluate the uniformity of the end quenching process across ML80 subsized end quench specimens and Grade 483 Q&T full sized end quench specimens.

HRC measurements were taken on two flat edges, ground on opposite sides of the specimen diameter (180° apart), as shown in Figure 3.13. Grinding was performed with a computer numerical control (CNC) surface grinder with a water coolant, and a smooth surface with variations less than 10 µm was achieved. Indentations for hardness measurements were made at 1.6 mm (1/16 inch) increments along the length of end quench specimens, beginning at 1.6 mm from the quenched end.

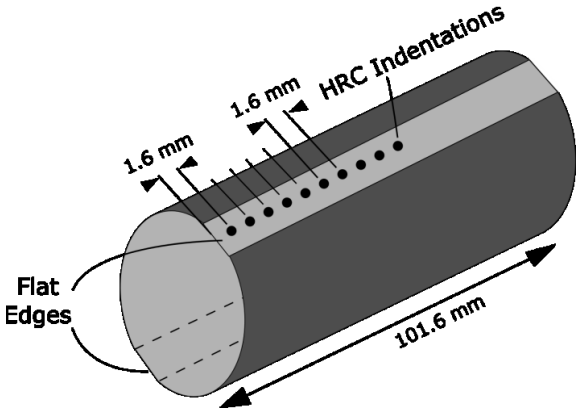

Figure 3.13 – Flat edges are ground into end quench specimens for HRC testing at 180° apart.

3.3.2 Vicker's Hardness Testing

For ML80 subsized specimens, HV measurements were done on specimens ML80-S7, ML80-S8 and ML80-S9 (Table 3.5). HV measurements were used to compare properties at the outer dimension and along the center of subsized end quench specimens, as well as to investigate the steel in the as-received state. For Grade 483 Q&T full-sized specimens, HV measurements were

performed on specimens TCPL-S3 and TCPL-S8 (Table 3.6). These hardness measurements are used to correlate to metallographic measurements providing a robust metric relating the microstructure across different specimens. HV measurements were performed with a 1 kg force and a dwell time of 10 seconds.

Specimen ML80-S9 was examined by Vickers hardness measurement in the as-received state. Piece C (Figure 3.11) was examined in two mutually perpendicular radial directions (Figure 3.14a) to determine if there were any variations across the subsized specimens owing to differences across the ML80 casing thickness. Measurements were made at 0.2 mm increments in either direction. Piece D was examined at 0.5 mm spacings along the center (Figure 3.14b) to determine if any differences were present along the length of the specimen. The same measurement arrangement was used for Grade 483 Q&T full sized specimen TCPL-S9. Measurements were made at 0.5 mm increments on Piece C and 0.3 mm increments on Piece D for specimen TCPL-S9.

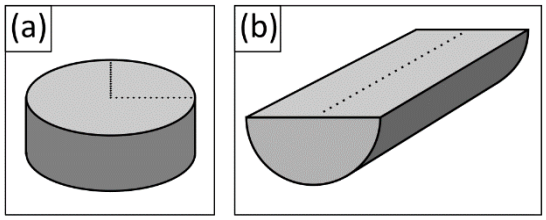

Figure 3.14 – Hardness measurements made on as-received ML80 specimen in (a) the radial direction and (b) along the length of the specimen.

Subsized specimen ML80-S7 were cut along the axial direction, and then HV indentations were made along the centerline of the sample (Figure 3.15a). Indentations were made at 0.5 mm increments along the specimen depth. Subsized specimen ML80-S8 was sectioned into 12 disc samples (Section 3.2.4), with HV measurements performed 1 mm away from the outer edge of the disc surface (Figure 3.15b).

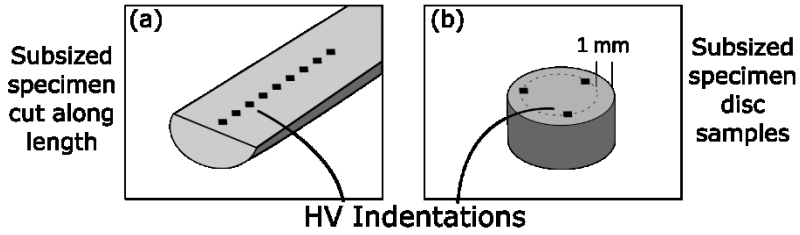

Figure 3.15 – HV measurements were made (a) along the center axis of an ML80 subsized end quench specimen, and (b) near the outer edge of ML80 disc samples.

Full-sized specimen TCPL-S3 is sectioned into 9 disc samples (Section 3.2.4), with HV measurements made at the center of the disc surface (Figure 3.16a). Full-sized specimen TCPL-S8 was ground flat on two opposing edges, as in the case of HRC measurements (Section 3.3.1). HV measurements were made along one of the flat edges (Figure 3.16b). Indentations were made at 0.1 mm increments along the specimen depth. These measurements provide better resolution of the change in hardness values than were available from HRC measurements.

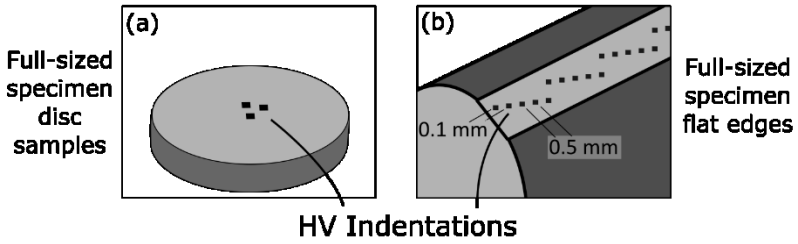

Figure 3.16 – HV measurements on Grade 483 Q&T specimens were made (a) at the center of disc samples and (b) on a flat edge near the outer surface.

3.4 Microstructure Characterization

Metallography was performed on disc samples from end quench specimens ML80-S5 and TCPL-S3 and from pieces of as-received specimens ML80-S9 and TCPL-S9. This section discusses metallographic analysis of those specimens, including sample preparation, etching procedures and microstructure fraction measurement. Metallographic analysis is followed by electron backscatter diffraction (EBSD) analysis of end quench specimens ML80-S7 and TCPL-S1. Metallographic analysis was used to measure microstructure fraction and EBSD analysis was used to account for grain orientation and to provide further evidence of the presence of martensite.

3.4.1 Preparation of Etching Surface

From as-received specimens ML80-S9 and TCPL-S9, Piece B (Figure 3.11 and Figure 3.12) was also examined by metallography. Disc samples from subsized specimen ML80-S5 and full sized specimen TCPL-S3 were prepared for metallographic analysis. Discs were ground and polished using an AutoMet 250 autopolisher using standard grinding and polishing methods for steels. The final polishing state was achieved using a 0.05 µm alumina suspension to produce a mirror finish. The sample was then washed with water and ethanol to remove any residue left from the polishing process, and dried using compressed air. An Olympus BX61 optical microscope was used to ensure no scratches were found on disc sample faces prior to the application of metallographic analysis.

3.4.2 Metallographic Etching

Disc samples from subsized specimen ML80-S5 and full sized specimen TCPL-S3 were etched using a two stage tint etchant. The first stage was a spray-etch for 10 s with a 2% Nital solution, followed by an ethanol wash and drying by compressed air. The second stage was a 15 s immersion in a 10% solution of aqueous $Na_2S_2O_5$, called sodium metabisulfite. The second stage was followed by water washing, ethanol washing, and then drying by compressed air. Micrographs of disc sample surfaces were collected by an Olympus BX61 optical microscope.

3.4.3 Microstructure Fraction Analysis by Point-Count Method

Microstructure fractions were calculated from micrographs taken from disc surfaces of ML80 subsized specimen ML80-S5 and Grade 483 Q&T full sized specimen TCPL-S3. Micrographs were taken from 11 disc sample surfaces of subsized specimen ML80-S5 and from 14 disc sample surfaces of full sized specimen TCPL-S3. Five micrographs were taken for each surface, making a total of 125 characterized images. Following the method described in ASTM Standard E562-11 [108], a 10x10 line grid was super-imposed over each image, as seen in Figure 3.17. At each intersection of gridlines the microstructure was recorded. The microstructure fraction for each sample is calculated according to Equation 3.2:

$$P_{p(i)} = \frac{P_i}{P_T}, \qquad \text{(Equation 3.2)}$$

where $P_{p(i)}$ is the microstructure fraction of the i^{th} constituent, P_i is the number of points counted in the test grid of constituent i and P_T is the total number of points in the grid, i.e. 100. The microstructure fraction of each constituent is averaged for each of the five images from each sample surface. The standard deviation in the microstructure fraction value is obtained using Equation 3.3 [108]:

$$s = \left[\frac{1}{n-1}\sum_{i=1}^{n}\left(P_p(i) - \overline{P}_p\right)^2\right]^{1/2}, \qquad \text{(Equation 3.3)}$$

where s is the standard deviation, expressed as a unitless fraction, n is the number of images recorded per disc sample face (n=5 in this work), and $\overline{P}_p$ is the average fraction of each microstructure for each disc sample face.

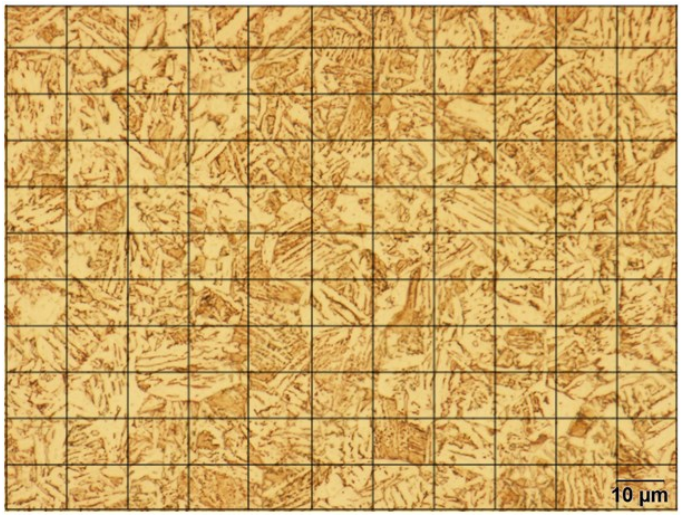

Figure 3.17 – Microstructure analysis using a 100-point count for each micrograph. The example shown is from 9.5 mm from the quenched end of specimen TCPL-S3.

Point counts on microstructures were evaluated using the following criteria:

1) The microstructure at the line crossing location is counted, as best determined visually, as opposed to counting the microstructure dominating the area surrounding the intersection.
2) When uncertainty arises between two microstructures, half a count is given to each.
3) CCT curves are used to inform decisions on which microstructures are present.
4) Comparisons are made between different depths to understand changes in colour and morphology of microstructures, further informing decisions on the microstructures present.
5) Darker browns are considered candidates for being martensitic, while light coloured grains are typically classified as bainite, ferrite or pearlite, depending on grain morphology.
6) Bainite and pearlite are differentiated using CCT curves and by grain patterns. Lamellar formations are necessary for pearlite microstructures.
7) Microhardness values are used to help identify the microstructure present in morphologies appearing consistently in micrographs.
8) Data from EBSD measurements is used to help inform microstructure classifications near the quenched end of both ML80 and Grade 483 Q&T specimens.

The disc samples of ML80 and Grade 483 Q&T steel examined for microstructure fraction were also examined using microhardness measurements. Specimen ML80-S5 was examined at depths of 0.0 mm, 5.9 mm, 12.5 mm and 50 mm to help inform microstructure identification. Specimen TCPL-S3 was examined at depths of 0.0 mm, 8.2 mm, 20.7 mm and 50 mm. Microhardness

measurements were made with a 50 gf indentation with a dwell time of 10 seconds. Specific regions of interest were identified after tint etching and were measured using Vickers microhardness measurements by careful placement of indentations at the desired location.

3.4.4 Electron Backscatter Diffraction (EBSD)

Analysis by EBSD was performed at two location of ML80 subsized specimen ML80-S7 and two locations of Grade 483 Q&T full sized specimen TCPL-S1. From each specimen, one of the locations was on the surface of the quenched end and the second location was in the axial direction of the specimens. Figure 3.18a shows the location of sample surfaces for specimen ML80-S7 and Figure 3.18b shows sample surfaces for specimen TCPL-S1. EBSD measurements were conducted on a Zeiss Sigma Field Emission SEM with an 'HKL' EBSD system. Measurements were performed at a step-size of 0.1 µm, a voltage of 20 kV, an aperture diameter of 60 µm and a sample tilt of 70°. Measurement was performed on specimens mounted in an electrically conductive epoxy.

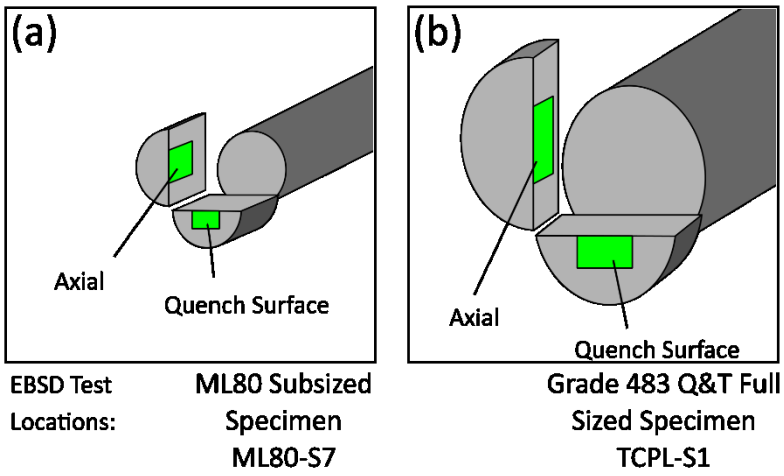

Figure 3.18 – Samples for EBSD analysis were taken on the quench face and along the depth axis for (a) an ML80 subsized specimens and (b) a Grade 483 Q&T full sized specimens.

The purpose of EBSD measurement was to confirm that the quenched ends of the specimens were fully martensitic. EBSD was also used to compare the microstructure in the radial and axial direction to determine if differences between the two orientations may have contributed to variations in ultrasonic parameters measured on Grade 483 Q&T specimens.

EBSD measurements were made using a step-size of 0.3 µm on the quench surface sample from ML80-S7 and TCPL-S1. These measurements were used to determine the phase fraction of retained austenite present within the steel microstructure. The step size was chosen in order to balance the ability to detect retained austenite while also encompassing a large enough region of the microstructure to be representative of the specimen.

Reference library entries were used for ferrite, cementite and retained austenite phases when collecting data by EBSD. The reference library entries are compared to the data collected at each measurement location, enabling the EBSD software to classify the phase at each measurement location. Martensite is identified in EBSD measurements as ferrite but can be differentiated from α-ferrite due to the strain in the lattice [109]. The lattice strain reduces the agreement between measurements and the reference library, which is shown in band contrasts maps produced by the EBSD analysis software.

3.5 Ultrasonic Signal Collection

This section discusses the specifications of each of the three ultrasonic transducers used in this work. Next, signal collection from ML80 subsized specimens is discussed, followed by signal collection from Grade 483 Q&T full sized specimens. Lastly, this section lists the type of ultrasonic analysis that was performed on each end quench specimen.

3.5.1 Ultrasonic Transducers

Two longitudinal wave transducers, the V202-RM and the V203-RM, and one shear wave transducer, the V221-BA-RM, were used for ultrasonic analysis. Information on these transducers is shown in Table 3.8. All transducers use a piezoelectric oscillating element, attached to a fused silica medium with acoustic impedance of 13×10^6 Pa×s/m^3. Longitudinal transducers V202-RM and V203-RM both use an additional acrylic delay block, with acoustic impedance of 2.47×10^6 Pa×s/m^3. UT was conducted in pulse-echo mode, where the same transducer was used to produce and to receive the ultrasonic signal. All UT was conducted at a 10MHz pulse frequency.

Table 3.8 – Ultrasonic probes used for ultrasonic signal measurement.

Probe Designation	Center Frequency (MHz)	Contact Diameter (mm)	Wave Type	Coupling Fluid
V202-RM	10	6.4	Longitudinal	Motor oil
V203-RM	10	3.2	Longitudinal	Motor oil
V221-BA-RM	10	19.1	Shear	Shear wave gel

Ultrasonic probes were placed against the surface of samples with a small amount of coupling fluid in between. Pressure was applied to the probe by hand to reduce the coupling fluid to a thin layer to produce ultrasonic signals with the largest peak amplitudes. Ultrasonic signals were gathered from ML80 subsized end quench specimens ML80-S2 and ML80-S9 (Section 3.5.2), and from Grade 483 Q&T full sized specimens TCPL-S1, TCPL-S3, TCPL-S8 and TCPL-S9 (Section 3.5.3). Longitudinal ultrasonic signals were collected from ML80 subsized end quench specimen ML80-

S2. The specimen was sectioned into 3 disc samples. Two longitudinal ultrasonic signals were collected for each disc sample using the V203-RM longitudinal transducer, as other transducers were too large to fit on the disc surfaces.

3.5.2 Signal Collection from ML80 Specimens

Ultrasonic measurements were made on Pieces A and E from as-received subsized end quench specimen ML80-S2. The test pieces had thicknesses of 14.35±0.01 and 14.71±0.02 mm respectively. The thickness values were obtained using 6 measurements with a digital micrometer. Ultrasonic probes were placed against the center of the disc sample face for longitudinal wave collection. As with measurements on specimen ML80-S2, only probe V203-RM was used due to the small diameter of disc sample faces and the inability to collect ultrasonic signals from specimens smaller than the ultrasonic transducer contact surface.

Ultrasonic longitudinal wave signals were collected from disc samples of specimen ML80-S2, by placement of ultrasonic probe V203-RM at the center of disc sample surfaces, as shown in Figure 3.19. Only one probe was used for ultrasonic measurement due to the small face size of disc samples from ML80 subsized end quench specimens. Other ultrasonic probes, when placed in contact with ML80 disc samples, would overhang the disc surface, resulting in poor signal quality. Disc sample locations and thicknesses can be found in Appendix A.1.1.

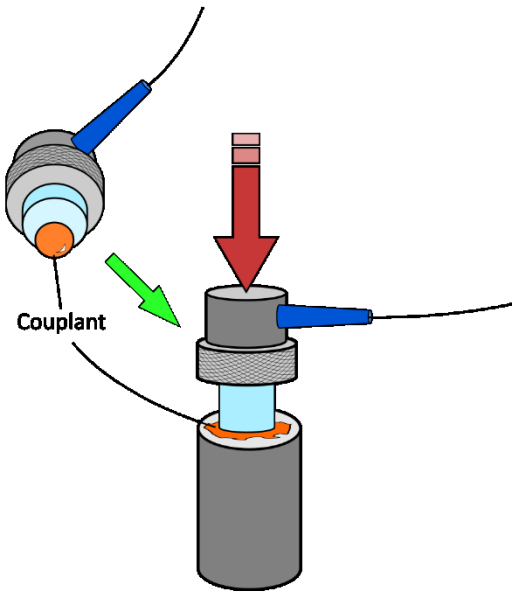

Figure 3.19 – Ultrasonic longitudinal velocity was measured on ML80 subsized end quench specimens in the axial direction using probe V203-RM.

3.5.3 Signal Collection from Grade 483 Q&T Specimens

Ultrasonic signals were collected from disc samples of Grade 483 Q&T full sized end quench specimens, TCPL-S1 and TCPL-S3. Longitudinal ultrasonic signals were collected using probe V202-RM, as shown in Figure 3.20. Five signals were collected from each disc sample in the longitudinal wave mode. Two shear wave signals were gathered for each disc sample using probe V221-BA-RM using shear waves.

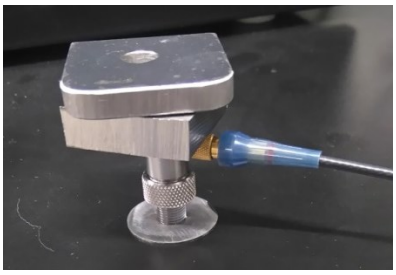

Figure 3.20 – Longitudinal wave probe V202-RM held steady with weight blocks on a disc sample of a Grade 483 Q&T end quench specimen.

Longitudinal ultrasonic signals were also collected from the Grade 483 Q&T full sized specimen TCPL-S8 without cutting it into discs. Measurements were performed in the radial direction of the specimen by placing the ultrasonic transducer on one of the flat edges ground for HRC testing, as shown in Figure 3.21. One signal was collected for each probe at each measurement location. The sample diameter, used for ultrasonic calculations, was measured with a digital micrometer (Section 3.2.5).

Ultrasonic data was collected for Grade 483 Q&T full sized end quench specimen TCPL-S8 using both longitudinal wave probes V202-RM and V203-RM. Ultrasonic signals were collected at a variety of different distances from the quenched end of the specimen by moving the location of the ultrasonic probe along the length of the ground edge. The distances where ultrasonic signal collection was performed, along with the probe used at each distance, are shown in Table 3.9. Probe V203-RM could not be used at a depth of 2 mm as the large contact diameter of the probe (Section 3.5.1) would hang over the edge of the specimen causing poor signal quality.

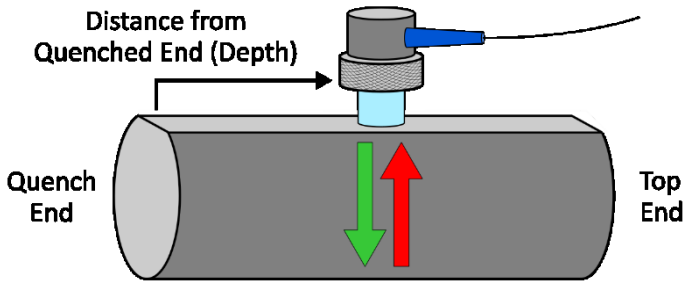

Figure 3.21 – Longitudinal velocity measurements across Grade 483 Q&T full sized end quench specimen TCPL-S8 were conducted with the ultrasonic probe against the specimen's flat edge.

Table 3.9 – The location and longitudinal wave probe used to make ultrasonic measurements across Grade 483 Q&T full sized specimen TCPL-S8.

Distance from Quenched End (mm)	Probe Used for Measurement
2	V203-RM
4	V202-RM, V203-RM
6	V202-RM, V203-RM
8	V202-RM, V203-RM
10	V202-RM, V203-RM
15	V202-RM, V203-RM
20	V202-RM, V203-RM

Ultrasonic longitudinal and shear wave data were collected from as-received specimen TCPL-S9 (Section 3.2.4). Measurements were made on Pieces A and E (Section 3.2.4, Figure 3.12), which were surface ground to a thickness of 15.017±0.002 and 15.0.13±0.001 mm. Thickness values were obtained using 10 measurements near the center of the disc samples with a digital micrometer. Five ultrasonic signals were collected with shear wave probe V221-BA-RM and each of the longitudinal wave probes V202-RM and V203-RM, as shown in Figure 3.22.

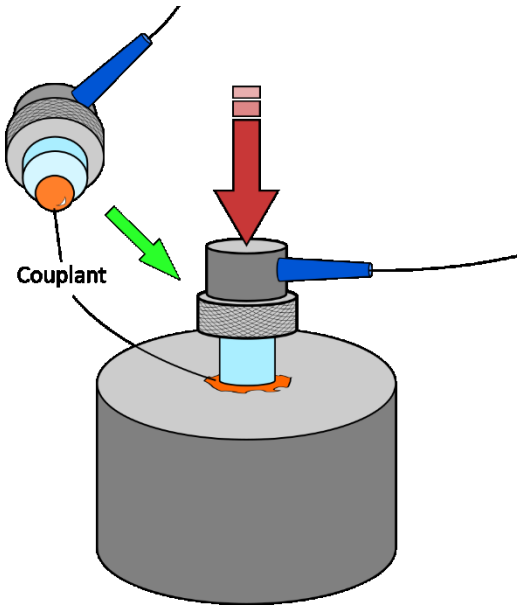

Figure 3.22 – Measurements made on Pieces A and E of ML80-S9 and TCPL-S9 across thickness of the disc.

3.6 Ultrasonic Calculations

This section discusses the method for calculating ultrasonic velocity, followed by two methods of calculating ultrasonic attenuation. Both methods of measuring ultrasonic attenuation provide an estimate of the rate of energy loss as ultrasonic waves pass through the material [110]. One of the methods uses the amplitude of signal peaks to calculate attenuation. This method will be referred to as 'amplitude attenuation' measurement. The second method of attenuation calculation uses the signal energy of individual backwall echoes to estimate energy loss and will be called 'energy attenuation'.

Table 3.10 shows the type of attenuation measurement that was performed for each end quench specimen of ML80 and Grade 483 Q&T steel. Energy attenuation was not calculated for longitudinal wave signals for specimens TCPL-S1 and TCPL-S3 because individual backwall echoes are not spaced far enough apart to be isolated for signal energy measurement.

Table 3.10 – Amplitude attenuation and energy attenuation calculated for ultrasonic signals of different specimens.

Specimen	Wave Mode	Velocity	Amp. Atten.	Energy Atten.
ML80-S2	Longitudinal	yes	yes	yes
TCPL-S1	Longitudinal	yes	yes	no
TCPL-S1	Shear	yes	yes	yes

TCPL-S3	Longitudinal	yes	yes	no
TCPL-S3	Shear	yes	yes	yes
TCPL-S8	Longitudinal	yes	yes	yes

3.6.1 Ultrasonic Velocity

Calculations of ultrasonic velocity were carried out in MATLAB, with digital ultrasonic signals imported as '.txt' files. In MATLAB, signals were smoothed to reduce noise using a 100 MHz low-pass Hamming filter [102]. The frequency cutoff of 100 MHz was used because it is ten times the peak frequency produced by the transducer and ultrasonic pulse transmitter, and because the cutoff provided good visual quality in smoothing the noise in ultrasonic signals. Ultrasonic velocity was measured by calculating the difference between subsequent peaks in an ultrasonic signal. Figure 3.23a shows the full ultrasonic signal, captured for a martensitic sample of full sized end quench specimen TCPL-S3. Figure 3.23b shows an enlarged portion of the signal, with signal peaks highlighted in blue.

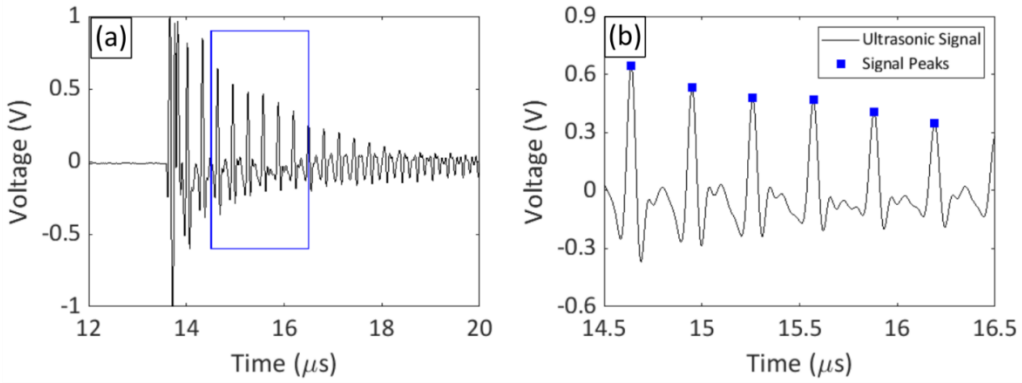

Figure 3.23 – (a) A longitudinal ultrasonic signal at the quenched end of Grade 483 Q&T end quench specimen TCPL-S3. (b) A section of the signal, with backwall echoes marked.

Ultrasonic velocity, *v* (m/s), was calculated according to Equation 3.4:

$$v = \frac{2d}{\Delta t'} \qquad \text{(Equation 3.4)}$$

where *d* is the sample thickness, in mm, and Δt is the average time separation, in s, of neighboring ultrasonic peaks. Ultrasonic signals bounce off the sample backwall, travelling through the sample twice between emission and collection, producing the factor of 2 in the denominator of Equation 3.4. Appendix A.2.3 discusses error calculations for ultrasonic velocity measurement.

3.6.2 Ultrasonic Amplitude Attenuation

Ultrasonic attenuation was calculated from the peak voltages of ultrasonic backwall echoes. Energy is lost as the wave travels through the material, leading to exponential decay in the peak amplitude of ultrasonic signals, as described by Equation 3.5:

$$\beta = \beta_0 e^{-\alpha t}, \qquad \text{(Equation 3.5)}$$

where β is the peak amplitude, measured in volts (V), *t* is time (μs), and β_0 and α are constants, with units of volts and mm^{-1}, respectively. The constant α is often called the Attenuation Coefficient. Appendix A.3 shows how to calculate attenuation in units of dB/mm from the exponential decay relationship in Equation 3.5. The amplitude attenuation will be denoted by the variable A_{dB} and is typically calculated according to Equation 3.6:

$$A_{dB} = \frac{20}{d}\log_{10}\left(\frac{A_1}{A_2}\right), \qquad \text{(Equation 3.6)}$$

where A_{dB} has units of dB/mm, *d* is the sample thickness, in mm, and A_1 and A_2 are the amplitudes of the first and second backwall echoes, respectively, in volts.

3.6.3 Ultrasonic Energy Attenuation

When calculating ultrasonic energy attenuation, each backwall echo signal is isolated from the full ultrasonic signal and the Fourier Transform (FT) is applied. The FT is a signal processing tool which is used to measure the strength of the frequency components of a signal. The FT is given by Equation 3.7:

$$F[k] = \sum_{t=0}^{N-1} f(t) e^{-j\frac{2\pi}{N}kt}, \qquad \text{(Equation 3.7)}$$

where *f(t)* is the ultrasonic backwall echo signal with units of volts. The echo signals *f(t)* is a function of time, t, with units of seconds and is sampled at integer *N* points. The FT of the echo signal is *F[k]* and has units of frequency, *k*, in Hz. The letter *j* is the imaginary unit vector $\left(\sqrt{-1}\right)$. For energy attenuation calculations, zero-padding is used to make N=65,536, allowing for a smooth frequency domain representation of the echo signal. Figure 3.24 shows an ultrasonic backwall echo (Figure 3.24a) and its FT (Figure 3.24b). Zero-padding is not shown in Figure 3.24a. Energy attenuation could not be calculated for longitudinal ultrasonic signals from specimens TCPL-S1 and TCPL-S3, because of overlap in neighboring backwall echoes. The overlap prevented isolation of individual backwall echoes.

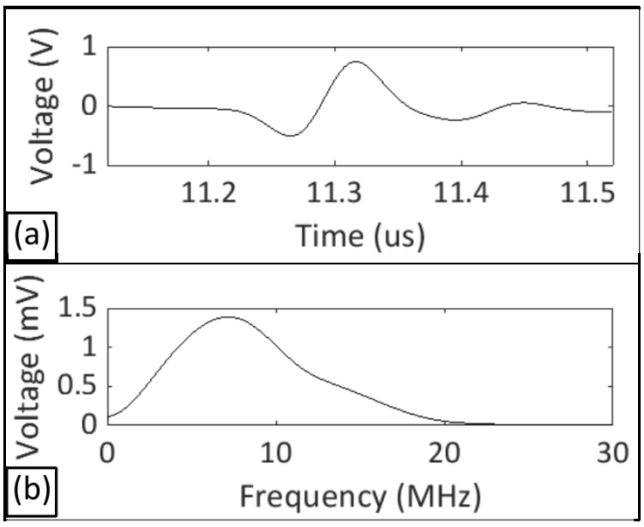

Figure 3.24 – (a) An ultrasonic backwall echo, from a shear wave signal of a Grade 483 Q&T end quench specimen, and (b) its Fourier transform.

The energy of a backwall echo signal, E_{echo}, was be computed from the FT according to Equation 3.8:

$$E_{echo} = \frac{1}{N}\sum_{k=1}^{N}|F_{echo}(k)|^2, \qquad \text{(Equation 3.8)}$$

where E_{echo} has units of J, $F_{echo}(k)$ is the FT of the ultrasonic signal, with units of volts, with integer N frequency samples. By Parseval's theorem, E_{echo}, calculated from the FT is equal to the energy calculated from the time-domain signal [111, p. 240]. For ultrasonic energy attenuation, the decaying strength of ultrasonic backwall echo energy is used to calculate the attenuation, as is the case with ultrasonic amplitude attenuation measurements [110]. The energy contained within subsequent backwall echoes follows an exponential decay, as shown in Equation 3.9:

$$E = E_0 e^{-\beta t}, \qquad \text{(Equation 3.9)}$$

where E is the energy contained in a backwall echo in J, t is the time with units of s, and E_0 and β are constants with units of J and mm^{-1}, respectively. Appendix A.3 shows how to calculate attenuation from the relationship in Equation 3.9.

Chapter 4 – Results and Discussion

This chapter presents data from measurements on two types of Jominy end quench specimens, ML80 subsized specimens and Grade 483 Q&T full sized specimens. Hardness measurements are made by Rockwell C Hardness (HRC) and Vicker's Hardness (HV) testing, which is presented for both specimen types. Microstructure fraction is shown, as well as results from EBSD made at the quenched end of specimens. Ultrasonic velocities are then presented, including a discussion on disc sample thickness, followed by results from amplitude attenuation and energy attenuation. All measured results can be found the tables in Appendix A.1.

4.1 Hardness Testing Results

This section presents HRC and HV measurements from ML80 subsized end quench specimens and Grade 483 Q&T full sized specimens. Hardness results from as-received specimens ML80-S9 and TCPL-S9 are also presented in this section. HRC is used to show that a satisfactory level of uniformity was achieved through the end quenching process. HV measurements are used to show that the difference in the radial direction of specimens is minimal. HV measurements are also used as a means of relating microstructure fraction with ultrasonic velocity and with ultrasonic attenuation (Sections 4.3, 4.4, 4.5 and 4.6).

4.1.1 Hardness of As-Received Steel

Hardness was measured in two perpendicular radial directions on ML80 subsized specimen ML80-S9, kept in the as-received state (Section 3.3.2). Eighteen measurements were made in each of the radial directions, spaced 0.15 mm apart. Measurements were also made along the axial direction of the specimen, with spacing between indentations made at 0.5 mm increments. The average and standard deviation of each of these three sets of measurements can be seen in Table 4.1.

Variations in hardness values for ML80-S9 were minimal in both the radial and axial directions. The uniformity of the as-received specimen shows that there were no fluctuations in material hardness along the specimen geometry. The uniformity of as-received specimens helps to ensure that the materials properties of end quench specimens would not be affected by difference retained through the heating and end quenching process.

ML80 casing steel was produced using a TMCP process, with the goal of producing a refined microstructure. High hardness values are expected to result from this process. The hardness values obtained for the as-received specimen ML80-S9 are lower than most hardness results obtained for ML80 end quench specimens. ML80 end quench specimens are, however, taken from the center of the ML80 casing, where some deviation in properties are known to occur [4].

Microstructure analysis of the specimen will be discussed later in this chapter (Section 4.2.5) and is used to help shed light on the hardness values obtained for the ML80 as-received specimen.

Table 4.1 – Hardness measurements made on as-received specimen ML80-S9 along two radial and one axial direction.

ML80-S9	Average Hardness (HV)	St. Dev. (HV)
Axial Direct	219	6
Radial Direction 1	225	5
Radial Direction 2	224	4

Full sized end quench specimen TCPL-S9 was examined in the as-received state. Hardness was measured in two mutually perpendicular radial directions and in the axial direction. Measurements in the radial directions were made at 0.5 mm increments, and measurements in the axial direction were made at 0.3 mm increments. The average hardness and standard deviation values are shown in Table 4.2.

As with measurements made on specimen ML80-S9, hardness values from Grade 483 Q&T as-received specimen TCPL-S9 show a high degree of uniformity. The uniformity of hardness measurements suggests that the microstructure across the geometry of Grade 483 Q&T specimens was also uniform. A uniform microstructure prior to heat treatment helped ensure that no region within the end quench specimen would show unique material characteristics due to retention of properties through the heating and quenching process.

Hardness values from specimen TCPL-S9 are low compared to measurements made on TCPL-S3 and TCPL-S8. This result is surprising as the Q&T process applied to the Grade 483 Q&T steel is expected to produce a tempered martensite microstructure with high hardness. The microstructure will be further evaluated later in this chapter (Section 4.2). The production of end quench specimens from the center of the steel fitting may be responsible for the low hardness measured in the as-received specimen. The original quenching tempering processes applied to the Grade 483 Q&T steel may have had a reduced effect on the center of the fitting wall, due to the 50 mm thickness of the fitting wall. The thickness of the fitting wall may have prevented a martensitic microstructure from forming during quenching. The absence of a martensitic microstructure means that a hard, tempered martensite microstructure would not be produced from tempering, resulting in low hardness of the as-received specimen.

Table 4.2 – Hardness measurements made on as-received specimen TCPL-S9 along two radial and one axial direction.

TCPL-S9	Average Hardness (HV)	St. Dev. (HV)
Axial Direct	211	9
Radial Direction 1	209	7
Radial Direction 2	213	8

4.1.2 Rockwell C Hardness

HRC measurements were taken on ML80 subsized end quench specimens ML80-S1, ML80-S3 and ML80-S6. Hardness was collected twice for each specimen, once on each of the two opposing flat edges (Section 3.3.1). HRC values are shown in Figure 4.1. A decrease in hardness is observed between the quenched end and a depth of 8 mm, suggesting a drastic change in microstructure is occurring at these depths. Specimen ML80-S1 shows the lowest hardness at the quenched end than the other specimens and has a maximum of 39.3 HRC. No individual specimen had the lowest or highest hardness at all depths.

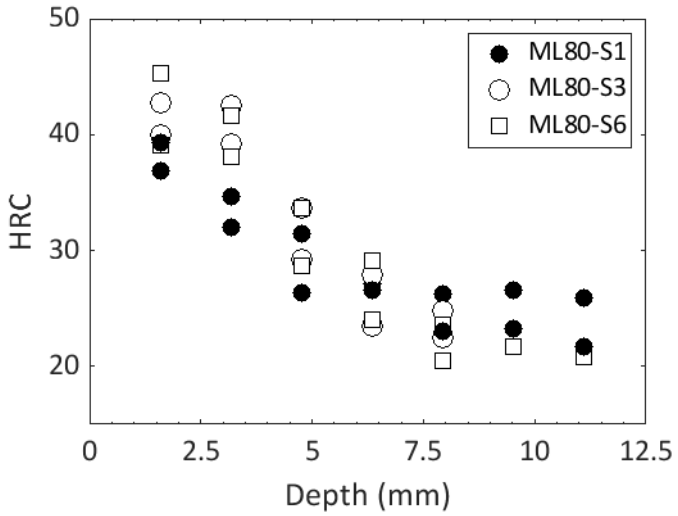

Figure 4.1 – HRC measurements for ML80 end quench specimens. Measurements below 20 HRC were not recorded.

HRC measurements were made on Grade 483 Q&T full sized end quench specimens TCPL-S2, TCPL-S4, TCPL-S5 and TCPL-S6. Data was recorded from the two opposing flat edges for each specimen. HRC results are shown in Figure 4.2. HRC measurements are only performed to a depth of 8mm for Grade 483 Q&T specimens because further measurements dropped below 20 HRC. Below 20 HRC Rockwell C hardness measurements are deemed to be inaccurate and were not recorded. Over the examined region a drastic change in hardness is observed, suggesting that a change in microstructure is occurring over this region. None of the samples is consistently higher

or lower in hardness than the other. The results suggest that uniformity across specimens has been achieved during end quenching.

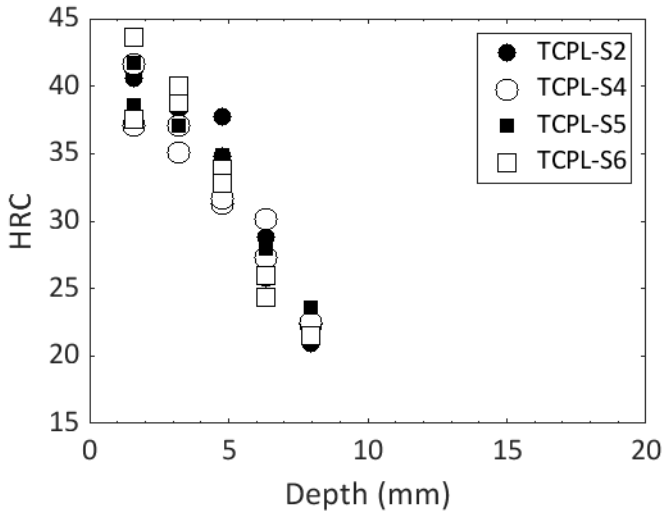

Figure 4.2 – HRC measurements for Grade 483 Q&T steel end quench specimens. Measurements below 20 HRC were not recorded.

HRC values at the quenched end of ML80 and Grade 483 Q&T specimens agree with literature values for martensite hardness based on carbon content. The carbon content of ML80 subsized end quench specimens is 0.25 wt. %. Hardness measurements on these specimens are between 37 and 46 HRC at 1.6 mm from the quenched end (Figure 4.1). Figure 4.3 shows a hardness of 43 HRC for a 95% martensite microstructure, and 39 HRC for an 80% martensite microstructure [112]. These hardness values show that end quenching of ML80 subsized specimens was successful, likely producing a martensitic microstructure across the samples specimens examined by HRC measurements.

In the case of ML80-S1 (with a maximum hardness of 39.3 HRC) the microstructure at the quenched end may not be fully martensitic, but a high fraction of martensite is achieved, likely above 80 %. For subsized end quench specimen ML80-S5, microstructure fraction measurements (Section 4.2.5.1) show hardness results consistent with a martensitic microstructure. Results of hardness and microstructure fraction measurements suggest that end quenching of ML80 specimens produced a high martensite fraction at the quenched end, though the fraction may not be 100% for all specimens.

The carbon content of Grade 483 Q&T full sized end quench specimens is 0.17 wt. %. Hardness for these specimens is between 37 and 44 HRC. The 95% martenite hardness shown in Figure 4.3 is 38 HRC which is on the lower end of the hardness that is observed for Grade 483 Q&T end quench specimens. The HRC results suggest that martensite fractions of 95% or greater are

present at 1.6 mm from the quenched end. This microstructure fraction estimate agrees with metallographic results (Section 4.2.4.2) from this work.

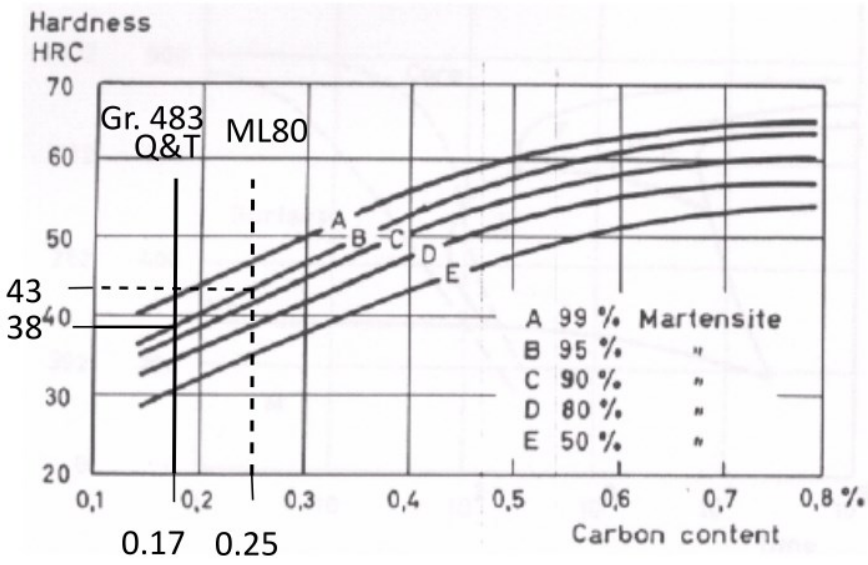

Figure 4.3 – The relationship between carbon content and Rockwell C Hardness (HRC) [112] for martensitic microstructures.

4.1.3 Vicker's Hardness

HV measurements were made at the center and near the outer edge of ML80 subsized and Grade 483 Q&T full sized specimens (Section 3.3.2). Figure 4.4 shows HV measurements for specimens ML80-S7 and ML80-S8. Little difference is seen between the measurements, which suggests that variations in hardness in the radial direction of end quench specimens is minimal. ML80 subsized specimens show the highest rate of change in hardness between depths of 2.5 and 10 mm. The change in hardness indicates the region where the transition between hard and soft microstructures is most likely to occur.

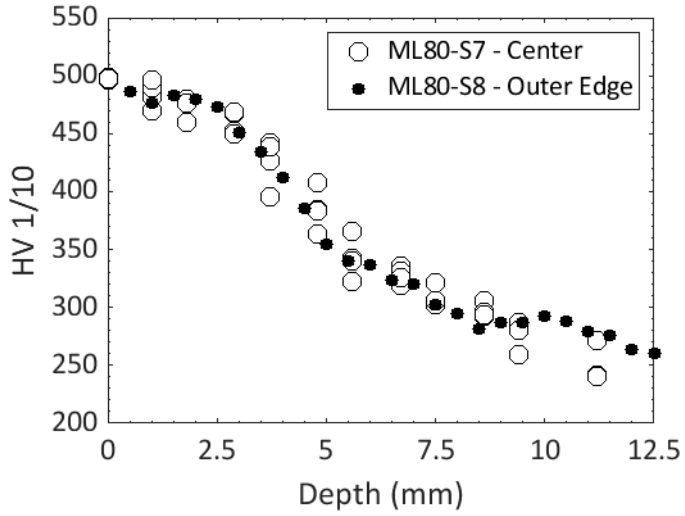

Figure 4.4 – HV measurements for ML80 end quench specimens.

HV was measured at the center of full sized end quench specimen TCPL-S3 and along a flat edge near the outer diameter of specimen TCPL-S8 (Section 3.3.2). These measurements are shown in Figure 4.5, with a high degree of consistency between the two sets of measurements. Regions of highest change in hardness are observed at depths of 4-12 mm.

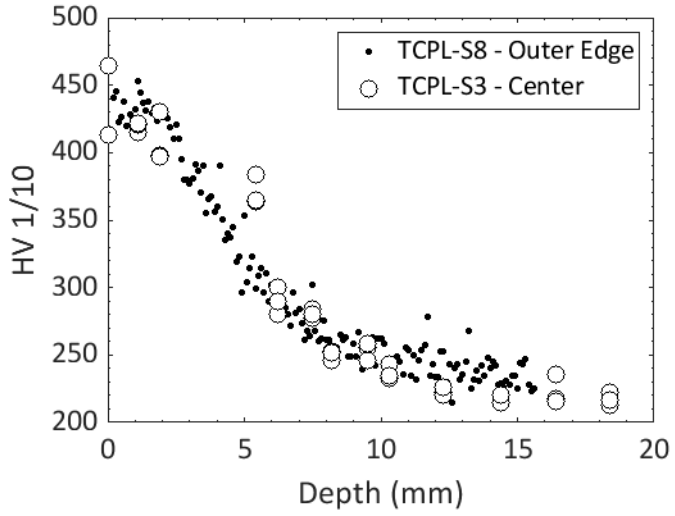

Figure 4.5 – HV measurements for Grade 483 Q&T end quench specimens.

The measured hardness values were compared with hardness values from the CCT diagram for the steel similar to Grade 483 Q&T steel (Figure 3.5) using the values for Jominy end quench cooling rates from the literature (Section 2.2, Table 2.1) [105]. Hardness values measured on specimens TCPL-S3 and TCPL-S8 within 0.2 mm of the depths listed in Table 2.1 are plotted along

with cooling rates given on the CCT curve (Section 3.1.2, Figure 3.5). As an example, between depths of 1.4 and 1.8 mm, the literature estimates cooling rates between 158 and 238 °C/s [37]. Measurements of hardness at that depth, from TCPL-S3 and TCPL-S8, are between 421 and 438 HV. At cooling rates of 220 and 120 °C/s, the CCT curve (Figure 3.5) shows hardness values of 412 and 414 HV, respectively. There is a 1.7% difference between the hardness measurements obtained experimentally, and those predicted by the CCT curve, showing good agreement between the experimentally obtained hardness values and the values found in the literature.

The entries in Table 2.1 were obtained from the literature and relate Jominy end quench specimen depth to cooling rate. The experimentally obtained hardness values from specimens TCPL-S3 and TCPL-S8 can be compared to the cooling rates for each of the entries in Table 2.1. In this manner, hardness values obtained near the same distance from the quenched end of the specimen can be compared to cooling rates predicted at those distances. Figure 4.6 shows Grade 483 Q&T hardness values from within 0.2 mm of the Table 2.1 entries for distance from the quenched end of the specimen. There values are compared to cooling rate-hardness pairs from the CCT curve (Figure 3.5). The comparison shows good agreement for hardness values measured on Grade 483 Q&T specimens and hardness values predicted on the CCT curve.

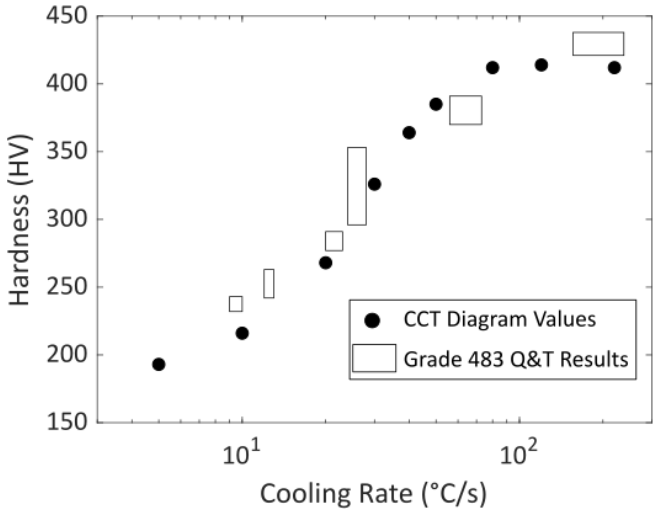

Figure 4.6 – A comparison of hardness values from Figure 3.5 and measurements made on specimens TCPL-S3 and TCPL-S8.

4.2 Microstructure Analysis

This section presents analysis of microstructures from ML80 subsized specimen ML80-S5 and Grade 483 Q&T specimen TCPL-S3. Identification of microstructures by optical microscopy is discussed first, with examples of microstructures shown from optical micrographs. Results from

microhardness measurements are presented next, with examples given for both ML80 and Grade 483 Q&T steel types. Microhardness measurements are used to support the identifications made using optical microscopy. Measurements using electron backscatter are discussed next, showing the phases that were identified at the quenched end of the Jominy specimens. Quantitative results from microstructure fractions are presented next, first for specimen ML80-S5 and then for specimen TCPL-S3. Microstructure from as-received specimens are presented last in this section.

4.2.1 Microstructure of As-Received Specimens

Specimen ML80-S9 was examined in the as-received state (Figure 4.7). The specimen is composed primarily of a ferrite phase which can be identified by the light brown colour resulting from tint etching. Average hardness values of 219 HV to 225 HV (Section 4.1.1) were measured, lower than those found on disc samples from specimen ML80-S5. Hardness measurements on the as-received specimens corroborate the identification of ferrite.

The TMCP process undergone by the ML80 casing steel is expected to produce a textured microstructure of bainite or acicular ferrite [9]. Texture is not clearly visible from the micrograph in specimen ML80-S9 in Figure 4.7. The grain boundaries of the specimen are composed of small black circles. Multiple etching trials were attempted and rule out the possibility of over-etching or under-etching.

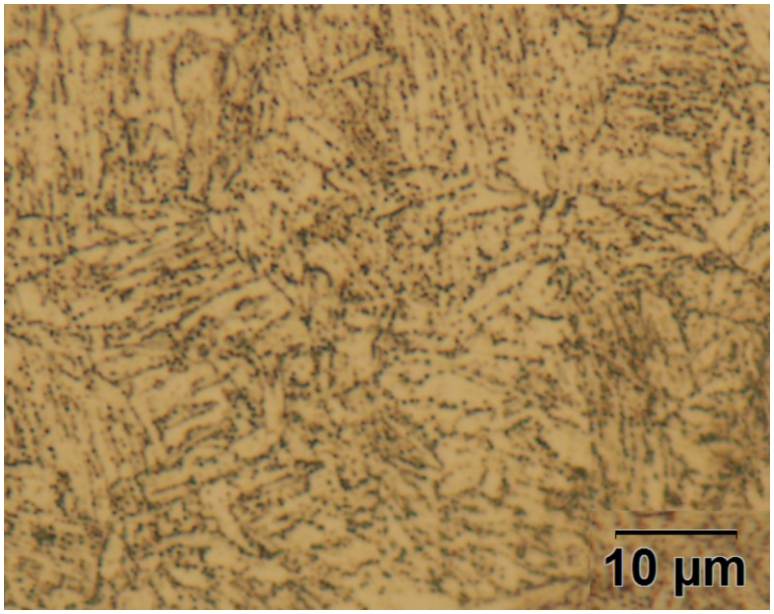

Figure 4.7 – Optical micrograph from Piece B of as-received specimen ML80-S9.

Precipitation strengthening provides an important contribution to strength of low alloy steels [9]. Literature sources show that the presence of molybdenum in microalloyed steels during TMCP

assists in the formation of carbide and nitride precipitates [113] [114]. Figure 4.8 shows an SEM image of the microstructure from Figure 4.7, from the as-received specimen ML80-S9. The particles observed through optical microscope can be seen throughout the microstructure. In steel with similar Si and Mo nominal concentrations, the literature shows the development of precipitates of similar size along prior austenite grain boundaries [115], although titanium content was higher in the literature. The microstructure in the as-received ML80 specimen can be concluded to contain precipitates. The effect of microstructure on ultrasonic velocity and attenuation is the subject of this work, and precipitation has not been investigated in relation to ultrasonic parameters in this work.

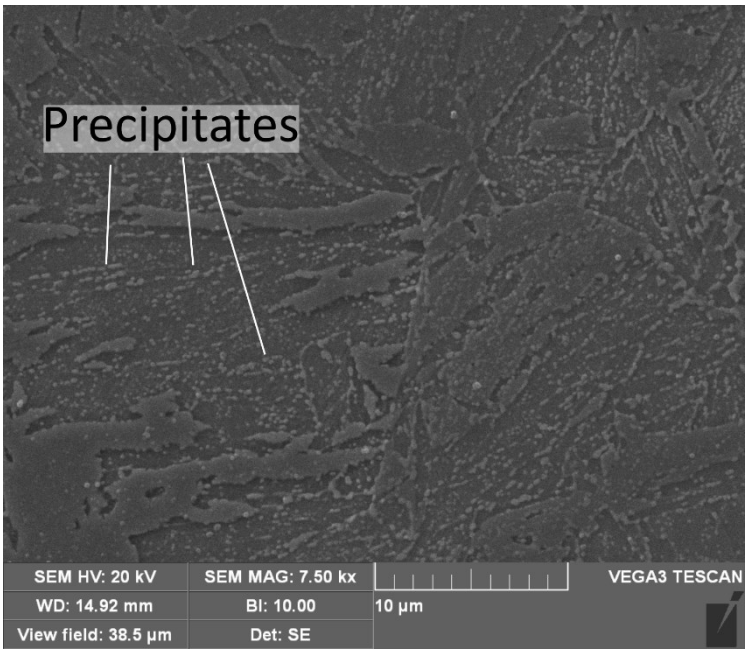

Figure 4.8 – An image of the ML80-S9 as-received specimen by SEM, showing small, rounded particles scattered throughout the microstructure.

Metallographic analysis was carried out on Grade 483 Q&T as-received specimen TCPL-S9 (Section 3.4.2) by optical microscopy (Figure 4.9). Blocky ferrite formations can be seen, as well as scattered elongated bainitic grains. Dark regions are visible at the grain boundaries but cover only a small portion of the micrograph surface. These dark regions contain martensite, based upon the colour produced by the tint etch. Hardness values on the as-received specimen are similar to those measured at a depth of 15-20 mm on specimen TCPL-S3 and TCPL-S8, where a primarily ferritic microstructure was measured (Section 4.2.4.2), confirming the dominance of ferrite in the microstructure. Microstructure fraction counting was not carried out on as-received samples, as the goal of this work is to examine the relationship between end quenching and ultrasonic parameters.

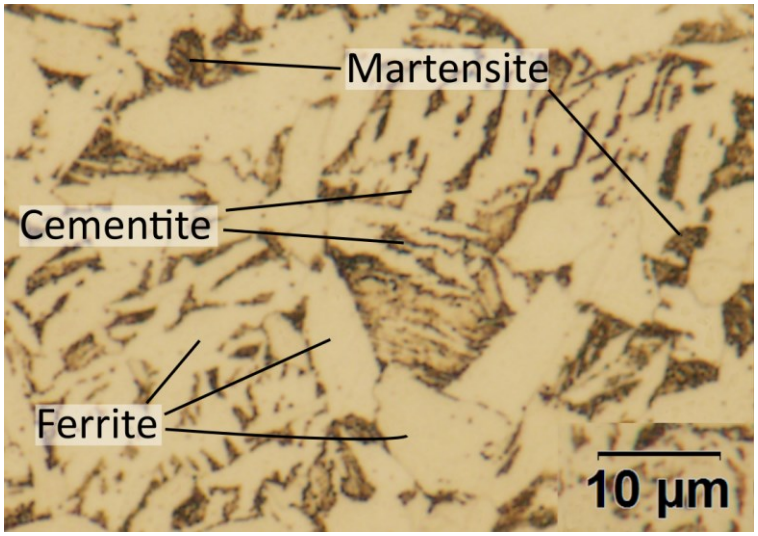

Figure 4.9 – A micrograph taken from as-received specimen TCPL-S9.

The microstructure for the as-received specimen of TCPL-S9 was not a tempered martensite microstructure as would have been expected from the Q&T heat treatment process. Tempered martensite is composed of elongated, chaotically organized grains resulting from the transition from martensite to ferrite. Grain morphologies in TCPL-S9 do not match the appearance of tempered martensite [65]. Hardness values, between 209 HV and 213 HV, are too low to be tempered martensite [61]. The observed microstructure may be a result of the thickness of the Q&T fittings. End quench specimens were taken from the center of the fitting wall, where the effect of quenching may have been reduced enough not to produce a martensitic microstructure necessary for producing tempered martensite.

4.2.2 Optical Microscopy Identification

For subsized end quench specimen ML80-S5, 11 disc faces were examined after tint-etching in order to quantify microstructure fraction. Five images were captured for examination by the ASTM point count method (Section 3.4.3) for each disc face. Throughout the length of the specimen martensite took on a darker brown colour than the surrounding microstructure. Figure 4.10 shows martensite at the quenched end of the specimen (a), and at depths of 3.3 mm (b) and 5.9 mm (c). Martensite formations beyond 5.9 mm had similar colour and morphology but were generally smaller and sparsely placed.

At the quenched end of the specimen (Figure 4.10a), martensite composed the vast majority of the microstructure, but appeared in varying shades of brown. Microhardness measurements show that the different grain appearances at the quenched end of the specimen are martensitic (Section 4.2.3.1). The automatic exposure and contrast adjustments made by the optical microscope contribute to differentiation in shades of brown exhibited by the martensitic microstructure near the quenched end of the specimen.

As distance from the quenched end increased martensite colony size decreased. At a depth of 3.3 mm (Figure 4.10b) martensite was differentiated by both the darker brown colour and the absence of internal features within grain formations. At greater depths, such as the microstructure from a 5.9 mm depth (Figure 4.10c) martensite colonies form a smaller fraction of the microstructure and were identified by the dark brown colour. Smaller features could not be distinguished at greater depths, but it is unclear if this is due to the absence of internally visible features or due to the limited resolution of the microscope. Microhardness measurements support the identifications shown in Figure 4.10, as does the CCT curve provided earlier (Figure 3.2) where a cooling rate of 56-73 °C/s is used to estimate microstructure [37].

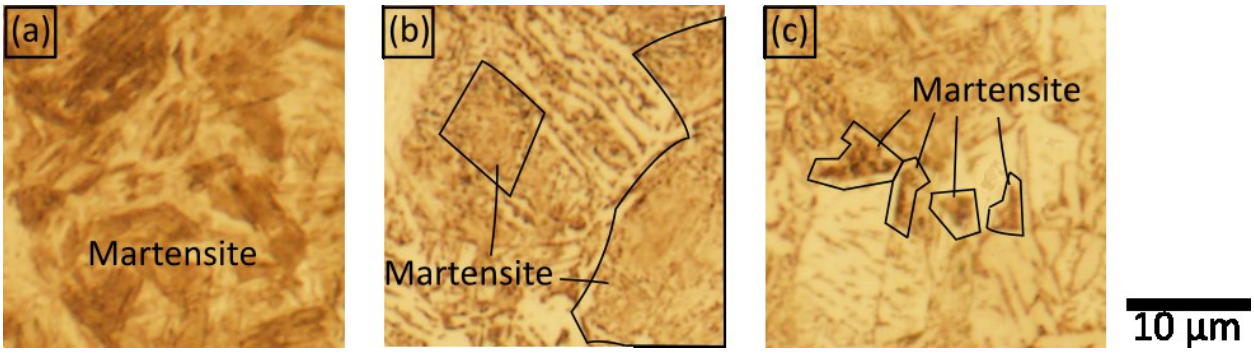

Figure 4.10 – Martensite formations in specimen ML80-S5 at depths of (a) 0.0 mm, (b) 3.3 mm and (c) 5.9 mm.

From the CCT curve for L80 steel (Figure 3.2, Section 3.1.1), bainite was expected to occur in ML80 end quench specimens for cooling rates of 120-150 °C/s. Nunura et al. [37] estimate cooling rates of Jominy end quench specimens to be 158-238 °C/s at a distance of 1.6 mm from the quenched end. From this estimated cooling rate, bainite was not expected to be found in the first disc sample from specimen ML80-S5.

At depths of 1.1 mm, the martensitic microstructure began giving way to lighter coloured grain morphologies. In some cases these regions could be identified as bainite, due to the light colour of the grains and the randomly oriented pattern of the elongated laths as shown in Figure 4.11a. The outlined region in Figure 4.11a shows a network of elongated grains, which due to the light colour of the grain after tint etching, helped in identifing this microstructure as bainite.

In some cases, microstructure formations were too small to identify clearly, as in Figure 4.11b. These types of grain morphologies were observed in fewer than 2 % of grid intersection points counted at a depth of 1.1 mm, and less than 0.5 % of grid intersections at a depth of 0 mm.. In those cases, the microstructure was categorized as unknown and appears black in the microstructure fraction plot for specimen ML80-S5. Images in Figure 4.11 appear unclear due to the limited resolution available by optical microscopy. Optical microscope images were captured electronically. Digital images resolution is limited by pixel density, limiting clarity of smaller microstructure features. These small unknown microstructures were not examined by SEM. The

unknown microstructures formed a smaller fraction of the counted microstructure points that did the standard deviation resulting from variation across the images from each disc surface.

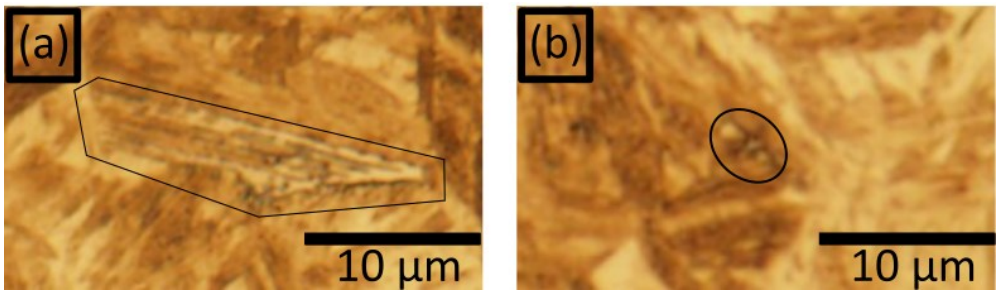

Figure 4.11 – (a) A bainitic structure and (b) and unknown microstructure found at 1.1 mm from the quenched end of specimen ML80-S5.

Figure 4.12 shows morphologies of bainite colonies at depths of 2 mm (a), 4.6 mm (b) and 9.8 mm (c). Bainite begins as networks of light coloured grains within the martensitic microstructure (Figure 4.12a) and was identified by the elongated appearance of each grain, along with the interwoven pattern of the grains. At greater depths (Figure 4.12b) bainite colonies were larger and became more difficult to distinguish from the surrounding ferrite. In these cases, bainite was identified by the interwoven pattern of elongated grains, separated by carbides. Sharp grain boundaries with straight edges were used to differentiate bainite from ferrite. As the ferrite fraction increases (Figure 4.12c), bainite is identified by the smaller grain spacing, in conjunction with the straight grain edges and elongated grain shapes.

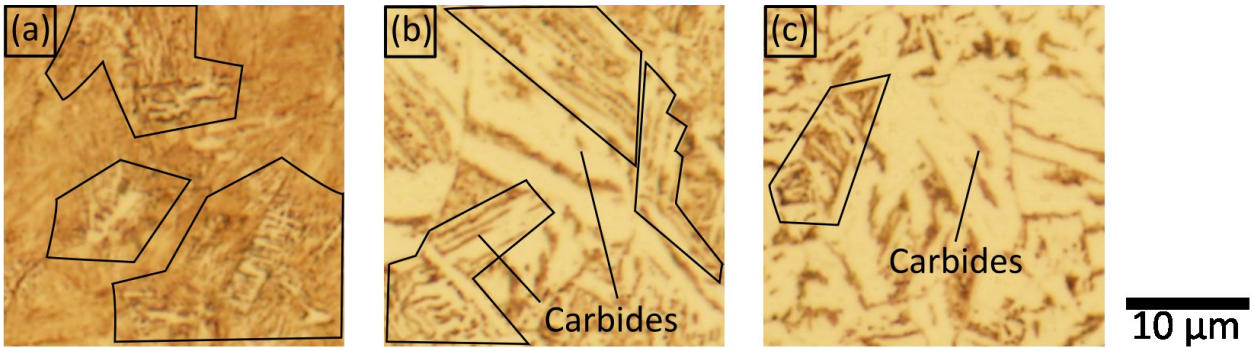

Figure 4.12 – Bainite morphologies, outlined in black, for specimen ML80-S5 at depths of (a) 4.1 mm, (b) 8.2 mm and (c) 12.3 mm.

In end quench specimen ML80-S5, ferrite grains were identified by their blocky shape and light colour. Ferrite was found at 3.3 mm from the quenched end of the specimen (Figure 4.13a), near bainite networks. Ferrite was differentiated from bainite by the smaller aspect ratio of ferrite grains and the uneven grain boundaries. Ferrite grain sizes were larger at increasing distances from the quenched end of the specimen (Figure 4.13b) and were found in larger networks at the furthest end from the specimen quenched end (Figure 4.13c). Between ferrite grains formations of carbides were observed, which were identified by their brown colour.

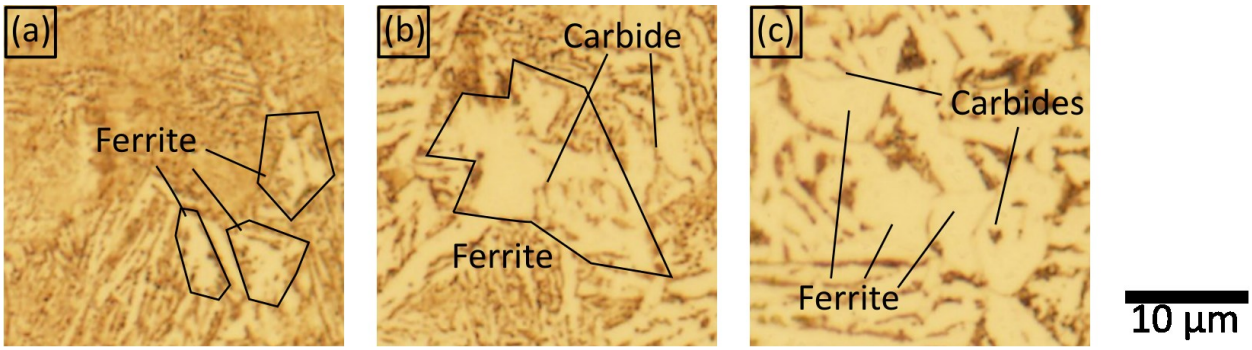

Figure 4.13 – Ferrite formations in specimen ML80-S5, showing increasing size through depths of (a) 3.3 mm, (b) 7.2 mm and (c) 12.5 mm.

Figure 4.14 shows a microstructure region which may have been identified as pearlite if it had fallen at the intersection point on a point count grid. A few lamellar structures like Figure 4.14 were observed during microstructure fraction counting of specimen ML80-S5.

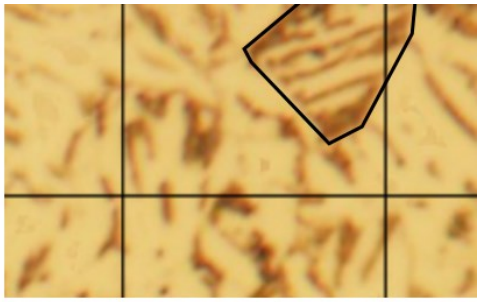

Figure 4.14 – Outlined in black is a region that may be pearlite, from Disc 9 of specimen ML80-S5.

Measurements of microstructure fraction were made on 14 disc faces from 10 disc samples of full sized end quench specimen TCPL-S3. A CCT curve was provided in Section 3.1.2 (Figure 3.5) for a steel with nominal chemistry similar to the Grade 483 Q&T steel. Microstructures in specimen TCPL-S3 were identified with the help of the CCT curve. Figure 4.15 shows martensite from disc samples at 3 different depths along the specimen length axis. In Figure 4.15a, a micrograph from the quenched end of the specimen is shown. Variations in brown saturation are shown and were examined by microhardness measurements to determine if different microstructures were present. The results from those measurements are discussed in Section 4.2.3.2 and show that both light and dark regions in the quenched end microstructure are martensite. The CCT curve shows that bainite may not have begun to form at the quenched end of the specimen and EBSD measurements show only a very small fraction of retained austenite.

As distance from the quenched end of the specimen increases, martensite represents a reduced fraction of the microstructure. In Figure 4.15b, at 7.5 mm from the quenched end, the darkest coloured regions appear in large formations separated by lighter coloured grains. Microhardness

measurements were again used to confirm that the dark regions had the highest hardness and were classified as martensitic. At greater distances from the quenched end, such as Figure 4.15c taken at a depth of 14.4 mm, martensite is identified by the dark brown colour resulting from the tint etching process.

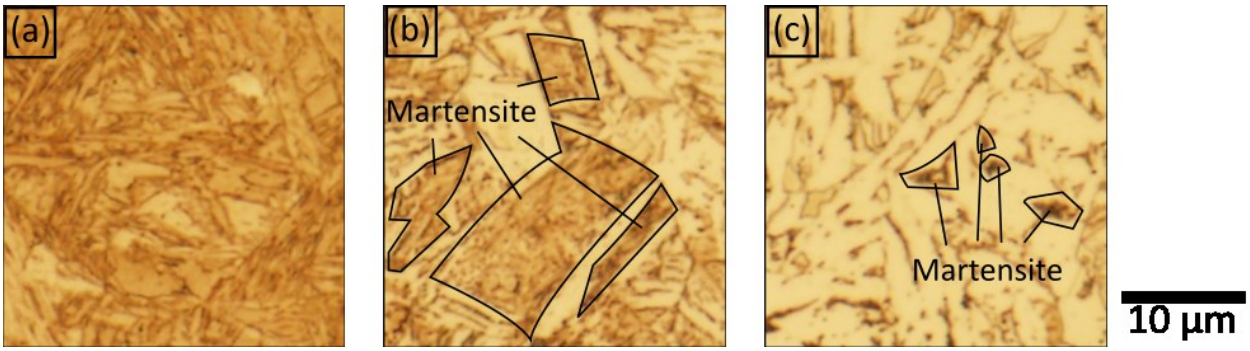

Figure 4.15 – Martensite in Grade 483 Q&T specimen TCPL-S3 at depths of (a) 0.0 mm, (b) 7.5 mm, and (c) 14.4 mm.

In micrographs from specimen TCPL-S3, bainite is identified by its light brown colour and its elongated grains formed into non-lamellar networks. Figure 4.16 shows bainite morphologies from three different depths. Bainite is easily differentiated from martensite, due to the lighter colour of bainite grains, as shown in Figure 4.16a. In some instances, the difference between bainite and ferrite is slight. At a depth of 8.2 mm (Figure 4.16b), grain boundaries between bainite grains run in straight lines. At a depth of 12.3 mm (Figure 4.16c) grain boundaries appear rough and are shorter in length. The appearance of bainite in the form of networks helps to identify bainite. Networks are seen when a woven pattern of grains can be identified and indicates that the grains have formed in a mixed direction according to their lengths. Literature results suggest that bainite can have carbides form in the interlath regions [12], which can be seen in Figure 4.17 within the bainite regions.

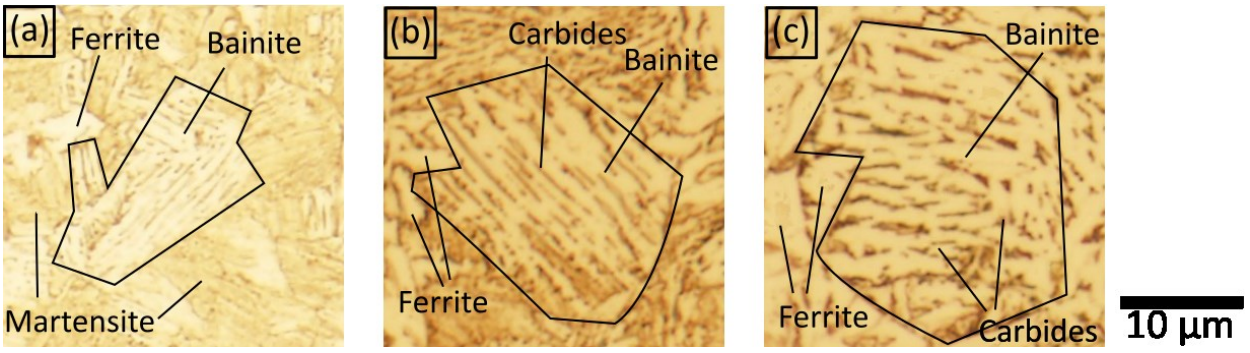

Figure 4.16 – Bainite formations, outlined in black, in specimen TCPL-S3 at depths of (a) 4.1 mm, (b) 8.2 mm and (c) 12.3 mm.

Ferrite was found extensively in micrographs from end quench specimen TCPL-S3, as shown for depths of 6.2 mm, 10.3 mm and 18.4 mm in Figure 4.17. Ferrite was identified by its polygonal

morphology and light colour. From Figure 4.17a, ferrite first appears as small blocks, separated within the matrix of martensite and bainite. As distance from the quenched end increases (Figure 4.17b and Figure 4.17c) the size of ferrite grains increases.

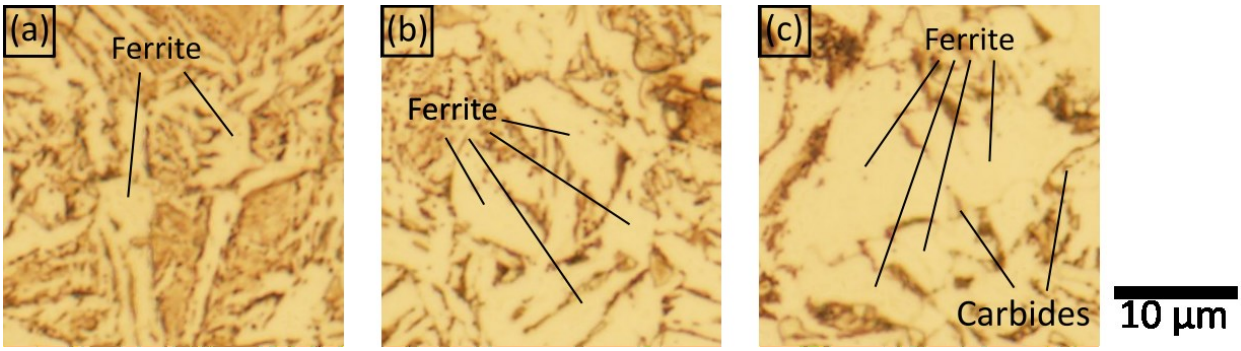

Figure 4.17 – Ferrite formations in specimen TCPL-S3 at depths of (a) 6.2 mm, (b) 10.3 mm, and (c) 18.4 mm.

In several instances, grain morphologies were found which may be identified as pearlite due to the regular spacing and repeating pattern of dark and light colours. An area is shown in Figure 4.18 which may correspond to the edge of a pearlite colony. A regular spacing of dark and light patterns is visible, and the distances of 18.4 mm from the quenched end of the specimen coincides with a cooling rate near 10 °C/s, where the CCT curve (Figure 3.5) shows that a pearlite microstructure will begin to form.

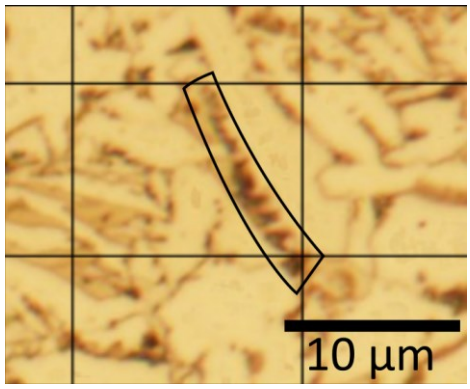

Figure 4.18 – A dark-light pattern from TCPL-S3, Disc 8, identified as either pearlite or martensite.

4.2.3 Microstructure Identification by Microhardness Measurements

The microstructure in end quench specimens of ML80 and Grade 483 Q&T steel was identified using a grid-based point-count method, described in Section 3.4.3. Identification of the microstructure was accomplished with the aid of CCT curves (Figure 3.2, Section 3.1.1 and Figure 3.5, Section 3.1.2), by observing microstructure morphologies and by making microhardness measurements on individual microstructural constituents. This section provides results from

microhardness measurements on specimen ML80-S5 and specimen TCPL-S3 to help support microstructure identification. Summaries of microhardness results are presented for each steel type at the end of the respective subsection. Micrographs with labelled point count grids for both steel types can be found in Appendix A.4.1.

4.2.3.1 ML80 Microhardness

Microhardness measurements on disc samples from ML80-S5 were used to support the microstructures identified during point counting. Indentations were made on optically identifiable microstructural features. Measurements were made on disc samples at the quenched end of the specimen (Disc 1), along with disc samples from depths of 5.9 mm (Disc 6), 12.5 mm (Disc 11) and 50 mm (Disc 12).

The microhardness values measured on disc samples from ML80-S5 are lower than hardness measurements made on other ML80 specimens (Section 4.1.3). This result is as expected, as the literature suggests that microhardness measurements are typically lower than hardness values made with higher indentation forces [30]. In that study, indentations made with smaller forces were measured at higher optical magnifications. The higher magnifications result in increased uncertainty when identifying the edges of microhardness indentation. The difficulty in identifying the edges led to consistently lower hardness results when measurements were made with smaller indentation forces.

Microstructure measurements on Disc 1 were made to determine if all microstructure features observed by optical microscopy were martensitic. The cooling rate at this depth is expected to be above 250 °C/s [37]. Two major microstructural constituents were examined for this disc sample. One constituent consisted of densely populated elongated needles (Figure 4.19a). The other constituent had the appearance of one large grain with no substructure visible after the etching procedure (Figure 4.19b). Images on the left shows the microstructure prior to hardness indentation while the images on the right show the same location after indentation. Neither microstructure constituent produced consistently higher microhardness values, leading to the conclusion that both constituents are of the same type. Average hardness values of 461 HV were measured across Disc 1 with a spread of 25 HV from highest to lowest measurement. The 25 HV variation between microhardness measurements is lower than the variation seen in other disc samples of ML80-S5, as discussed later in this section.

The difference in grain morphology seen in Figure 4.19 may be a result of the crystallographic orientation of grains. Attack etchants, such as Nital, can have different etching speeds depending on the grain orientation [116], which may cause some regions to have fewer features shown after etching. Based on the microhardness values obtained, both microstructure constituents are classified as martensite in this work. Cooling rates on Jominy end quench specimens from the literature estimate cooling rates at this depth above 250 °C/s, where the CCT curve (Figure 3.2)

shows a solely martensitic microstructure. The estimates of cooling rate corroborate the microstructure identified by microhardness measurements.

Microhardness values measured at the quenched end of Disc 1 from specimen ML80-S5 are 37 HV higher than measurements made at the EBSD measurement location of ML80-S7 (Section 4.2.4.1). The reason for this difference may be due to additional difficulty in edge detection on indentations made on the previously etched discs from specimen ML80-S5. Hardness measurements at high optical magnifications are known to be a large source of error in microhardness measurements, due to low optical resolution at these magnifications [30].

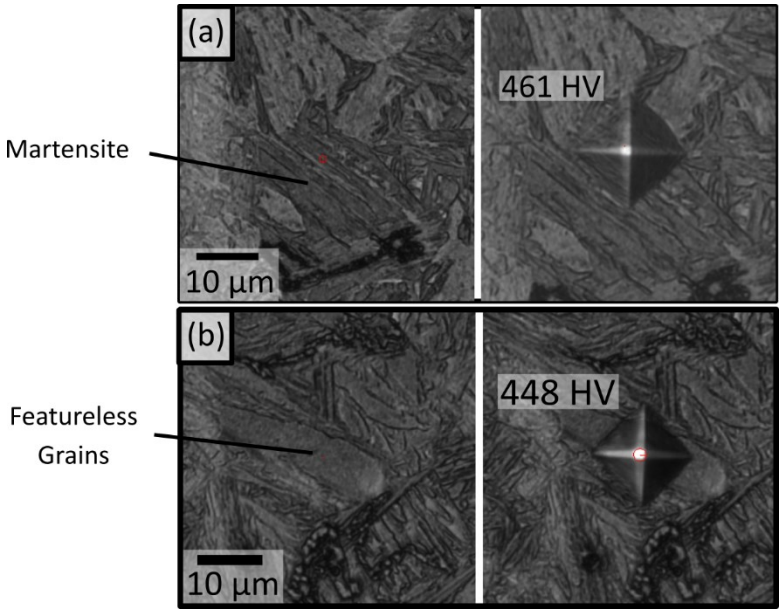

Figure 4.19 – Microhardness measurements made on, (a) a dense needle-shaped region and (b) a larger, uniform grain. Images on the left are prior to indentation, while those on the right are after indentation.

Microhardness measurements made on Disc 6 of ML80-S5 are shown in Figure 4.20. Three microstructural features were examined, including dark regions with densely-packed features (Figure 4.20a), large uniform light coloured regions (Figure 4.20b) and regions with randomly oriented grains of light colour (Figure 4.20c). The region is shown prior to indentation on the left of each image and after indentation on the right. Dark features consistently gave the highest hardness values, with average values of 288 HV. These values are consistent with the expectation of tint etching darkening martensite in the microstructure. Lighter regions (Figure 4.20b) produced the lowest hardness values, with an average of 240 HV. Elongated light grains (Figure 4.20c) gave medium hardness values, with an average of 257 HV.

At a depth of 5.9 mm, measured on Disc 6 from ML80-S5, cooling rates around 25 °C/s are expected [37]. At that cooling rate a mixed microstructure of martensite, bainite and ferrite is

expected from the CCT curve (Figure 3.2, Section 3.1.1). Hardness values split into three groups associated with distinct grain morphologies, making identification of microstructures straightforward. The difference between martensite hardness observed on Disc 6 and on Disc 1 (Figure 4.19) can be explained by the presence of the surrounding microstructure. The hardness of the surrounding microstructure is inadvertently tested along with the individual grain being examined. The softer overall microstructure of Disc 6 reduces the hardness encountered by the indenter, as it does not provide the same resistance to indentation as the surrounding microstructure in Disc 1. The softer microstructure around the indentation region causes a reduction in the hardness value measured for the same microstructural constituent.

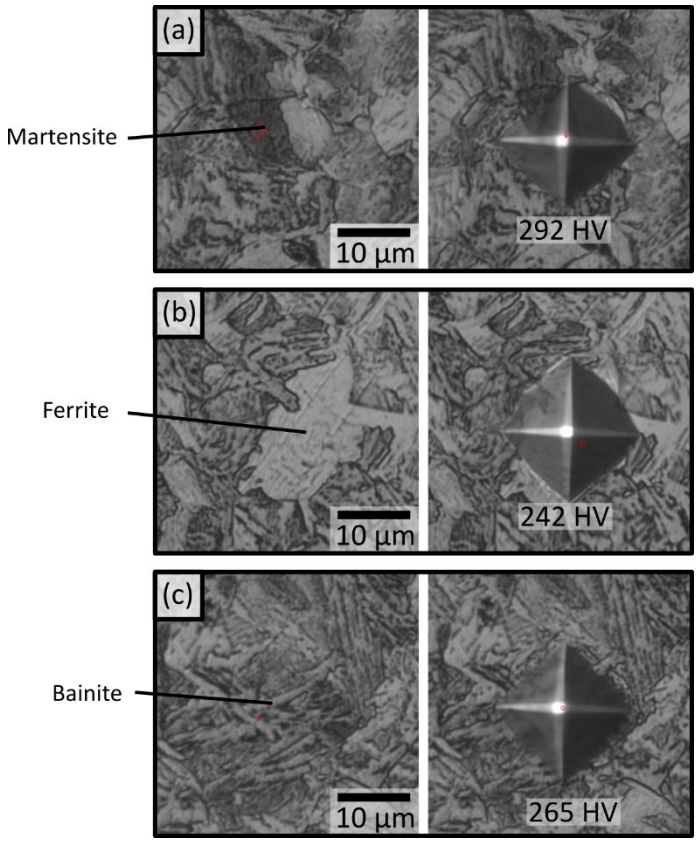

Figure 4.20 – Microhardness indentations on Disc 6 of specimen ML80-S5. Microstructures are identified as (a) martensite, (b) ferrite and (c) bainite. Images on the left are prior to indentation, while those on the right are after indentation.

Microstructure morphologies at a depth of 12.5 mm from Disc 11 fell into two categories, either small, intricate groups of elongated grains (Figure 4.21a) or large blocky light coloured grains (Figure 4.21b). Microhardness measurements showed that larger grain shapes produced lower hardness values. This observation is in line with the CCT curve suggesting that a primarily bainite and ferrite mixture would be present at 12.5 mm (Figure 3.2), where a cooling rate near 10 °C/s

is expected. Larger grains were identified as ferrite, while smaller grains with elongated needles were identified as bainite. Martensite was identified by the dark brown colour visible on optical micrographs, but these regions were too small to examine by microhardness measurements.

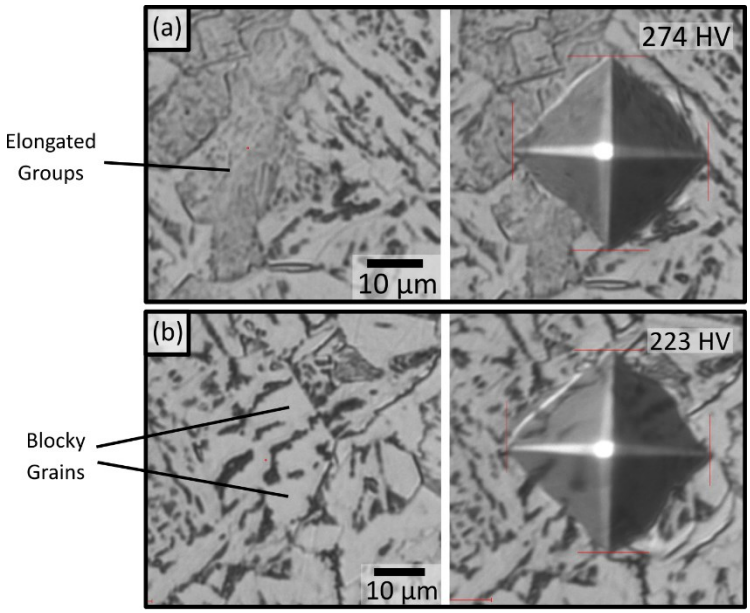

Figure 4.21 – ML80-S5 Disc 11, with microstructures identified as (a) a mixture of martensite and bainite and (b) primarily ferrite. Images on the left are prior to indentation, while those on the right are after indentation.

Microhardness measurements were made at a depth of 50 mm on specimen ML80-S5. Cooling rates at these depths are expected to be below 3.5 °C/s [35]. This disc was sectioned exclusively for microhardness measurements. Figure 4.22 shows microhardness indentations made on that specimen. Microstructure regions with more complicated grain patterns (Figure 4.22a) generally produced higher hardness values, while ferrite grains (Figure 4.22b) gave lower hardness values. The more complicated grain patterns are expected to be pearlitic, based on analysis of the CCT curve (Figure 3.2), and owing to the extensive presence of dark coloured carbides within the grains. A more careful analysis with EBSD or SEM microscopy would be needed to clearly identify the microstructure regions that are pearlitic. In this work priority was placed on ultrasonic testing analysis, which was not conducted on specimens from depths of 50 mm, so further analysis of the microstructure at these depths was not pursued.

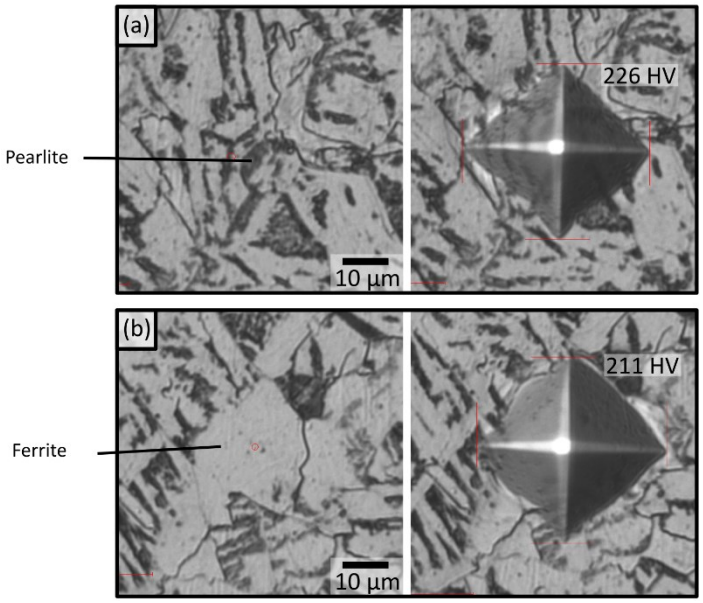

Figure 4.22 – Microhardness indentations made at 50 mm from the quenched end of the specimen, showing (a) a microstructure of either bainite or pearlite and (b) ferrite. Images on the left are prior to indentation, while those on the right are after indentation.

Higher microhardness results were consistently identified with martensitic microstructures, while lower values were observed for bainitic and ferritic microstructures. Pearlite was only observed at a depth of 50 mm, where lower cooling rates were expected (Figure 3.2). Complete results from microhardness measurements can be found in Appendix A.1.2.

Table 4.3 – Results from microhardness measurements shown for specimen ML80-S5.

Figure	Disc Number	Depth (mm)	Hardness (HV)	Approximate Cooling Rate (°C/s)	Microstructure Identified
Figure 4.19a	1	0.0	461	>250	Martensite
Figure 4.19b	1	0.0	448	>250	Martensite
Figure 4.20a	6	5.9	292	25	Martensite
Figure 4.20b	6	5.9	242	25	Ferrite
Figure 4.20c	6	5.9	265	25	Bainite
Figure 4.21a	11	12.5	274	10	Martensite/Bainite
Figure 4.21b	11	12.5	223	10	Ferrite
Figure 4.22a	12	50	226	<3.5	Pearlite
Figure 4.22b	12	50	221	<3.5	Ferrite

4.2.3.2 Grade 483 Q&T Microhardness

Microhardness measurements were made on disc samples from specimen TCPL-S3. Disc samples used were from depths of 0.0 mm (quenched face of Disc 1), 8.2 mm (Disc 6), 20.7 mm (Disc 10) and 50 mm (Disc 11). Microhardness measurements were used to help identify the microstructure visible by optical microscopy. Indentations made on Disc 1 from specimen TCPL-S3 showed an average hardness value of 453 HV, with a spread in values of 12 HV between the highest and lowest measurements. These measurements are close to the hardness values obtained by measurements performed on specimens TCPL-S3 and TCPL-S8 (Section 4.1.3). The similarity in measurements between micro- and macrohardness values differs from the expectation set by the literature and measurements on ML80 specimens. Literature sources state that microhardness values are expected to be lower than macrohardness measurements performed on the same steel [30], which was found to hold true for measurements on specimen ML80-S5 (Section 4.2.3.1). A comparison of microhardness indentations made at the quenched end of specimen TCPL-S3 in Figure 4.23 and those made on specimen ML80-S5 (Figure 4.19) show that indentation edges are clearer on Disc 1 from specimen TCPL-S3. The clearer indentation edges make hardness value readings easier to determine and contributes to the similarity between microhardness and macrohardness values.

Figure 4.23 shows indentations made on two common grain morphologies that were observed at the quenched end of specimen TCPL-S3 (Disc 1, on the quench face); a large, featureless grain (Figure 4.23a) and a collection of small elongated grains (Figure 4.23b). At the quenched end of the Jominy specimens, cooling rates above 250 °C/s are expected from the literature [37]. Hardness values were similar across the two morphologies, with two measurements made for each morphology. This result was interpreted to mean that both morphologies had the same microstructure. The differences in appearance observed between the two morphologies can arise within the same microstructure when etched using attack etchants (i.e. Nital) or tint etchants (i.e. sodium metabisulfite) [31, pp. 623, Ch. 9]. Certain grain orientations may be preferentially etched, resulting in differences in appearance when observed by optical microscopy.

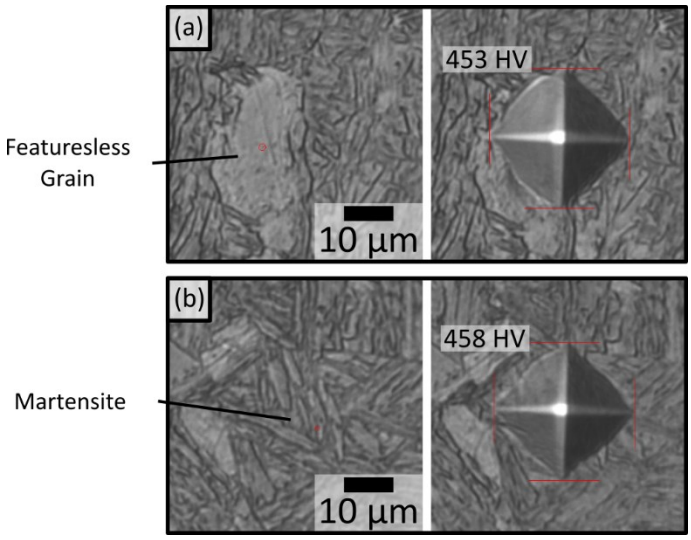

Figure 4.23 – Microhardness indentations made at the quenched end of specimen TCPL-S3, showing martensite in both (a) and (b). Images on the left are prior to indentation, while those on the right are after indentation.

Microhardness values on Disc 1 from specimen TCPL-S3 were on average 53 HV higher than measurements made on the EBSD region of TCPL-S1. As was discussed for measurements on ML80 specimens (Section 4.2.3.1), edge detection was more challenging on etched disc samples, which may have caused an increase in microhardness results on specimen TCPL-S3 compared to those made over EBSD measurements for specimen TCPL-S1.

Analysis of the macrohardness measurements on TCPL-S1 (Section 4.1.2) showed that some regions of bainite may be present in the microstructure, while microhardness values for TCPL-S3 suggest martensite is present across the microstructure. This difference may have resulted during quenching, if specimen TCPL-S1 was not moved from the furnace to the quench unit quickly enough, a reduced cooling rate at the quenched end would result producing a larger fraction of bainite.

For Disc 6, at 8.9 mm from the quenched end the cooling rate is estimated at 15 °C/s [37]. There were three primary microstructure morphologies. On the left side of Figure 4.24, pre-indented microstructures can be seen for featureless grains (Figure 4.24a), dark grains with some internal structure (Figure 4.24b) and elongated, light coloured grains formed into a network (Figure 4.24c). Microhardness values taken at each of these locations can be seen on the right-side images of Figure 4.24.

Light, featureless grains produced the lowest hardness values (Figure 4.24a), dark regions produced the highest values (Figure 4.24b) and networks of light grains produced intermediate microhardness values (Figure 4.24c). From these results, the three regions were identified as ferrite, martensite and bainite, respectively. The microstructure in Figure 4.24c was identified as

bainite instead of pearlite because the CCT curve for the steel (Figure 3.5) did not show pearlite at the cooling rate expected at this depth and because networks did not show the lamellar morphology expected of pearlite.

Hardness values of martensite are lower for Disc 6 (8.9 mm depth) than for Disc 1 (0 mm depth). The difference in the hardness of martensite results from the indentation size being larger than the microstructural constituent being examined. Hardness measurements on Disc 6 include the martensite grain as well as the surrounding bainite and ferrite. The presence of the surrounding microstructure reduces the overall hardness value obtained.

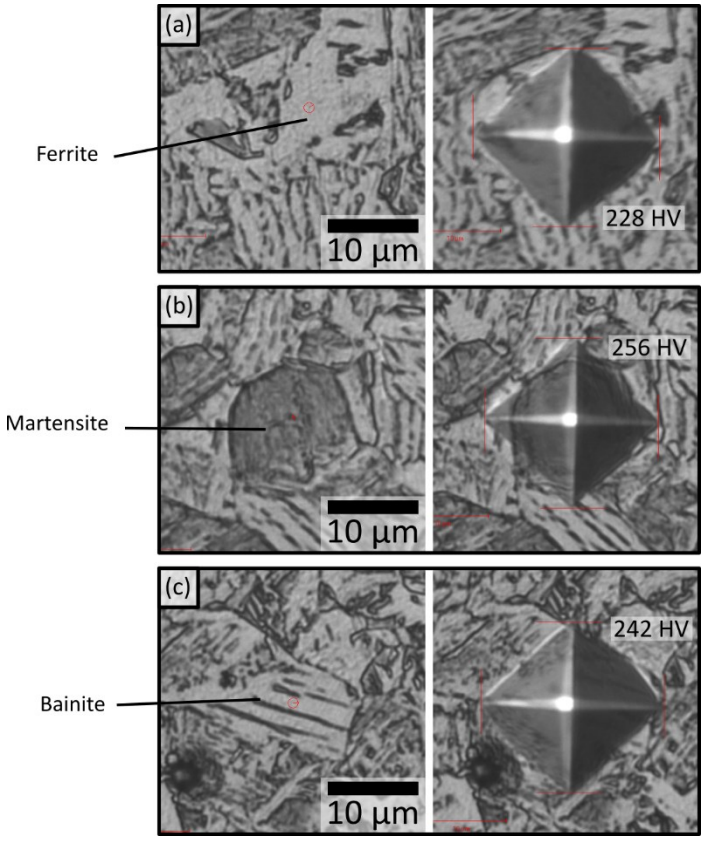

Figure 4.24 – The queched end face of Disc 4 from specimen TCPL-S3, with microstrucures of (a) ferrite and bainite, (b) martensite, and (c) ferrite surrounded by bainite. Images on the left are prior to indentation, while those on the right are after indentation.

Microhardness measurements were made at 20.7 mm from the quenched end of specimen TCPL-S3 on Disc 10, where cooling rates near 5 °C/s are expected [37]. Microstructures were investigated on large light-coloured regions (Figure 4.24) and on regions densely populated by dark grain boundaries resulting from tint etching. Microhardness values were lowest on light regions and increased with an increasing density of darker lines, as shown in Figure 4.25. Light regions were identified as ferrite while darker regions were identified based on the morphology

of the dark lines, typically as bainite. Larger dark grain morphologies can be seen in Figure 4.25b, but were too small to be isolated for microhardness testing. The possible presence of pearlite within these darker regions can be dismissed, as at the carbon concentrations used in this research, interlamellar spacing of pearlite would be visible at the magnifications used [117].

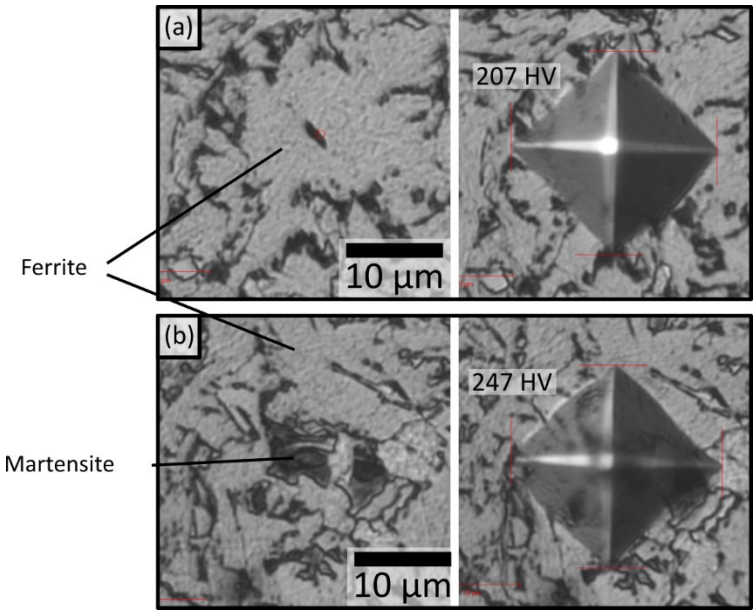

Figure 4.25 – Microhardness indentations made on specimen TCPL-S3 on Disc 11, located 20.7 mm from the quenched end of the specimen, with (a) ferrite and (b) ferrite with martensite. Images on the left are prior to indentation, while those on the right are after indentation.

An additional disc sample was sectioned from specimen TCPL-S3 at 50 mm from the quenched end of the specimen. At this distance from the quenched end of the specimen, cooling rates below 3.5 °C/s are expected [35]. Microstructural features on this disc sample showed two primary morphologies. One morphology showed large grains, identified as ferrite due to their low microhardness values and polygonal shape (Figure 4.26a). The other microstructure was identified as either pearlite or bainite and consisted of elongated grain boundaries (Figure 4.26b and c). Dark regions in the microstructure consist of grain boundaries and cementite [116].

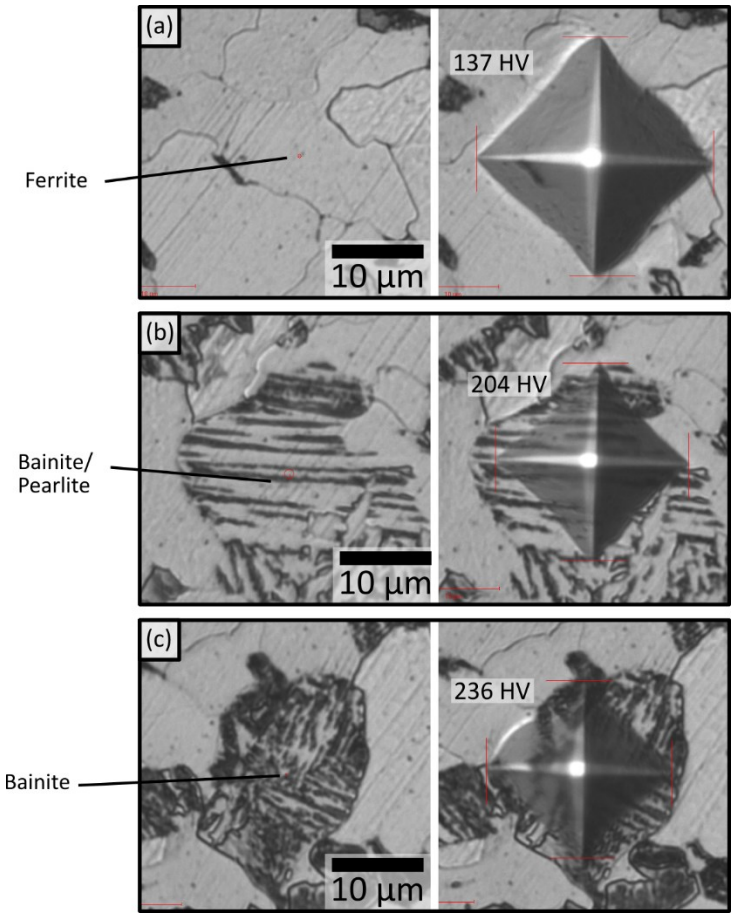

Figure 4.26 – Microhardness indentations made 50 mm from the quenched end of specimen TCPL-S3, on microstructures of (a) ferrite, (b) pearlite or bainite and (c) bainite, with some martensite around the grain boundaries. Images on the left are prior to indentation, while those on the right are after indentation.

In Table 4.4 a summary of the microhardness measurements presented in this subsection can be seen. Martensite is observed through the different depths at which microhardness measurements were made, while bainite and ferrite are observed for Disc 4 at a depth of 8.9 mm. These results are supported by the CCT curve for this steel (Figure 3.5) which shows bainite beginning to form at cooling rates near 120 °C/s and ferrite forming at 40 °C/s. Pearlite is observed at the lowest cooling rates, far from the quenched end of the specimen. Complete results from microhardness testing can be found in Appendix A.1.4.

Table 4.4 – Results for microhardness measurements shown for specimen TCPL-S3.

Figure	Disc Number	Depth (mm)	Hardness (HV)	Approximate Cooling Rate (°C/s)	Microstructure Identified
Figure 4.23	1 – Quench side	0.0	453	>250	Martensite
Figure 4.23	1 – Quench side	0.0	458	>250	Martensite
Figure 4.24	4 – Quench side	8.9	228	15	Ferrite/Bainite
Figure 4.24	4 – Quench side	8.9	256	15	Martensite
Figure 4.24	4	8.9	242	15	Ferrite
Figure 4.25	10	20.7	207	5	Ferrite
Figure 4.25	10	20.7	247	5	Ferrite/Martensite
Figure 4.26	11	50	137	<3.5	Ferrite
Figure 4.26	11	50	204	<3.5	Pearlite/Bainite
Figure 4.26	11	50	236	<3.5	Bainite/Marensite

4.2.4 Electron Backscatter Diffraction

This section presents Electron Backscatter Diffraction (EBSD) maps collected from regions on ML80 specimen ML80-S7 and Grade 483 Q&T specimen TCPL-S1 (Section 3.4.4). EBSD involves measuring diffraction patterns at each location on a test specimen and comparing them to diffraction patterns for known phases from a reference library. Reference library entries for ferrite, cementite and austenite were used for EBSD measurements on both ML80 and Grade 483 Q&T steel types.

Band contrast maps and phase maps indicate that strained ferrite dominates the microstructure of both steel types. Microhardness measurements and Kernel Average Misorientation (KAM) maps are used to confirm a martensitic microstructure by determining that very fine-grained structures are found across the samples, often with further substructure within them. The type of substructure is consistent with martensitic microstructures. Pole figures are used to confirm that no preferred orientation was found within the sample areas. Further information from EBSD analysis can be found in Appendix A.5.

4.2.4.1 ML80 Subsized Specimen ML80-S7

In a band contrast map, the grey scale indicates the degree of agreement with measurements made by EBSD and the reference library used to identify phases. White would indicate perfect agreement, while black would indicate an inability to categorize the examined region. Martensite is identified in band contrast maps as strained ferrite, appearing in shades of grey due to only moderate agreement between measurements and reference library entries [109]. Measurements made on grain boundaries appear black in band contrast maps due to the presence of dislocations. A band contrast map in the radial direction of specimen ML80-S7 is shown in Figure 4.27. Most of the grains in Figure 4.27 have an elongated structure and are light grey in colour. These features of the grains support identification of the microstructure as martensitic and will be examined more closely during the remainder of this section.

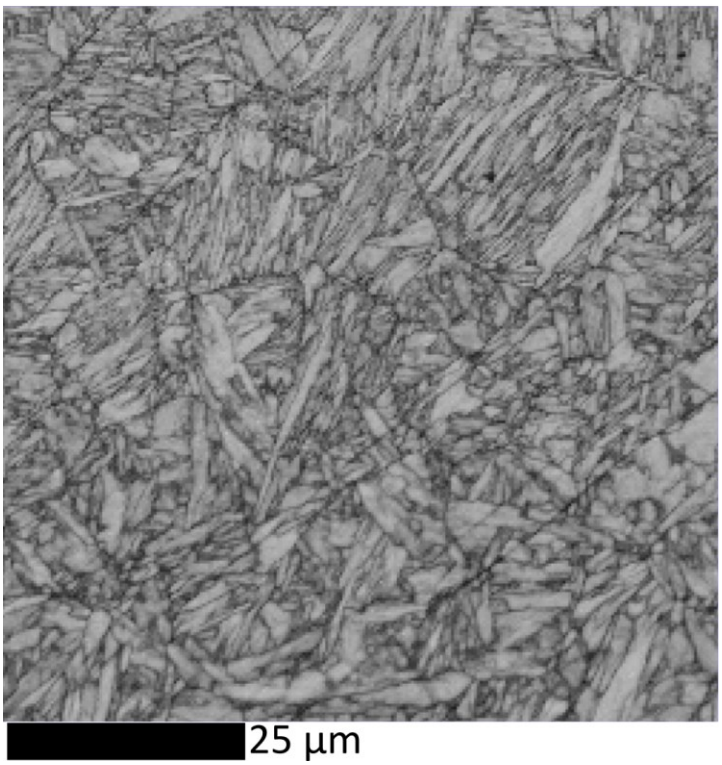

Figure 4.27 – The band contrast map resulting from EBSD measurements made on ML80 end quench specimen ML80-S7.

EBSD measurements were used to produce a phase map with colour coding for each of the phases detected. EBSD maps taken of end quench specimens used reference library entries for ferrite, austenite and cementite. Martensite was indexed as strained ferrite, with changes in the crystal structure causing mismatch between measurements and the reference library. The degree of mismatch depended on the carbon concentration and its effect on the lattice parameters of the martensite crystal [118] [119].

Figure 4.28 shows a phase map taken from specimen ML80-S7 in the radial direction. In Figure 4.28, blue is used to indicate ferrite (and strained ferrite), green indicates austenite and yellow indicates cementite. As with band contrast maps, black indicates regions where a match between measurements and the EBSD reference library could not be found. Figure 4.28 indicates that less than 0.5 % of the map is composed of retained austenite, found either in individual measurement points or in groups as large as 4 measurements.

The small fraction of retained austenite in the ML80 as-received microstructure is not surprising, since the steel has low silicon content [17]. A reduction in step size used for EBSD measurements is unlikely to affect the retained austenite fraction. The measurement area examined by the electron beam is smaller than the step size. Reducing the step size would not allow unclassified black regions in Figure 4.28 to be differentiated into one of the blue, green or yellow phase classifications. Instead, a reduced step size would only allow smaller retained austenite regions, which may have been missed, to be detected.

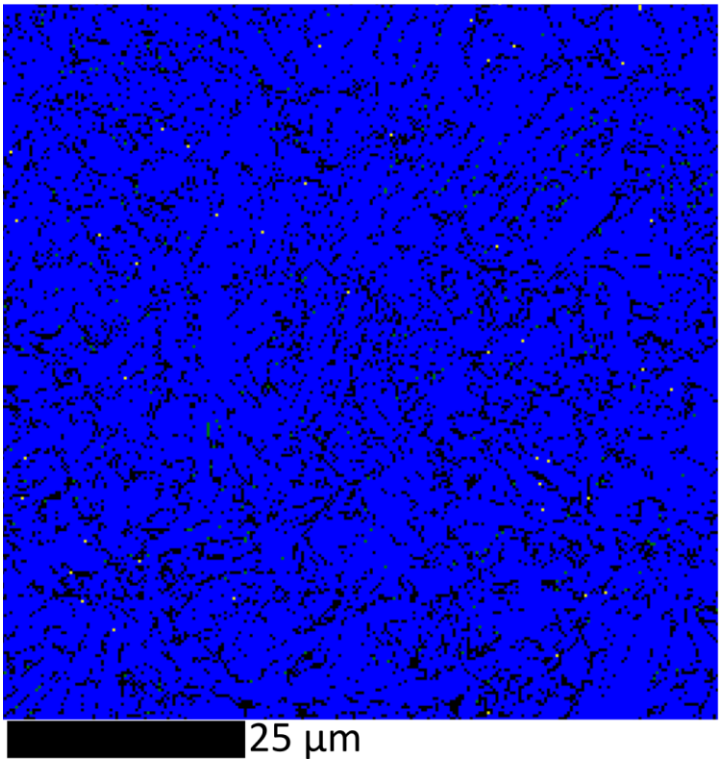

Figure 4.28 – The phase map from specimen ML80-S7 showing BCC structures (blue), retained austenite (yellow) and cementite (green).

In order to establish the phase present in the blue regions of the phase map, microhardness measurements were made on specimen ML80-S7 on the same region examined by EBSD. A 50 gf Vickers indentation with a 10 second dwell time was used. Microhardness measurements on specimen ML80-S7 produced an average of 423 HV with a spread of 25 HV. The polished and

unetched surface of specimen ML80-S7 after EBSD measurement simplified edge detection, reducing uncertainty in the microhardness measurements.

Microhardness values taken on the EBSD map region coincide with hardness values for a mixed martensite and bainite microstructure from the CCT curve for the L80 steel (Figure 3.2). It has been discussed that the differences between the L80 and ML80 steels may mean that the maximum hardness of ML80 steels is lower. Lower maximum hardness for the ML80 steel would mean that hardness values identified as a mix of martensite and bainite in the L80 CCT curve could be a fully martensitic microstructure in the ML80 steel. Literature results also state that microhardness values are often lower than macrohardness values measured on the same steel [30]. These two factors mean that microhardness values made on the quenched surface of ML80-S7 are consistent with a martensitic microstructure.

An inverse pole figure (IPF) map indicates crystallographic orientation of the scan location using colours. Figure 4.29 shows the indent locations that were made on specimen ML80-S7 overlaid onto an IPF map. The colour legend for the IPF map is shown on the right side of Figure 4.29. Indentation regions were selected where microstructure classification was the most uncertain. These regions included large uniformly oriented grains and regions where the recrystallization map indicated substructure (see Figure 4.30).

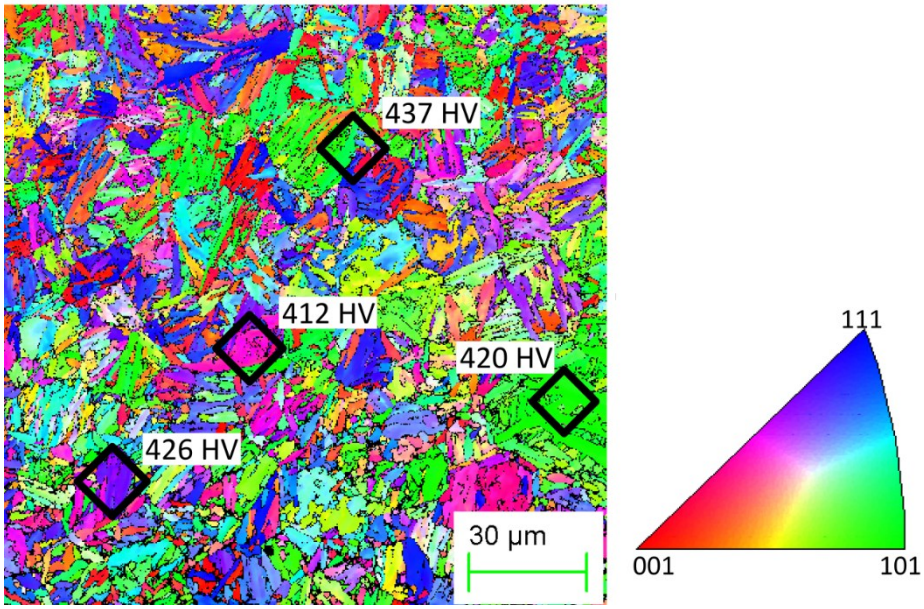

Figure 4.29 – (Left) IPF orientation map with the locations of microhardness measurements in the axial direction of subsized specimen ML80-S7. (Right) Colour legend for the IPF map is included.

Figure 4.30 shows microhardness indentation locations overlaid on a recrystallization map taken in the radial direction at the quenched end of specimen ML80-S7. A recrystallization map uses

colour codes to identify crystal structure and is produced by the EBSD software. In the case of Figure 4.30, red regions are deformed, blue regions are recrystallized and yellow regions are substructured. Deformation occurs in regions under strain and is identified by EBSD measurements that do not match reference library entries. Recrystallized regions are identified by the crystal structure being without any major deformation. Substructure indicates the existence of minor differences across the grain which do not appear in measurements of crystallographic orientation.

A comparison of strained and substructured regions is made to help determine if major difference in microhardness values may indicate differences in phase or microstructure at these locations. Microhardness in the substructured region (Figure 4.30, right-most indentation) was very close to microhardness in the deformed regions of the EBSD map. The similarity in values indicates that the same microstructure is present in both types of regions. Due to the sparsity of recrystallized grains in the EBSD map (Figure 4.30, blue), direct measurement of the hardness of these regions could not be evaluated. Due to the low fraction of retained austenite locations in the EBSD map (i.e., less than 0.5 % retained austenite, Figure 4.28), recrystallized regions can be ruled out as being composed of retained austenite.

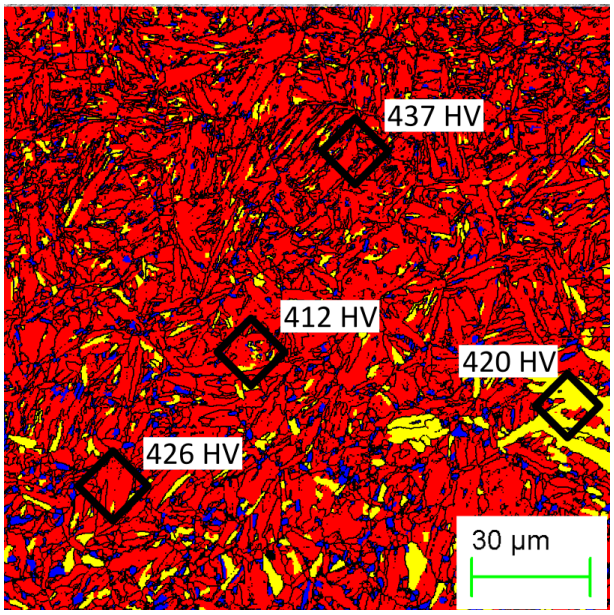

Figure 4.30 – A recrystallization map with the locations of microhardness indentations for the axial direction of ML80-S7. The map shows deformed (red), recrystallized (blue) and substructured (yellow) regions.

Another set of EBSD measurements was collected for ML80 subsized specimen ML80-S7 (Section 3.4.4) at the quenched surface and in the axial direction near the quenched end of the specimen. KAM maps show the difference in crystallographic orientation between each EBSD scan location

(i.e. pixels on the KAM map), called the kernel, and its neighboring scan locations [120] [121]. The colour of each pixel represents the average difference between the scan location and its neighbors. The KAM maps in Figure 4.31 show the average difference in misorientation with a colour scale between 0 and 2 degrees. Blue regions indicate that very little change in grain orientation exists being neighboring measurement points, while light green regions show an average of 0.5-1° difference in grain orientation between neighboring scan locations. Regions with yellow or red colouring indicate misorientation between scan locations of 1-1.5° and 1.5-2°, respectively.

KAM maps from EBSD measurements on subsized specimen ML80-S7, at the quench surface, are shown in Figure 4.31a. Results from the axial direction are shown in Figure 4.31b. Both KAM maps show that orientation differences between 0.5° and 1.5° dominate the microstructure. Regions in blue are found scattered throughout the microstructure, where no average orientation difference between neighboring scans was found. The dominant green colour of the KAM map indicates that most of the microstructure is composed of very fine-grained regions with low angle grain boundaries. A fine-grained structure is consistent with a martensite microstructure. Individual regions delineated by black boundaries in Figure 4.31a and Figure 4.31b are martensite packets. Individual martensite laths are shown by the fluctuations in colour on the KAM maps, but are difficult to uniquely identify at each location [109].

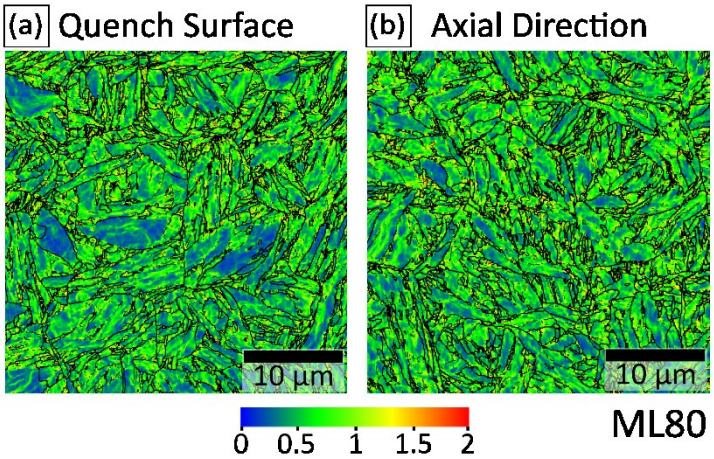

Figure 4.31 – KAM maps of (a) the quench surface and (b) the axial direction of specimen ML80-S7, showing the average difference in local grain orientation (in degrees).

Although regions in blue do not show any average orientation differences, differences may still exist between neighboring scan locations [122]. An example region is shown in Figure 4.32, where a KAM maps and recrystallization map of the same region is shown. Large blue regions in Figure 4.32a show that average grain misorientation is low. The recrystallized map in that region indicates that substructure is detected due to shifts in grain orientation which did not appear in

the KAM map. Substructure is a measure of grain orientation shifts detected by the EBSD software during analysis of the specimen.

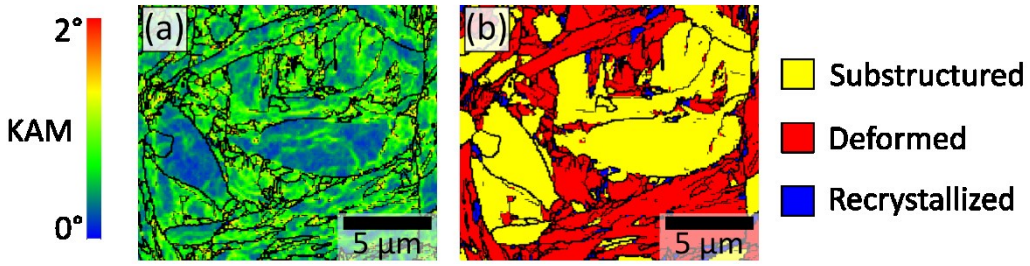

Figure 4.32 – A portion of (a) a KAM map and (b) a recrystallization map of the quench surface of ML80 subsized end quench specimen ML80-S7.

Differentiating martensitic and bainitic microstructure is difficult from an analysis of EBSD maps from ML80-S7. The band contrast map (Figure 4.27) indicating strained ferrite suggests that the vast majority of the EBSD map is composed of martensite, as do microhardness measurements performed on the region. KAM map locations showing small amounts of average misorientation are also found to have substructure within them (Figure 4.31), indicating that a fine-grained structure is present. Fine grained structures are also consistent with a martensitic microstructure.

The use of EBSD allows the analysis of preferential grain orientation in ML80 subsized end quench specimen ML80-S7. The pole figure (PF) of the radial direction of specimen ML80-S7 is shown in Figure 4.33a. PFs show all possible grain orientations, with a count showing the number of times each orientation was measured. A maximum count of 5 is observed which is a relatively low count. The low maximum count shows that grain orientations are arranged stochastically, without preferred grain orientation.

The PF from the axial direction of specimen ML80-S7 is shown in Figure 4.33b. The maximum count of 7 along the depth axis shows that there is no preferred grain orientation through the EBSD experiment. Taken together, Figure 4.33 shows that the end quench specimen ML80-S7 does not exhibit preferred grain orientation in the region of the quenched end.

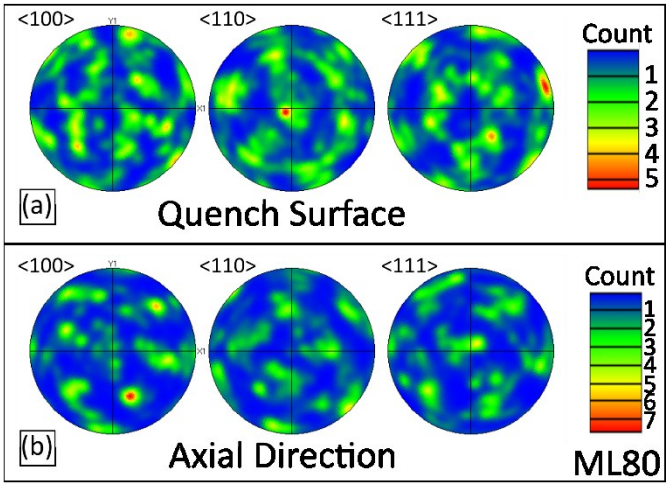

Figure 4.33 – Pole figures from (a) the quench surface and (b) in the axial direction at the quench surface of end quench specimen ML80-S7.

4.2.4.2 Grade 483 Q&T Full Sized Specimen TCPL-S1

In Figure 4.34 a band contrast map is presented from EBSD measurements in the radial direction of specimen TCPL-S1. The band contrast map shows a light grey colour across most of the map, indicating a mismatch between the measured EBSD patterns and the reference library used to identify phases. The uniformity of the grey colour across the map suggests that the same microstructure is present throughout. Individual grains throughout the band contrast map are thin and elongated in shape. The light grey colour, which can result from lattice strain, and the lath shape of grains are consistent with a martensitic microstructure. Small black features can be seen along grain boundaries in Figure 4.34 which were not categorized by EBSD measurements. These features may be precipitates, as the Grade 483 Q&T steel contains solutes known to produce precipitates during the TMCP process, including Mo, V and Ti [114]. The identification of these particles was not undertaken in this work due to the small fraction of the microstructure to which they contribute. Two large diagonal lines were identified on the band contrast map, running from the bottom-left to the top-right of the image. The lines were not visible by optical microscope before or after EBSD measurement and their origin could not be determined.

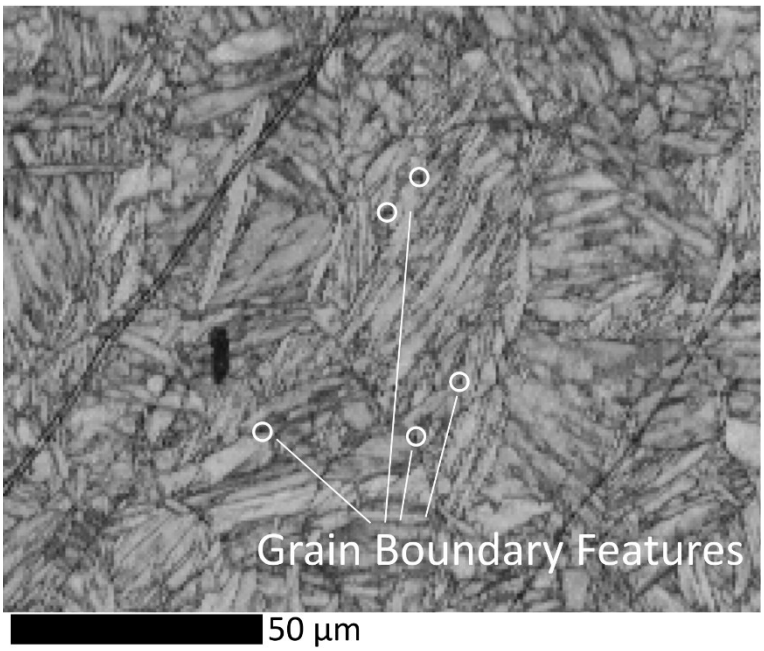

Figure 4.34 – A band contrast map from the quench surface of Grade 483 Q&T specimen TCPL-S1. Some black particles, possibly precipitates, are circled in white.

EBSD measurements at the quench surface of specimen TCPL-S1 were used to produce a phase map with colour coding for each of the phases detected. Reference library entries for ferrite, cementite and austenite were used, with martensite identified as strained ferrite [109]. Figure 4.35 shows a phase map taken from specimen TCPL-S1. The map indicates ferrite (blue), austenite (yellow), cementite (green) and regions which could not be classified by the software (black). Figure 4.35 indicates that less than 0.5 % of the map is composed of retained austenite, found either at individual measurement points, or in small clusters of measurements. As with the ML80 steel, the low silicon content (0.3 wt. %) is not expected to produce large fractions of retained austenite [17]. A comparison of the band contrast map (Figure 4.34) and the phase map (Figure 4.35) shows that most of the microstructure is strained ferrite, with the shades of grey in the band contrast map suggesting that the same amount of strain is observed throughout the map.

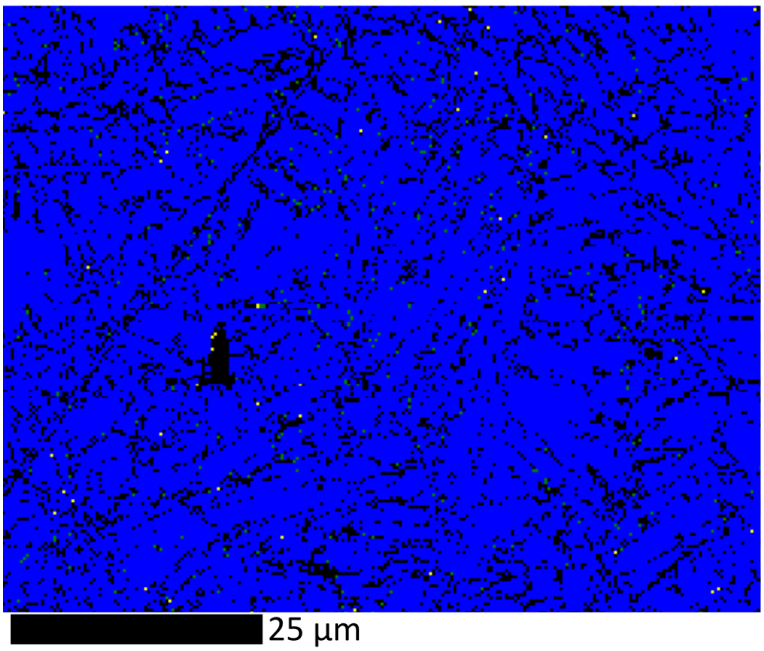

Figure 4.35 – Phase map, showing ferrite and martensite (blue), retained austenite (yellow) and cementite (green) from the EBSD measurements on the quenched surface of TCPL-S1.

To help identify the microstructure observed in EBSD measurements, microhardness indentations were made within the EBSD measurement location for specimen TCPL-S1. Average microhardness values of 394 HV were obtained, with a spread in values of 25 HV. A CCT curve for a steel with a composition similar to the Grade 483 Q&T steel is shown earlier in this work (Figure 3.5, Section 3.1.2). On the CCT curve, hardness values for a martensitic microstructure are approximately 410 HV, which are close to microhardness values obtained on the EBSD examination surface of specimen TCPL-S1. Microhardness indentation locations and values are shown in Figure 4.36, overlaid onto an IPF map, with the legend for the colour coding shown on the right side of the image. Indentation were made at locations where the microstructure was most uncertain, including larger grains with uniform crystallographic orientation identified using the IPF map. The similarity in hardness values from the CCT curve (Figure 3.5) and those shown in Figure 4.36 is consistent with martensite being present in the microstructure.

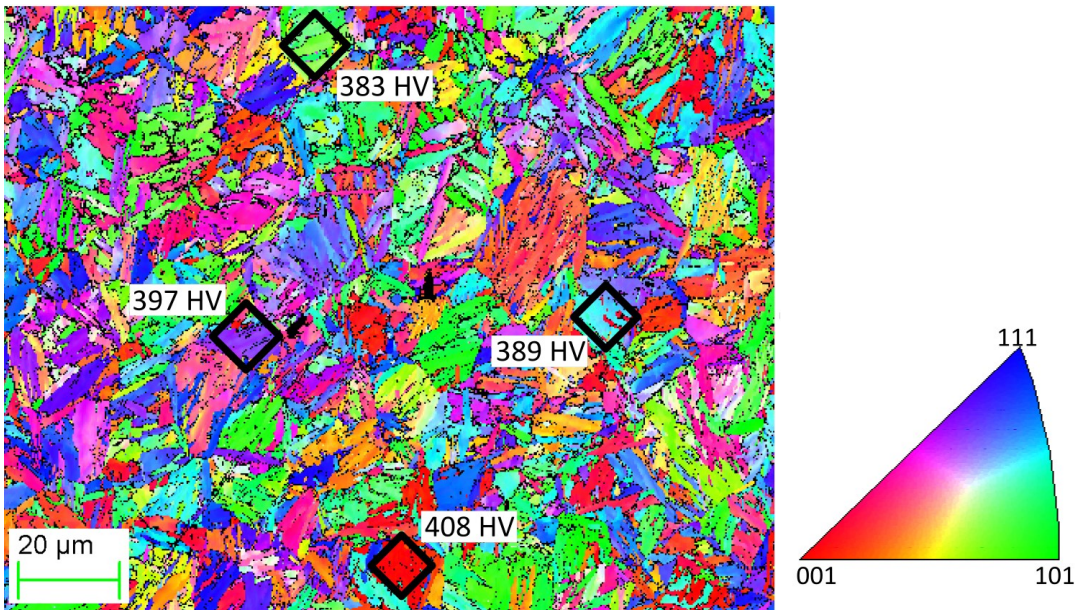

Figure 4.36 – IPF orientation map showing hardness indentation locations in the axial direction for specimen TCPL-S1.

A recrystallization map shows deformation of the crystal lattice in red, recrystallized grains in blue and regions with substructure in yellow. Deformation is determined by mismatch between diffraction pattern measurements and entries from the reference library. In band contrast maps, recrystallized gains appear grey, indicating that they do contain some strain resulting in mismatch between measurement and library entries. Substructure regions are identified as having substructure not visible in IPF maps.

Figure 4.37 shows microhardness indentation locations overlain on a recrystallization map from specimen TCPL-S1. Microhardness measurements were made on substructured regions and deformed regions. Recrystallized regions could not be individually examined due to their small size. The highest microhardness measurements were made where a deformed structure was observed. Measurements on regions with substructure have lower microhardness values.

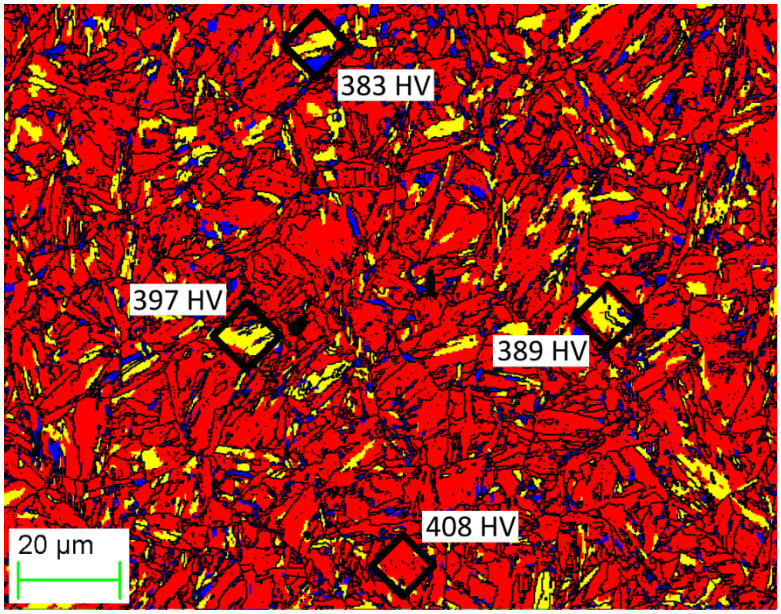

Figure 4.37 – Recrystallization map with hardness indentation locations in the axial direction for specimen TCPL-S1. Regions are indicated as deformed (red), substructured (yellow) and recrystallized (blue).

Microhardness values on specimen TCPL-S1 span a range of 25 HV. From the microhardness measurements, the deformed region (red) produced the highest hardness value. The presence of substructure (yellow) had reduced microhardness values and the lowest values were measured where both substructure and recrystallization (blue) were present. The differences in microhardness values indicate that the substructured regions from specimen TCPL-S1 may be of a different microstructure than the deformed regions.

The phase map (Figure 4.35) indicates that the deformed, substructure and recrystallized regions were all identified as ferrite. The ferrite identification by EBSD measurement applies to martensite, bainite and ferrite. From the phase map it cannot be concluded what type of microstructure is present at each of the indentation locations. A comparison of the microhardness results with the CCT curve for a similar steel (Figure 3.5) suggests that a mix of bainite and martensite could be present at the quenched end of the specimen. The difference between microhardness and macrohardness results reported in the literature [30] makes it hard to confirm microstructure constituents.

Determining the difference between martensite and bainite is difficult using measurements by EBSD. The uniform colour, indicating a uniform strain observed from the band contrast map (Figure 4.34) suggests that the same microstructure may be present throughout the EBSD map. The phase map (Figure 4.35) does not provide the ability to differentiate martensite and bainite. Microhardness measurements on the substructured regions (Figure 4.37) of the EBSD map suggest that a different microstructure may be present at these locations. Microhardness values

themselves do not clearly indicate which microstructure is present at each measurement location. Microhardness measurements were performed on disc samples from specimen TCPL-S3 in Section 4.2.3.2, which are used to help inform microstructure classification decisions by optical microscopy.

Pole figures from EBSD analysis were gathered from the quench surface and in the axial direction of specimen TCPL-S1. The PFs in Figure 4.38a correspond to the radial direction of the specimen. A maximum domain count of 7 is observed. The PF taken in the axial direction of specimen TCPL-S1 is shown in Figure 4.38b. The PF has a maximum count of 5. The low count values show that grain orientations are distributed across the PF without preferential orientations. The pole figures shown in Figure 4.38 indicate that no preferred grain orientation was found at the quenched end of specimen TCPL-S1.

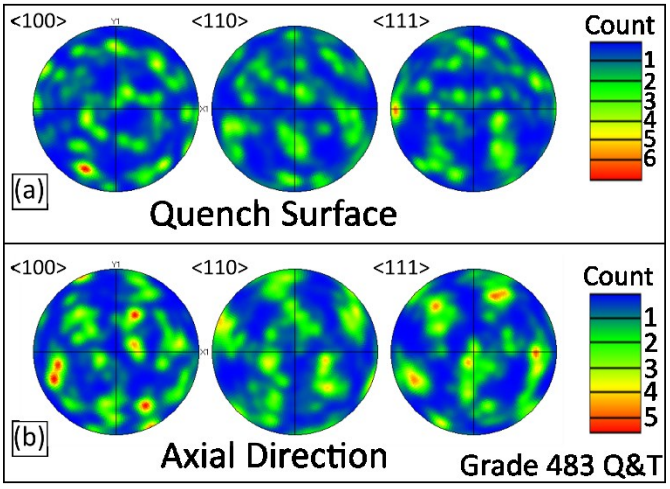

Figure 4.38 – Pole figures from the (a) radial direction and (b) the axial direction of end quench specimen TCPL-S1.

4.2.5 Microstructure Fractions

Microstructure fractions were measured on disc samples from both ML80 and Grade 483 Q&T steels. Specimen ML80-S5 and specimen TCPL-S3 were examined by a point count method to determine microstructure fractions. These fractions have been converted to percentages for presentation in figures. Microstructure fractions and results from microhardness measurements are presented for both steel types, with a discussion of ML80 end quench specimens first, followed by a discussion of Grade 483 Q&T specimens.

4.2.5.1 ML80 Steel Disc Samples

Microstructure fraction measurements (Section 3.4.3) were performed on ML80 subsized end quench specimen ML80-S5, as shown in Figure 4.39. The microstructure fraction in Figure 4.39 has been converted to percentage for ease of communication. The microstructure fraction of

martensite in specimen ML80-S5 shows a rapid drop after a depth of 1.6 mm. Figure 4.39 also shows hardness from along the centerline of subsized specimen ML80-S7, where a drop in hardness is observed at 2.5 mm. HRC measurements on ML80 specimens (Section 4.1.2) showed that there were some variations between end quench specimens. The different depths at which changes are observed in specimens ML80-S5 and ML80-S7 can result from increased martensite fractions in specimen ML80-S7 between depths of 1.6 mm and 2.5 mm.

Microstructure fractions on specimen ML80-S5 can be compared to the expected microstructures based on Jominy specimen cooling rates and the CCT curve provided earlier in this work (Section 3.1.1). A martensitic quenched end, as predicted by cooling rates above 150 °C/s are confirmed by microstructure fraction measurements. The appearance of bainite near 2 mm from the quenched end is expected for cooling rates below 100 °C/s. Bainite fraction continues to increase until a depth of 7.5 mm. Though CCT curves do not provide precise microstructure fraction estimates, the increasing size of the bainite region on the CCT curve suggests that the bainite fraction will increase with decreasing cooling rate, which was observed in microstructure fraction measurements. Ferrite is predicted by the CCT curve at cooling rates between 50 and 100 °C/s. These cooling rates are expected somewhere between 1.6 mm and 3.2 mm from the specimen quenched end [37], as was found during microstructure fraction measurement. Martensite fraction is predicted to drop substantially by cooling rates of 10 °C/s, which is approximately where measurements ended on specimen ML80-S5 (Table 2.1). In the bainite and ferrite regions, carbides have been identified within the microstructure (Section 4.2.2). Carbides result from solute rejection during cooling from austenite to ferrite [5, p. 333], and generally occur along grain boundaries [12].

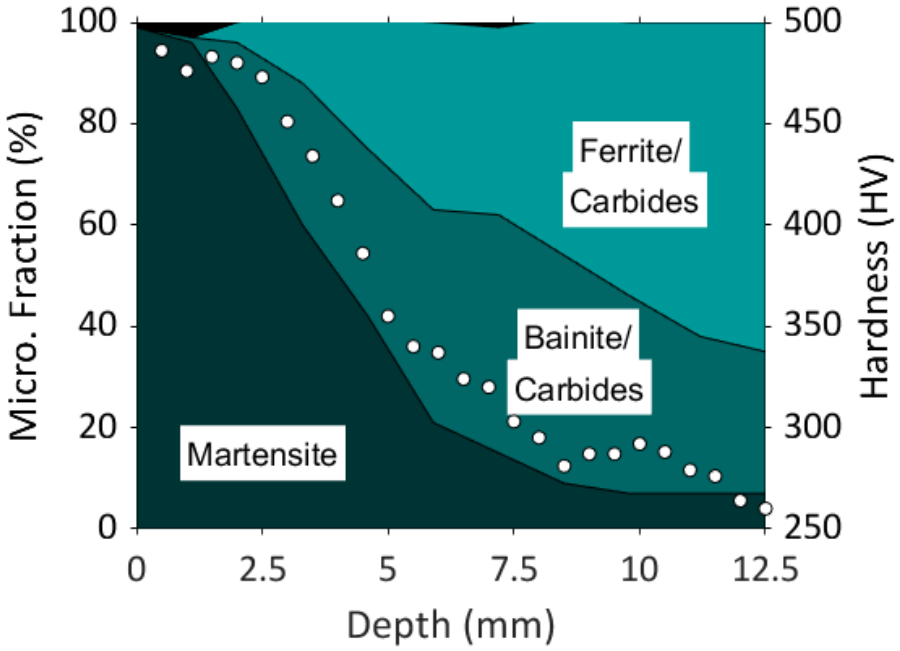

Figure 4.39 – Microstructure (ML80-S5) and hardness (ML80-S7) showing a decrease in martensite fraction at the same depths as a decrease in hardness.

4.2.5.2 Grade 483 Q&T Steel Disc Samples

Microstructure fraction was measured for Grade 483 Q&T full sized end quench specimen TCPL-S3, which is shown in Figure 4.40. For specimen TCPL-S3 a rapid drop in martensite fraction is observed after a depth of 2 mm. This coincides with the decrease in hardness observed for HV measurements taken on the same specimen, also shown in Figure 4.40. At depths more than 10 mm the ferrite fraction increases and the rate of decrease of hardness values also slows.

Microstructures measured by point-counting are similar to estimates made using end quench cooling rates (Table 2.1) and the CCT curve (Figure 3.5). As predicted from the CCT curve (Section 3.1.2), a martensitic quenched end was found for specimen TCPL-S3. Bainite was found in the microstructure at 1.1 mm from the quenched end. While the CCT curve doesn't show bainite forming until cooling rates below those expected at 1.1 mm, the lower Mn content of the Grade 483 Q&T steel would facilitate bainite formation [123].

Ferrite was expected to form at cooing rates below 50 °C/s, which should occur near 3.2 mm from the quenched end of the specimen. Ferrite was observed at 1.9 mm from the quenched end, although cooling rates at this depth are expected to be higher than 50 °C/s. Pearlite was not observed in the microstructure, even at depths as high as 20 mm. Molybdenum content is higher in the Grade 483 Q&T steel than in the CCT curve steel, which may have suppressed pearlite formation [123], but nominal concentration is low in both steels. A lower cooling rate

during quenched for specimen TCPL-S3 compared to the literature could be responsible for the absence of pearlite in the measurements. As was observed in the ML80 steel (Section 4.2.5.1), carbides were identified along the grain boundaries within both the ferrite and bainite regions.

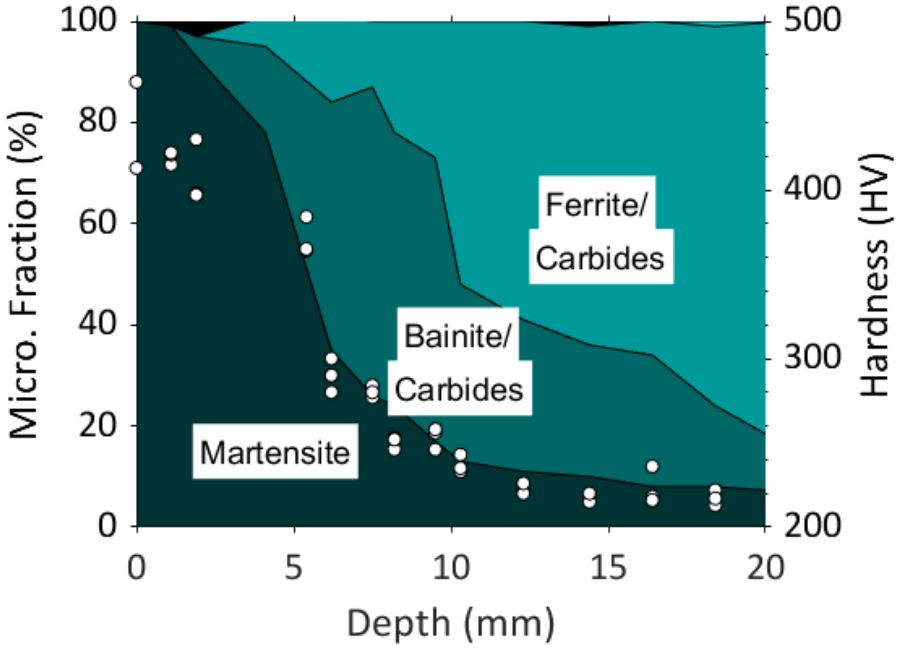

Figure 4.40 – Microstructure and hardness from specimen TCPL-S3, showing a drop in martensite fraction at the same depth as a drop in hardness.

4.3 As-Received Ultrasonic Measurements

This section presents measurements of ultrasonic velocity and attenuation made on as-received specimens from ML80 and Grade 483 Q&T steel types. Longitudinal velocity and attenuation values are measured for ML80-S9. Longitudinal and shear velocity and attenuation are measured on specimen TCPL-S9.

4.3.1 ML80-S9 Ultrasonic Measurements

Ultrasonic signals were collected for Pieces A and E of as-received specimen ML80-S9 (Section 3.5.2). Ultrasonic longitudinal velocity and attenuation were calculated and are shown in Table 4.5. Agreement in values between both Pieces is seen for velocity and attenuation values.

Longitudinal velocity values are higher than the values observed for ML80 specimen ML80-S2 (Section 4.4.1), but within the bounds expected from the literature [61]. As was observed in Section 4.1.1, the hardness of the as-received specimen was approximately 210 HV, falling on the lower end of the 200-500 HV range measured for specimens ML80-S7 and ML80-S8. Literature

results suggest that higher velocities are expected to be observed for lower hardness steels, coinciding with the ultrasonic velocities measured in the as-received specimens.

The microstructure of as-received specimen ML80-S9 showed a series of small dark regions along the grain boundaries. These dark regions may be precipitates resulting from the TMCP process, as discussed previously (Section 4.2.1). The presence of these precipitates may have an additional effect on the effective velocity measured through the as-received ML80 specimen. Although small particles would not play a role in scattering ultrasonic waves, they could cause a change in the medium, affecting the effective velocity [15]. The role that precipitates may have on altering the effective ultrasonic velocity has not been examined in this work.

Attenuation values measured through the as-received specimen were strongly affected by measurement error. The attenuation values fall within the range of values measured on specimen ML80-S2. The microstructure observed for the as-received ML80 specimen may have played a role in the attenuation. The large thickness of ML80-S9 ultrasonic testing samples may also have affected attenuation values, with thicker samples showing lower attenuation values, as discussed later in this chapter (Section 4.7.2).

Table 4.5 – Results from ultrasonic testing performed on as-received specimen ML80-S9.

	Long. Velocity (m/s)	Attenuation (dB/mm)
Piece A	5963±20	0.24±0.12
Piece E	5953±23	0.24±0.11

4.3.2 TCPL-S9 Ultrasonic Measurements

Ultrasonic measurements were made on Pieces A and E of as-received specimen TCPL-S9 (Section 3.5.3). Ultrasonic signals were measured using two ultrasonic probes (Section 3.5.1). Velocity and amplitude attenuation values were calculated for ultrasonic signals from both probes and are shown in Table 4.6. Ultrasonic longitudinal values are consistent across all values in Table 4.6 and are higher than any of the velocity values measured in the radial direction of specimen TCPL-S8 (Section 4.5). Hardness values of 210 HV measured for as-received specimen TCPL-S9 are lower than most hardness measurements made for the Grade 483 Q&T steel specimens. The higher ultrasonic velocity measured for as-received specimen TCPL-S9 is predicted by literature results showing an inverse relationship between hardness and ultrasonic velocity [1].

Ultrasonic velocity measurements from as-received specimen TCPL-S9 are higher than values measured for specimen TCPL-S8. Section 4.3.1 discusses some reasons why the range of velocity values observed in specimen TCPL-S8 may be limited, but differences in velocity resulting from the microstructure may also play an important role. Microstructure analysis and microstructure measurements show that the as-received specimens resembled what was seen at distances of

15-20 mm from the quenched end. At these distances, lower hardness values and primarily ferritic microstructures are observed, which are correlated with higher ultrasonic velocities in the literature.

Amplitude attenuation values are obtained from measurement of echo amplitude for four backwall echoes from each of the 5 signals collected, and are shown in Table 4.6. Attenuation values show a wide scatter between test pieces and ultrasonic probes. The spread in attenuation values may be a result of the noise present in the ultrasonic signals. Accurate measurement of ultrasonic attenuation remains one of the key challenges faced in this work and has been cited in the literature as being difficult to measure accurately [55] [85].

Table 4.6 – Longitudinal ultrasonic measurements made on two pieces of as-received specimen TCPL-S9. Measurements were made with two longitudinal wave probes.

	Long. Velocity (m/s)	Attenuation (dB/mm)
Piece A (V202-RM)	5928±2	0.11±0.06
Piece E (V202-RM)	5929.1±0.5	0.24±0.11
Piece A (V203-RM)	5929±1	0.30±0.03
Piece E (V203-RM)	5930±1	0.27±0.04

Shear wave measurements show agreement across both Pieces A and E in terms of velocity and attenuation values and are shown in Table 4.7. Shear wave velocities are comparable to tempered martensite velocities measured in the literature [2] [65]. Like longitudinal velocity values, shear velocity measurements are on the higher side of velocities expected from the literature. Due to the large size of the shear wave probe used in this work, only a few additional measurements of shear velocity and attenuation are available with which to compare. Amplitude attenuation results are lower for the as-received specimens than on disc samples of specimens TCPL-S1 and TCPL-S3. Thicker specimens can reduce attenuation values as backwall reflection causes a significant amount of wave scattering [45, pp. pp. 29, 165]. This effect is investigated further in this chapter (Section 4.7.2).

Table 4.7 – Shear wave measurements from as-received specimen TCPL-S9.

	Shear Velocity (m/s)	Attenuation (dB/mm)
Piece A	3231±14	0.42±0.09
Piece E	3231±16	0.49±0.11

Literature sources cite transducer contact as a source of error in attenuation values [1] [64]. Standard deviation values that are calculated for attenuation provide an estimate of uncertainty in the individual signal or signals being examined. Additional error resulting from transducer contact quality is a source of error that cannot be estimated. Standard methods for ensuring repeatability in attenuation measurements can be difficult to develop and depend on a variety of variables, including the quantity of coupling fluid used, the temperature of the fluid and workpiece and the duration of transducer contact [4, p. 42]. Attenuation, although considered a better source of information for estimating microstructure in steel than velocity [82] [92], is not always a practical means of measurement. This is especially true for shear measurements, where the viscous wave couplant thickness has a large effect on ultrasonic signal quality.

Using the method described for disc samples from Grade 483 Q&T end quench specimens (Equation 4.1), Poisson's ratio can be calculated from the ultrasonic measurements made on as-received specimen TCPL-S9. Longitudinal peak separation values (Equation 4.2) are obtained by averaging the peak separation values from probes V202-RM and V203-RM. Poisson's ratio values are near to the 0.2877 expected from the literature for ferrite-pearlite microstructures [50].

Table 4.8 – Poisson's ratio calculated for as-received Grade 483 Q&T steel.

	Poisson's ratio
Piece A	0.289±0.003
Piece E	0.289±0.004

4.4 Ultrasonic Measurements on ML80 Steel

This section presents measurements of ultrasonic longitudinal velocity and attenuation for Jominy end quench specimen ML80-S2. Ultrasonic velocity values are compared to measurements of hardness and microstructure obtained from specimens ML80-S7 and ML80-S5. Ultrasonic velocity was the lowest for disc samples with high hardness and a martensitic microstructure. Ultrasonic amplitude and energy attenuation values for specimen ML80-S2 are compared to hardness values, showing increasing attenuation with increasing hardness. Amplitude attenuation measurements are compared to microstructure fractions. Increasing attenuation values are correlated with increases in martensite fraction and decreases in pearlite and ferrite fraction. ML80 end quench specimens were not examined using ultrasonic shear waves because the specimens were too small to examine with the shear wave probe.

4.4.1 Disc Sample Velocity

Measurements of longitudinal velocity for ML80 subsized end quench specimens were performed on disc samples cut from specimen ML80-S2. Results of velocity measurements for

ML80 subsized specimen discs are shown in Figure 4.41. The velocity is lowest near the quenched end, at 5929 m/s, where the highest martensite fraction is expected. The low velocity near the quenched end of the specimen agrees with results from the literature [65] [83], which show martensite having lower ultrasonic velocity than polygonal ferrite, pearlite and bainite microstructures.

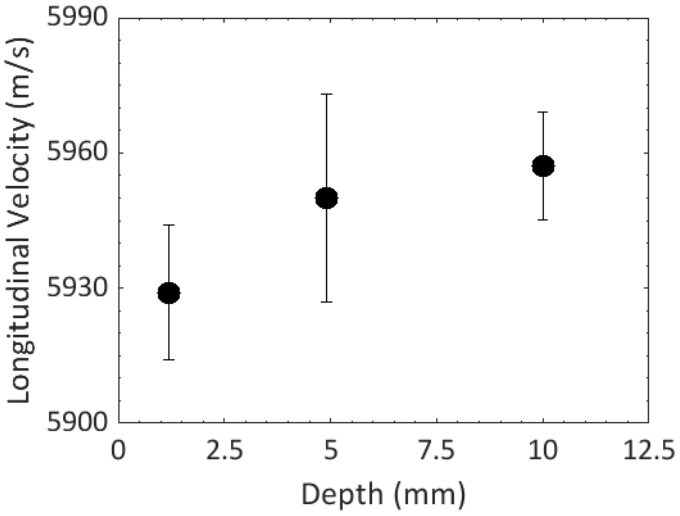

Figure 4.41 – Longitudinal velocity for disc samples of ML80 specimen ML80-S2.

Longitudinal velocity for disc samples of ML80-S2 and hardness values for specimen ML80-S7 are shown in Figure 4.42a. At the depth value of each velocity measurement (ML80-S2) a 3-point average of hardness values from specimen ML80-S7 was taken. The 3-point average hardness value provides a representative hardness for each longitudinal velocity measurement, as shown explicitly in Figure 4.42b. Ultrasonic velocity is lowest at a hardness value of 480 HV, as is expected from the literature, where increasing hardness is correlated with decreasing ultrasonic longitudinal velocity [2]. A large error value is seen at a hardness of 389 HV, resulting from uncertainty in disc sample thickness and the spread in ultrasonic peak separation times. The error on this measurement makes it difficult to determine a relationship between hardness and velocity for ML80 steel.

Results from HRC measurements on ML80 subsized end quench specimens (Section 4.1.2) show differences of around 8 HRC at a depth of 1.6 mm. These hardness values suggest a variation in martensite fraction of around 20%. Due to the variation between specimens, it would be preferable to use hardness values, rather than depth, as a means of comparing between ML80 end quench specimen. However, comparisons between specimens ML80-S2 and ML80-S7 must be made using the depth because hardness values were not collected for specimen ML80-S2.

The use of depth to compare between specimens limits the precision of comparisons between ultrasonic measurements, hardness and microstructure. Using the distance from the quenched to compare measurements made for ML80 specimens does provide qualitative insight into the relationship between ultrasonic measurements and materials properties. The insight is available because the hardness and microstructure changes occurring with increasing distance from the quenched end of Jominy specimens is well documented [33] [36].

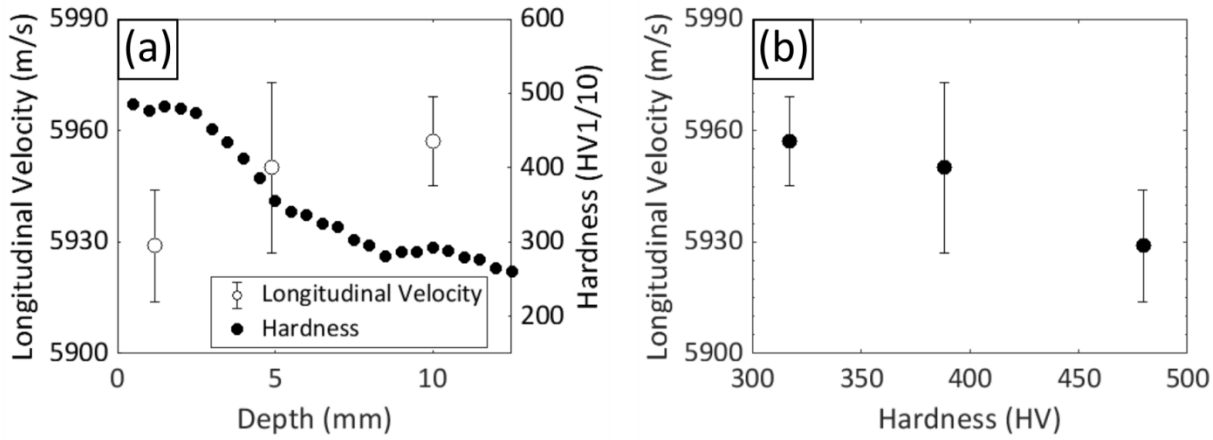

Figure 4.42 – (a) Ultrasonic longitudinal velocity (ML80-S2) and hardness (ML80-S7) as a function of sample depth. (b) Longitudinal velocity as a function of hardness.

Ultrasonic velocity for specimen ML80-S2 is compared to microstructure fraction from specimen ML80-S5 in Figure 4.43. The comparison is made using the depth at each ultrasonic measurement location and the depth at each microstructure fraction measurement location (Section 4.2.5.1). By interpolating between the depths where measurements were made on ML80-S5, a representative microstructure was found for each ultrasonic measurement made on specimen ML80-S2. The comparison of microstructure and ultrasonic velocity could be improved if hardness values were measured for specimen ML80-S2 (which was examined by UT) and for specimen ML80-S5 (which was examined by metallography). Hardness measurements would provide a more robust metric by which comparisons can be made across end quench specimens.

For the martensite, bainite and ferrite microstructure fractions (Section 4.2.5.1), Figure 4.43 shows the microstructure fraction and ultrasonic longitudinal velocity. Velocity is lowest at high volume fractions of martensite and increases as the martensite fraction drops, as expected from the literature [1] [61]. Velocity is lowest when ferrite is not present in the microstructure and is highest at a ferrite fraction of 61%.

The ultrasonic velocity measurement at a depth of 4.9 mm for specimen ML80-S2 has a large standard deviation, making it difficult to observe any trend in ultrasonic velocity measurements. ML80-S2 samples were cut to a larger thickness to reduce error measurements in velocity, but as

discussed later in this chapter (Section 4.7.1), fabrication of samples is one of the most difficult variables to control in ultrasonic velocity measurements.

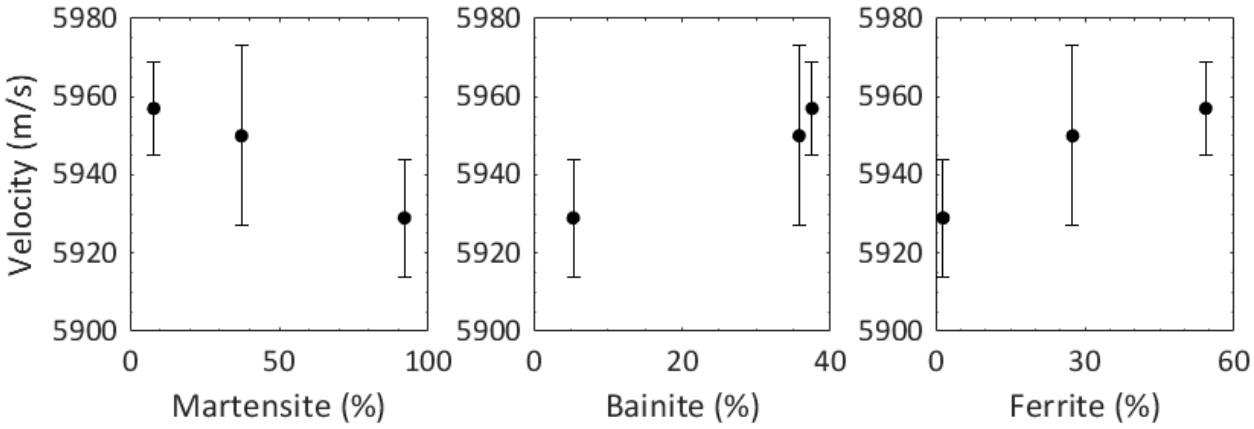

Figure 4.43 – The martensite, bainite and ferrite fractions of each of the ultrasonic velocity measurements performed on specimen ML80-S2.

Bainite and ferrite are both composed of α-ferrite and share similar ultrasonic velocities [3]. Bainite generally has larger dislocation densities and smaller grain sizes than ferrite [12]. As the microstructure along an end quench specimen changes from martensite to bainite, and then from bainite to ferrite, the steel is changing from a metastable martensite phase into two different morphologies of ferrite. Ultrasonic velocity follows suite, with the most drastic changes occurring with the change from martensite, while differences are less pronounced for the change from bainite to ferrite [1].

In measurements on ML80 subsized specimen ML80-S2, the small number of specimens that were examined by ultrasonic testing resulted in a reduced ability to observe ultrasonic changes occurring during the various stages of microstructures transition. Higher martensite fractions showed the lowest ultrasonic velocity but additional measurements between martensite fractions of 37 and 92% would be necessary to establish the role that microstructure plays in affecting the ultrasonic velocity.

Unique ultrasonic velocities could not be obtained for the individual bainite and ferrite microstructure constituents. The mixed bainite and ferrite microstructure illustrates one of the difficulties in making ultrasonic measurements on Jominy end quench specimens. These specimens are continuously cooled at differing rates along the length of the specimen, producing mixed microstructures. Using heat treatment methods to produce microstructures with uniquely bainitic and ferritic microstructures, the difference in ultrasonic velocity between the two could be established. Additional development of heat treatment methods to produce these samples would be necessary to pursue this line of inquiry.

4.4.2 Disc Samples Attenuation

Measurement of ultrasonic amplitude attenuation was conducted on disc samples of subsized end quench specimen ML80-S2. Attenuation values can be seen in Figure 4.44. Attenuation is highest near the quenched end of the specimen, decreasing at greater depths. These amplitude attenuation values are within the range found in the literature [49]. Additionally, since hardness decreases with increasing depth for Jominy end quench specimens, the trend of decreasing attenuation with increasing hardness agrees with literature results relating ultrasonic velocity and hardness [1].

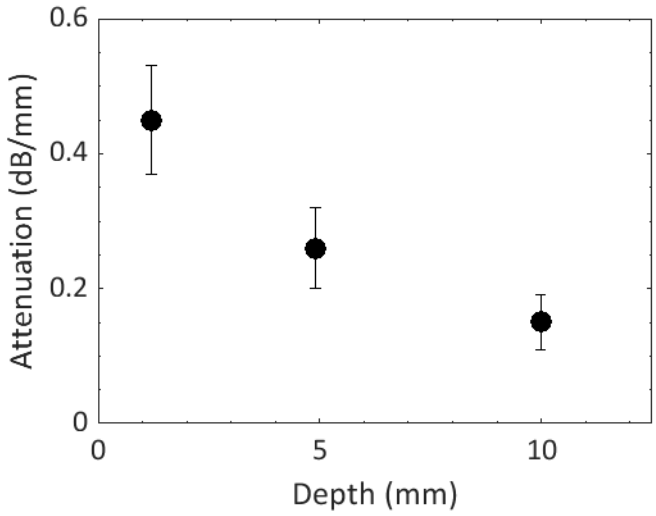

Figure 4.44 – Amplitude attenuation measurements for disc samples of ML80 subsized end quench specimen ML80-S2.

Energy attenuation was measured on specimen ML80-S2 and is shown in Figure 4.45. The highest attenuation is observed near the quenched end of the specimen, where a higher martensite fraction is expected. The presence of large error bars at a depth of 5 mm results from the uncertainty in specimen thickness and from fluctuations in echo energy. Both factors are largest for the disc sample at a depth of 5 mm. It is unclear why fluctuations in echo energy are greater for this disc sample.

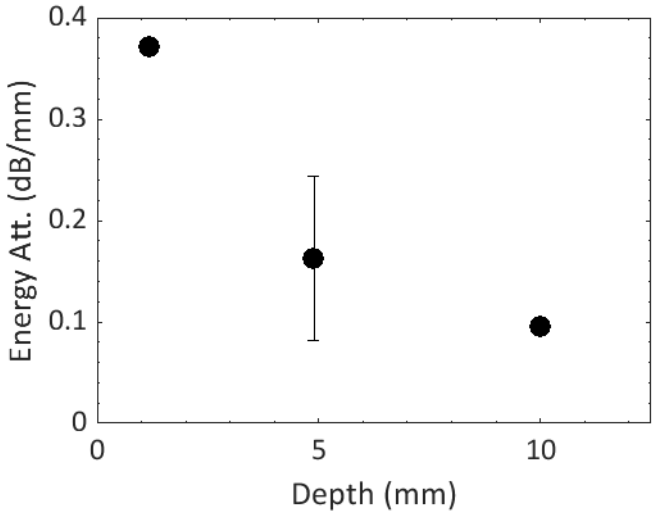

Figure 4.45 – Energy attenuation measurements for disc samples of ML80 subsized end quench specimen ML80-S2.

The average energy attenuation value for disc samples of ML80-S2 was 0.21 dB/mm, while the average amplitude attenuation was 0.28 dB/mm. Attenuation values measured by signal energy were lower than values measured by peak amplitude, while literature results show higher attenuation using energy calculations [110]. Note however that literature values of energy attenuation are calculated using only a portion of the ultrasonic echo (specifically the energy at the full-width at half-maximum, or FWHM), which may alter the magnitude of energy attenuation values [110].

A comparison of the magnitudes of amplitude and energy attenuation values from this work with values from the literature is of little significance. The relative magnitude of the two attenuation values is prone to changes in amplitude attenuation brought about by wave scattering within the material, signal noise, and by frequency-dependence, also known as wave dispersion [97] [124] [125] [126]. Standardized methods of sample preparation, sample geometry and ultrasonic wave parameters would be needed for accurate comparisons of attenuation values between experiments.

Wave dispersion is the property of waves in a material to exhibit different travel speeds for different frequency components. The variations in travel speed generally cause the wave to dissipate over time and decrease the peak amplitude of the wave [45, p. 31]. The degree to which wave dissipation occurs will change the amplitude attenuation of an ultrasonic signal and may depend on a variety of factors, including material properties and the frequency components present in an ultrasonic pulse. These factors make it difficult to make a direct comparison of the magnitude of ultrasonic amplitude attenuation and energy attenuation values.

Hardness values for disc samples of subsized sample ML80-S2 are shown with ultrasonic amplitude attenuation in Figure 4.46a, and with ultrasonic energy attenuation in Figure 4.46b. An increase in both amplitude and energy attenuation is observed with increasing hardness. Appendix A.6 compares the effectiveness of using amplitude attenuation and energy attenuation methods in more detail.

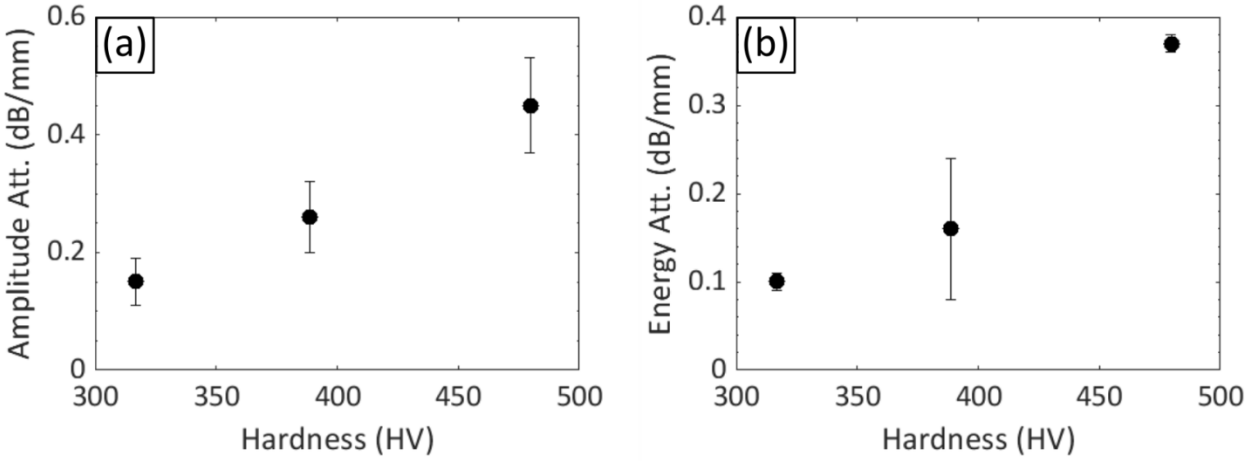

Figure 4.46 – Ultrasonic (a) amplitude attenuation and (b) energy attenuation plotted against the hardness values of disc samples for specimen ML80-S2.

In Figure 4.47, the microstructure fraction of ML80-S2 disc samples are each individually plotted against the ultrasonic amplitude attenuation, using the same method outlined for velocity measurements for ML80-S2 (Section 4.4.1). Martensite fraction shows a nearly linear relationship with attenuation. The linear relationship is the result of the attenuation through martensite being higher than it is through the other microstructures, as confirmed by the literature [2].

As the martensite fraction is reduced, an increase is observed in the fraction of other microstructures. It is therefore the transition from a martensitic microstructure to a ferritic microstructure that causes the changes in ultrasonic amplitude attenuation, resulting in the trend shown between ferrite fraction and amplitude attenuation values.

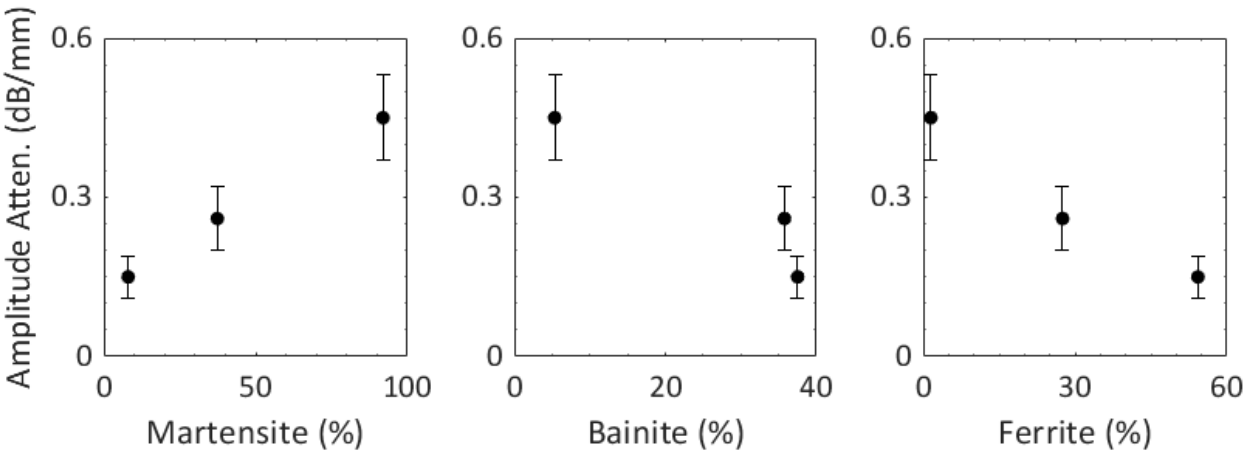

Figure 4.47 – The martensite, bainite and ferrite fractions of each of the ultrasonic amplitude attenuation measurements performed on specimen ML80-S2.

The trend observed for attenuation of ML80-S2 disc samples opposes results from some of the literature [4] [15] [49], where increasing hardness was correlated with decreasing attenuation. It should be noted that in those literature sources, comparisons were made across samples with similar microstructures and different grain sizes, rather than across vastly different microstructures, as is done in this work. In Jominy end quench specimens, the microstructure varied with depth. These microstructure changes may be responsible for the relationship between hardness and ultrasonic attenuation. These problems are complicated by the difficulty in making accurate measurements of ultrasonic attenuation, as outlined later in this chapter (Section 4.7.2).

As with measurements of ultrasonic velocity on specimen ML80-S2, additional measurements would be needed to gain accurate insight into how microstructure changes affect attenuation values [69]. This would require ultrasonic testing of end quench samples with a wider variation in microstructures. Due to the increased thickness of disc samples examined for specimen ML80-S2, measurement at martensite fractions between 37 and 92 % would require the use of additional end quench specimens. Additionally, a more rigorous method for comparing specimens would be needed, such as the use of hardness to compare microstructure to the ultrasonic measurement location.

Energy attenuation values are compared to microstructural microstructure fractions on disc samples of ML80-S2 in Figure 4.48. Microstructure fraction results are obtained by comparing the depth of disc samples used for metallography and those used for ultrasonic testing. As with amplitude attenuations, higher energy attenuation is observed for high martensite fractions. Microstructure fraction is shown after conversion to percentage for ease of understanding.

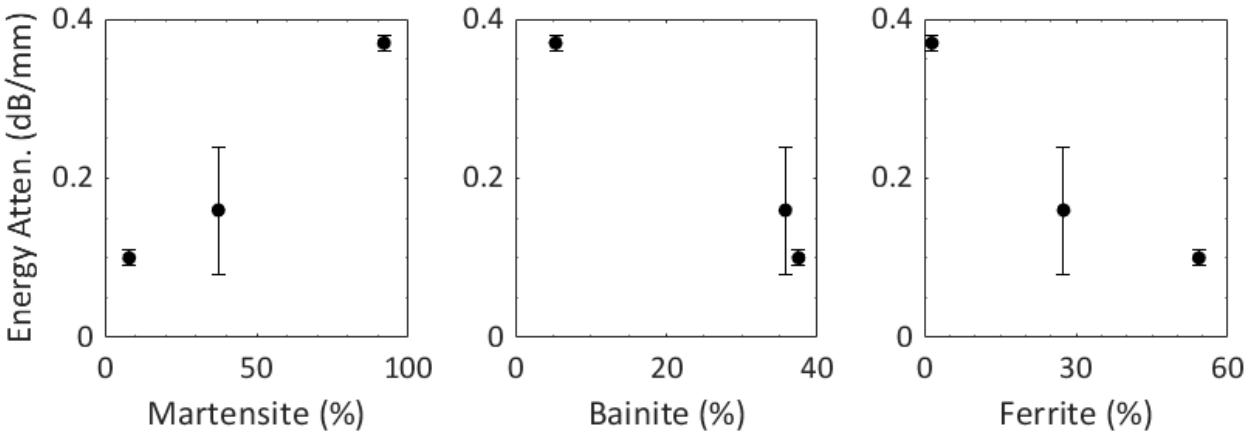

Figure 4.48 – Microstructure related to energy attenuation values measured for subsized specimen ML80-S2.

The small diameter of ML80 subsized end quench specimens means that hardness measurements can only be made on the specimens after disc samples are sectioned and ultrasonic measurements are made (Section 3.2.1). This process makes precise selection of microstructure or hardness for ultrasonic testing impossible. The variation between specimens and the uncertainty associated with using depth measurements to compare microstructure across specimens should be considered in future work and has been discussed previously (Section 4.4.1).

Literature sources state that ultrasonic attenuation values show greater changes across microstructures than do ultrasonic velocity values [92], making attenuation a better candidate for monitoring microstructure in steel. Measurements of attenuation in this work highlight the deviation in amplitude and energy attenuation values based on sample thickness and signal noise affecting pulse amplitude and energy content. When comparing standard deviation values between the energy attenuation and amplitude attenuation methods, energy attenuation values seem to provide more consistent accuracy. Future work could help to established preferred methods for attenuation measurement.

4.5 Ultrasonic Measurements for Grade 483 Q&T – Radial Direction

This section presents longitudinal ultrasonic measurements of velocity, amplitude attenuation and energy attenuation for Grade 483 Q&T steel specimen, TCPL-S8. Ultrasonic measurements on this specimen are made in the radial direction of the specimen. Ultrasonic velocity is compared to hardness values measured on the same specimen, and to microstructure fraction values for specimen TCPL-S3. Measurements of amplitude and energy attenuation are compared to hardness measurements for specimen TCPL-S8, and amplitude attenuation values are compared to microstructure fraction values for specimen TCPL-S3.

4.5.1 Radial Direction Velocity

Ultrasonic longitudinal velocity was measured across the radial direction of Grade 483 Q&T specimen TCPL-S8 at varying depths (Section 3.5.3). The results are shown in Figure 4.49. Although they are difficult to distinguish, measurements with both longitudinal wave probes were performed at a depth of 4 mm. Near the quenched end of the specimen the lowest ultrasonic velocity of 5906.7 m/s was measured. This velocity is approximately 10 m/s and 20 m/s higher than the velocity measured in martensitic samples by Gur and Tuncer [2] and Freitas et al. [1], respectively. The difference observed between measured ultrasonic velocities and literature results may be explained by considering the ultrasonic probes used to make measurements.

Ultrasonic probe dimensions did not allow ultrasonic measurement directly at the quenched end of the specimen. The measurement nearest the quenched end, at a depth of 2 mm, could only be made with the small V203-RM longitudinal wave probe. At a measurement depth of 2 mm the ultrasonic probe spanned a region between depths of 0.4 and 3.6 mm, which may have consisted of a mixed microstructure. A mixed microstructure at this depth would produce ultrasonic velocities higher than those found for martensitic samples alone. The presence of a mixed microstructure may be responsible for the difference observed between the lowest ultrasonic value measured on specimen TCPL-S8 and those found in the literature [1] [2].

The total range of ultrasonic velocities for specimen TCPL-S8 is 13 m/s, which is less than the 35 m/s difference measured by Gur and Tuncer [2] and the 45 m/s difference measured by Freitas et al [1]. Measurements of ultrasonic velocity for specimen TCPL-S8 at higher depths suffered from the same drawback as was observed near the quenched end. Measurements of velocity at a depth of 20 mm were made through a combination of bainite, pearlite and ferrite microstructures. The literature reports bainite velocity to be 10 m/s lower than pearlite and ferrite, so the effective velocity of a mixed microstructure would be lower than for a uniformly pearlitic or ferritic microstructure, contributing to the reduced velocity range measured on specimen TCPL-S8.

Longitudinal wave probe V202-RM showed consistently higher velocity than probe V203-RM. The reason for differences in velocity between probes is not known. One plausible explanation depends on the different frequency profiles of each transducer. Different frequency ultrasonic waves are reported to have slight differences in velocity [1] [124] [126] [125]. Between the two transducers, a slight difference in frequency profiles may result in different travel speeds of ultrasonic peaks.

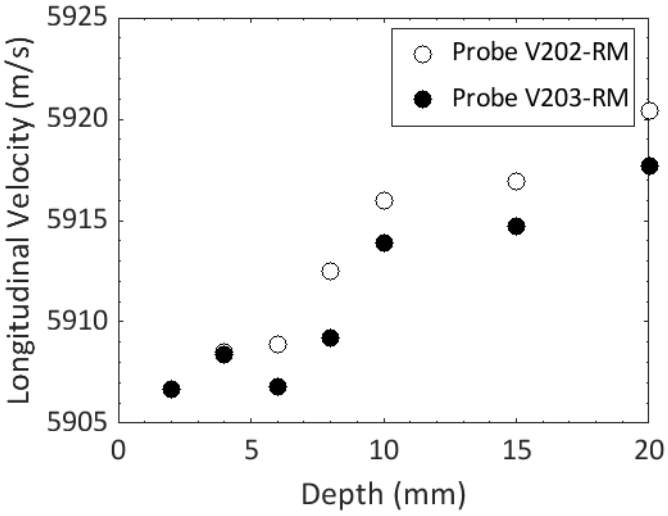

Figure 4.49 – Longitudinal velocity in the radial direction for Grade 483 Q&T specimen TCPL-S8 using two ultrasonic probes.

Vicker's hardness was measured for specimen TCPL-S8 near the outer diameter (Section 4.1.3). Figure 4.50 shows ultrasonic longitudinal velocity for specimen TCPL-S8 plotted against hardness. Hardness in Figure 4.50 is given as the average hardness spanned by the longitudinal wave probe used for each measurement. Ultrasonic velocity decreased as hardness increased, in agreement with results from the literature [2]. The reasons for the differences between the velocity of probes V203-RM and V202-RM are not understood (Section 3.5.1). For probe V203-RM an increase in velocity is observed near a hardness value of 350 HV, which drops again above 400 HV. These values suggest that it may be difficult to determine an exact relationship between hardness and ultrasonic velocity. It can be noted that probe V202-RM does not show this behavior.

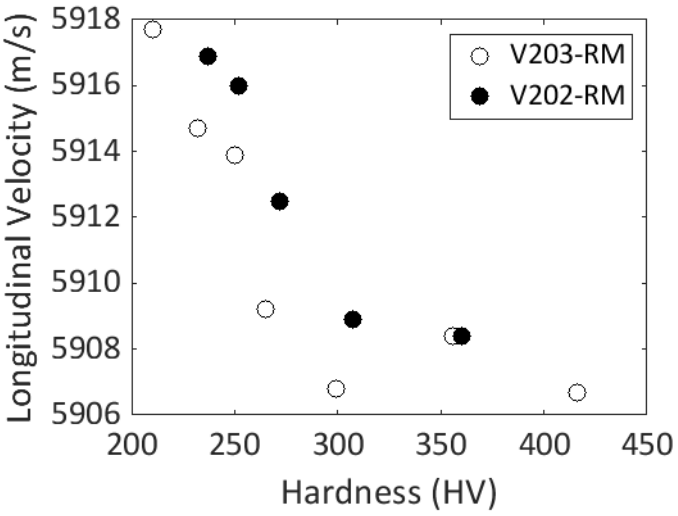

Figure 4.50 – The relationship between ultrasonic longitudinal velocity and hardness for Grade 483 Q&T specimen TCPL-S8.

Using hardness values from the outer edge of Grade 483 Q&T specimen TCPL-S8 (Section 4.1.3) and microstructure fraction measurements for disc samples of specimen TCPL-S3, an equivalent microstructure was estimated for specimen TCPL-S8. To provide this estimate, an average of the hardness values spanned by longitudinal wave probes was taken for each ultrasonic measurement location for specimen TCPL-S8. By linear interpolation, using the hardness measurements for specimens TCPL-S8 and TCPL-S3, and the microstructure fractions from specimen TCPL-S3, representative microstructures were determined for each of the ultrasonic test locations for specimen TCPL-S8, as shown in Figure 4.51.

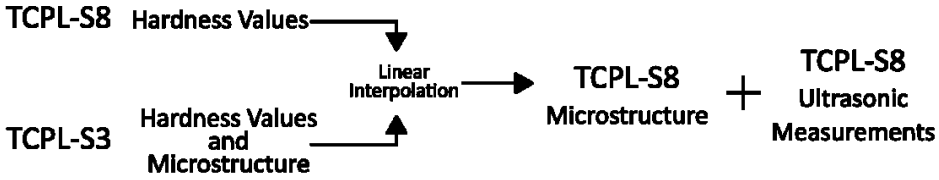

Figure 4.51 – For specimen TCPL-S8, ultrasonic measurements are correlated to microstructure fractions using a comparison with data from specimen TCPL-S3.

The microstructure fractions of martensite, bainite and ferrite are plotted against the longitudinal velocity for TCPL-S8 in Figure 4.52. Pearlite did not contribute large enough fraction of the microstructure to be shown in the plot. A decrease in velocity was observed with an increase in martensite amount from 10 % to 31.9 % (Figure 4.52, left). Ultrasonic velocities for higher martensite fractions were between 5906 and 5909 m/s. Literature sources suggest that dislocation density plays an important role in ultrasonic velocity changes across different microstructures [61] [82]. From this information, ultrasonic velocity is expected to vary with all

martensite fraction measurements. It is unclear why no velocity change is observed beyond 31.9 % martensite. Further investigations on the relationship between ultrasonic velocity and microstructure are necessary.

Increasing ferrite fractions (Figure 4.52, right), which occurred as distance from the quenched end of the specimen increased, produced an increase in ultrasonic velocity. Bainite fraction (Figure 4.52, center) was not closely correlated with ultrasonic velocity, with low ultrasonic velocities occurring at both high and low bainite volume fractions. As distance from the quenched end of the specimen increased, bainite fraction increased initially, and then decreased. Lower bainite fractions are therefore associated with both the lowest and highest ultrasonic velocities observed. Bainite is expected to produce intermediate velocities, when compared with martensite and ferrite, which can be explained by the intermediate dislocation densities present in bainite.

The change in velocity with martensite fraction can be attributed to the change from martensite to a ferritic crystal structure, which encompasses both ferrite and bainite. Reduction in the martensite volume fraction increased the longitudinal wave velocity, which remained high with bainite and ferrite occupying the majority of the microstructure, in agreement with literature results [2] [1]. Ultrasonic velocity measurement seems to provide a method for observing microstructure changes from martensite to ferrite due to the increase in velocity. Estimating microstructure from velocity would however prove difficult, as many of the velocity values are observed for a wide variety of microstructure fraction values. Figure 4.52, on the left, shows that low velocities occur over a wide range of martensite fractions. Differentiating martensite fractions within this wide range would not be possible using ultrasonic velocity measurements alone.

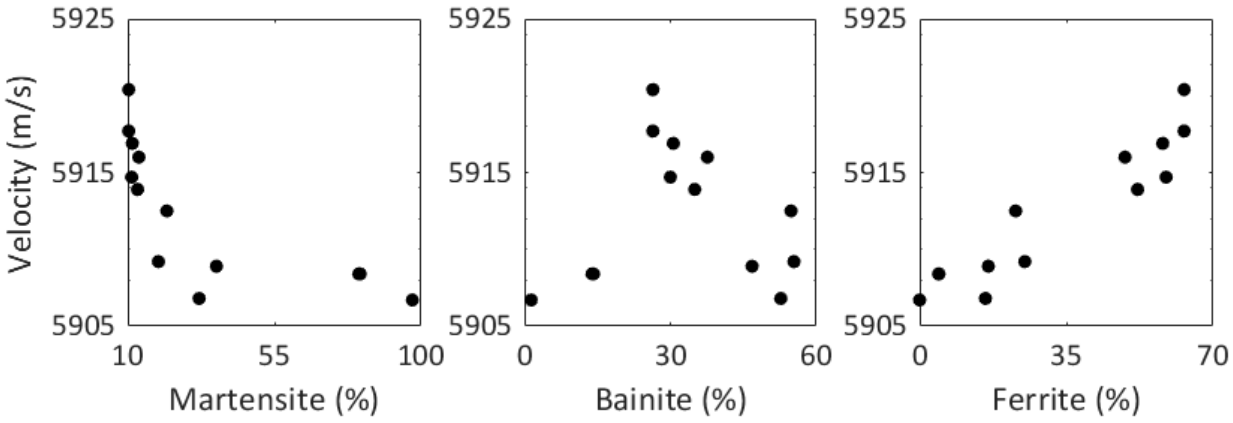

Figure 4.52 – The martensite, bainite and ferrite fractions of each of the ultrasonic velocity measurements performed in the radial direction specimen TCPL-S8.

Retained austenite was detected in very small quantities (i.e., less than 0.5 %) during EBSD measurements on full sized specimen TCPL-S1 (Section 4.2.4.2). As only the effective ultrasonic velocity can be measured, the effect of retained austenite on the effective velocity is estimated at 1.5 m/s based on an ultrasonic velocity in austenite of 5600 m/s [56] [66]. This effect would be undetectable amid the other microstructure changes measured on Grade 483 Q&T specimens. Retained austenite fraction is additionally expected to decrease as distance from the quenched end of the specimen increases [19] further reducing the velocity change it produces at higher depths. For this reason, the effect of retained austenite is ignored for discussions of ultrasonic velocity in this work.

4.5.2 Radial Direction Attenuation

Ultrasonic amplitude attenuation was measured in the radial direction of Grade 483 Q&T full sized end quench specimen TCPL-S8. Attenuation from these measurements are shown in Figure 4.53. Attenuation is highest near the quenched end of the specimen using probe V203-RM, with a value of 0.25 dB/mm. Amplitude attenuation is constant for all other measurements, with an average of 0.13 dB/mm. These amplitude attenuation values are of a similar order to those from the literature [15], specifically those found for thick samples. Sample thickness has a drastic effect on ultrasonic attenuation and is discussed later in this chapter (Section 4.7.2).

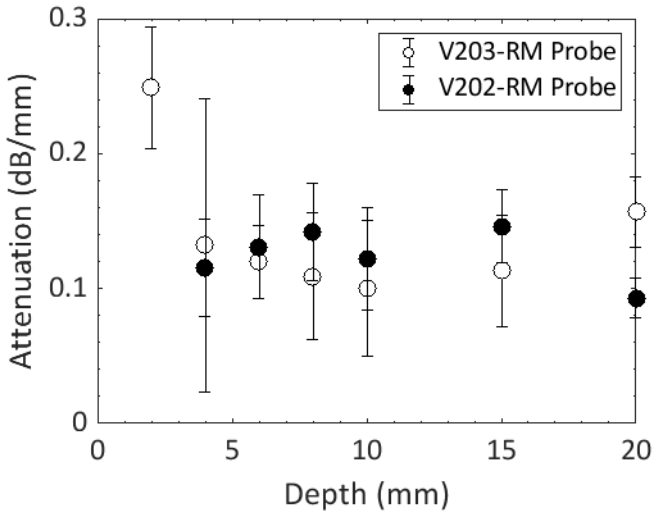

Figure 4.53 – Ultrasonic amplitude attenuation values in the radial direction of Grade 483 Q&T specimen TCPL-S8.

Energy attenuation was measured from ultrasonic signals collected across Grade 483 Q&T specimen TCPL-S8 (Figure 4.54). The size of error bars was not calculated for these measurement due to the small number of backwall echoes available for calculation of energy attenuation (Section 3.5.3). The error in measurements of energy attenuation for specimen TCPL-S8 is therefore underrepresented in Figure 4.54. This illustrates one of the major issues with ultrasonic

attenuation calculations using backwall echo energy. Several echoes are needed to increase accuracy in attenuation values. A comparison of energy attenuation and amplitude attenuation is given in Appendix A.6.

The average energy attenuation for specimen TCPL-S8 (Figure 4.54) was 0.094 dB/mm, lower than most energy attenuation values measured by Li et al. [93] on specimens of a similar thickness. The difference between these measurements and those in the literature may be due to the use of stainless steel in the literature study. Higher energy attenuation is found near the quenched end of the specimen at a value of 0.173 dB/mm, with attenuation decreasing at greater depths. Energy attenuation is consistent between measurements by probes V202-RM and V203-RM. Only two ultrasonic echoes were used for each measurement and location, resulting in the absence of an error estimate for these measurements.

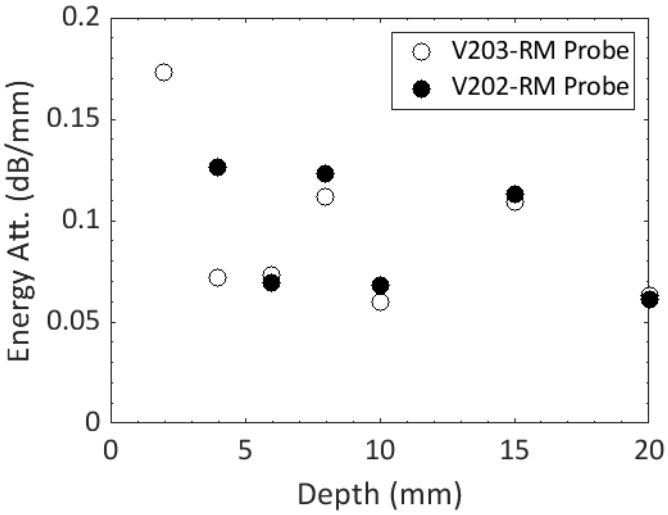

Figure 4.54 – Ultrasonic energy attenuation values in the radial direction of Grade 483 Q&T specimen TCPL-S8.

Ultrasonic amplitude attenuation (Section 3.6.2) is plotted against hardness for Grade 483 Q&T full sized end quench specimen TCPL-S8 in Figure 4.55a. Hardness values are reported as the average hardness value spanned by the ultrasonic probe, using hardness values measured on the same specimen. Both amplitude and energy attenuation produce maximum values at the highest hardness but do not show any trend for hardness values below 400 HV. Energy attention (Figure 4.55b) show large fluctuations for regions with lower hardness. These measurements show a slight increase in energy attenuation with increasing hardness, but the increases are less than the fluctuations observed.

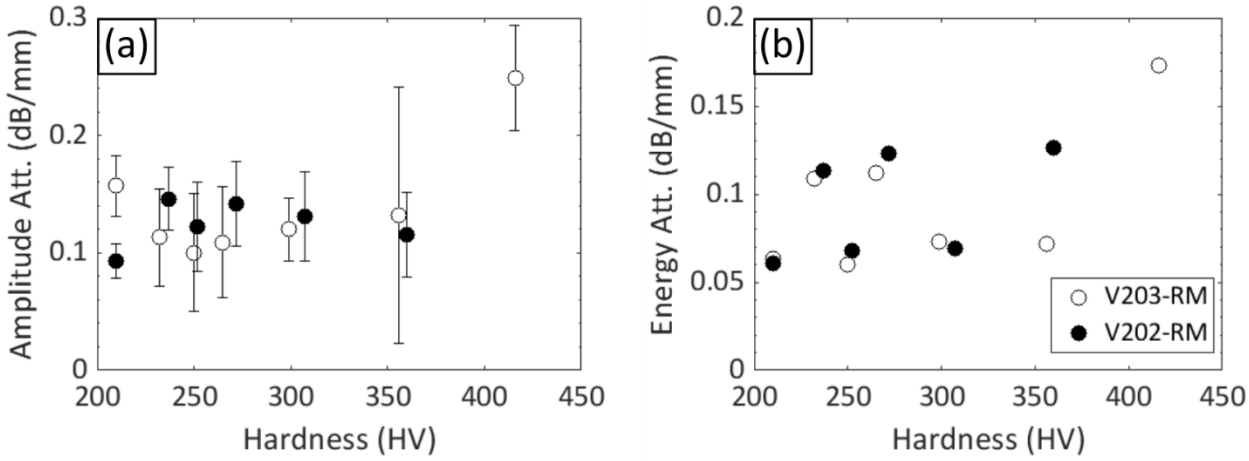

Figure 4.55 – (a) Ultrasonic amplitude attenuation and (b) energy attenuation plotted against hardness for measurements in the radial direction of specimen TCPL-S8.

As with measurements of attenuation in ML80 disc samples (Section 4.4.2), amplitude attenuation is consistently higher than energy attenuation. The reason for this difference is unknown but may be tied to the shape of the waveform and the complicated behavior of waves propagating through materials. Amplitude and energy attenuation values do not show the same behavior for measurements between 200 and 400 HV.

For hardness values between 200 and 400 HV, energy attenuation values show a wide range. Between hardness values of 250 and 272 HV, a range in energy attenuation of 0.06-0.12 dB/mm is measured for specimen TCPL-S8. Figure 4.56 shows optical micrographs from metallographic analysis (Section 4.2.2) of disc samples from Grade 483 Q&T specimen TCPL-S3.

Microstructures are shown from disc samples surfaces with hardness values of 280 HV (Figure 4.56a) and 253 HV (Figure 4.56b), which are similar to the two hardness values of 250 and 272 HV from specimen TCPL-S8. Despite the small difference in hardness, the microstructures differ greatly, with Figure 4.56a showing a larger martensite fraction, in dark-brown. Ferrite and bainite regions, seen as light brown stripes and blocks, are seen in Figure 4.56b. The variations in microstructure, may contribute to the fluctuations seen in energy attenuation for specimen TCPL-S8, because the attenuation through martensite is known to be higher than other microstructures [1] [61].

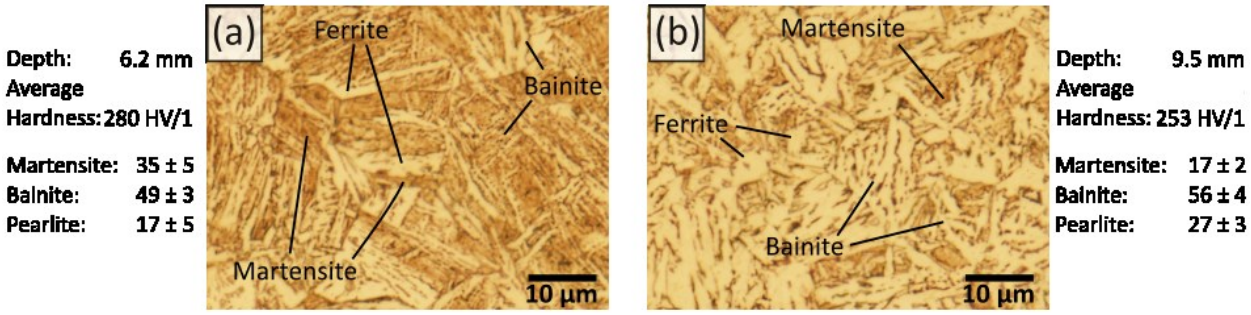

Figure 4.56 – Optical micrographs from Grade 483 Q&T specimen TCPL-S3 at locations with hardness values of (a) 280 HV and (b) 253 HV, similar to hardness values measured on specimen TCPL-S8.

Ultrasonic amplitude attenuation is plotted against microstructure fraction for measurements in the radial direction of specimen TCPL-S8 in Figure 4.57. Microstructure fractions are taken from the comparison of ultrasonic velocity and microstructure for the same specimen (Section 4.5.1). The ultrasonic measurement at a martensite fraction of 97% had the highest amplitude attenuation, at 0.25 dB/mm, while all other attenuation measurements were between 0.10 and 0.15 dB/mm. Though this suggests that attenuation is highest through martensite, as expected from the literature [1], the lack of trend for other attenuation measurements means that a direct relationship between microstructure and attenuation cannot be made from these measurements.

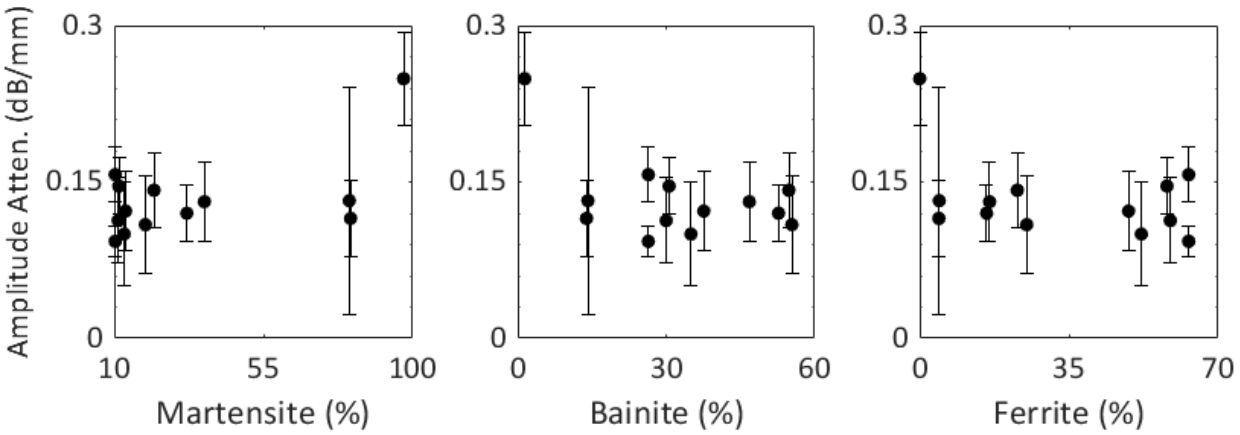

Figure 4.57 – The martensite, bainite and ferrite fractions of each of the ultrasonic amplitude attenuation measurements performed for specimen TCPL-S8.

Unlike ultrasonic velocity, attenuation measurements are affected by the factors of transducer contact and surface finish [1]. Ultrasonic backwall echo amplitudes are affected by signal noise more strongly than ultrasonic velocity. Very precise methods for surface finishing and control over transducer coupling would be necessary for reliable attenuation measurement. These

methods would be too difficult to implement in practical situations. Ultrasonic attenuation has not proven to be a useful tool for making estimates of steel microstructure.

Energy attenuation values are compared to microstructure for measurements in the radial direction of Grade 483 Q&T full sized end quench specimen TCPL-S8 in Figure 4.58. Microstructure values are obtained by comparing hardness on TCPL-S8 with hardness measured on TCPL-S3, for which metallography was also performed. Energy attenuation is highest for regions with high martensite microstructure fraction.

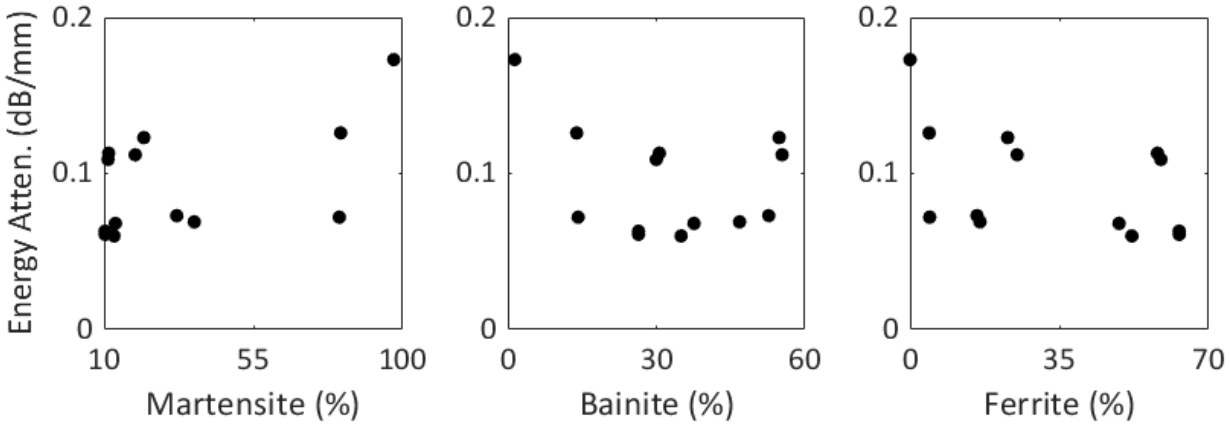

Figure 4.58 – Microstructure related to energy attenuation values measured in the radial direction of Grade 483 Q&T end quench specimen TCPL-S8.

4.6 Ultrasonic Measurements for Grade 483 Q&T – Disc Samples

This section presents ultrasonic velocity and attenuation for disc samples of Grade 483 Q&T end quench specimens TCPL-S1 and TCPL-S3. Measurements from ultrasonic longitudinal and shear wave modes are shown. Ultrasonic velocities at the quenched end of the specimens are higher than expected, and possible explanations are provided for the discrepancy in values between measurements on disc samples and measurements in the radial direction of specimen TCPL-S8. Ultrasonic amplitude attenuation values are given for both wave modes and ultrasonic energy attenuation values are given for shear wave signals. Ultrasonic amplitude attenuation values from specimen TCPL-S3 are compared to hardness values and microstructure fractions obtained for the same specimen.

4.6.1 Disc Sample Velocity

Ultrasonic velocity was measured for disc samples of Grade 483 Q&T specimens TCPL-S1 and TCPL-S3, as shown in Figure 4.59. Longitudinal velocity was highest at depths of 0.5 mm (6161 m/s) and 0.6 mm (6167 m/s), where hard microstructures were measured. These values are in opposition to results from the literature, where martensitic microstructures exhibit longitudinal

velocities around 5890 m/s [1] [2] [70]. The longitudinal velocity values were 4.6% higher than those reported in the literature. An explanation for this discrepancy is provided later in this section (Section 4.6.2). Longitudinal velocity values at higher depths (i.e. softer microstructures) agreed with literature results for ferrite and pearlite microstructures (around 5950 m/s) [1] [2]. Standard deviation values were an average of 0.6% of the plotted value for longitudinal velocity.

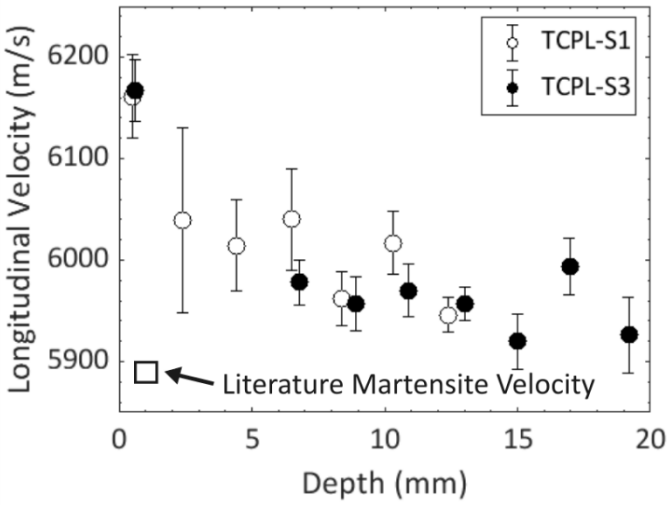

Figure 4.59 – Longitudinal velocity for Grade 483 Q&T specimen disc samples, as a function of the sample depth.

Shear velocities measured for specimens TCPL-S1 and TCPL-S3 are shown in Figure 4.60. Results from these measurements showed higher shear velocity at depths of 0.5 mm (3333 m/s) and 0.6 mm (3351 m/s). These velocities were 4.5% higher than literature results for shear velocity in martensitic steel samples (3195 m/s) [1] [2]. A discussion of this discrepancy is provided later in this section (Section 4.6.2). Literature results showed shear velocities in softer microstructures around 3235 m/s, which agreed with measurements made at higher depths for disc samples of Grade 483 Q&T specimens TCPL-S1 and TCPL-S3. Standard deviation values were on average 1.4% of the shear velocity value.

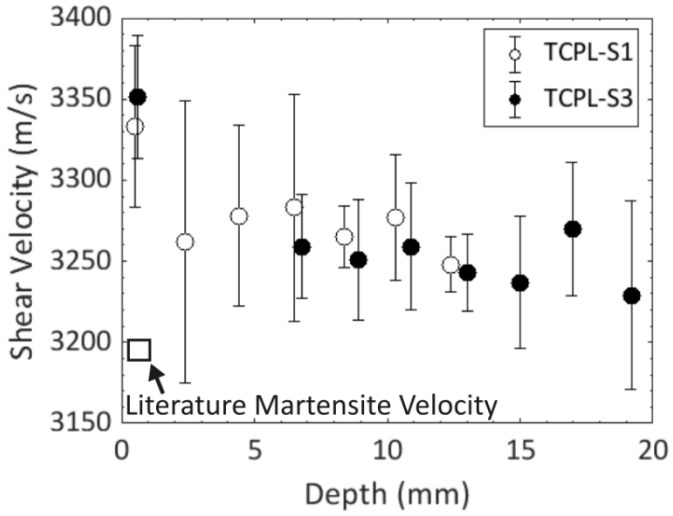

Figure 4.60 – Shear velocity for Grade 483 Q&T disc samples.

4.6.2 Velocity Discrepancies at the Quenched End

The ultrasonic velocities for specimens TCPL-S1 and TCPL-S3 (Section 3.5.3) show a discrepancy in the measurement of longitudinal and shear velocities at the quenched end. Measured velocities near the quenched end of specimen TCPL-S8 are much lower than for specimens TCPL-S1 and TCPL-S3. EBSD analysis shows that no drastic difference exists in microstructure between the radial and axial directions at the quenched end (Section 4.2.4.2), ruling out texture effects as an explanation for velocity discrepancy. Additionally, differences in grain size cannot account for the velocity differences observed in Grade 483 Q&T full sized end quench specimens. Grain size is reported in the literature to have an effect of no more than 0.2% of the total ultrasonic velocity [127] for low carbon steels.

Ultrasonic velocity is calculated according to Equation 3.4 (Section 3.6.1):

$$v = \frac{2d}{\Delta t}, \qquad \text{(Equation 3.4)}$$

meaning the error may have occurred either due to incorrect measurement of the distance of wave travel, d, or incorrect measurement of the time between subsequent backwall echoes, Δt.

Sample thickness measurements were examined first to account for the high velocity in specimens TCPL-S1 and TCPL-S3. A second set of thickness measurements was performed on disc samples from full sized specimen TCPL-S1. Table 4.9 shows the second thickness values, which were obtained from 10 measurements near the center of disc samples using the Mitutoyu MDC-Lite digital micrometer, alongside the original thickness values.

Differences between the first and second measurements are as high as 0.02 mm, or approximately 2% of the thickness. The disc sample at 0.5 mm could not be measured a second

time as it had previously been sectioned for EBSD analysis. Disc samples from specimen TCPL-S3 had been used for metallography and could not have thickness measurements performed a second time.

Table 4.9 – Two sets of thickness measurements were made for disc samples, each producing different thickness values.

Depth at Center	First Measurement (mm)		Second Measurement (mm)	
(mm)	Thickness	St. Dev.	Thickness	St. Dev.
0.5	0.71	0.01	--	--
2.4	0.91	0.01	0.91	0.01
4.4	1.22	0.01	1.24	0.01
6.5	1.17	0.02	1.19	0.01
8.4	0.80	0.01	0.81	0.01
10.3	1.22	0.01	1.24	0.02
12.4	1.19	0.01	1.21	0.01

Figure 4.61 shows longitudinal and shear velocity measured using both the first and second thickness measurements for disc samples of end quench specimen TCPL-S1. For longitudinal velocity, shown in Figure 4.61a, an average difference of 81 m/s is found using the first (open circles) and second thickness measurements (solid circles), with a maximum difference of 124 m/s. For shear velocity, in Figure 4.61b, an average difference of 44 m/s is found with a maximum difference of 68 m/s. These differences are much less than the 270 m/s and 160 m/s discrepancies found for the disc samples at the quenched end of specimens TCPL-S1 and TCPL-S3.

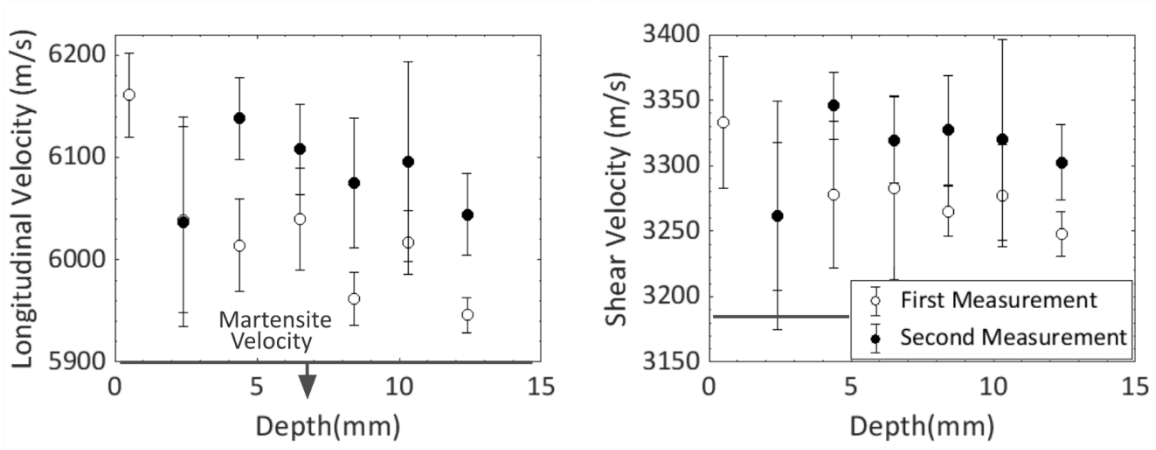

Figure 4.61 – A comparison of longitudinal and shear velocity values using the first a second thickness measurements of disc samples for specimen TCPL-S1.

For specimen TCPL-S1 at a depth of 0.5 mm, longitudinal wave signals have an average peak separation of 0.232 µs. Using this peak separation and literature values of longitudinal velocity through martensite (5890 m/s), an estimate of sample thickness of 0.68 mm is made. This thickness would mean sample thickness measurements are in error by 0.03 mm, with the same error in thickness measurement found using literature results for martensite shear velocity (3195 m/s).

To reconcile the ultrasonic velocity for specimen TCPL-S3 at a depth of 0.6 mm and the literature results for velocity through martensite, a sample thickness error of 0.05 mm is necessary. This thickness error is greater than any differences observed between first and second thickness measurements on discs of TCPL-S1 (Table 4.9). If errors in thickness measurements are to blame for inaccurate velocity results, the uneven distribution in thickness measurement error between different disc samples cannot be satisfactorily explained.

After exploring the possibility of inaccurate thickness measurements, the possibility of inaccurate peak separation measurements must also be explored. Inaccuracy in peak separation measurement could be the cause of the velocity variation observed in disc samples of Grade 483 Q&T specimens TCPL-S1 and TCPL-S3. More than 50 peak values were obtained for each disc sample from longitudinal wave signals, with 15 peak values obtained from shear waves. The large number of measurements suggests that peak separation values were measured accurately from each ultrasonic signal.

A systematic error in signal collection may have occurred during UT at the quenched end of specimens TCPL-S1 and TCPL-S3. Specimens TCPL-S1 and TCPL-S3 were measured at different times, with longitudinal and shear waves measured during different experimental sessions. The order of measurement reduces the probability that the same systematic error occurred during

signal collection at the quenched end of both specimens, because such a systematic error would likely have affected other samples as well.

A clear explanation for the discrepancy is not available. Possible explanations are that disc sample thickness was not measured accurately or that a systematic error occurred in ultrasonic signal collection. Error in disc sample thickness is the best candidate for explaining the velocity results from end quench specimens TCPL-S1 and TCPL-S3. The erroneous velocities were measured on the thinnest disc samples. Due to the problems with ultrasonic velocity measurement of specimens TCPL-S1 and TCPL-S3, velocity results from these specimens will not be presented in further sections of this work.

It must be noted that the problems facing ultrasonic velocity measurements for Grade 483 Q&T steel disc samples are not sources of concern for measurements for other specimens, i.e. ML80-S2 and TCPL-S8. The distance travelled by waves in disc samples of ML80 steel and in the radial direction of the Grade 483 Q&T steel specimen is much greater and was able to be accurately estimated by digital micrometer, to the degree that the error in velocity measurement is less than the difference in velocities measured in those specimens. Additionally, due to the prevalence of literature sources showing decreasing ultrasonic velocity with increasing hardness, only the velocity values from disc samples of TCPL-S1 and TCPL-S3 are suspect.

4.6.3 Calculation of Poisson's ratio

In the Literature Review (Section 2.3.1) the relationship between ultrasonic longitudinal and shear velocity was expressed in terms of Young's modulus (in Pa), E, density (in kg/m^3), ρ, and Poisson's ratio, ν. These are found as Equations 2.4 and 2.5, namely,

$$V_L = \sqrt{\frac{E}{\rho}\frac{(1-\nu)}{(1+\nu)(1-2\nu)}}, \qquad \text{(Equation 2.4)}$$

and,

$$V_T = \sqrt{\frac{E}{2\rho}\frac{1}{(1+\nu)}} \qquad \text{(Equation 2.5)}$$

Taking the ratio of Equations 2.4 and 2.5, a result can be obtained for Poisson's ratio, as shown in Equation 4.1:

$$\nu = \frac{2-\gamma}{2(1-\gamma)}, \qquad \text{(Equation 4.1)}$$

where $\gamma = (V_L/V_T)^2$, and V_L and V_T are the longitudinal and shear velocities (in m/s), respectively. Since both the longitudinal and shear velocities depend on the thickness of the disc samples by Equation 3.4, the value of γ can be simplified, as shown in Equation 4.2:

$$\gamma = \left(\frac{\Delta t_T}{\Delta t_L}\right)^2, \qquad \text{(Equation 4.2)}$$

where Δt_T is the average time between subsequent backwall echoes for shear waves (in μs) and Δt_L is the average time between subsequent backwall echoes for longitudinal waves (in μs). The values of time between backwall echoes, or peak separation, can be found in Appendix A.1. In this way, the propagation of standard deviation in measurement can be calculated [128] to produce the error equation shown in Equation 4.3:

$$\frac{\delta\nu}{\nu} = 2\sqrt{2}\sqrt{\left(\frac{\delta\Delta t_T}{\Delta t_T}\right)^2 + \left(\frac{\delta\Delta t_L}{\Delta t_L}\right)^2}, \qquad \text{(Equation 4.3)}$$

where the symbol, δ, denotes the standard deviation of the proceeding variable. The advantage of calculating Poisson's ratio from the peak separations of longitudinal and shear ultrasonic echoes is that it eliminates the sample thickness from the calculation. In the case of Grade 483 Q&T disc samples, the measurement of sample thickness was a large source of measurement uncertainty. Using Poisson's ratio, a comparison can be made between the different disc samples without the need to include the largest source of uncertainty, i.e. the disc sample thicknesses.

Since both longitudinal and shear velocities have been measured for disc samples from specimens TCPL-S1 and TCPL-S3, calculations of Poisson's ratio at each measurement location can be made. Figure 4.62 shows the calculated Poisson's ratio for these disc samples. Values for Poisson's ratio are between 0.285 and 0.294, spanning slightly more than the range expected from the Literature Review (Section 2.3.1). Values nearest the quenched end of the specimen are higher than those at greater depths, but the large standard deviation values make any trend insignificant. Error bars are an average of 1.3 % of the plotted values which is greater than the error bar value for longitudinal velocity calculations (Figure 4.59), and less than the value observed for shear velocity calculations (Figure 4.60)

Although the largest source of standard deviation, the disc sample thickness, has been eliminated from the calculation of Poisson's ratio, the uncertainty in the calculated values remains large enough to obscure any trend in the data. For the measurement nearest the quenched end of specimen TCPL-S1, the variation in backwall separation was only 5 ns. The close spacing of the ultrasonic echoes (of 0.232 μs) made the small variation have a significant effect on the standard deviation.

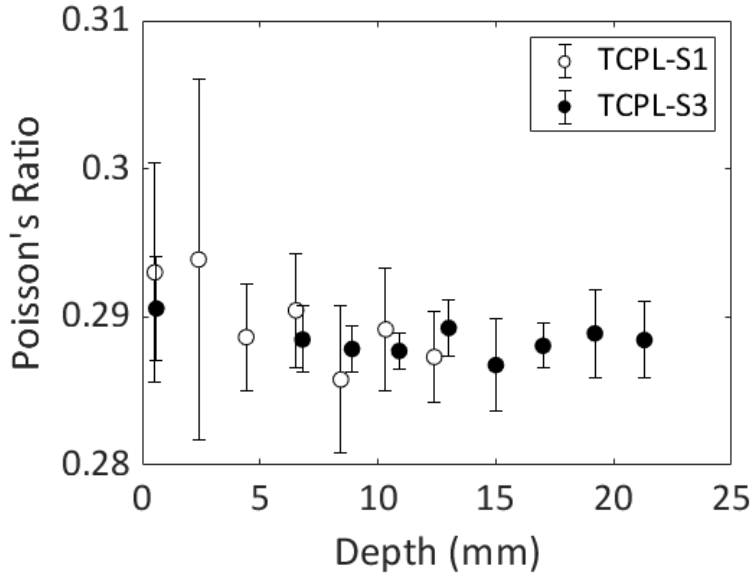

Figure 4.62 – Calculation of Poisson's ratio for disc samples from Grade 483 Q&T specimens TCPL-S1 and TCPL-S3.

Sample thickness was the largest source of uncertainty in calculating ultrasonic velocity for disc samples of specimen TCPL-S1 and TCPL-S3. Calculation of Poisson's ratio provided an alternative physical parameter which could be calculated without the use of the disc sample thickness, but the propagation of standard deviation in the calculations resulted in a similar standard deviation values when compared to direct calculations made for longitudinal and shear wave velocities.

4.6.4 Disc Sample Attenuation

Ultrasonic amplitude attenuation was measured for longitudinal and shear waves on disc samples from Grade 483 Q&T full sized end quench specimens TCPL-S1 and TCPL-S3. Longitudinal amplitude attenuation is shown in Figure 4.63, with an average attenuation of 0.64 dB/mm, which is higher than the values found in the literature [1] [61]. The high attenuation values may be a result of the increased number of reflections occurring at the front and backwalls of the disc samples due to the samples being thin. For specimen TCPL-S1, attenuation values at the quenched end are higher than other attenuation measurements, in agreement with literature results showing higher attenuation for martensitic microstructures. Specimen TCPL-S3 shows stable attenuation values across all depths, with only a mild increase for martensitic microstructures at the quenched end.

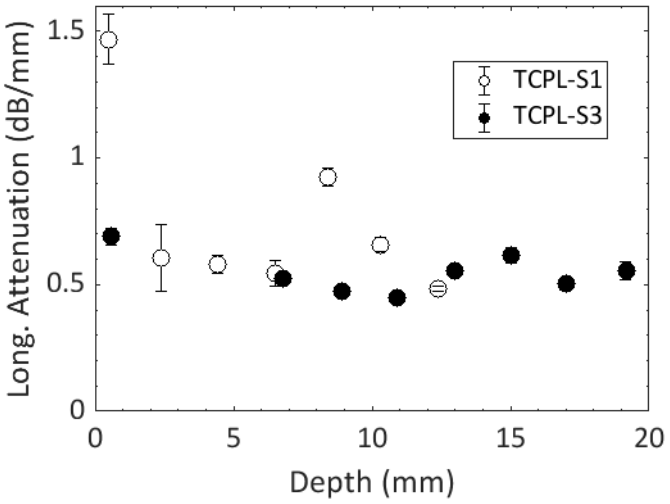

Figure 4.63 – Amplitude attenuation of longitudinal waves for Grade 483 Q&T disc samples.

Ultrasonic amplitude attenuation of shear waves for disc samples of specimens TCPL-S1 and TCPL-S3 are shown in Figure 4.64. Average attenuation values of 0.57 dB/mm were measured, with a more distinct increase at the quenched end of both specimens. These attenuation values are higher than those found in the literature [61], which is likely a result of the small sample thickness of these disc samples. The effect of sample thickness on attenuation results is discussed later in this chapter (Section 4.7.2).

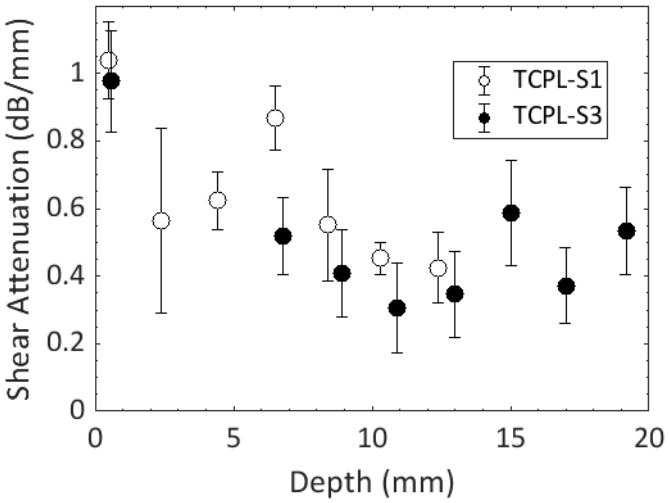

Figure 4.64 – Amplitude attenuation of shear waves for Grade 483 Q&T disc samples.

Energy attenuation was calculated for the shear wave mode of disc samples from Grade 483 Q&T specimens TCPL-S1 and TCPL-S3. The attenuation values are shown in Figure 4.65. In this case,

the highest attenuation value is measured at the quenched end for specimen TCPL-S3, but no significant trend is visible for any of the other attenuation values.

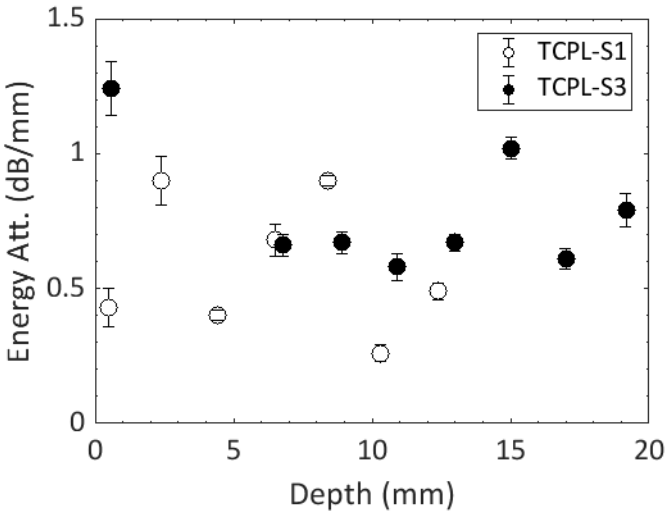

Figure 4.65 – Energy attenuation values of shear waves for Grade 483 Q&T disc samples.

Amplitude attenuation and energy attenuation plots differ for measurements on disc samples of Grade 483 Q&T steel. A decrease in attenuation is seen further from the quenched end for amplitude attenuation. No trend is observed in energy attenuation values, which are spread over a large range. Since attenuation is measured on a decibel scale, small deviations, such as errors in sample thickness measurements (Section 4.6.2) should not have as great an effect as was observed for ultrasonic velocity measurements.

Frequency dependent attenuation may account for the differences seen between amplitude and energy attenuation values. Frequency dependent attenuation may change the shape of ultrasonic backwall echoes which would affect the amplitude attenuation values more strongly. Due to the lack of ultrasonic velocity information and the indistinct trends in longitudinal amplitude attenuation values and shear energy attenuation values for specimens TCPL-S1 and TCPL-S3, further discussion of results from these measurements will not be presented. Appendix A.7 presents an attempt to use spectral analysis to measure the frequency dependent attenuation in specimens TCPL-S1 and TCPL-S3.

Ultrasonic amplitude attenuation of shear waves is correlated to hardness values for disc samples for specimen TCPL-S3, which is shown in Figure 4.66. The highest attenuation was measured at the highest hardness value, corresponding to the disc sample closest to the quenched end of the specimen. Between 200 and 300 HV the attenuation dropped with increasing hardness (around 225 HV) and increased again after 250 HV. Literature sources report increasing attenuation with increasing grain sizes for similar microstructures [49]. Changes in grain size were not measured

directly in this work but may provide a qualitative explanation for the dip in attenuation seen near 225 HV. Measurements from disc samples for specimen TCPL-S1 are not included as no hardness measurements were available for that specimen.

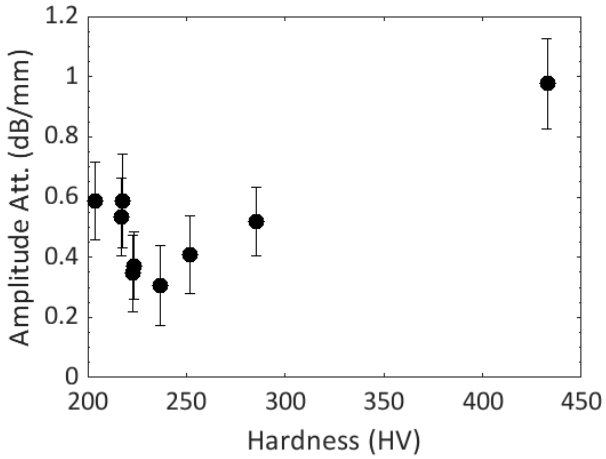

Figure 4.66 – Amplitude attenuation of shear waves plotted as a function of hardness for disc samples of Grade 483 Q&T specimen TCPL-S3.

Figure 4.67 shows portions of three optical micrographs taken for disc samples of specimen TCPL-S3. Qualitatively, Figure 4.67a has larger grain sizes than Figure 4.67b, with the spacing between the dark brown grain boundaries being much larger. The sample with larger grain size also has higher amplitude attenuation values which may be explained by the relationship of increasing attenuation with increasing grain size described in the literature [49]. In Figure 4.67c, from a depth of 8.9 mm from the quenched end of the specimen there remains some martensite, visible as dark brown regions. The additional martensite explains the increase in attenuation seen in this region.

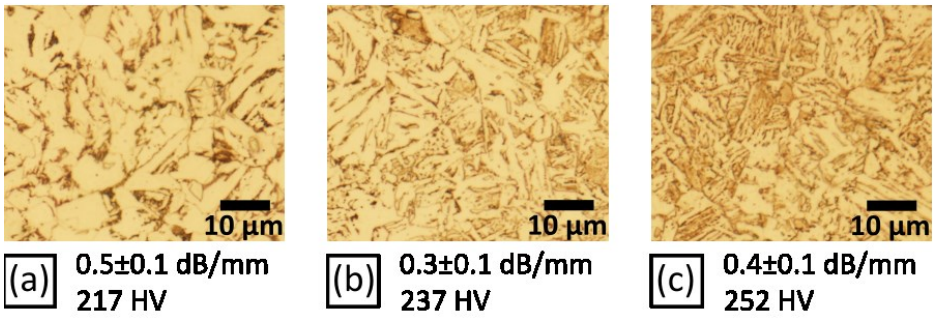

Figure 4.67 – Optical micrographs from specimen TCPL-S3 at hardness values of (a) 217 HV, (b) 237 HV and (c) 252 HV. These locations correspond to a fluctuation in amplitude attenuation for the shear wave mode.

Ultrasonic amplitude attenuation of shear waves in disc samples of Grade 483 Q&T steel are higher than attenuation values measured in the radial direction of specimen TCPL-S8, made of the same steel type. The disc sample nearest the quenched end for specimen TCPL-S3 has a thickness of 0.71 mm while measurements on specimen TCPL-S8 are performed across a thickness of 22 mm. The larger thickness of specimen TCPL-S8 results in fewer wave reflections per unit distance of wave travel when compared to disc samples of specimens TCPL-S1 and TCPL-S3. The reduced number of reflections causes a reduction in amplitude attenuation and energy attenuation. The effect of sample thickness on ultrasonic attenuation values is discussed later in this chapter (Section 4.7.2).

Ultrasonic amplitude attenuation for disc samples of TCPL-S3 is compared to microstructure fraction in Figure 4.68. Specimens with high martensite and low ferrite fractions have the highest amplitude attenuation values, as expected from the literature [1]. Attenuation values are lower for samples with high ferrite and bainite fractions, but a relationship between microstructure and ultrasonic attenuation is not clear. Disc samples with 0% and 63% ferrite fraction are the thinnest and coincide with the highest amplitude attenuation values. This relationship between disc thickness and attenuation may serve to obscure any trend between microstructure fraction and attenuation described by the literature [3].

The literature suggests that within similar microstructures larger grain sizes would cause greater wave attenuation [55] [49] [82]. However, as grain size was not measured in this work it is not possible to determine if it influenced ultrasonic attenuation.

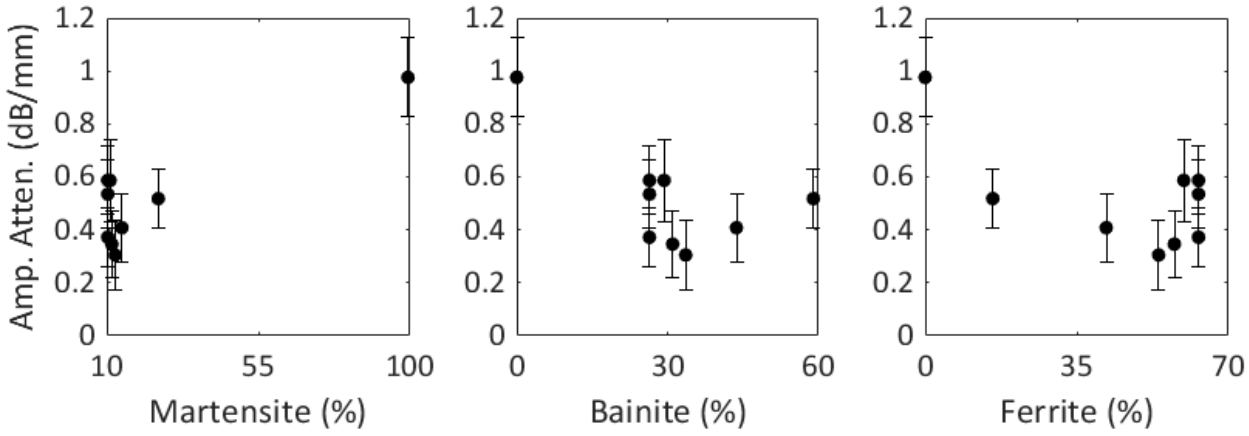

Figure 4.68 – The martensite, bainite and ferrite fractions of each of the ultrasonic amplitude attenuation measurements for shear waves for specimen TCPL-S3.

Attenuation values are not affected by uncertainty in sample thickness as strongly as velocity measurements [92], and can be related to microstructure fraction in samples with less precise fabrication methods. This can make amplitude and energy attenuation measurements attractive

for use in practical applications where less control can be exercised in sample preparation. Several factors contribute to energy attenuation measurements being a preferable candidate for measurements of ultrasonic attenuation. Signal noise and interference between echoes can make echo amplitudes difficult to calculate, reducing the accuracy of amplitude attenuation measurements.

4.7 Challenges in Ultrasonic Parameter Measurements

This section discusses the difficulty in making accurate comparisons of microstructure fraction, hardness and ultrasonic parameters using Jominy end quench specimens. The difficulty of making samples with precise microstructures and sample dimensions is discussed first, followed by the challenge with trying to measure ultrasonic attenuation on disc samples of Jominy end quench specimens.

4.7.1 Difficulties using End Quench Specimens

Measurements of ultrasonic velocity on disc samples of specimen ML80-S2 illustrate the difficulties in using end quench specimens to correlate velocity and microstructure. One of the difficulties is due to the spread of error bars in ultrasonic measurements. Disc samples cut from subsized end quench specimens are not uniform in thickness and produce standard deviations as high as 20 m/s. The same problem was seen in making disc samples from Grade 483 Q&T full sized specimens, where standard deviations of nearly 100 m/s were obtained.

The problem associated with disc sample thickness could be reduced by cutting disc samples with greater thickness. Thicker samples can be used to control the error in velocity measurements but would encompass a wider range of microstructures along their length. Control over the microstructures present in a disc samples poses a challenge because the microstructure is not known prior to sectioning the specimen. Without knowing the microstructure beforehand, a target microstructure cannot be produced in the disc sample.

Some control over microstructure can be exercised by changing the thickness and location of disc samples. Many end quench specimens would be needed for this purpose. Uncertainty in producing a desired microstructure would remain, as microstructure would be measured after sectioning was completed. This method would allow the creation of additional disc samples with martensite fractions between 50 and 100%. Additional disc samples with high martensite content would allow for a better understanding of how ultrasonic parameters vary in martensitic samples.

4.7.2 Effect of Sample Thickness on Attenuation

Ultrasonic attenuation values vary as a result of a variety of factors, including the thickness of the disc samples being examined. Table 4.10 shows attenuation information from disc samples from

ML80 and Grade 483 Q&T end quench specimens. From the data in Table 4.10, the effect of disc sample thickness can be understood.

Information for disc samples #1 and #3 from ML80-S2 shows that Disc #3 is 2.2 times thicker than Disc #1. Attenuation values can be compared, showing that Disc #1 has 3.0 times the amplitude attenuation and 3.7 times the energy attenuation of Disc #3. This analysis shows that lower sample thickness does not fully account for the trend in ultrasonic attenuation observed in ML80 disc samples. The disc sample near the quenched end of ML80-S2 has a smaller thickness than the others. Lower sample thickness results in a higher number of reflections for ultrasonic waves. Interfaces are known to be a source of energy loss for travelling ultrasonic waves, contributing to attenuation [129].

Disc #5 from Grade 483 Q&T specimen TCPL-S3 has an amplitude attenuation of 0.45 dB/mm. Disc #5 from TCPL-S3, Disc #3 from ML80-S2 and TCPL-S8 are not expected to have any martensite fraction. The decreasing attenuation with increasing sample thickness suggests that thickness plays an important role in ultrasonic amplitude attenuation.

Table 4.10 – Ultrasonic attenuation values of each of the disc samples from specimen ML80-S2.

Specimen	Disc Sample #	Sample Thickness (mm)	Amplitude Attenuation (dB/mm)	Energy Attenuation (dB/mm)
ML80-S2	1	2.35	0.45	0.37
ML80-S2	3	5.11	0.15	0.10
TCPL-S3	5	1.22	0.45	--
TCPL-S8	--	22.4	0.120	0.073

4.8 Summary of Results and Discussion

HRC and HV measurements on subsized and full sized specimens indicate success in the end quenching process. Rapid drops in hardness were observed in the first 10 mm of depth for specimens of both types of steel. Microstructure fraction identification showed that a fully martensitic microstructure was achieved at the quenched end of ML80 and Grade 483 Q&T specimens, which was confirmed by EBSD analysis. The decrease in martensite fraction coincides with the decrease in hardness.

Ultrasonic longitudinal velocity was measured for ML80 and Grade 483 Q&T steels. Shear velocity was measured only in Grade 483 Q&T steel, due to the inability to use shear wave probes on other steel samples. Velocity for ML80 and Grade 483 Q&T steels was lowest near the quenched end of Jominy specimens. Measurements of velocity on disc samples of Grade 483 Q&T steel were rejected due to concerns over the accuracy of measurements.

Ultrasonic amplitude attenuation was measured for ML80 and Grade 483 Q&T steels. Amplitude attenuation was highest near the quenched end of Jominy specimens, where higher hardness and higher martensite fractions were measured. In ultrasonic energy attenuation measurements for ML80 and Grade 483 Q&T steels, higher attenuation values are also found near the quenched end of Jominy specimens. Measurements of energy attenuation were consistently lower than amplitude attenuation.

The use of ultrasonic velocity measurements for the identification of microstructure fraction was shown to be possible using results from ML80 and Grade 483 Q&T Jominy end quench specimens. Estimation of martensite fraction from velocity measurements was attempted, but error in ML80 measurements prevent making estimates with a high degree of accuracy. In Grade 483 Q&T steel, few ultrasonic measurements were made with a martensite fraction >50%. Due to the limited number of ultrasonic measurements with high martensite fraction, estimation is limited in applicability to low martensite fractions.

Jominy end quench specimens are not well suited to the correlation of ultrasonic parameters, hardness values and microstructure fractions. A satisfactory balance of sample dimensions for accurate ultrasonic velocity measurements and microstructure control (particularly high martensite fraction) could not be achieved, resulting in large standard deviation in ultrasonic velocity and attenuation measurements and in a limited number of samples with high martensite fraction.

Chapter 5 - Conclusions

Measurements of Vicker's hardness, ultrasonic velocity and attenuation, and microstructure fraction were performed on Jominy end quench specimens of ML80 casing steel and Grade 483 Q&T fitting steel.

1. Hardness values of discs from ML80 subsized end quench specimens between 250 and 486 HV. Ultrasonic longitudinal velocity (5929-5957 m/s) decreased with increasing hardness. Ultrasonic longitudinal amplitude attenuation (0.15-0.4 dB/mm) and energy attenuation (0.1-0.37 dB/mm) increased with increasing hardness.
2. Hardness in the radial direction of Grade 483 Q&T end quench specimens was between 237 and 416 HV. Ultrasonic longitudinal velocity (5906.7-5920.4 m/s) decreased with increasing hardness. Ultrasonic longitudinal amplitude attenuation (0.09-0.25 dB/mm) and energy attenuation (0.06-0.17 dB/mm) increased with increasing hardness.
3. Energy attenuation values are an average of 82% of the amplitude attenuation values.

Ultrasonic measurements show that sample geometry is an important factor measuring ultrasonic velocity and attenuation. End quench specimens allowed for correlation of microstructure with ultrasonic parameters, showing that ultrasonic velocity is higher in specimens with low martensite fractions and high ferrite fractions.

6.1 Future Work

Increased accuracy in ultrasonic measurements can be used for precise prediction of steel microstructure. Increased accuracy can be achieved using steel specimens with large dimensions and uniform microstructures. These measurements could be applied to predictive models of martensite fraction to determine the success of the method.

Additional calculation methods can be used to assess steel using UT. Further comparison of ultrasonic amplitude and energy attenuation would help determine which method is superior for predicting steel properties. The use of additional frequency spectrum methods should be investigated. Methods such as frequency-band power measurement and cross-correlation between echo signals may provide powerful tools for analyzing steel using ultrasonic testing.

Bibliography

[1] V. L. d. A. Freitas, V. H. C. de Albuquerque, E. d. M. Silva, A. A. Silva and J. M. R. S. Tavares, "Nondestructive characterization of microstructures and determination of properties in plain carbon steel using ultrasonic measurements," *Materials Science and Engineering A,* vol. 527, pp. 4431-4437, 2010.

[2] C. H. Gur and B. O. Tuncer, "Microstructural investigation of ASE 1040 steel specimen by ultrasonic measurements," *Material Characterisation,* vol. 47, no. 7, pp. 421-424, 2005.

[3] P. Behjati, H. Vahid Dastjerdi, R. Mahdavi and D. Rasouli, "Effect of Microstructure on Attenuation Mechanism of Ultrasonic Waves in Carbon Steels," *Materials Science and Technology,* vol. 26, no. 4, pp. 482-486, 2010.

[4] J. Kennedy, Ultrasonic Evaluation of Microstructure in Pipe Steels, Edmonton, AB: Dept. Of Chemical and Materials Engineering, University of Alberta, 2015.

[5] W. D. Callister Jr. and D. G. Rethwisch, Materials Science and Engineering: An Introduction, 9 ed., Hoboken, NJ: John Wiley & Sons, Inc., 2014.

[6] S. Shanmugam, R. D. K. Misra, J. Hartmann and S. G. Jansto, "Microstructure of high strength niobium-containing pipeline steel," *Materials Science and Engineering A,* vol. 441, pp. 215-229, 2006.

[7] A. I. Filho, R. V. de Silva, P. G. B. de Oliveira, J. Batista, R. Martins, W. W. B. Filho and M. Strangwood, "Influence of Niobium and Molybdenum on mechanical strength and wear resistance of microalloyed steels," *Materials Research,* vol. 20, no. 4, pp. 1029-1034, 2017.

[8] K. Ravi, V. Ramaswamy and T. K. G. Namboodhiri, "Effect of molybdenum on the resistance to H2S of high sulphr microalloyed steels," *Materials Science and Engineering,* vol. 169, no. 1, pp. 111-118, 1993.

[9] T. N. Baker, "Microalloyed steels," *Iron & Steelmaking,* vol. 43, no. 4, pp. 264-307, 2016.

[10] N. Isasti, D. Jorge-Badiola, M. L. Taheri, B. Lopez and P. Uranga, "Effect of composition and deformation on coarse-grained austeniite transformation in Nb-Mo microalloyed steels," *Metallurgical and Materials Transactions A,* vol. 42, no. 1, pp. 3729-3742, 2011.

[11] L. R. Cupertino Malheiros, E. A. Pachon Rodriquez and A. Arlazarov, "Mechanical behavior of tempered martensite: Characterization and modelin," *Materials Science & Engineering A,* vol. 706, no. 1, pp. 38-47, 2017.

[12] H. I. Aaronson, G. Spanos and W. T. Reynolds Jr., "A progress report on the definitions of bainite," *Scripta Materialia,* vol. 47, no. 1, pp. 139-144, 2002.

[13] E. I. Galindo-Nava and P. E. J. Rivera-Diaz-del-Castillo, "Understanding the factors controlling the hardness in martensitic steels," *Scripta Materialia,* vol. 110, no. 1, pp. 96-100, 2016.

[14] T. Ohmura, K. Tsuzaki and S. Matsuoka, "Nanohardness measurement of high-purity Fe-C martensite," *Scripta Materialia,* vol. 45, pp. 889-894, 2001.

[15] M. Hamidnia and F. Honarvar, "Measurement of elastic properties of AISI 52100 alloy steel by ultrasonic nondestrucctive methods," *Journal of Mechanics of Materials and Structures,* vol. 7, no. 10, pp. 951-961, 2012.

[16] G. F. Vander Voort, "Martensite and retained austenite," *Industrial Heating,* vol. 4, 2009.

[17] F. M. C. Cera, B. Schulz, S. Papaefthymiou, A. Artigas, A. Monsalve and R. H. Petrov, "The effect of ultrafast heating on cold-rolled low carbon steel: Formation and decomposition of austenite," *Metals,* vol. 321, no. 6, 2016.

[18] Y.-j. Li, X.-l. Li, G. Yuan, J. Kang, D. Chen and G.-d. Wang, "Microstructure and partitioning behavior characteristics in low carbon steel treated by hot-rolling direct quenching and dynamical partitioning processes," *Materials Characterization,* vol. 121, pp. 157-165, 2016.

[19] X. Tan, Y. Xu, X. Yang, Z. Liu and D. Wu, "Effect of partitioning procedure on microstructure and mechanical properties of a hot-rolled directly quenched and partitioned steel," *Materials Science & Engineering A,* vol. 594, pp. 149-160, 2014.

[20] M. Masoumi, L. F. G. Herculano and H. F. G. de Abreu, "Study of texture and microstructure evaluation of steel API 5L X70 under various thermomechanical cycles," *Materials Science & Engineering A,* vol. 639, pp. 550-558, 2015.

[21] J. Xu, R. D. K. Misra, B. Guo, V. S. A. Challa and L. Zheng, "High strength (560 MPa) quenched and tempered pipeline steels," *Materials Science and Technology,* vol. 29, no. 10, pp. 1241-1246, 2013.

[22] H. Terasaki and Y.-i. Komizo, "Corelation between the microstructural development of bainitic ferrite and the characteristics of martensite-austenite constituent," *Metallurgical and Materials Transactions A,* vol. 44, no. 1, pp. 5289-5293, 2013.

[23] N. Takayama, G. Miyamoto and T. Furuhara, "Chemistry and three-dimensional morphology of martensiite-austenite constituent in the bainite structure of low-carbon low-alloy steels," *Acta Materialia,* vol. 145, pp. 154-164, 2018.

[24] M. Mohammadijoo, J. Valloton, L. Collins, H. Henein and D. G. Ivey, "Characterization of martensite-austenite constituents and micro-hardness in intercritical reheated and coarse-grained heat affected zones of API 70 HSLA steel," *Materials Characterization,* vol. 142, pp. 321-331, 2018.

[25] X. Liang, M. Hua and A. J. DeArdo, "The mechanism of martensite-austenite microconstituents formation during thermomechanical controlling processing in low carbon bainitic steel," *Materials Science Forum,* Vols. 783-786, pp. 704-7012, 2014.

[26] S. K. Basiruudin, D. Chakrabarti and S. Chatterjee, "Microstructural engineering and strength-impact toughness prediction in ultra-low carbon bainitic steel," *Materials Science and Technology,* vol. 34, no. 15, pp. 1910-1918, 2018.

[27] *ASTM E18-19, Standard Test Methods for Rockwell Hardness of Metallic Materials,* West Conshohocken, PA: ASTM International, 2019.

[28] *ASTM E384-17, Standard Test Method for Microindentation Hardness of Materials,* West Conshohocen, Pa: ASTM Internation, 2017.

[29] C. Chuenarrom, P. Benjakul and P. Daosodsai, "Effect of indentation load and time on Knoop and Vickers microhardness tests for enamel and dentin," *Materials Research,* vol. 12, no. 4, pp. 473-476, 2009.

[30] G. F. Vander Voort and R. Fowler, "Low-Load Vickers Microindentation," *Advanced Materials & Processes,* pp. 28-33, April 2012.

[31] "ASM Handbook," ASM International, 2010.

[32] *ASTM A255-10, Standard Test Methods for Determining Hardenability of Steel,* West Conshohocken, PA: ASTM International, 2014.

[33] W. H. Bruckner, "The Hardenability of Carburizing Steels," *University of Illinois Bulletin,* vol. 37, no. 13, 21 November 1939.

[34] F. J. Semel and D. A. Lados, "Simulated effects of martensite start temperature, thermal conductivity and pore content on end quench cooling rate," *Powder Metallurgy,* vol. 52, no. 4, pp. 282-290, 2009.

[35] S. G. Chen, C.-I. Weng and J. Lin, "Inverse estimation of transient temperature distribution in the end quenching test," *Journal of Materials Processing Technology,* vol. 86, pp. 257-263, 1999.

[36] D. Homberg, "A numerical simulation of the jominy end-quench test," *Acta materialia,* vol. 44, no. 11, pp. 4375-4385, 1996.

[37] C. R. N. Nunura, C. A. dos Santos and J. A. Spim, "Numerical-Experimental correlation of microstructures, cooling rates and mechanical properties of AISI 1045 steel during the Jominy end-quench test," *Materials and Design,* vol. 76, pp. 230-243, 2015.

[38] E. Lopéz, J. B. Hernandez, G. Solorio, H. J. Vergara, O. Vasquez and P. Garnica, "Mathematical model of heat transfer to predict distribution of hardness through the Jominy bar," *Revista de Metalurgia,* vol. 49, no. 2, pp. 111-121, 2013.

[39] A. Sugianto, M. Narazaki, M. Kogawara and A. Shirayori, "Validity of heat transfer coefficient based on cooling time, cooling rate, and heat flux on Jominy end quench test," in *Materials Science and Technology*, Detroit, Michigan, 2007.

[40] H. S. Fong, "Further observations on the Jominy end quench test," *Journal of Materials Processing Technology,* vol. 38, pp. 221-226, 1993.

[41] J. Krautkramer and H. Krautkramer, Ultrasonic Testing of Materials, 4, Ed., Berlin: Springer-Verlag Berlin Heidelberg, 1990.

[42] G. Lamouche, S. Bolognini and S. E. Kruger, "Influence of steel heat treatment on ultrasonic absorption measured by laser ultrasonics," *Materials Science and Engineering A,* vol. 370, no. 2, pp. 401-406, 2004.

[43] C. J. Hellier, Handbook of Nondestructive Evaluation, McGraw-Hill, 2003.

[44] "NDT Resource Center," Collaboration for Nondestructive Testing, 1999. [Online]. Available: https://www.nde-ed.org/GeneralResources/MaterialProperties/UT/ut_matlprop_metals.php. [Accessed 12 March 2019].

[45] J. D. Achenbach, Wave propagation in elastic solids, 2 ed., Amsterdam: North-Holland Publishing Company, 1976.

[46] J. Miklowitz, The Theory of Elastic Waves and Waveguides, North-Holland Publishing Company, 1978.

[47] J. L. Davis, Wave Propagation in Solids and Fluids, Springer-Verlag New York Inc., 1988.

[48] C. S. Kim, S. I. Kwun and I. K. Park, "Characterization of creep-fatigue in ferritic 9Cr-1Mo-V-Nb steel using ultrasonic velocity," *Journal of Nuclear Materials,* vol. 377, no. 3, pp. 496-500, 2008.

[49] S. I. Kwun, S. T. Hong and W. Y. Choo, "Ultrasonic nondestrucctive evaluation of microstructure and strength of carbon steels," *Journal of Materials Science Letters,* vol. 19, pp. 1453-1456, 2000.

[50] S. A. Kim and W. L. Johnson, "Elastic constants and internal friction of martensitic steel, ferritic-pearlitic steel, and alpha-iron," *Materials Science and Engineering A,* Vols. 452-453, pp. 633-639, 2007.

[51] G. M. Goodrich, Ed., "Iron Castings Engineering Handbook," Des Plaines, Illinois: American Foundary Society, 2003, p. 223.

[52] S. H. Khan and A. N. Khan, "Evaluation of austenite phase in high-carbon steel by ultrasonic longitudinal velocity," *Journal of Testing and Evaluation,* vol. 44, no. 3, pp. 1112-1118, 2016.

[53] Y. Zhang, X. Wang, Q. Yang, F. Dong, X. Du and A. Yin, "Characterizationg of mean grain size of interstitial-free steel based on laser ultrasonic," *Journal of Materials Science,* vol. 53, no. 11, pp. 8510-8522, 2018.

[54] S. Z. Khan, T. M. Khan, Y. F. Joya, M. A. Khan, S. Ahmed and A. Shah, "Assessment of material properties of AISI 316L stainless steel using non-destructive testing," *Nondestructive Testing and Evaluation,* vol. 31, no. 4, pp. 360-370, 2016.

[55] P. Palanichamy, A. Joseph, T. Jayakumar and B. Raj, "Ultrasonic velocity measurements for estimation of grain size in austenitic stainless steel," *NDT&E International,* vol. 28, no. 3, pp. 179-185, 1995.

[56] A. Kumar, T. Jayakumar and B. Raj, "Ultrasonic spectral analysis for microstructural characterization of austenitic and ferritic steels," *Philosophical Magazine A,* vol. 80, no. 11, pp. 2469-2487, 2000.

[57] A. Kumar, T. Jayakumar, P. Palanichamy and B. Raj, "Influence of grain size on ultrasonic spectral parameters in AISI type 316 stainless steel," *Scripta Materialia,* vol. 40, no. 3, pp. 333-340, 1999.

[58] S. A. Barannikova, A. V. Bochkareva, A. G. Lunev, G. V. Shlyakhova and L. B. Zuev, "Changes in Ultrasonic Velocity in the Plastic Deformation of High-Chromium Steel," *Izvestiya Vysshikh Uchebnykh Zavedenii, Chernaya Metalluriya,* vol. 46, no. 8, pp. 558-564, 2016.

[59] T. R. G. Kutty, K. N. Chandrasekhara, J. P. Panakkal, S. K. Ghosal and P. K. De, "Use of ultrasonic velocity for nondestructive evaluation of ferrite content in duplex stainless steels," *NDT International,* vol. 20, no. 6, pp. 359-361, 1987.

[60] A. Kumar, K. Laha, T. Jayakumar, K. B. S. Rao and B. Raj, "Comprehensive microstructural characterization in modified 9Cr-1Mo ferritic steel by ultrasonic measurements," *Metallurgical and Materials Transactions A,* vol. 33, no. 6, pp. 1617-1626, 2002.

[61] I. Mutlu, E. Oktay and S. Ekinci, "Characterization of microstructure of H13 tool steel using ultrasonic measurements," *Russian Journal of Nondestructive Testing,* vol. 49, no. 2, pp. 112-120, 2013.

[62] C.-H. Hsu, H.-Y. Teng and Y.-J. Chen, "Relationship between ultrasonic characteristics and mechanical properties of tempered martensitic stainless steel," *Journal of Materials Engineering and Performance,* vol. 13, no. 5, pp. 593-599, 2004.

[63] A. B. Bouda, A. Benchaala and K. Alem, "Ultrasonic characterization of materials hardness," *Ultrasonics,* vol. 38, pp. 224-227, 2000.

[64] A. B. Bouda, S. Lebaili and A. Benchaala, "Grain size influence on ultrasonic velocities and attenuation," *NDT&E International,* vol. 36, no. 1, pp. 1-5, 2003.

[65] T. Lukomski and T. Stepinski, "Steel hardness evaluation based on ultrasound velocity measurements," *Materials Characterisation,* vol. 52, no. 11, pp. 592-596, 2010.

[66] K. V. Rajkumar, A. Kumar, T. Jayakumar, B. Raj and K. K. Ray, "Characterization of aging behavior in M250 grade maraging steel using ultrasonic measurements," *Metallurgical and Materials Transactions A,* vol. 38, no. 2, pp. 236-243, 2007.

[67] M. Vasudevan, P. Palanichamy and S. Venkadesan, "A novel technieuq for characterizing annealing behaviour," *Scripta Metallurgica et Materialia,* vol. 30, no. 11, pp. 1479-1483, 1994.

[68] K. Vijayalakshmi, V. Muthupandi and R. Jayachitra, "Influence of heat treatment on the microstructure, ultrasonic attenuation and hardness of SAF 2205 duplex stainless steel," *Materials Science and Engineering A,* vol. 529, pp. 447-451, 2011.

[69] H. Carreon, G. Barrera, C. Natividad, M. Salazar and A. Contreras, "Relation between hardness and ultrasonic velocity on pipeline steel welded joints," *Nondestructive Testing and Evaluation,* vol. 31, no. 2, pp. 97-108, 2016.

[70] V. V. Murav'ev, O. V. Murav'eva and K. V. Petrov, "Connection between the properties of 40Kh-steel bar stock and the speed of bulk and Rayleigh waves," *Russian Journal of Nondestructive Testing,* vol. 53, no. 8, pp. 560-567, 2017.

[71] F. Dupont-Marillia, M. Jahazi, S. Lafreniere and P. Belanger, "Influence of local mechanical properties of high strength steel from large size forged ingot on ultrasonic wave velocities," *AIP Conference Proceedings,* vol. 1806, no. 1, p. 09002, 2017.

[72] E. A. Motova, N. E. Nikitina and Y. P. Tarasenko, "Concerning the possibility of examining compressor blades according to attenuation and speed of ultrasound," *Journal of Machinery Manufacture and Reliability,* vol. 42, no. 4, pp. 335-340, 2013.

[73] S. E. Kruger and E. B. Damm, "Monitoring austenite decomposition by ultrasonic velocity," *Materials Science and Engineering A,* vol. 425, no. 1-2, pp. 238-243, 2006.

[74] A. A. Buenos, P. Pereira Jr, P. R. Mei and A. A. dos Santos, "Influence of grain size on the propagation of Lcr waves in low carbon steel," *Journal of Nondestructive Evaluation,* vol. 33, pp. 562-570, 2014.

[75] P. Pereira, A. A. Buenos and A. A. Santos, "On the evaluation of the effect of microstructure on the SNR of ultrasonic images and on the velocity of Lcr waves," *Journal of Testing and Evaluation,* vol. 45, no. 4, pp. 1401-1409, 2017.

[76] B. Ahn, S. S. Lee, S. T. Hong, H. C. Kim and S.-J. L. Kang, "Application of the acoustic resonance method to evaluate the grain size of low carbon steels," *NDT&E International,* vol. 32, pp. 85-89, 1999.

[77] S. Kendarian, T. P. Berndt, R. E. Green Jr. and B. B. Djordjevic, "Ultrasonic monitoring of dislocations during fatigue of pearlitic rail steel," *Materials Science and Engineering A,* vol. 348, no. 1-2, pp. 90-99, 2003.

[78] B. Buitrago, I. Irausquin and J. Mendoza, "Ultrasonic velocity and attenuation in carbon steel specimens," *Revista Técnica de la Facultad de Ingeniería. Universidad del Zulia,* vol. 27, no. 1, pp. 20-25, 2004.

[79] N. W. Ashcroft and N. D. Mermin, Solid State Physics, 1 ed., Saunders College Publishing, 1976.

[80] C. Kittel, Introduction to Solid State Physics, 8 ed., John Wiley & Sons Inc, 2005.

[81] V. J. Minkiewicz, G. Shirane and R. Nathans, "Phonon dispersion relation for iron," *Physical Review,* vol. 162, no. 3, pp. 538-531, 1967.

[82] B. Ahn and S. S. Lee, "Effect of microstructure of low carbon steels on ultrasonic attenuation," *IEEE Transactions on Ultrasonics, Ferroelectrics and Frequency Control,* vol. 47, no. 3, pp. 620-629, 2000.

[83] M. M. El Rayes, E. A. El-Danaf and A. A. Almajid, "Characterization and correlation of mechanical, microstructural and ultrasonic properties of power plant steel," *Materials Characterization,* vol. 100, pp. 120-134, 2015.

[84] H. Ogi, T. Hamaguchi and M. Hirao, "In-situ monitoring of ultrasonic attenuation during rotating bending fatigue of carbon steel with electromagnetic acoustic resonance," *Jourmal of Alloys and Compounds,* vol. 310, no. 1-2, pp. 436-439, 2000.

[85] S.-Y. Hsia and Y.-T. Chou, "Assessing the Hardness of Quenched Medium Steel Usin an Ultrasonic Nondestructive Method," *Advances in Materials Science and Engineering,* vol. 2015, pp. 1-8, 2015.

[86] S. Kendarian, T. P. Berndt, R. E. Green Jr. and B. B. Djordjevic, "Ultrasonic attenuation and velocity in pearlitic rail steel during fatigue using longitudinal wave probing," *Journal of Testing and Evaluation,* vol. 31, no. 2, pp. 98-105, 2002.

[87] H. Ogi, N. Suzuki and M. Hirao, "Noncontact ultrasonic spectroscopy on deforming polycrystalline copper: Dislocation damping and acoustoelasticity," *Metallurgical and Materials Transactions A,* vol. 29A, pp. 2987-2993, 1998.

[88] M. P. Blodgett and D. Eylon, "The influence of texture and phase distortion on ultrasonic attenuation in Ti-6Al-4V," *Journal of Nondestructive Evaluation,* vol. 20, no. 1, pp. 1-16, 2001.

[89] T. Ohtani, K. Nishiyama, S. Yoshikawa, H. Ogi and M. Hirao, "Ultrasonic attenuation and microstructural evolution throughout tension-compression fatigue of a low-carbon steel," *Materials Science and Engineering A,* vol. 442, no. 2, pp. 466-470, 2006.

[90] N. Y. Nikitina, "On the specifics of measuring attenuation and velocity of ultrasound in media with microstructure," *Acoustical Physics,* vol. 56, no. 6, pp. 919-923, 2010.

[91] O. Dupond, N. Feuilly, B. Chassignole, T. Fouquet, J. Moysan and G. Corneloup, "Relation between ultrasonic scattering and microstructure of polycrustalline materials," in *Journal of Physics: Conference Series*, 2011.

[92] H. Fei, A. Yin and Q. Yang, "Grain size measurement in steel by laser ultrasonics based on time domain energy," *Materials Transactions,* vol. 56, no. 6, pp. 808-812, 2015.

[93] M. Li, T. Zhou and Y. Song, "Material grain size characterization method based on energy attenuation coefficient spectrum and support vector regression," *Ultrasonics,* vol. 69, pp. 1-10, 2016.

[94] M. d. S. Mesquita and S. Halldorsdottir, "Data Analysis: Filtering, Crosscorrelation, Coherence and Applications to Geophysical Data using Matlab," Bjerknes Center for Climate Research, 2005.

[95] M. Noipak and B. Khwansri, "The investigation of ultrasonic energy attenuation in AISI 316 stainless steel weld joint," *Key Engineering Materials,* vol. 7511, pp. 207-212, 2017.

[96] R. L. Smith, "Ultrasonic Materials Characterization," *NDT International,* vol. 20, no. 1, pp. 43-48, 1987.

[97] G. K. Sharma, A. Kumar, C. B. Rao, T. Jayakumar and B. Raj, "Short time Fourier transform analysis for understanding frequency dependent attenuation in austenitic stainless steel," *NDT&E International,* vol. 53, no. 1, pp. 1-7, 2013.

[98] P. Petculescu, R. Zagan, G. C. Prodan and A. Danisor, "Ultrasonic spectroscopy based on wavelets transform for materials characterization," *Romanian Journal of Physics,* vol. 50, no. 7-8, pp. 701-710, 2005.

[99] P. Govindan, A. Kasaeifard and J. Saniie, "Ultrasonic chirplet echo parameter estimation using time-frequency distributions," in *IEEE International Ultrasonics Symposium Proceedings*, Taipei, 2015.

[100] M. Stranza, O. Louis, D. Polyzos, F. Boulpaep, D. van Hemelrijck and D. G. Aggelis, "Wave dispersion and attenuation on human fremur tissue," *Sensors,* vol. 14, pp. 15067-15083, 2014.

[101] B. Zhao, O. A. Basir and G. S. Mittal, "Estimation of ultrasound attenuation and dispersion using short time Fourier transform," *Ultrasonics,* vol. 43, pp. 375-381, 2005.

[102] N. M. Bilgutay, X. Li and J. Saniie, "Spectral analysis of randomly distribued scatterers for ultrasonic grain size estimation," *Ultrasonic,* vol. 27, no. 1, pp. 19-25, 1989.

[103] M. Le, J. Kim, S. Kim and J. Lee, "B-scan ultrasonic testing of rivets in multilayer structures based on short-time Fourier transform analysis," *Measurement,* vol. 128, no. 6, pp. 495-503, 2018.

[104] in *AWS D1.1:2010 - Structural Welding Code - Steel*, 22 ed., American Welding Society, 2010.

[105] A. L. Affolter, "Mechanical properties of low carbon martensite," 1971.

[106] EVRAZ North America, *CCT curve for L80 casing steel.*

[107] *PRCI Research Exchange Meeting,* Houston, TX: Pipeline Research Council International, 2017.

[108] *ASTM E562-11, Standard Test Method for Determining Volume Fraction by Systematic Manual Point Count,* West Conshohocken, PA: ASTM International, 2011.

[109] S. Morito, H. Tanaka, R. Konishi, T. Furuhara and T. Maki, "The morphology and crystallography of lath martensite in Fe-C alloys," *Acta Materialia,* vol. 51, pp. 1789-1799, 2003.

[110] S. H. He, B. B. He, K. Y. Zhu and M. X. Huang, "Evolution of dislocation density in bainitic steel: Modeling and experiments," *Acta Materialia,* vol. 149, pp. 46-56, 2018.

[111] T. K. Rawat, "Zero-Phase Filter," in *Digital Signal Processing*, New Delhi, Oxford University Press, 2015.

[112] P. D. Hodgson, K. M. Browne, R. K. Gibbs and T. T. Pham, "The mathematical modeling of temperature and microstruture during spray cooling," in *1st International conference of quenching and control of distortion, Quenching and distortion control*, Chicago, IL, USA, 1992.

[113] N. G. Shaposhnikov, A. V. Koldaev, A. I. Zaitsev, I. G. Rodionova, D. L. D'yakonov and N. A. Arutyunyan, "Features of titanium carbide precipitation in low-carbon high-strength steels microalloyed with titanium and molybdenum," *Metallurgist,* vol. 60, no. 7-8, pp. 810-816, 2016.

[114] C. Ledermueller, H. I. Pratiwi, R. F. Webster, M. Eizadjou, S. P. Ringer and S. Primig, "Microalloying effects of Mo versus Cr in HSLA steels with ultrasfine-grained ferrite microstructures," *Materials & Design,* vol. 185, pp. 1-12, 2020.

[115] E. J. Pavlina, C. J. Van Tyne and J. G. Speer, "Effects of combined silicon and molybdenum alloying on the size and evoluation of micralloy precipiates in HSLA steels containing niobium and titanium," *Materials Characterization,* vol. 102, pp. 35-46, 2015.

[116] G. F. Vander Voort, "Etching Isothermally Treated Steels," *Heat Treeating Progress,* vol. 1, 2001.

[117] P. K. Katiyan, S. Misra and K. Mondal, "Corrostion behavior of annealted steels with different carbon contents (0.002, 0.17, 0.43 and 0.7% C) in freely aerated 3.5% NaCl solution," *Journal of Materials Engineering and Performance,* vol. 28, no. 7, pp. 4041-4052, 2019.

[118] S. Morito, J. Nishikawa and T. Maki, "Dislocation density within lath martensite in Fe-C and Fe-Ni alloys," *ISIJ International,* vol. 43, no. 9, pp. 1475-1477, 2003.

[119] N. Gunkelmann, H. Ledbetter and H. M. Urbassek, "Experimental and atomistic study of the elastic properties of alpha' Fe-C matensite," *Acta Materialia,* vol. 60, no. 12, pp. 4901-4907, 2012.

[120] Y.-W. Chen, Y.-T. Tsai, P.-Y. Tung, S.-P. Tsai, C.-Y. Chen, S.-H. Wang and J.-R. Yang, "Phase quantification in low carbon Nb-Mo bearing steel by electron backscatter diffraction technique coupled with kernel average misorientation," *Materials Characterization,* vol. 139, pp. 49-58, 2018.

[121] G. Nolze, M. Jurgens, J. Olbricht and A. Winkelmann, "Improving the precision of orientation measurements from technical materials via EBSD pattern matching," *Acta Materialia,* vol. 159, no. 8, pp. 408-415, 2018.

[122] V. K. Gupta and S. R. Agnew, "A simple algorithm to eliminate ambiguities in EBSD orientation map visualization and analysis: Application to faitgue carck-tips/wakes in aluminum alloys," *Microscopy and Microanalysis,* vol. 16, no. 6, pp. 831-841, 2010.

[123] Y. J. Park and F. B. Fletcher, "Effects of manganese, chromium, and molybdenum on the isothermal transformation of austenite in eutectoid steels," *Journal of Heat Treating,* vol. 4, no. 3, pp. 247-252, 1986.

[124] M. Molero, I. Segura, S. Aparicio, M. G. Hernandez and M. A. G. Izquierdo, "On the measurement of frequency-dependent ultrasonic attenuation in strongly heterogeneous materials," *Ultrasonics,* vol. 50, no. 8, pp. 824-828, 2010.

[125] M. A. Zimmer, L. D. Bibee and M. D. Richardson, "Measurement of the frequency dependence of the sound speed and attenuation of seafloor sands from 1 to 400 kHz," *IEEE Journal of Oceanic Engineering,* vol. 35, no. 3, pp. 538-557, 2010.

[126] K. A. Wear, "The effects of frequency-dependent attenuation and dispersion on sound speed measurements: Applications in human trabecular bone," *IEEE Transactions on Ultrasonic, Ferroelectrics, and Frequency Control,* vol. 47, no. 1, pp. 265-273, 2000.

[127] A. A. Buenos, A. A. dos Santos Junior, A. R. Rodrigues and R. C. Tokimatsu, "Application of acoustoelasticity to measure the stress generated by milling in ASTM A36 steel plates," *Journal of the Brazilian Society of Mechanical Sciences and Engineering,* vol. 35, no. 4, pp. 525-536, 2013.

[128] J. R. Taylor, An Introduction to Error Analysis: The Study of Uncertainties in Physical Measurements, 2nd ed., University Science Books, 1992.

[129] S. Mariani, T. V. Nguyen, F. L. de Scalea and M. Fateh, "High speed non-contact ultrasonic guided wave inspections of rails," in *Proceedings of the 2014 Joint Rail Conference*, Colarado Springs, Co, 2014.

[130] M. Zhou, L. Du, Y. Zhao and X. Liu, "Microstructure characteristics and mechanical properties of X80 pipeline steels," *Journal of Wuhan University of Technology - Materials Science Edition,* vol. 27, no. 2, pp. 252-255, 2012.

[131] J. M. Radzikowska, "Metallography and Microstructure of Cast Iron," ASM International, Materials Park, Ohio.

[132] L. Zhang and D. C. Guo, "A general etchant for revealing prior-asutenite grain boundaries in steels," *Materials Characterization,* vol. 30, no. 4, pp. 299-305, 1993.

[133] R. A. Barros, A. J. Abdalla, H. L. Rodreques and M. d. S. Pareira, "Characterization of a AISI/SAE 4340 steel in different microstructural conditions," in *Materials Science Forum*, 2014.

[134] A. W. Orlowicz and M. Tupaj, "The effect of austenitizing conditions in the ductile iron hardeneing process on longitudinal ultrasonic wave velocity," *Metalugija,* vol. 53, no. 2, pp. 212-214, 2014.

[135] V. Ozkan, I. H. Sarpun, A. Erol and A. Yonetken, "Influence of mean grain size with ultrasonic velocity on microhardness of B4C-Fe-Ni composite," *Journal of Alloys and Compounds,* vol. 574, pp. 512-519, 2013.

[136] A. Popov, V. Kavardzhikov and D. Pashkouleva, "Non-destructive evaluation of the yield stress for low carbon steel by ultrasound measurements," *Russian Journal of Nondestructive Testing,* vol. 49, no. 6, pp. 328-333, 2013.

[137] E. Abbasi and W. M. Rainforth, "Microstructural evolution of Nb-V-Mo and V containing TRIP-assisted steels during thermomechanical processing," *Journal of Materials Science & Technology,* vol. 33, no. 4, pp. 311-320, 2017.

[138] T. N. Baker, "Processes, microstructure and properties of vanadium microalloyed steels," *Materials Science and Technology,* vol. 25, no. 9, pp. 1083-1107, 2009.

[139] M. O'Donnell, E. T. Jaynes and J. G. Miller, "Kramers-Kronig relationship between ultrasonic attenuation and phase velocity," *Journal of the Acoustical Society of America,* vol. 69, no. 3, pp. 696-701, 1981.

[140] O. Engler and V. Randle, "Introduction to Texture Analysis: Macrotexture, Microtexture, and Orientation Mapping," CRC Press, 2009, p. 362.

[141] X. Guo, "A statistical study on the relationship between tensile strength and ultrasonic velocity of cast iron," *International Journal of Cast Metals Research,* vol. 16, no. 1-3, pp. 221-225, 2003.

[142] P. Palanichamy, M. Vasudevan, T. Jayakumar, S. Venugopal and B. Raj, "Ultrasonic velocity measurements for characterizing the annealing behaviour of cold worked austenitic stainless steel," *NDT&E International,* vol. 33, no. 4, pp. 253-259, 2000.

[143] V. A. Lobodyuk, Y. Y. Meshkov and E. V. Pereloma, "On tetragonality of the martensite crystal lattice in steels," *Metallurgical and Materials Transactions A,* vol. 50, no. 1, pp. 97-103, 2019.

[144] D. Dragoni, D. Ceresoli and N. Marzari, "Vibrational and thermoelastic properties of bcc iron from selected EAM potentials," *Computational Materials Science,* vol. 152, pp. 99-106, 2018.

[145] G. R. Speich and W. C. Leslie, "Elastic constants of martensite," *Metallurgical Transactions,* vol. 4, no. 8, pp. 1873-1875, 1973.

[146] F. E. Stanke and G. S. Kino, "A unified theory for elastic wave propagation in polycrystalline materials," *The Journal of the Acoustical Society of America,* vol. 75, no. 3, pp. 665-681, 1984.

Appendices

A.1 Selected Tables of Values

This section shows the data for the ML80 subsized end quench specimen and Grade 483 Q&T full sized end quench specimens. The data pertains to specimens that were analyzed by metallography and by ultrasonic testing. Values from HRC measurements, HV measurements and data for disc samples not examined by UT or metallography are not included here.

A.1.1 ML80-S2 Values

Subsized specimen ML80-S2 was sectioned into disc samples (Section 3.2.4), which were examined using ultrasonic testing (Section 3.5.2) by longitudinal wave modes only. Hardness and microstructure fractions shown have been interpolated from other ML80 specimen data (Section 4.4.1).

Table A.1 – Data from disc samples of ML80-S2.

Disc Sample #	Thickness	Depth	Hardness	Interpolated Microstructure (%)			
	(mm) ± err.	(mm)	(HV 1/10)	M	B	P	F
1	2.353 ± 0.003	1.2	480	92	5	2	0
2	3.56 ± 0.01	4.9	389	37	36	28	0
3	5.115 ± 0.007	10.0	317	8	38	54	0

Table A.2 – Data from longitudinal wave mode measurements on disc samples of ML80-S2.

Disc Sample #	Peak Separation	Velocity	Amp. Atten.	Energy Atten.
	(μs) ± err.	(m/s) ± err.	(dB/mm) ± err.	(dB/mm) ± err.
1	0.794 ± 0.002	5929 ± 15	0.45 ± 0.08	0.37 ± 0.01
2	1.196 ± 0.003	5950 ± 23	0.26 ± 0.06	0.16 ± 0.08
3	1.717 ± 0.002	5957 ± 12	0.15 ± 0.04	0.10 ± 0.01

A.1.2 ML80-S5 Values

Subsized end quench specimen ML80-S5 was examined by metallographic methods to determine microstructure fraction of disc samples (Section 3.4), with data from Table A.3 shown graphically in the body of this work (Section 4.2.5).

Table A.3 – Microstructure fractions measurements from discs of ML80-S5.

Depth	Microstructure Fraction (% ± % Error)				
(mm)	Martensite	Bainite	Ferrite	Pearlite	Unknown
0.0	99±1	0±0	0±0	0±0	1±1
1.1	96±2	1±1	0±0	0±0	3±1
2.0	83±3	13±3	4±2	0±0	0±0
3.3	60±5	28±4	14±3	0±0	0±0
4.6	42±7	33±4	26±5	0±0	0±0
5.9	21±3	42±5	37±3	0±0	0±0
7.2	15±2	47±4	37±3	0±0	0±0
8.5	9±1	45±5	47±5	0±0	0±0
9.8	7±2	39±5	54±5	0±0	0±0
11.2	7±2	31±4	62±5	0±1	0±0
12.5	7±2	28±5	65±5	0±0	0±0

Table A.4 – Microhardness measurement results from specimen ML80-S5.

Disc Number	Depth (mm)	Appearance	Hardness (HV0.05/10)
1	0.0	Elongated needles	461
1	0.0	Elongated needles	473
1	0.0	No substructure	448
1	0.0	No substructure	462
6	5.9	Uniform dark	284
6	5.9	Uniform dark	292
6	5.9	Uniform light	242
6	5.9	Light grains	250
6	5.9	Uniform light	233
6	5.9	Uniform light	245
6	5.9	Light grains	265
11	12.5	Elongated	274
11	12.5	Blocky	224
11	12.5	Blocky	223
12	50	With substructure	227
12	50	No substructure	209
12	50	With substructure	226
12	50	No substructure	211

A.1.3 TCPL-S1 Values

Disc samples of Grade 483 Q&T full sized end quench specimen TCPL-S1 were examined by both ultrasonic longitudinal and shear wave modes (Sections 3.5.3 and 4.6). Due to the small spacing between backwall echoes there were no energy attenuation measurements performed on longitudinal wave signals from this specimen.

Table A.5 – General measurements from disc samples of Grade 483 Q&T specimen TCPL-S1. *Thickness values from first measurement

Disc Sample #	Thickness (mm) ± err.	Depth (mm)	Hardness (HV 1/10)
1	0.71 ± 0.02*	0.5	435
2	0.91 ± 0.06*	2.4	403
3	1.22 ± 0.05*	4.4	382
4	1.17 ± 0.06*	6.5	283
5	0.8 ± 0.01*	8.4	251
6	1.22 ± 0.03*	10.3	237
7	1.19 ± 0.01*	12.4	223

Table A.6 – Longitudinal ultrasonic data from disc samples of TCPL-S1.

Disc Sample #	Peak Separation (μs)	Velocity (m/s) ± err.	Amp. Atten. (dB/mm) ± err.
1	0.232	6161 ± 41	1.47 ± 0.1
2	0.301	6039 ± 91	0.60 ± 0.1
3	0.404	6014 ± 45	0.58 ± 0.04
4	0.388	6040 ± 50	0.54 ± 0.05
5	0.268	5962 ± 26	0.93 ± 0.04
6	0.406	6017 ± 31	0.66 ± 0.03
7	0.401	5946 ± 17	0.48 ± 0.01

Table A.7 – Shear wave data from disc samples of TCPL-S1.

Disc Sample #	Peak Separation (μs)	Velocity (m/s) ± err.	Amp. Atten. (dB/mm) ± err.	Energy Atten. (dB/mm) ± err.
1	0.428	3333 ± 50	1.04 ± 0.11	0.43 ± 0.07
2	0.557	3262 ± 87	0.56 ± 0.27	0.90 ± 0.09
3	0.742	3278 ± 56	0.62 ± 0.09	0.40 ± 0.02
4	0.715	3283 ± 70	0.87 ± 0.1	0.68 ± 0.06
5	0.489	3265 ± 19	0.55 ± 0.17	0.90 ± 0.02
6	0.745	3277 ± 39	0.45 ± 0.05	0.26 ± 0.03
7	0.733	3248 ± 17	0.42 ± 0.11	0.49 ± 0.03

A.1.4 TCPL-S3 Values

Grade 483 Q&T full sized end quench specimens were examined by metallographic analysis (Sections 3.4.2 and 4.2) and by ultrasonic testing (Sections 3.5.3 and 4.5) Due to the small spacing between backwall echoes, energy attenuation was not calculated for longitudinal wave modes from this specimen.

Table A.8 – Microstructure fraction and microstructure measurements from disc samples of TCPL-S3.

Depth	Hardness	Microstructure Fraction (% ± % Error)				
(mm)	(HV 1/10)	Martensite	Bainite	Ferrite	Pearlite	Unknown
0.0	447	100±0	0±0	0±0	0±0	0±0
1.1	419	99±0	0±0	0±0	0±0	1±0
1.9	408	93±2	4±2	0±0	0±0	2±1
4.1	371	78±2	17±3	6±3	0±0	0±0
6.2	280	35±5	49±3	17±5	0±0	0±0
7.5	290	26±6	61±8	13±2	0±0	0±0
8.2	250	24±3	54±4	22±7	0±0	0±1
9.5	253	17±2	56±4	27±3	0±0	0±0
10.3	237	13±3	35±4	52±4	0±0	0±0
12.3	223	11±2	30±5	59±5	0±0	0±0
14.4	245	10±2	26±5	63±7	0±0	0±0
16.4	232	8±3	26±6	66±5	0±0	0±0
18.4	217	8±1	16±6	75±6	1±1	0±0
20.7	204	7±2	9±4	84±5	0±1	0±0

Table A.9 – General information for disc samples from TCPL-S3.

Disc Sample #	Thickness (mm) ± err.	Depth (mm)	Hardness (HV 1/10)
1	0.96 ± 0.03	0.6	433
3	1.23 ± 0.03	6.8	285
4	1.21 ± 0.04	8.9	252
5	1.22 ± 0.04	10.9	233
6	1.19 ± 0.02	13.0	230
7	1.19 ± 0.03	15.0	241
8	1.18 ± 0.04	17.0	227
9	1.23 ± 0.05	19.2	213
10	0.93 ± 0.06	21.3	204

Table A.10 – Data from longitudinal wave mode testing on TCPL-S3.

Disc Sample #	Peak Separation (µs)	Velocity (m/s) ± err.	Amp. Atten. (dB/mm) ± err.
1	0.310	6167 ± 30	0.69 ± 0.03
3	0.412	5978 ± 22	0.52 ± 0.02
4	0.405	5957 ± 26	0.47 ± 0.02
5	0.409	5970 ± 26	0.45 ± 0.02
6	0.399	5957 ± 17	0.56 ± 0.02
7	0.402	5920 ± 27	0.62 ± 0.03
8	0.395	5994 ± 28	0.50 ± 0.02
9	0.414	5926 ± 37	0.56 ± 0.04
10	0.311	5967 ± 51	0.68 ± 0.05

Table A.11 – Data from shear wave mode testing of TCPL-S3.

Disc Sample #	Peak Separation (μs)	Velocity (m/s) ± err.	Amp. Atten. (dB/mm) ± err.	Energy Atten. (dB/mm) ± err.
1	0.571	3351 ± 38	0.98 ± 0.15	1.24 ± 0.1
3	0.755	3259 ± 32	0.52 ± 0.11	0.66 ± 0.04
4	0.742	3251 ± 37	0.41 ± 0.13	0.67 ± 0.04
5	0.749	3259 ± 39	0.30 ± 0.13	0.58 ± 0.05
6	0.732	3243 ± 24	0.35 ± 0.13	0.67 ± 0.03
7	0.735	3237 ± 41	0.59 ± 0.16	1.02 ± 0.04
8	0.724	3270 ± 41	0.37 ± 0.11	0.61 ± 0.04
9	0.761	3229 ± 58	0.54 ± 0.13	0.79 ± 0.06
10	0.570	3254 ± 79	0.59 ± 0.13	0.91 ± 0.03

Table A.12 – Microhardness results from specimen TCPL-S3.

Disc Number	Depth (mm)	Appearance	Hardness (HV0.05/10)
1 – Quench side	0.0	Elongated needles	458
1 – Quench side	0.0	Elongated needles	448
1 – Quench side	0.0	No substructure	453
1 – Quench side	0.0	No substructure	439
4 – Quench side	8.9	Featureless	233
4 – Quench side	8.9	Featureless	228
4 – Quench side	8.9	Dark	256
4 – Quench side	8.9	Dark	254
4 – Quench side	8.9	Network of grains	245
4 – Quench side	8.9	Network of grains	242
10	20.7	Uniform light	207
10	20.7	Uniform light	203
10	20.7	Dark features	247
10	20.7	Dark features	223
11	50	Uniform light	137
11	50	Uniform light	149
11	50	Uniform light	167
11	50	Grain network	236
11	50	Grain network	204
11	50	Grain network	218

A.1.5 TCPL-S8 Values

Ultrasonic measurements were taken in the radial direction on Grade 483 Q&T end quench specimen TCPL-S8 (Section 3.5.3). Only longitudinal wave mode data was collected for this specimen (Section 4.5).

Table A.13 – General information for Grade 483 Q&T specimen TCPL-S8.
Microstructure data has been interpolated (Section 4.2.5).

Depth	Thickness	Probe	Hardness	Interpolated Microstructure (%)			
(mm)	(mm) ± err.		(HV 1/10)	M	B	P	F
2	22.3805 ± 0.0007	V203-RM	416	97	1	0	0
4	22.3915 ± 0.0005	V203-RM	356	81	14	5	0
6	22.4040 ± 0.0002	V203-RM	299	32	53	16	0
8	22.4130 ± 0.0005	V203-RM	265	19	55	25	0
10	22.4305 ± 0.0006	V203-RM	250	13	35	52	0
15	22.4390 ± 0.0004	V203-RM	232	11	30	59	0
20	22.4605 ± 0.0006	V203-RM	210	10	26	63	0
4	22.3915 ± 0.0005	V202-RM	360	81	14	4	0
6	22.4040 ± 0.0002	V202-RM	307	37	47	16	0
8	22.4130 ± 0.0005	V202-RM	272	22	55	23	0
10	22.4305 ± 0.0006	V202-RM	252	13	38	49	0
15	22.4390 ± 0.0004	V202-RM	237	11	31	58	0
20	22.4605 ± 0.0006	V202-RM	210	10	26	63	0
30	22.4735 ± 0.0003	V202-RM	--	--	--	--	

Table A.14 – Ultrasonic data from longitudinal wave mode testing on TCPL-S8.

Depth	Probe	Peak Separation	Velocity	Amp. Atten.	Energy Atten.
(mm)		(μs)	(m/s) ± err.	(dB/mm) ± err.	(dB/mm) ± err.
2	V203-RM	7.578	5906.7 ± 0.2	0.25 ± 0.05	0.173
4	V203-RM	7.580	5908.4 ± 0.4	0.13 ± 0.11	0.072
6	V203-RM	7.586	5906.8 ± 0.2	0.12 ± 0.03	0.073
8	V203-RM	7.586	5909.2 ± 0.2	0.11 ± 0.05	0.112
10	V203-RM	7.586	5913.9 ± 0.3	0.10 ± 0.05	0.060
15	V203-RM	7.588	5914.7 ± 0.2	0.11 ± 0.04	0.109
20	V203-RM	7.591	5917.7 ± 0.1	0.16 ± 0.03	0.063
4	V202-RM	7.580	5908.4 ± 0.1	0.11 ± 0.04	0.126
6	V202-RM	7.583	5908.9 ± 0.2	0.13 ± 0.04	0.069
8	V202-RM	7.582	5912.5 ± 0.2	0.14 ± 0.04	0.123
10	V202-RM	7.583	5916.0 ± 0.2	0.12 ± 0.04	0.068
15	V202-RM	7.585	5916.9 ± 0.2	0.15 ± 0.03	0.113
20	V202-RM	7.588	5920.4 ± 0.1	0.09 ± 0.01	0.061
30	V202-RM	7.592	5920.1 ± 0.1	--	--

A.2 Velocity Calculations

This appendix section shows example calculations from theoretical estimates of ultrasonic longitudinal velocity. The methods used to calculate ultrasonic velocity from ultrasonic time-domain signals is also presented, as is the method for calculation error values for velocity measurements. Velocity calculations from ultrasonic signals and velocity error calculations are used for all velocity measurements made in this work, based on measured ultrasonic signals.

A.2.1 Velocity Calculations from Ultrasonic Theory

Estimates of ultrasonic velocity can be obtained from literature results. Equation 2.4 can be used to estimate longitudinal velocity and Equation 2.5 can be used to estimate shear velocity for materials where the Poisson's ratio, density and Young's modulus is known. Sample calculations of longitudinal velocity are shown below. Values of Young's modulus, (E, in kg/ms^2), density (ρ, in kg/m^3) and Poisson's ratio (ν) are taken from Table 2.2.

$$V_L = \sqrt{\frac{E}{\rho}\frac{(1-\nu)}{(1+\nu)(1-2\nu)}}, \qquad \text{(Reference to Equation 2.4)}$$

$$V_L = \sqrt{\frac{203.5\,\frac{kg}{ms^2}}{7690\,\frac{kg}{m^3}}\frac{(1-0.2921)}{(1+0.2921)(1-2*0.2921)}},$$

$$V_L = 5905\,\frac{m}{s},$$

Sample calculations for shear velocity for martensitic steel is shown below. Values of Young's modulus, (E, in kg/ms^2), density (ρ, in kg/m^3) and Poisson's ratio (ν) are taken from Table 2.2.

$$V_T = \sqrt{\frac{E}{2\rho}\frac{1}{1+\nu}}, \qquad \text{(Reference to Equation 2.4)}$$

$$V_T = \sqrt{\frac{203.5\,\frac{kg}{ms^2}}{2*7690}\frac{1}{1+0.2921\,\frac{kg}{m^3}}},$$

$$V_T = 3200\,\frac{m}{s},$$

A.2.2 Velocity Calculations from Ultrasonic Signals

Calculation of ultrasonic velocity relies on measurement on the time separation between adjacent backwall echoes from the ultrasonic signal collected through a sample. The time difference between echoes is measured using the time difference between adjacent peaks, as shown in Equation A.1:

$$t_{pk-pk} = \frac{1}{N}\sum_{n=1}^{N} t_{n+1} - t_n, \qquad \text{(Equation A.1)}$$

where $t_{pk\text{-}pk}$ is the average peak to peak time difference calculated from N+1 echoes. Time measurements t_n and t_{n+1} are the peak times of signal echoes n and n+1. Error in peak to peak time, $\sigma_{pk\text{-}pk}$ is given by the standard deviation of echo separation, shown in Equation A.2:

$$\sigma_{pk-pk} = \sqrt{\sum \frac{((t_{n+1} - t_n) - t_{pk-pk})^2}{N}} \qquad \text{(Equation A.2)}$$

Five longitudinal mode signals and two shear mode signals were captured for each coin sample of Grade 483 Q&T fitting steel. Three longitudinal wave signals were captured for each ML80 disc. Since ultrasonic testing is conducted in pulse-echo mode, ultrasonic echoes have been reflected off the sample backwall. Each signal pulse has travelled twice the sample thickness. Using the average peak-to-peak time calculated for a sample and wave mode, ultrasonic velocity, v_i (in m/s) is calculated according to Equation A.3:

$$v_i = \frac{d_i}{2\left(\overline{t_{pk-pk}}\right)_i} \qquad \text{(Equation A.3)}$$

where d_i is the sample thickness (in m) and $\left(\overline{t_{pk-pk}}\right)_i$ is the average peak-to-peak time for the sample (in seconds). The denominator factor of 2 comes from the passage of the wave through the sample twice. All calculations were performed and stored in MATLAB.

A.2.3 Error Calculations for Velocity Measurements

When measuring the velocity of ultrasonic waves there are two main sources of error. The first is from the thickness of the sample, based on the region that the wave may be passing through. The second is from the range of peak separations that are found during signal analysis, discussed in the previous section. Error values are added in quadrature[1], as can be seen in Equation A.4:

[1] Taylor, John R., "An Introduction to Error Analysis, 2nd Edition," Chapter 3: Propagation of Uncertainty, pp. 76, University Science Books, Colorado, 1997

$$\Delta v = \sqrt{\left(\frac{\partial v}{\partial d}\Delta d\right)^2 + \left(\frac{\partial v}{\partial t}\Delta t\right)^2}, \quad \text{(Equation A.4)}$$

where Δv is the error in velocity calculation, $\frac{\partial v}{\partial d}$ and $\frac{\partial v}{\partial t}$ are the error contributions of thickness and peak separation, respectively, and Δd and Δt are the thickness and peak separation uncertainty values.

A.2.4 Frequency Dependence of Ultrasonic Velocity

For determining the effect of changing frequency on velocity, it is useful to consider the dispersion relation resulting from the theoretical analysis of wave propagating in crystal structures. In this framework, atoms are considered as a network of masses, connected to neighboring atoms by massless springs[1], shown in Figure A.1. Periodic boundary conditions are applied, making the left and right-side boundaries form a continuous loop.

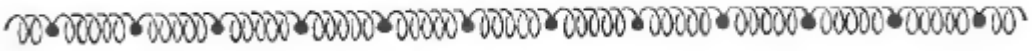

Figure A.1 – A 1-dimensional mass-and-spring network, used with periodic boundary conditions allows theoretical estimation of wave behaviour in solids[1].

The motion of the atoms can be determined by solving the equation of motion, where potential energy is a measure of the extension of the springs joining atoms, as,

$$F = ma = -Kx, \quad \text{(Equation A.5)}$$

where m (in kg) is the mass of the atom, a (in m/s^2) is the acceleration, K is the spring constant (in N/m) and x is the displacement of the atom from equilibrium. Such a system has, as a solution, an oscillatory motion of atoms[1]. The solution to this system is commonly expressed in angular frequency, ω (in Hz), whose relationship to frequency, f (also in Hz), is shown in Equation A.6:

$$\omega = 2\pi f, \quad \text{(Equation A.6)}$$

Angular frequency is expressed as a function of the wavenumber, k (in m^{-1}), whose relationship to the wavelength is given by Equation A.7:

$$k = \frac{2\pi}{\lambda}, \quad \text{(Equation A.7)}$$

where λ is the wavelength (in m). In the system described above, the motion of waves is governed by ω(k), which can be seen in Figure A.2. For small k values (i.e. large wavelengths), the

[1] Ashcroft, Neil W., Mermin, N. David, *Solid State Physics,* Saunders College Publishing, 1976

relationship decreases linearly. The largest wavenumber corresponds to wavelengths of *2a*, where a is the distance between neighboring atoms.

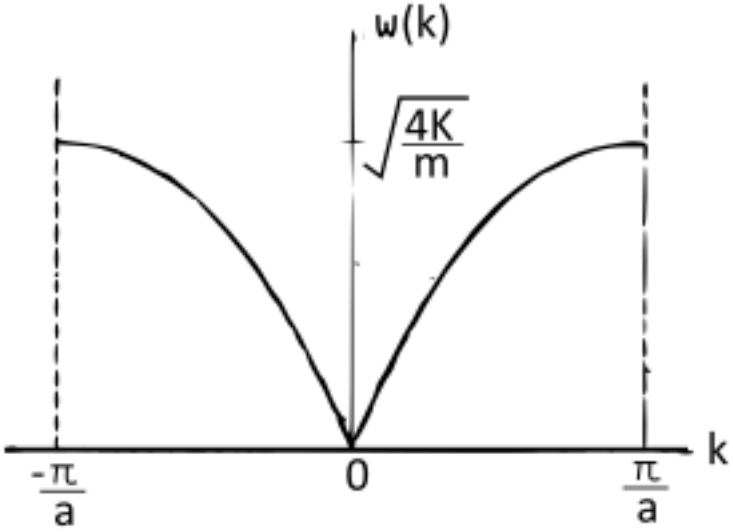

Figure A.2 – The dispersion relation, showing the relationship between angular frequency and wave number from the 1D model from Figure A.1[1].

The dispersion relation can be extended to three dimensions, where additional complexity is added in the form of an additional branch, called the optical branch, and with additional wave modes[1]. Additional complexity can also be introduced through the potential energy between interacting particles[1]. Figure A.3 shows the dispersion relation for germanium, showing (in ascending frequency) the transverse acoustic, longitudinal acoustic, longitudinal optical and transverse optical branches. The optical branch is not important for the work discussed here and will not be discussed in any further detail. It is important to note that for very large wavelengths, the acoustic branch always has a linear relationship with frequency[2]. This is important because of the relation formed by the slope of the dispersion relation gives the velocity of the acoustic wave for a given frequency and wavelength, as shown in Equation A.8.

$$V = \frac{\omega}{k} = f\lambda, \qquad \text{(Equation A.8)}$$

where f is the frequency, in Hertz, which is equal to s^{-1} and wavelength has units of m. The linearity of the acoustic wave branch at large wavelengths means that frequency dependant velocities are not observed, based upon the theory of phonon dispersion. It has been stated from

[1] Ashcroft, Neil W., Mermin, N. David, *Solid State Physics,* Saunders College Publishing, 1976
[2] Kittel, Charles, *Introduction to Solid State Physics*, John Wiley & Sons Inc, 2005, 8th Ed., pp 94

the literature that wave velocities in steel are approximately 5900 m/s,[1] and frequencies near 10 MHz are common in ultrasonic testing. From Equation A.8 it can be concluded that wavelengths in steel are approximately 0.59 mm long, which is several orders of magnitude larger than interatomic spacings. We therefore would conclude that ultrasonic waves fall well within the bounds of very large wavelengths from the standpoint of phonon dispersion.

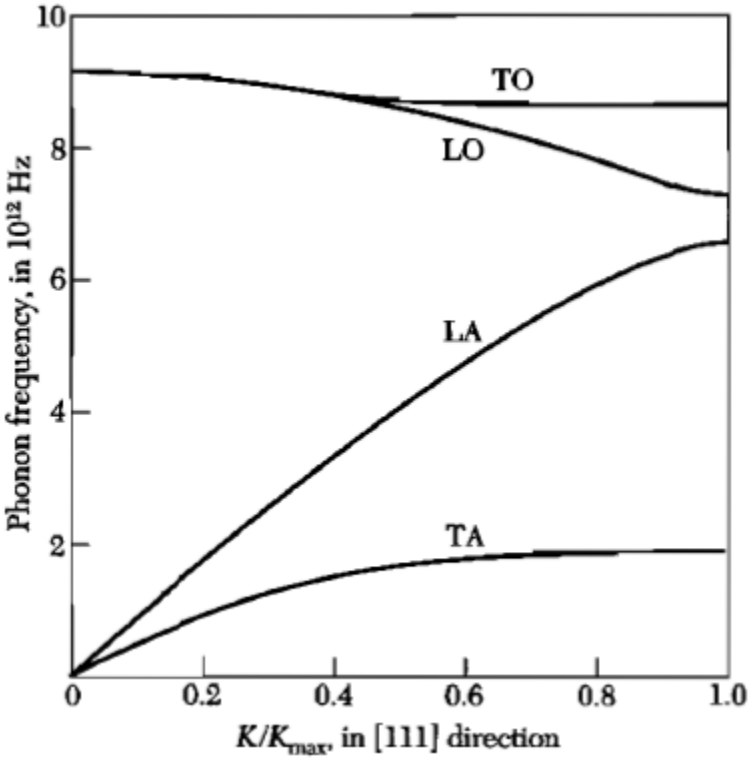

Figure A.3 – A dispersion curve for germanium, showing the transverse (T) and longitudinal (L) branches for both the acoustic (A) and optical (O) wave modes[2].

Minkiewicz et al.[3] measured the phonon dispersion in a single crystal ferrite sample by neutron scattering. A dispersion curve of similar shape to that observed in Figure A.3 was obtained for iron, further supporting the hypothesis that no frequency dependence would be observed in wave velocities used for ultrasonic testing.

[1]Hamidnia, M., Honarvar, F., Measurement of elastic properties of AISI 52100 alloy steel by ultrasonic nondestrucctive methods*, Journal of Mechanics of Materials and Structures*, pp 951-961, 2012

[2] Kittel, Charles, *Introduction to Solid State Physics*, John Wiley & Sons Inc, 2005, 8th Ed., pp 94

[3] V. J. Minkiewicz, G. Shirane, R. Nathans, Phonon dispersion relation for iron, Physical Review, 1967, pp 538-541

A.3 Attenuation Calculations

Ultrasonic peak amplitudes, used for amplitude attenuation calculations, and backwall echo energies, used for energy attenuation calculations, follow a similar mathematical form. They behave as exponential decay functions, as seen in Equation A.9:

$$y = ae^{-bt}, \qquad \text{(Equation A.9)}$$

Where t and y are the abscissa and ordinate, a and b are constants and e≈2.718 (Euler's number). A linear transformation is used to change the x-variable from the time-domain to the spatial-domain. Each point in the spatial domain represents the distance travelled by the ultrasonic pulse. The transformation yields a new exponential decay function, seen in Equation A.10:

$$y = ce^{-dx}, \qquad \text{(Equation A.10)}$$

where x is the new abscissa, and c and d are the new constants. Figure A.4 shows an example of the change of basis, where a sample thickness of 0.714 mm is used.

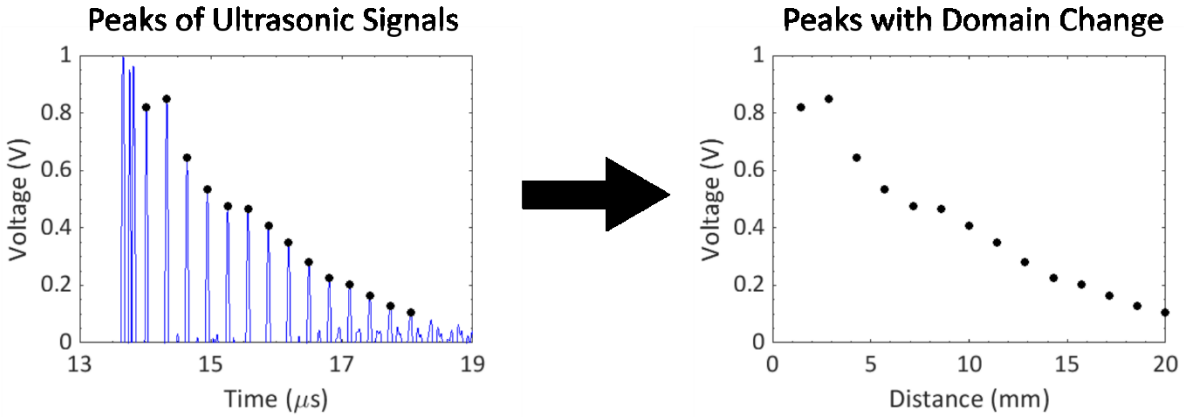

Figure A.4 – Calculation of attenuation requires converting from time to distance travelled by the wave. Both domains cause peaks to behave as decaying exponential functions.

Equation A.10 can be linearized by taking the natural logarithm of each side, as shown in Equation A.11:

$$ln(y) = ln(c) - dx \qquad \textit{(Equation A.11)}$$

A linear least squares regression is applied to ln(y) and x to determine the constant d, which represents the slope of the linearized equation, Equation A.11. The constant d is the attenuation coefficient from Equation A.10. The attenuation is the total fraction of y (from Equation A.9) by which the curve decreases for each unit of distance. The linear fit of Equation A.11, along with

the attenuation fit, is shown in Figure A.5. The attenuation, with units of $[x]^{-1}$ is determined using Equation A.12:

$$A = \exp(d) \qquad \text{(Equation A.12)}$$

From this value, the attenuation in decibels can be determined using Equation A.13:

$$A_{dB} = 20\log_{10}(A) \qquad \text{(Equation A.13)}$$

Note that this is the method used for all attenuation calculations in this work. The standard method of attenuation calculation using two peak amplitudes (Section 3.6.2) is included only for completeness, but cannot be applied to signals with more than two peaks. The standard attenuation method was developed prior to the use of digital signal storage and the ability to programmatically measure multiple peaks from the ultrasonic signal.

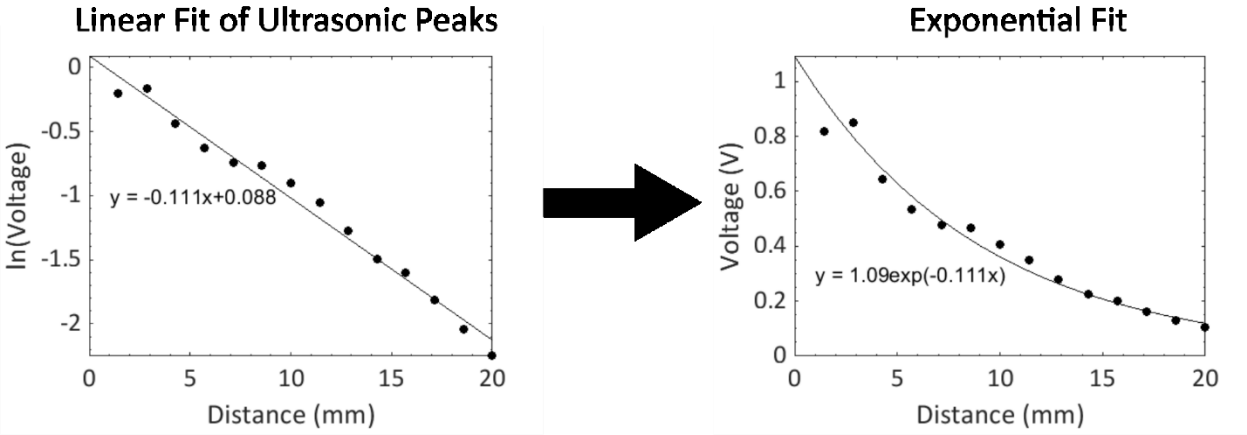

Figure A.5 – Fitting of the linearized equation can be converted to an exponential decay to give the best attenuation information.

A.3.1 Error Calculations for Attenuation Measurements

Calculation of error values for attenuation measurements is undertaken by using the standard method for linear regression, yielding an error value, d_{error} with units of $[x]^{-1}$. Since this method uses a non-linear conversion, maximum and minimum error values must be determined independently using Equation A.14:

$$A_{error} = exp\,(d \pm d_{error}) \qquad \textit{(Equation A.14)}$$

The attenuation values A_{error} can then be transformed into a decibel scale using Equation A.13.

A.4 Microstructure Analysis

This section shows micrographs from metallography and analysis of a CCT diagram from a steel with similar chemistry to the Grade 483 Q&T steel used in this work. The analysis of both show that the quenched ends of ML80 subsized specimen ML80-S5 and Grade 483 Q&T specimen TCPL-S3 are strongly dominated by the presence of martensite.

A.4.1 Examples of Micrograph Point Counts

Examples of micrographs with labelled intersections points are shown for subsized end quench specimen ML80-S5, Discs 4 (Figure A.6) and 8 (Figure A.7). Disc 4 was located at a depth of 3.3 mm from the quenched end of the specimen and Disc 8 was located at a depth of 8.5 mm. Labels are placed above their locations. Intersection points with two labels, separated by a slash, indicate points for which two possible options were considered equally likely. In those cases, a half a point is awarded to each of the microstructures in question.

In Figure A.6, martensite regions were identified by the darker brown appearance and the absence of visible internal features. At many intersection points it was unclear if internal structure was present, and judgement was used along with image magnification to determine the microstructure category. Lighter grains were identified as either bainite or ferrite and observation of the grain morphology was used to identify the microstructure. Grains with elongated shapes and overlapping grains were categorized as bainite, while regions with blocky shapes and uniform surfaces were classified as ferrite. The use of CCT curves was also used to help determine the microstructures that are expected in each disc sample.

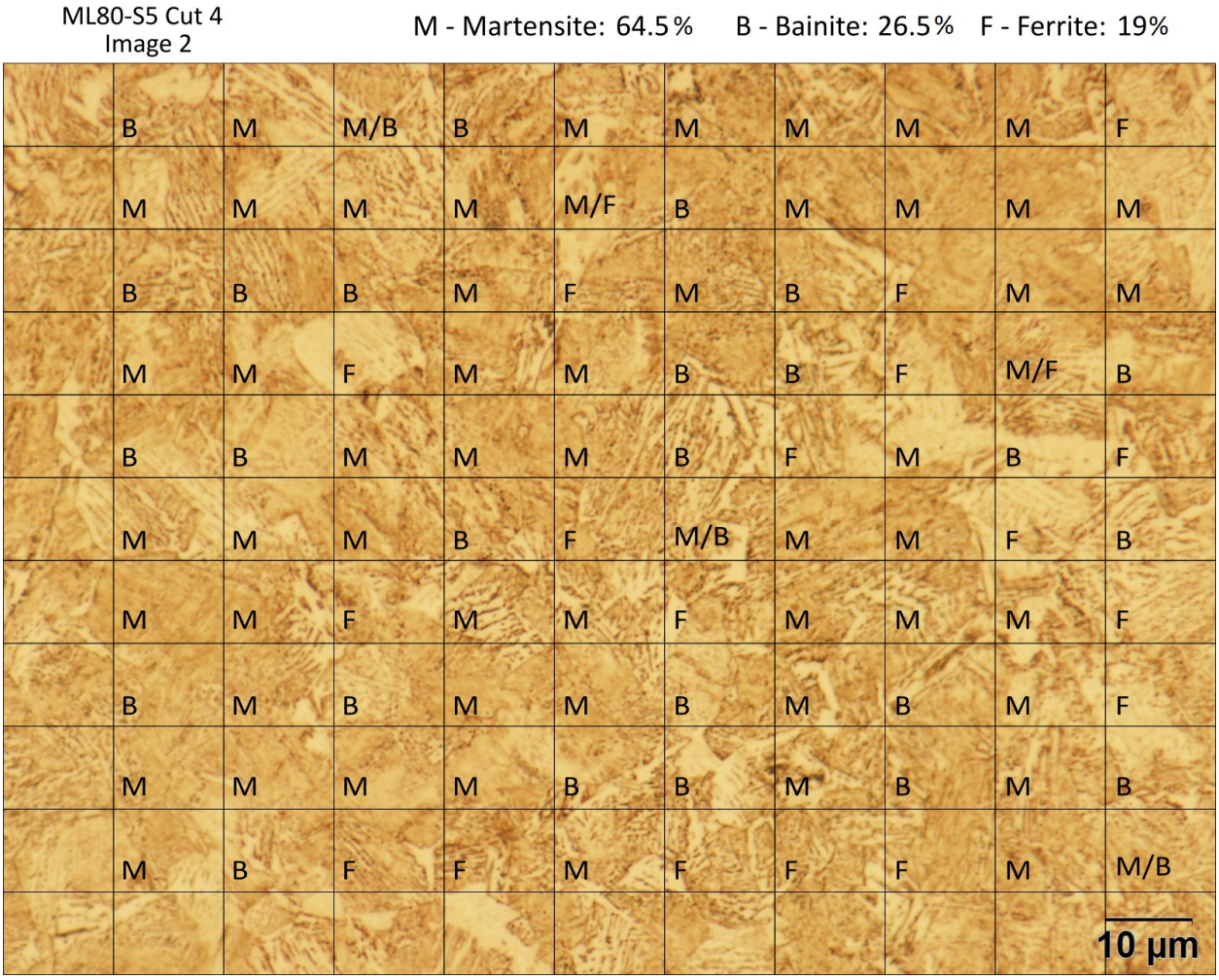

Figure A.6 – A labelled micrograph from Disc 4 of ML80-S2, with microstructure determine at 100 grid points, with the percentage of each microstructure from the image shown above.

Figure A.7 contains only a small fraction of points falling on dark brown regions, which appear in much smaller formations than was seen for Disc 4 (Figure A.7). A CCT curve for a steel similar to ML80 steel (Section 3.1.1) was used to help identify microstructures. No intersection points were identified as pearlite in the micrograph in Figure A.7. Bainite and ferrite were distinguished by the morphology of the light brown grains that constitute each of the microstructure. Bainite was identified by the appearance as a network of grains chaotically organized and appearing to have straight boundaries, giving an elongated appearance to each grain. Ferrite was identified by a less elongated shape, and the appearance of clusters of grains which did not appear to be formed into a network.

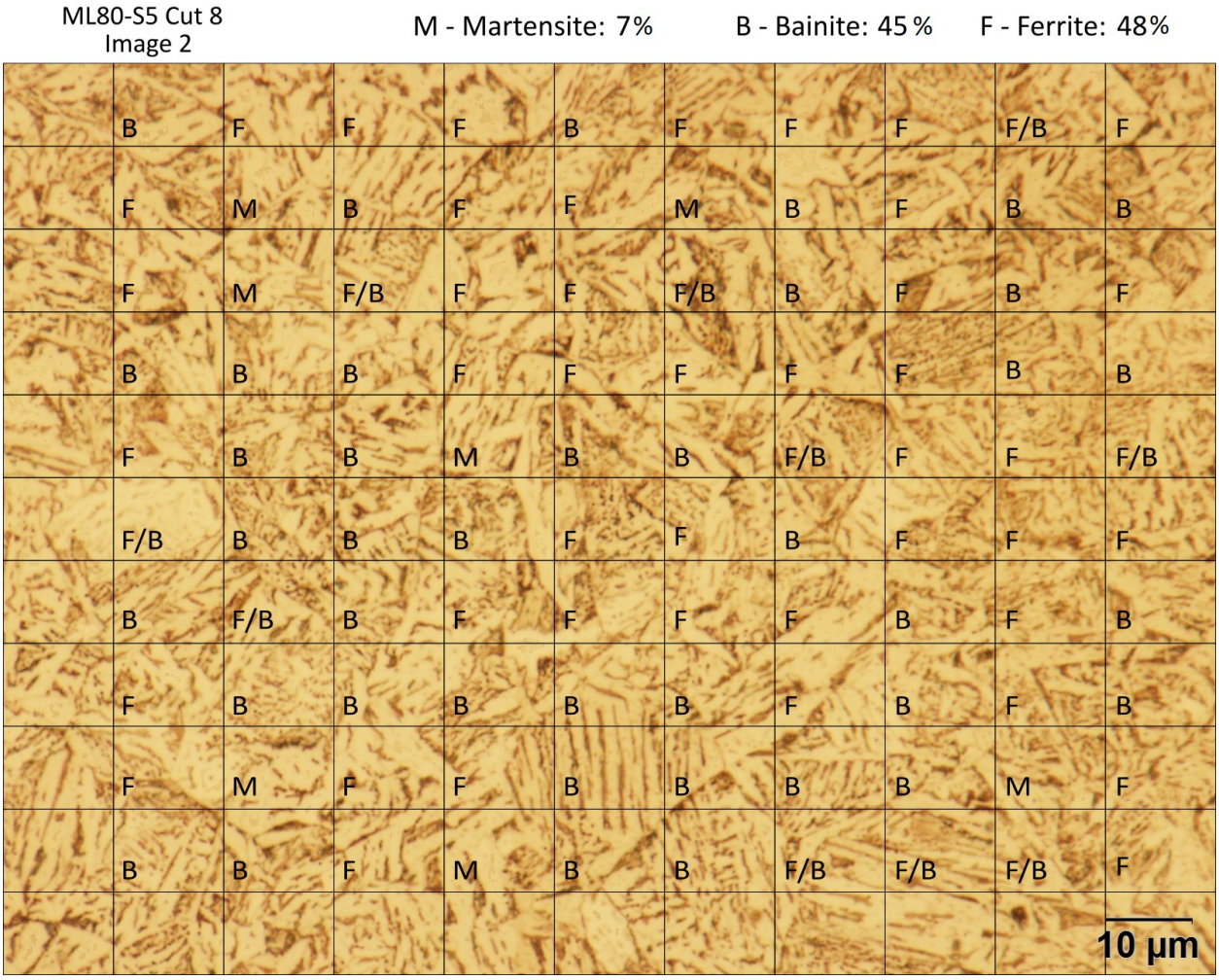

Figure A.7 – A labelled micrograph from Disc 8 of specimen ML80-S2.

Figure A.8 and Figure A.9 show micrographs of full sized specimen TCPL-S3, disc 3 and disc 6, respectively. Disc 3 was 6.2 mm from the quenched end of the specimen while disc 6 was 12.3 mm from the quenched end of the specimen. A transition can be seen from primarily martensite and bainite to primarily bainite and ferrite. Neither image has an example of pearlite at a line intersection point or of an unknown microstructural feature.

In Figure A.8, martensite was identified by the dark brown colour, resulting from the tint etchant used. Lighter regions were identified as bainite or ferrite depending on the morphology of the grains. Light coloured grains were identified as bainite when thin, elongated grains were grouped together into larger networks. Bainite grains in Disc 3 were arranged in parallel groups as well as in chaotic patterns. Ferrite was identified by polygonal shapes with smaller aspect ratios. The absence of lamellar structures, as well as the use of a CCT curve (Figure 3.5) helped to determine that pearlite was not present in the microstructure shown in Figure A.8. Brown grain boundaries

occasionally occurred within light coloured grains and made identification of some intersection points uncertain.

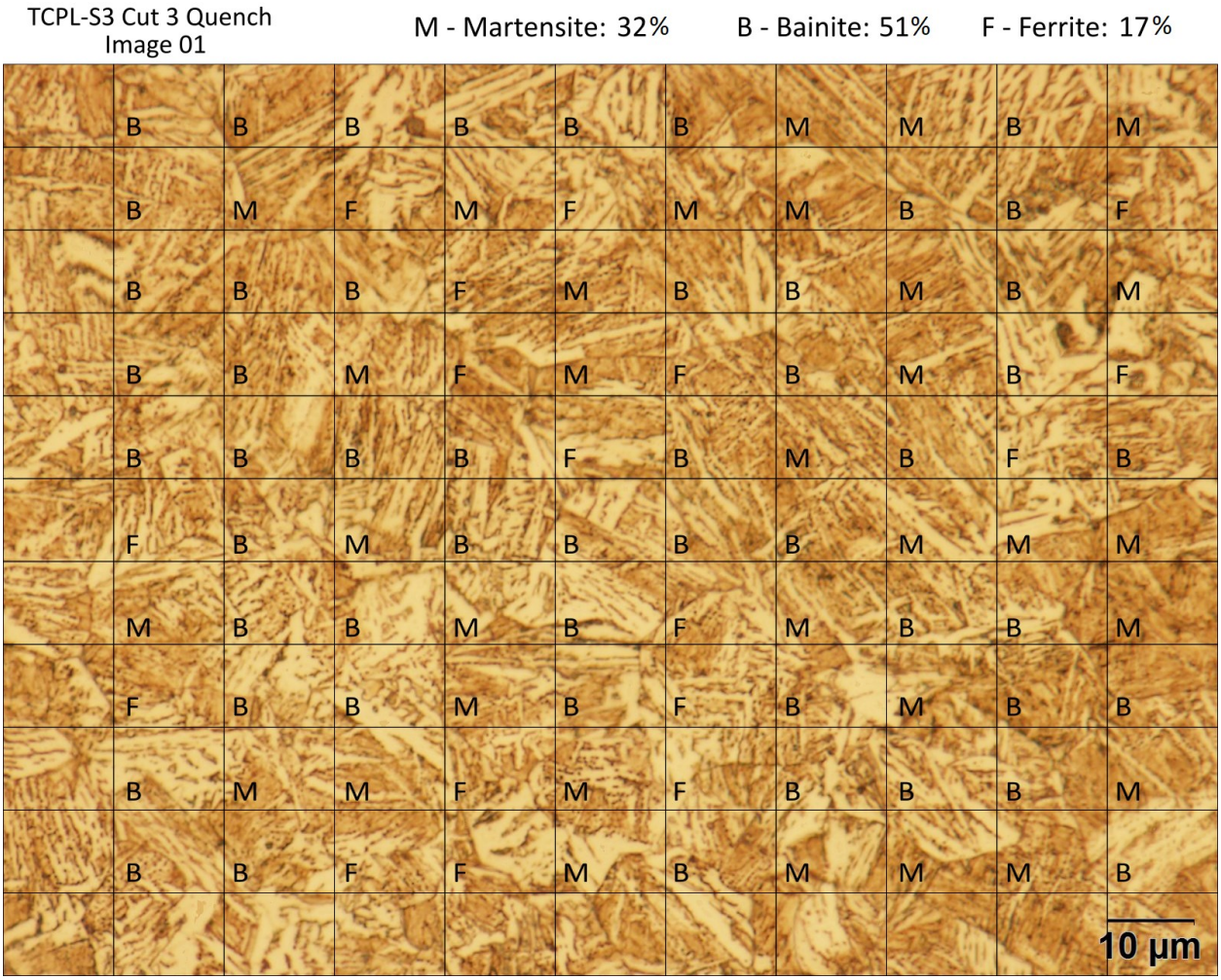

Figure A.8 – A labelled micrograph from the quench face of Disc 3 from specimen TCPL-S1.

In Figure A.9, fewer dark regions are seen, producing a smaller martensite fraction. Smaller dark brown regions were found when compared to disc samples closer to the quenched end of the specimen. These were identified as martensite. Large light grains were observed and using the same rules as above were identified as either bainite or ferrite. Lamellar structures were absent from the microstructure in Figure A.9, leading to an absence of pearlite in the final microstructure fraction.

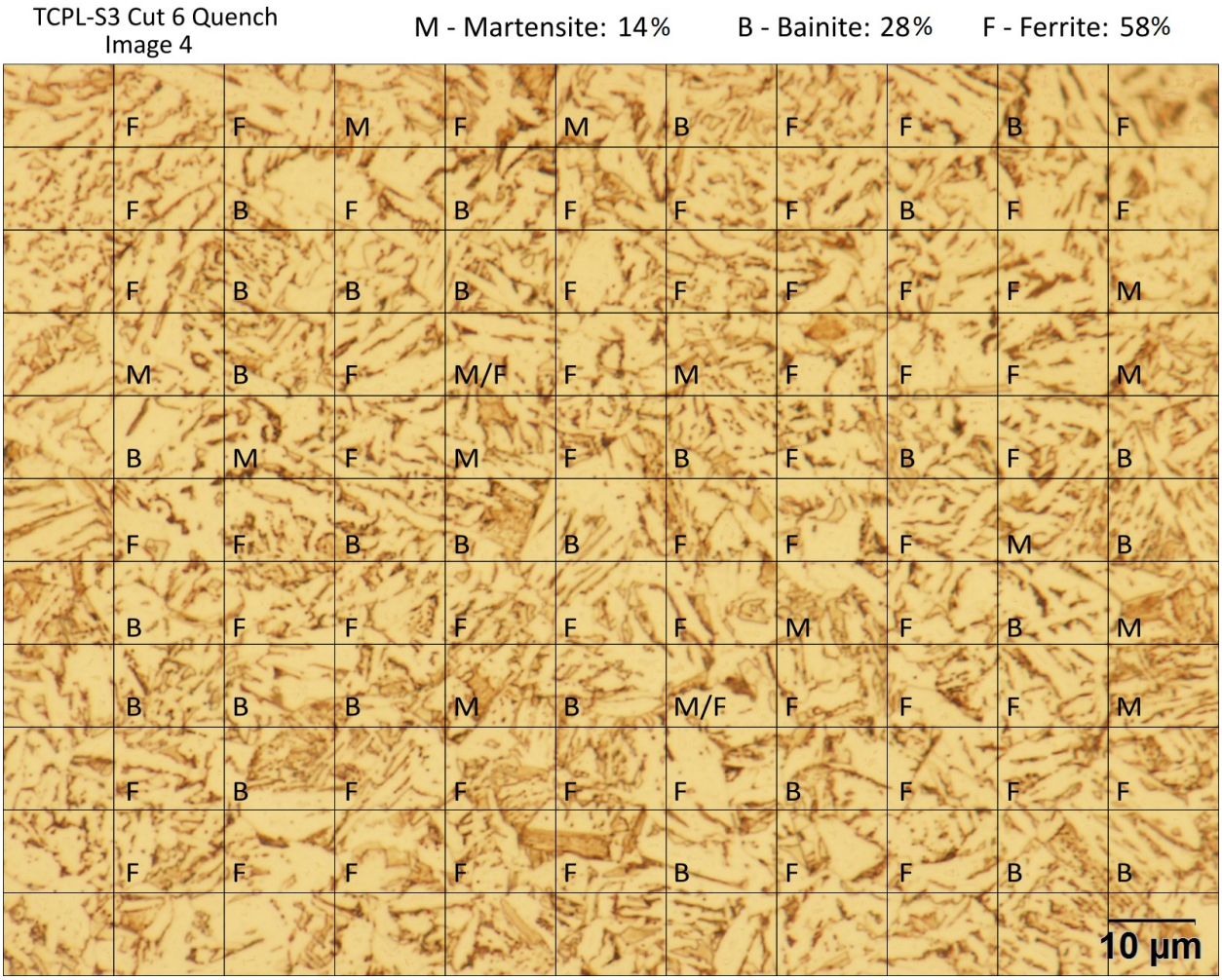

Figure A.9 – A labelled micrograph from Disc 6 of specimen TCPL-S1.

A.4.2 Martensitic Portions of Grade 483 Q&T Steel

The difficulty in distinguishing martensite and bainite by grain morphology led to additional etching tests to ensure that the quenched end of Jominy specimens were composed of martensite, as assessed during microstructure counting. Figure A.10 shows micrographs of Grade 483 Q&T full sized specimen TCPL-S3 at the quenched end (Figure A.10a) and at 10.9 mm from the quenched end (Figure A.10b). Both micrographs were taken after submerging and agitating for 3 minutes with Picral, without the use of a wetting agent, with an identical procedure for both. Figure A.10a only shows a weak trace of the microstructure, with a randomly oriented pattern of small features. Figure A.10b shows stronger microstructural features, with some blocky regions outlined by a dark etching pattern.

The difference between the micrographs in Figure A.10 can be explained by the presence of martensite at the quenched end of the specimen. Picral has a poor ability to reveal martensite,

causing less effect after etching than for other microstructures[1]. At the quenched end (Figure A.10a) of the specimen containing martensite, very little microstructure is revealed after a lengthy etch time, while at a depth of 10.9 mm (Figure A.3b) distinct microstructure features can be seen. The poor ability of Picral to reveal martensite, the small effect the etchant had on the quenched end of the specimen and the expectation of hard microstructures (such as martensite) at the quenched end provide evidence that the quenched end of both ML80 and Grade 483 Q&T end quench specimens contain large fraction of martensite.

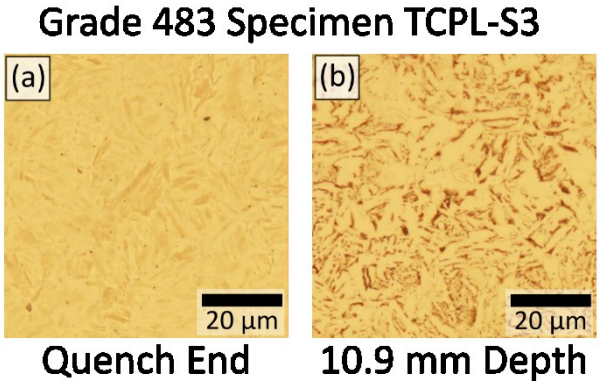

Figure A.10 – Two Grade 483 Q&T steel coins after 3 minutes of picral etching, (a) showing only faint microstructural features at the quenched end, compared to (b) more distinct features.

A etching test using Picral was undertaken on ML80 subsized end quench specimen ML80-S5, with identical results. As this test was performed only to help establish a choice for an etching process, optical micrographs from Picral ethcing of ML80-S5 were not kept at the time of investigation and are not shown here.

[1] Vander Voort, George F., "Etching Isothermally Treated Steels," *Heat Treating Progress*, 2001, and Radzikowska, Janina M., "Metallography and Microstructure of Cast Iron," *ASM International*, Materials Park, Ohio

A.5 EBSD

EBSD data can be seen for ML80 subsized end quench specimens, at the quench face and in the axial direction, in Figures A.11a-c and Figures A.11d-f respectively. Band contrast (a and e), inverse pole figure orientation maps (b and f), and inverse pole figures (IPF) (c and g) are shown. In the radial direction of specimen ML80-S7, the band contrast map (Figure A.11a) shows thin elongated grains. No preferred orientation of grains is visible. This is supported by the IPF orientation map and IPFs (Figure A.11b and c, respectively). In the axial direction for ML80 subsized specimen ML80-S7, the band contrast map (Figure A.11d) shows elongated grains of a similar scale to the quench face (Figure A.11a). The IPF orientation map (Figure A.11e) shows that many of the grains are organized into packets of similar orientation. The IPF shows no overall preferred orientation (Figure A.11f), with grain orientations being scattered throughout the projection sphere. Color in Figures A.11 b,c,e and f are used to help visually differentiate grain groupings where the same crystallographic orientation is found. The color is determined automatically using a mapping from the crystallographic angle.

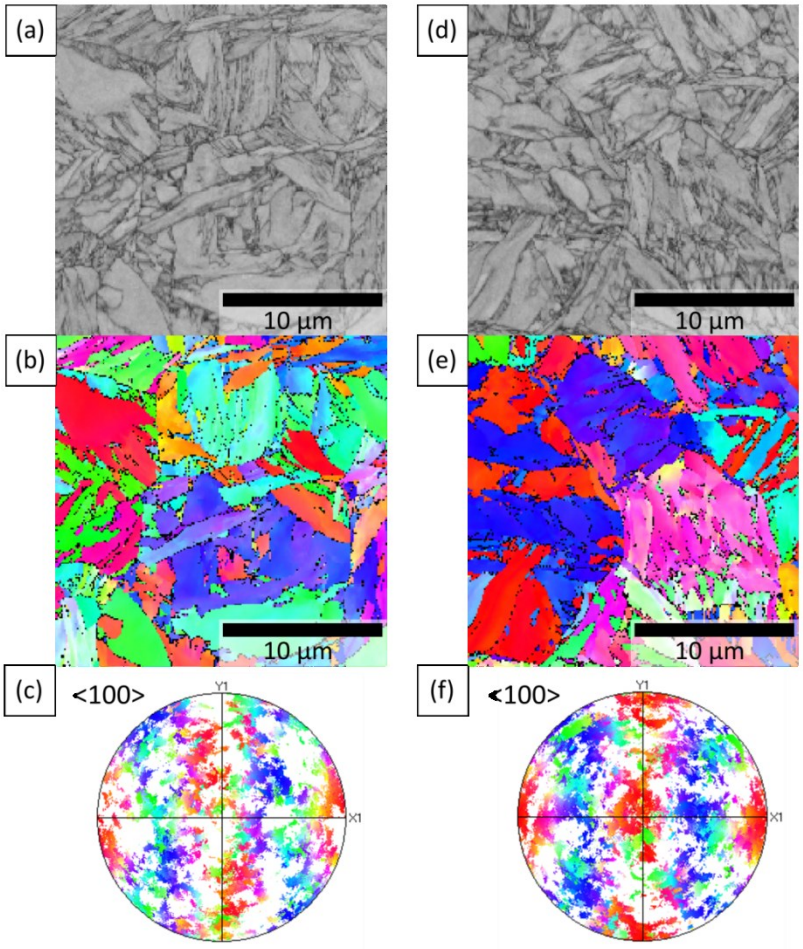

Figure A.11 – EBSD measurements were conducted on ML80 specimen ML80-S7 on the quench face (left column) and in the axial direction (right column). Band contrast (a and d), IPF orientation maps (b and e) and IPFs (c and f) are shown.

EBSD data can be seen for Grade 483 Q&T full sized end quench specimens, at the quench face and in the axial direction, in Figures A.12a-d and Figures A.12e-h respectively. Band contrast (Figure A.12 a and e), inverse pole figure orientation maps (Figure A.12 b and f), IPFs (Figure A.12 c and g) are shown. In the radial direction of specimen TCPL-S1, the band contrast map (Figure A.12a) shows elongated martensite grains. These grains are organized into groups in the IPF orientation map (Figure A.12b). The IPF shows no preferred orientation, with grains scattered throughout the projection sphere (Figure A.12c). In the axial direction of specimen TCPL-S1, the band contrast map (Figure A.12d) shows martensite grains, organized into packets in the IPF orientation map (Figure A.12e). The IPF (Figure A.12f) of the depth axis shows no preferred orientation of grains. The colour coding in Figure A.12 are the same as for Figure A.10 (above).

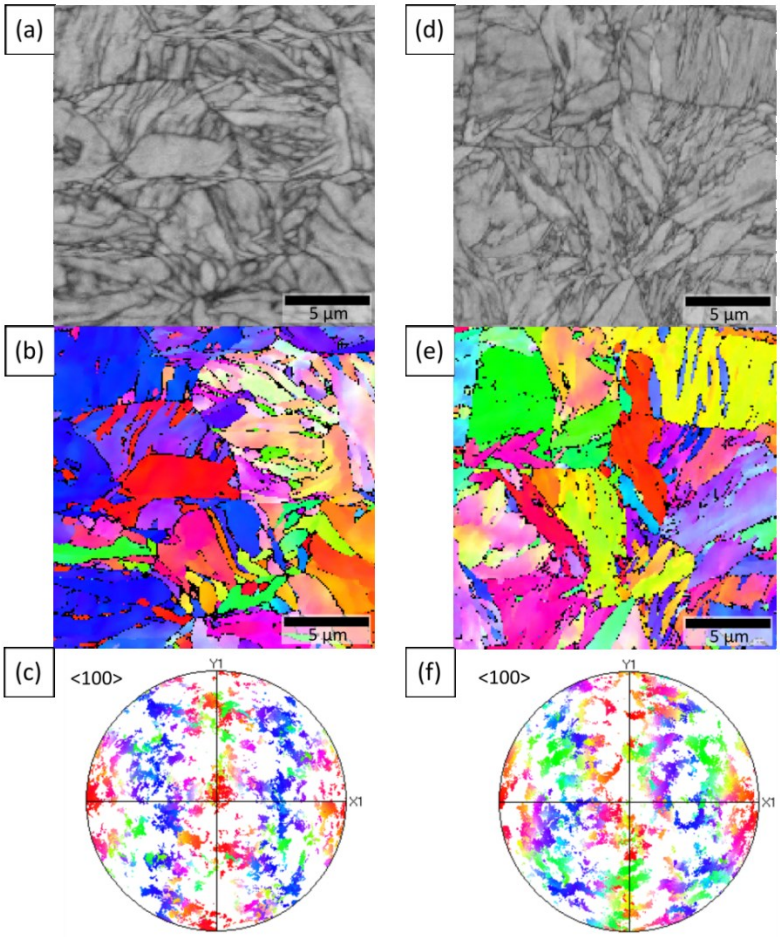

Figure A.12 - EBSD measurements were conducted for Grade 483 Q&T specimen TCPL-S1 on the quench face (left column) and in the axial direction (right column). Band contrast (a and d), IPF orientation maps (b and e) and IPFs (c and f) are shown.

A.6 Amplitude and Energy Attenuation

In Figure A.13, a comparison of attenuation by amplitude and energy measurements is given. The measurements come from disc sample #2 from ML80 subsized end quench specimen ML80-S2. Voltage values in Figure A.13a show the peak amplitude from the first three ultrasonic backwall echoes. Figure A.13b shows the energy obtained from the first three backwall echoes. Both Figure A.13a and A.13b use the same three ultrasonic signals. Amplitude attenuation values show a maximum difference of 7.7% from the average, while energy attenuation values vary by up to 12.5% from the average. For all measurements on ML80-S2, amplitude attenuation values vary between data signals by 9.2% and energy attenuation values vary by 14.4%. Note that additional peaks are used for amplitude attenuation values reported for ML80-S2 in this work.

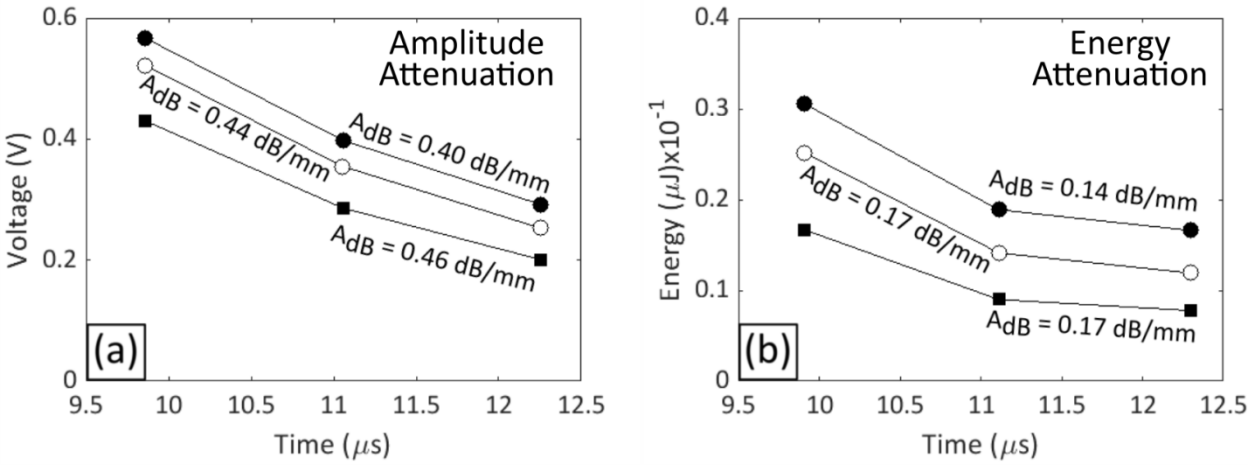

Figure A.13 –Attenuation of (a) backwall echo amplitudes showing less spread between data signals than (b) backwall echo energies, for the ML80-S2 disc sample at a depth of 4.9 mm.

Amplitude attenuation is the standard method used in ultrasonic evaluation, allowing easier comparison with the literature. Energy attenuation directly measures attenuation of ultrasonic waves, which amplitude attenuation measures only indirectly[1]. Amplitude attenuation measurements are more easily performed on signals with unwanted features. Unwanted signals features can include some echo overlap, as shown in Figure A.14a. Energy attenuation requires well-separated echoes to measure properly, as shown in Figure A.14b. Literature results suggest that energy attenuation values perform better in predictive analyses than amplitude attenuation and are additionally less prone to the effects of signal noise[1]. Further research would be required, comparing the two methods to determine which is best suited for measurements in steel.

[1] He, S. H.; He, B. B.; Zhu, K. Y.; Huang, M. X., "Evolution of dislocation density in bainitic steel: Modeling and experiments," Acta Materialia, vol. 149, pp. 46-56, 2018

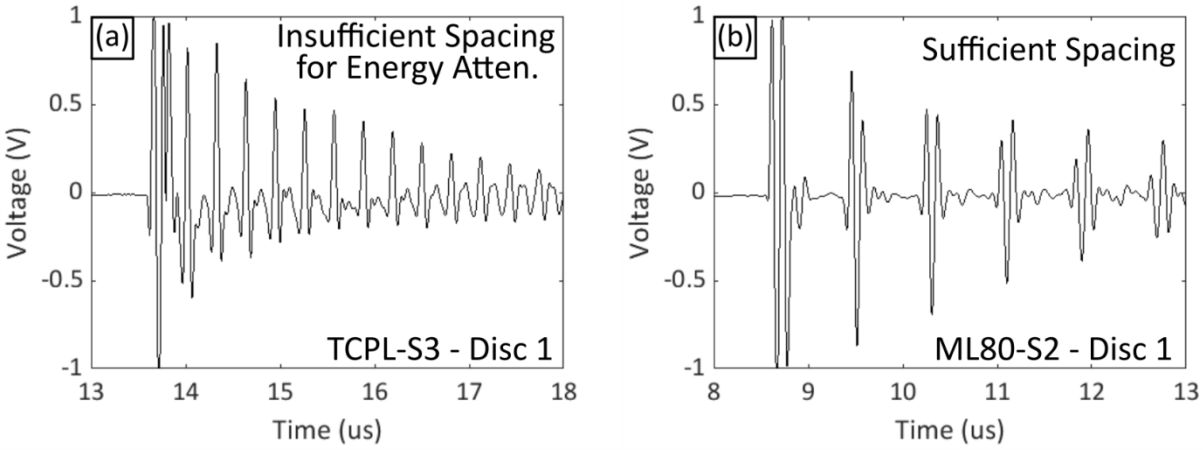

Figure A.14 – (a) Without sufficient spacing between echoes, ultrasonic energy attenuation cannot be measured. Additional spacing (b) between echoes provides space for isolating each echo.

A.7 Frequency Dependant Attenuation

For ultrasonic shear wave signals of Grade 483 Q&T specimen disc samples, the Fourier transform (Section 3.5.3) of a single backwall echo, called the short-time Fourier transform (STFT) produced either single-peaked or bimodal Fourier transform shapes. A single-peaked and a bimodal STFT can be seen in Figure A.15a and Figure A.15b, respectively.

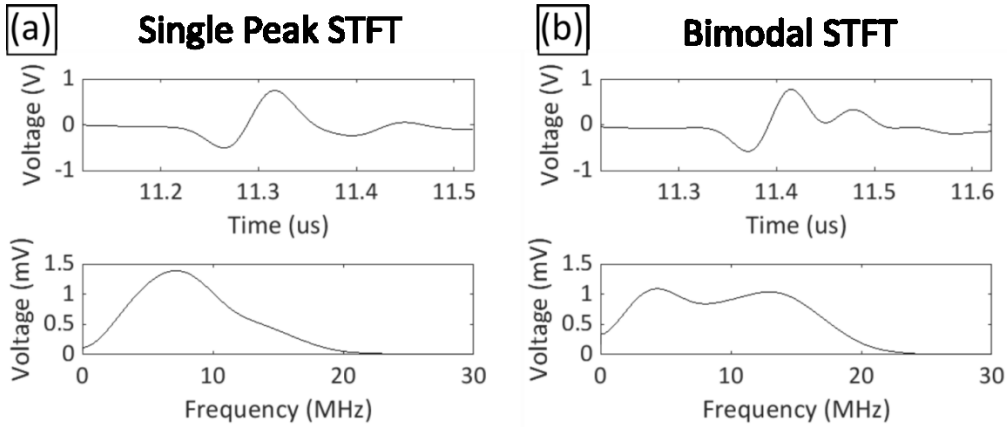

Figure A.15 – Backwall echoes (a and b top) and their STFTs (a and b bottom) for disc samples of Grade 483 Q&T end quench specimens, showing (a) a single peak STFT shape and (b) a bimodal STFT shape.

A.7.1 Peak Frequency of Ultrasonic Shear Wave Signals

Peak frequency measurements were made for Grade 483 Q&T full sized end quench specimens TCPL-S1 and TCPL-S3, using disc samples. Peak frequency was measured for the first five ultrasonic backwall echoes of ultrasonic signals with single-peak Fourier transform shapes. Figure A.16 shows the frequency spectrum for each of the first five backwall echoes of a martensitic disc sample from Grade 483 Q&T end quench specimen TCPL-S3. The peak frequency from each backwall echo is marked in blue.

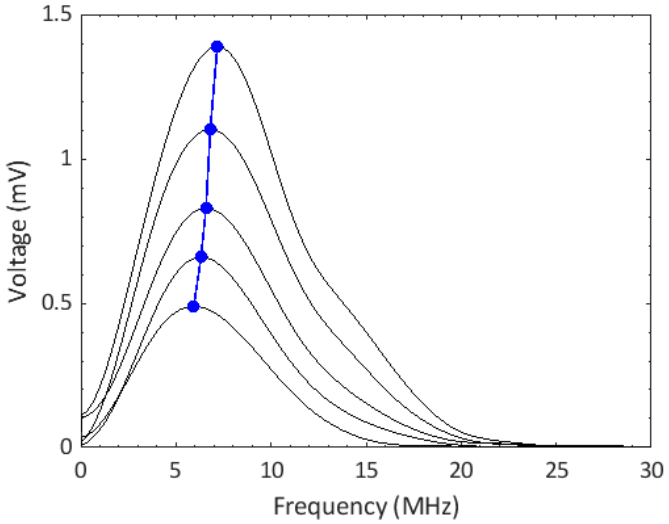

Figure A.16 – Ultrasonic shear wave echoes for disc samples of Grade 483 Q&T specimen TCPL-S3, shown with shrinking spectrum plots (black curves), with STFT spectrum peaks (blue line).

A.7.2 Peak Frequency Analysis

Peak frequency from ultrasonic shear wave signals was calculated for specimens of Grade 483 Q&T. The results of these measurements can be seen in Figure A.17.

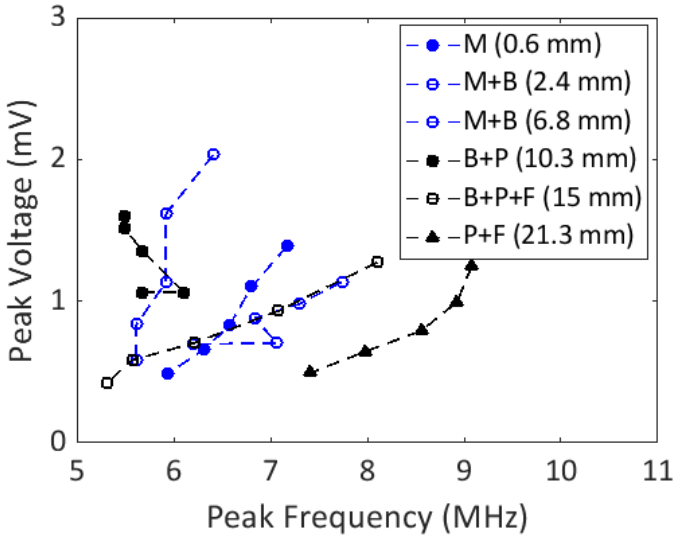

Figure A.17 – Peak frequency values for five backwall echoes from Grade 483 Q&T disc samples. Shear waves were used for these measurements.

Figure A.18 shows peak frequency measurements, normalized by maximum peak voltage and by the frequency of the first peak. Most disc samples show decreasing peak frequency, except for a

disc with a mixed bainite and pearlite microstructure. It is clear from Figure A.18 that peak frequency changes do not show distinct difference based on microstructure.

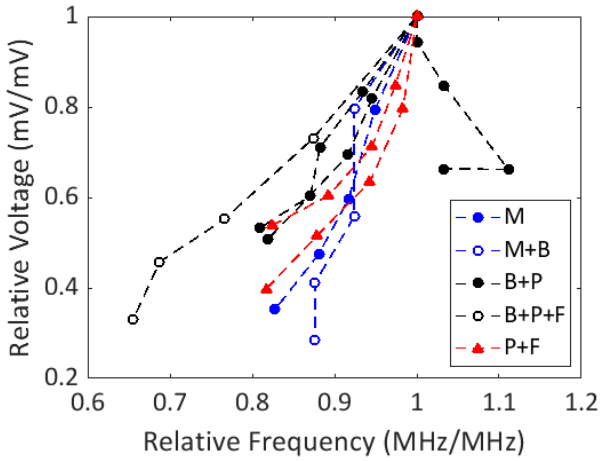

Figure A.18 – Peak frequency for the first 5 backwall echoes, using representative curves from each microstructure group. Data comes from the shear wave signal of Grade 483 Q&T end quench specimens.

A.8 Using Ultrasonic Measurements to Estimate Martensite Fraction

This section covers a method for modelling the martensite fraction through the wall of an ML80 casing and Grade 483 Q&T fitting based on ultrasonic measurements. For the ML80 casing model example, estimates are based on data from the disc samples of ML80 subsized end quench specimen ML80-S2. For the Grade 483 Q&T fitting, estimates are based on data in the radial direction of full sized end quench specimen TCPL-S8.

Data from other Grade 483 Q&T specimens is not used because a complete set of reliable velocity, amplitude attenuation and energy attenuation values are not available for those specimens. Improvements to the model are suggested, with information on drawbacks to the current method.

A.8.1 ML80 Model of Martensite Fraction

Martensite fraction is plotted against ultrasonic longitudinal velocity for disc samples of specimen ML80-S2 in Figure A.19. The three measurement points from the specimen have a linear arrangement and have been fit with a linear least-squares regression. Use of ultrasonic longitudinal values can be used to estimate martensite fraction from the linear fit to the data by this method.

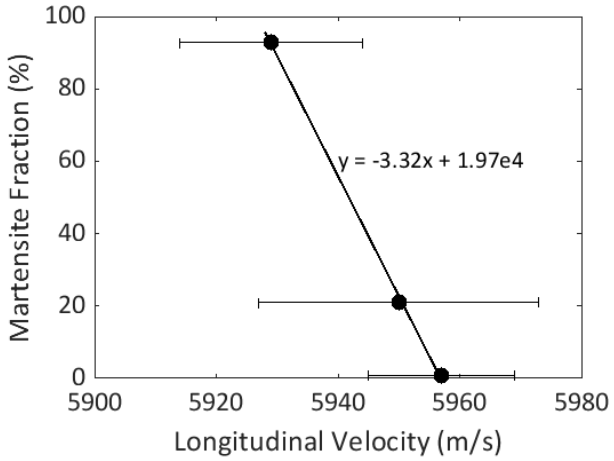

Figure A.19 – Linear fit of ultrasonic longitudinal velocity and martensite fraction for disc samples of specimen ML80-S2.

The relationship between martensite fraction and longitudinal velocity for ML80 steel is linear but consists of only 3 data points. The presence of additional measurements may provide a wider range of velocities or a curve for the relationship between microstructure and velocity. Additionally, the presence of large error bars for ultrasonic measurements prevents interpretation of measurements. This further illustrates problems with using Jominy end quench specimens for correlating microstructure to ultrasonic measurements. Estimation of

microstructure from disc samples of ML80 end quench specimens could not be accomplished for these disc samples given the sources of data for these specimens. Additionally, wide error bars are present on velocity measurements due to the problems faced in producing disc samples with enough thickness control.

A.8.2 Setup of Estimation Model for Martensite Fraction

In a real casing or fitting steel, microstructure may transition gradually across the wall width. This section models Grade 483 Q&T fitting walls using a series of layers to simulate the changes in microstructure occurring through the width, with each layer having a uniform microstructure. Figure A.20 shows this model with *n* layers of material, a_1,a_2,…a_n, where each layer is of a certain thickness, x_1, x_2,…x_n. The number of layers, *n*, is an integer.

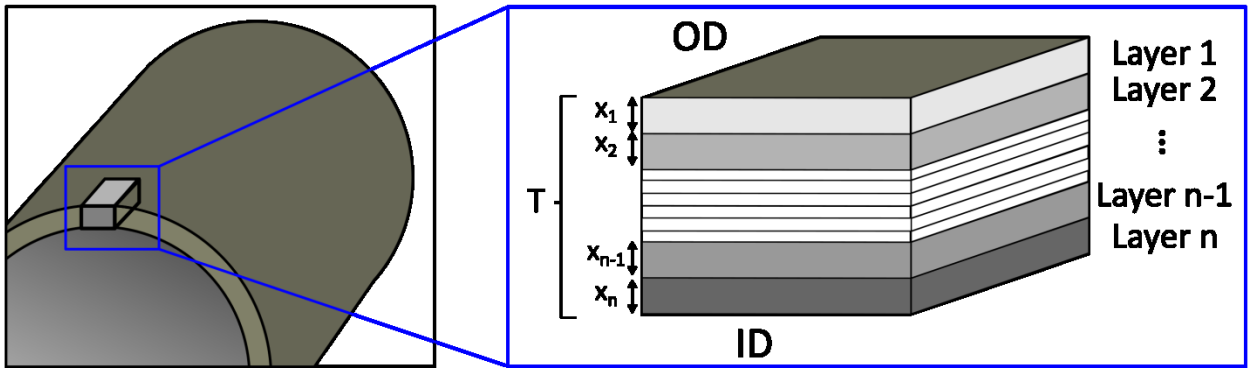

Figure A.20 – The layered structure of a model fitting wall, with *n* layers, each of a unique thickness.

The total thickness of the pipe wall, *T*, may be calculated according to Equation A.15:

$$T = \sum_{i=1}^{n} x_i, \qquad \text{(Equation A.15)}$$

where x_i is the thickness of the i^{th} layer, with both *T* and x_i having units of mm. Note the limitation that for all layers, $0 \le x_i \le T$, because no layer can be larger than the total pipe wall thickness. Layers can be repeated through the thickness of the wall.

The ultrasonic velocity follows a rule of mixtures. The velocity can be different for each layer, but the effective velocity of the entire system results from the thickness of each layer and the velocity of ultrasonic waves in that layer. The effective velocity, v_{eff}, (with units of mm/s) is calculated from Equation A.16:

$$v_{eff} = \sum_{i=1}^{n} \frac{x_i}{T} v_i = \frac{1}{T} \sum_{i=1}^{n} x_i v_i, \qquad \text{(Equation A.16)}$$

where v_{eff} is the overall velocity measured through the wall of the casing or fitting, and v_i is the ultrasonic velocity through the i^{th} layer of the steel (in mm/s). T is the total thickness of the material (in mm) and x_i is the thickness of the i^{th} layer (in mm).

The total martensite fraction, M_{total}, results from the sum of the martensite microstructure in each layer in the wall, and can be calculated from Equation A.17:

$$M_{total} = \sum_{i=1}^{n} \frac{x_i}{T} M_i = \frac{1}{T} \sum_{i=1}^{n} x_i M_i, \qquad \text{(Equation A.17)}$$

where M_i is the martensite fraction ($0 \leq M_i \leq 1$) of the i^{th} layer of the steel.

A.8.3 Grade 483 Q&T Model of Martensite Fraction

Hardness and ultrasonic velocity were measured along the outer diameter of Grade 483 Q&T full sized end quench specimen TCPL-S8. Hardness and microstructure were measured on disc samples from specimen TCPL-S3. Using hardness values from each specimen, microstructure fractions can be interpolated for each ultrasonic test location from specimen TCPL-S8 (Section 4.4.1).

Using the ultrasonic velocity measurements and interpolated microstructure fraction values, test locations of TCPL-S8 are used as layers for modelling martensite fraction in Grade 483 Q&T steel. Layers for this model are shown in Table A.13. Using each of the layers from Table A.13, along with Equations A.16, A.17 and A.18. Martensite fraction can be estimated based on ultrasonic longitudinal velocity for Grade 483 Q&T steel.

Table A.15 – Layers used for microstructure fraction modeling for Grade 483 Q&T fitting steel. Values come from measurements on specimen TCPL-S8 (Section 4.5.1).

Layer	Velocity (m/s)	Martensite Fraction (%)
1	5906.7	97.3
2	5906.8	80.9
3	5908.4	31.9
4	5908.4	19.4
5	5908.9	13.0
6	5909.2	11.2
7	5912.5	10.3
8	5913.9	81.3
9	5914.7	37.2
10	5916.0	22.0
11	5916.9	13.4
12	5917.7	11.4
13	5920.4	10.3

Figure A.21 shows the range of martensite velocities using layers from Grade 483 Q&T measurements. Measurements of Grade 483 Q&T steel do not show strictly increasing ultrasonic velocity for decreasing martensite fraction. The result of the model using TCPL-S8 is a broad range of microstructure fractions for each effective velocity. This range is particularly clear near 5907 m/s, where Layers 1 and 2 span a martensite range of 66.5 % with longitudinal velocity range of only 0.1 m/s. Both measurements were obtained using the small diameter longitudinal wave probe, V203-RM, so the wide range is not a result of ultrasonic probe variations (Section 4.5.1).

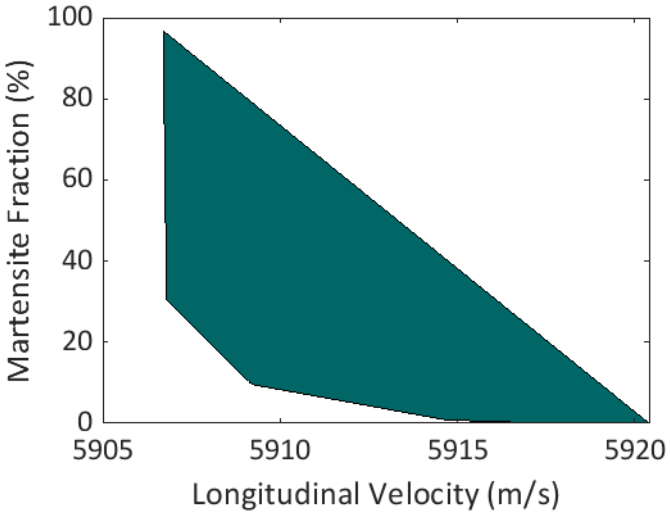

Figure A.21 – Martensite fraction range estimates for Grade 483 Q&T steel as a function of effective longitudinal velocity.

For each longitudinal velocity there may be a wide range of associated martensite fractions. Each martensite fraction within that range is a result of a different combination of layers (Table A.13) that can be used for this modelling exercise. To illustrate the importance of this point, an ultrasonic velocity of 5910 m/s will be considered. A martensite range between 8% and 65% is obtained from this velocity.

On the lowest end of the martensite fraction associated with an effective velocity of 5910 m/s is a fraction of 8%. Such a martensite fraction is obtained from a fitting wall with a combination of Layer 6, with a measured velocity of 5909.2 m/s and a martensite fraction of 9.6%, and Layer 9, with a measured velocity of 5914.7 m/s and a martensite fraction of 0.8%. A combination of 85% Layer 6 and 15% Layer 9 must be used to produce an effective velocity of 5910 m/s with a martensite fraction of 8%.

At the high end of the martensite fraction associated with an effective velocity of 5910 m/s is a fraction of 65% martensite, which results from a combination of Layers 1 and 13 (Table A.13). A wall thickness composed of 76% Layer 1 and 24% Layer 13 will produce the desired effective velocity and martensite fraction. There is a large difference in martensite fraction between the two layers, with Layer 1 having a martensite fraction of 96.8% and Layer 13 having a martensite fraction of 0%. A steel specimen is unlikely to be composed of such disparate microstructures.

Using an effective velocity of 5910 m/s, a wide range of martensite fraction was obtained, from 8-65%. A total martensite fraction of 65% has been shown to be a combination of very different microstructures. This is not the case for the 8% fraction. In general, for Grade 483 Q&T steel, within the possible range of martensite fractions associated with each effective velocity measurement, higher martensite fractions within the range result from combinations of layers

(from Table A.13) with greater differences between them. This fact helps to weight the likely martensite fraction a lower value within the range of possible martensite fractions.

A problem with the example using Grade 483 Q&T steel comes from velocities near 5907 m/s. Both Layers 1 and 2 (Table A.13) have velocities near 5907 m/s but have martensite fractions that differ greatly. The consideration that additional weight should be given to lower martensite fractions within the range means that using the data from specimen TCPL-S8, estimates of martensite fraction will never show when a high fraction of martensite is present. Estimates using this data will always imply that a microstructure with martensite fractions below 50% has a higher probability.

A.8.4 Improvements to Microstructure Fraction Estimation

The method described in this section of estimating martensite fraction based on ultrasonic measurements of velocity can be improved using samples with uniform microstructures with a single morphology. Test specimens with microstructures composed entirely of martensite, bainite, pearlite or ferrite could be used as layers for estimation of microstructure fraction. Additionally, measurements made on such specimens would allow the elimination of using hardness measurements as the intermediate variable for correlating microstructure and ultrasonic parameters.

Estimation of martensite fraction is not possible using the measured results of attenuation. Amplitude attenuation and energy attenuation values strongly depend on the sample dimensions of the ultrasonic test specimen (Section 4.7.2). Without the use of a standard sample geometry, ultrasonic attenuation cannot be compared across measurements effectively and cannot be used to estimate microstructures in steel specimens. The greatest shortcoming of using Jominy end quench specimens for comparing ultrasonic measurements to material properties is the inability to make samples with precise geometries. Regions of interest, such as regions with high martensite fraction, exist over only a small portion of end quench specimens. These small regions cannot be machined into samples on which accurate ultrasonic measurements can be made.

Ultrasonic measurements can be made more accurately for steel samples with a greater thickness. Heat treatment can be accomplished by quenching with a variety of mediums and the various microstructures that are formed can be used to correlate more accurate ultrasonic measurements with steel microstructure and hardness values. Thicker samples can easily be made planar using a surface grinder, which produces the best samples for ultrasonic measurements due to the uniformity in thickness produced. A surface grinder cannot be used to plane disc samples for Jominy end quench specimens because the strength of the magnetic sample holder depends on the volume of the sample being planed. Disc samples, due to their thinness and small diameter do not have enough volume to be kept steady during the machining process.

Estimation of martensite fraction from measurements of ultrasonic parameters could be extended to the use in steel welds if sufficiently accurate measurements could be made. Accurate measurement of ultrasonic parameters could allow estimation of small fractions of martensite that may be observed through a weld. The reinforcement and root regions of a weld make UT through a weld difficult, as wave travel distance may be difficult to determine precisely. Refraction may also cause uncertainty in estimating wave travel distance across a weld. Bending of ultrasonic wave paths would cause incorrect estimates of ultrasonic velocity to be measured[1]. Incorrect estimation of ultrasonic velocity would produce errors in microstructure fraction estimation.

[1] Carreon, H., Barrera, G., Natavidad, C., Salazar, M., Contreras, A., *Relation between hardness and ultrasonic velocity on pipeline steel welded joints*, Nondestructive Testing and Evaluation, vol 31, no. 2, pp. 97-108